Kinetic studies of ether low temperature combustion mechanisms using laser photolysis and modelling

David George Potter

Submitted in accordance with the requirements for the degree of Doctor of Philosophy

The University of Leeds

School of Chemistry

School of Chemical and Process Engineering

November 2019

The candidate confirms that the work submitted is his own, except where work which has formed part of jointly authored publications has been included. The contribution of the candidate and the other authors to this work has been explicitly indicated below. The candidate confirms that appropriate credit has been given within the thesis where reference has been made to the work of others.

Some of the work presented in Chapters 3, 4, and 6 has appeared in publication as follows:

Potter, D.G., Wiseman, S., Blitz, M.A. and Seakins, P.W. Laser Photolysis Kinetic Study of OH Radical Reactions with Methyl tert-Butyl Ether and Trimethyl Orthoformate under Conditions Relevant to Low Temperature Combustion: Measurements of Rate Coefficients and OH Recycling. *The Journal of Physical Chemistry A.* 2018, **122**(50), pp.9701-9711.

I was responsible for the experiments, data analysis and manuscript preparation. The contributions of the other authors were experimental work by SW, laboratory assistance from MAB, and scientific advice and help preparing the manuscript from MAB and PWS.

Some of the work presented in Chapter 4 has appeared in publication as follows:

Potter, D.G., Blitz, M.A. and Seakins, P.W. A Generic Method for Determining $R + O_2$ Rate Parameters via OH Regeneration. *Chemical Physics Letters.* 2019, **730**, pp.213-219.

I was responsible for the experiments, data analysis and manuscript preparation. The contributions of the other authors were laboratory assistance from MAB, and scientific advice and help preparing the manuscript from MAB and PWS.

Dedicated to my late grandfather Donald Clarke

Ideas are like rabbits. You get a couple and learn how to handle them, and pretty soon you have a dozen.

—John Steinbeck

Acknowledgements

Abstract

The laser flash photolysis – laser-induced fluorescence technique has been used to study the reaction kinetics of several potential biofuel ethers under low temperature combustion conditions, in order to extend the understanding of the reactions that occur in novel combustion engines. Biofuels offer a potentially carbon-neutral energy source that could contribute to climate change mitigation, and commercial interest has been given to the ether family of compounds, which display desirable fuel characteristics such as high energy densities and favourable ignition properties.

Chapter 3 presents a study of the reaction between the OH radical and trimethyl orthoformate (TMOF), diethyl- (DEE), di-*n*-butyl- (DBE), methyl *tert*-butyl- (MTBE), and dimethyl ether (DME), from 298 – 744 K in 13 – 190 Torr of nitrogen. This constitutes the first temperature-dependent study of OH + trimethyl orthoformate, and a significant extension of the temperature range of previous studies on the OH + di-*n*-butyl ether and OH + diethyl ether reactions. The temperature dependences of the rate coefficients for OH + ether (all in units of cm^3 molecule^{-1} s^{-1}) can be parameterised by:

$$k_{OH+TMOF}(298\text{–}744\text{ K}) = (8.0 \pm 12.2) \times 10^{-13}\,[(T/298)^{(2.6\pm1.2)} + (T/298)^{(-8.1\pm4.6)}] \times e^{(2.7\pm3.9)/RT},$$

$$k_{OH+DEE}(298\text{–}727\text{ K}) = (1.28 \pm 0.21) \times 10^{-11} \times e^{(-0.11\pm0.59)/RT},$$

$$k_{OH+DBE}(298\text{–}732\text{ K}) = (3.05 \pm 7.13) \times 10^{-12}\,(T/298)^{1.3\pm1.6} \times e^{(6.4\pm5.8)/RT},$$

$$k_{OH+MTBE}(298\text{–}680\text{ K}) = (9.8 \pm 21.6) \times 10^{-13}\,(T/298)^{2.7\pm1.5} \times e^{(2.5\pm5.6)/RT},\text{ and}$$

$$k_{OH+DME}(298\text{–}656\text{ K}) = (1.22 \pm 2.83) \times 10^{-15}\,(T/298)^{6.9\pm0.5} \times e^{(19.1\pm3.8)/RT}.$$

Chapter 4 presents a technique for determining R + O_2 rate coefficients and OH yields by the observation of OH regeneration from chemical activation. This technique was verified using the CH_3OCH_2 + O_2 reaction in the dimethyl ether system via comparison with previous measurements, and analyses using numerical integration software determined the optimum experimental conditions for the method. Potentially, this technique can be used to obtain rate parameters important for the combustion modelling of a wide range of potential fuel molecules. Rate coefficients for the system are reported at 291 – 483 K, in 4.1 – 32.6 Torr of nitrogen, and the mean room temperature rate coefficient was determined to be $k_{CH3OCH2+O2}$ = (0.94 ± 0.04) × 10^{-11} cm^3 molecule^{-1} s^{-1}, across all pressures explored.

Chapter 5 employed the technique described in Chapter 4 to present novel measurements of the $C_2H_5OC_2H_4$ + O_2 reaction rate coefficient integral to the low

temperature combustion of diethyl ether under experimental conditions of 298 – 464 K, in 5.2 – 28.4 Torr of nitrogen. The mean 298 K rate coefficient was determined to be $k_{C2H5OC2H4+O2}$ = $(3.10 \pm 0.55) \times 10^{-11}$ cm^3 molecule^{-1} s^{-1}. OH yields and rate coefficients were compared to *ab initio* calculations of the diethyl ether low temperature oxidation surface at the CCSD(T)/Jun-cc-pVTZ//M06-2X/Jun-cc-pVTZ level, using master equation methods. The transition state barrier to the OH product was required to be lowered by ~7 kcal mol^{-1} in order to achieve good agreement between experimental data and theoretical calculations.

Chapter 6 reports some initial observations of subsequent OH regeneration following the R + O$_2$ reaction at higher temperatures (~500 K and above), and some interesting unwanted chemistry occurring under high temperature and high O$_2$ conditions. The main recommendations for future work are further explorations of the source of this extraneous chemistry, and development of the data interpretation under such conditions. The investigation of a wide range of fuels' R + O$_2$ reactions using the method presented in Chapter 4 should also be carried out to improve estimated rates in combustion models.

Table of Contents

List of Figures

List of Tables

List of Abbreviations

AM	Absolute method
COP	Conference of the parties
DBE	Di-*n*-butyl ether
DCM	4-(dicyanomethylene)-2-methyl-6-(4-dimethylaminostyryl)-4H-pyran
DEE	Diethyl ether
DFT	Density functional theory
DIPE	Di-*iso*-propyl ether
DMB	2,3-dimethyl butane
DME	Dimethyl ether
DMM	Dimethoxymethane
EGME	Energy grained master equation
ETBE	Ethyl *tertiary*-butyl ether
FAGE	Fluorescence assay by gas expansion
FTIR	Fourier transform infrared spectroscopy
GC	Gas chromatography
GHG	Greenhouse gas
HCCI	Homogeneous charge compression ignition
HPMF	Hydroperoxymethyl formate
ILT	Inverse Laplace transform
IPCC	Intergovernmental panel on climate change
IR	Infrared
IUPAC	International union of pure and applied chemistry
JSR	Jet-stirred reactor
LASER	Light amplification by stimulated emission of radiation
LFP	Laser flash photolysis

LIF	Laser-induced fluorescence
MESMER	Master equation solver for multi energy-well reactions
MFC	Mass flow controller
MTBE	Methyl *tertiary*-butyl ether
OME	Oxymethylene ether
PES	Potential energy surface
PIMS	Photoionisation mass spectrometry
PM	Particulate matter
PMT	Photomultiplier tube
ppb	parts per billion
ppt	parts per trillion by volume
PTR-MS	Proton transfer reaction – mass spectrometry
RCP	Representative concentration pathways
RF	Resonance fluorescence discharge lamp
RM	Relative method
RRKM	Rice-Ramsperger-Kassel-Marcus
SAR	Structure activity relationship
SI	Spark-ignition
TAEE	*Tertiary*-amyl ethyl ether
TAME	*Tertiary*-amyl methyl ether
TIR	Transient infrared
TMOF	Trimethyl orthoformate
ZPE	Zero point energy
TST	Transition state theory
UV	Ultraviolet
VIS	Visible
YAG	Yttrium aluminium garnet

Chapter 1 Introduction

This chapter provides context to the work carried out in this thesis, by giving an overview of the motivations driving the research undertaken. Broadly, the introductory chapter focuses on the principles of climate change; the potential for transport biofuels to mitigate the severity of anthropogenic contribution to climate change; properties of the ethers studied in this thesis, focused on the well-researched dimethyl ether, and higher ethers; combustion mechanisms and engines; and the principles of chemical reactions utilised to formulate experiments and analyse the data that form this thesis.

1.1 Climate Change

Climate change and its potential solutions have become possibly the most important and debated scientific and political issue of recent times. Evidence collated from modern day temperature recordings [1], past temperature extrapolations such as those from ice-cores [2], and modelling studies [3], prove that global warming is heavily exacerbated by anthropogenic activity to a degree of certainty the Intergovernmental Panel on Climate Change (IPCC) now regard as "unequivocal" [4]. Increasing concentrations of CO_2 (Figure 1-1) and other greenhouse gases (GHGs) give rise to this atmospheric warming effect, in what is a well understood mechanism. Greenhouse gases are molecules which are infrared (IR) active, containing a permanent or transient dipole moment, where, upon absorbing infrared radiation, the dipole moment is induced by vibration and rotational-vibration [5]. UV/VIS (ultraviolet/visible) sunlight is re-radiated from the Earth's surface as IR radiation, and subsequently absorbed by the GHGs in the atmosphere. Once absorbed, the radiation can be emitted back towards the Earth's surface, heating up the surface, or the atmosphere through energy transfer. This mechanism traps heat in the atmosphere via certain gases, acting somewhat similarly to a greenhouse glass roof.

Carbon dioxide was first shown to absorb IR radiation by John Tyndall in 1859, along with other molecules such as water vapour, methane and ozone [6]. Now, it is virtually unanimously acknowledged that GHGs are the cause of current warming trends. Anthropogenic emissions from sources such as fossil fuels burned to generate energy; farming livestock for the food industry; and waste disposal, have led to an increase in carbon dioxide and other greenhouse gases that exhibit positive radiative forcing, since

the start of the industrial revolution in 1750 (Figure 1-1). The resultant temperature increase has also been observed over the past century (Figure 1-2), and when compared with long-term temperature records from ice-cores, the current trend in increasing temperature is not only more rapid than anything seen for thousands of years, but the temperature anomaly (the difference between measurement and reference, where the reference in this case is the temperature between 1961 and 1990) is also higher than previous measurements (Figure 1-3).
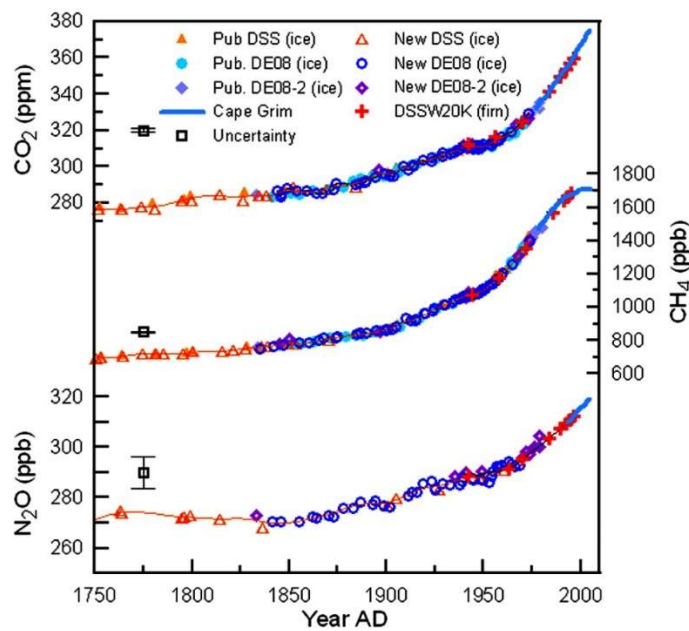
Figure 1-1: Law Dome ice core and firn air records since the year 1750, showing the increasing concentrations of three greenhouse gases. Contemporary records from Cape Grim are also shown. Thin lines are spline fits [7]: 20 year smoothing for methane and carbon dioxide, 40 year smoothing for N₂O. Reproduced from MacFarling Meure et al. [8].

Recently a more focused global effort to tackle climate change was renewed with the Paris Agreement, formulated at COP 21 (21st Conference of the Parties), laying out targets to limit warming to well below 2 ℃, ideally 1.5 ℃, and emphasising national action as the driver behind climate change mitigation [9]. The most recent IPCC assessment report projected temperature anomalies that may be reached in the future, using RCP (representative concentration pathways) based on GHG emissions [3]. Three out of four of their RCP scenarios exceed a warming of 2 ℃ by the year 2100. Only with aggressive mitigation does their most optimistic scenario manage to keep warming below

2 °C, highlighting the urgent need for countries to reduce their greenhouse gas emissions significantly.
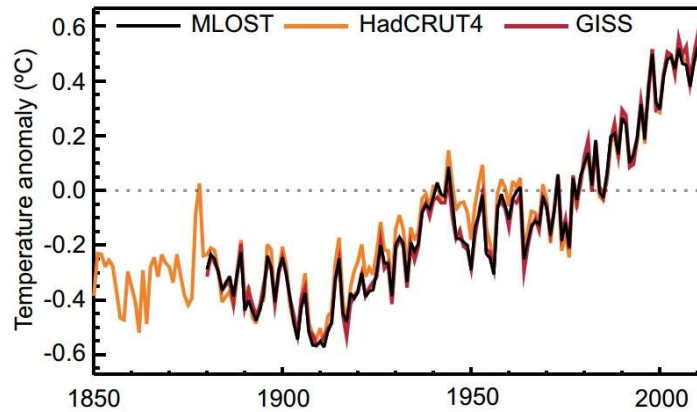
Figure 1-2: Increase in annual global mean surface temperature anomaly since 1850 AD, relative to a 1961 – 1990 climatology from the most recent version of the three land-surface air temperature and sea-surface temperature data sets combined (HadCRUT4, GISS and NCDC MLOST). Reproduced from Hartmann et al. [1].

Should atmospheric warming be allowed to continue at the current rate, by the end of the 21st century, the IPCC report states with high confidence (95%), that there will be "severe, widespread and irreversible impacts globally", as a result of a 3.7 – 4.8 °C predicted temperature anomaly by 2100, compared with pre-industrial levels [10]. The consequences could be catastrophic, and include species extinction, food security risks, and extreme weather events. To combat this threat, a plethora of methods for reducing CO_2 and other emissions have been proposed, including carbon capture and storage, geo-engineering, afforestation, and the use of alternative renewable energy sources.
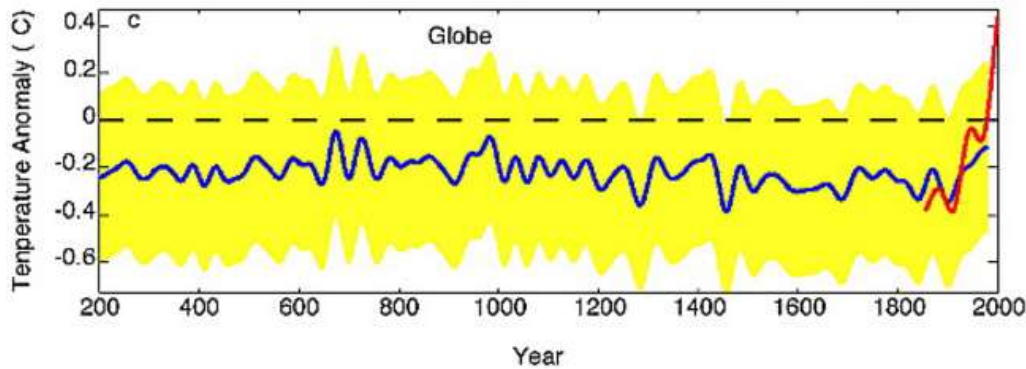
Figure 1-3: Reconstruction of previous two millennia temperature anomalies based on 1961–1990 instrumental reference period (dashed line). Blue line represents global mean surface temperature reconstruction, red line modern day observations. Yellow shading represents the 95% confidence limits. Reproduced from [11].

1.2 Biofuels

One renewable energy source is bioenergy, which has the potential to be carbon-neutral, and is essentially any source that derives its energy from biological organisms. In theory, any carbon that is released upon burning a bioenergy source, such as biomass, will have been recently sequestered from the atmosphere throughout the lifetime of the plant via photosynthesis. Thus, if the process of producing and transporting bioenergy does not use CO_2, no additional CO_2 is released into the atmosphere. Coupled with carbon capture and storage, bioenergy also has the potential for 'negative' carbon emissions [12].

A bioenergy source group that may have a large capacity for CO_2 emissions mitigation in the future is that of biofuels, where transport fuels are derived from renewable biological matter such as plants, animal wastes or organic manufacturing wastes. Biofuels could supplement or even replace the use of fossil fuels such as diesel and petrol, where 33% of UK CO_2 emissions arose from the transport sector in 2018 [13]. In the European Union, approximately 23% of GHG emissions are due to the transport sector [14]. Currently, biofuels account for approximately 3% of global transport demand [15], and in 2016 biofuels accounted for a 91% share of global renewable road transport fuel [16]. Bioethanol and biodiesel account for the majority of current biofuels, sharing 37% and 56% of the renewable fuel used in the UK in 2019 so far [17], and overall global transport biofuel manufacture grew ~7% year-on-year in 2018 [15]. Hydrogenated vegetable oils also hold a small, but increasing share in total biofuel production. Although their primary application is for road vehicles, biofuels began to see usage as an aviation fuel in 2016 [18]. Despite various advantageous properties of biofuels compared to

conventional fossil fuels, such as carbon-neutrality and renewable supply, there are also issues to consider, such as the food *vs* fuel debate, where food security would be at risk should extensive land be used to grow biofuels to substantially contribute to global energy [19]. In addition, careful production practices must be used to ensure deforestation and large energy consumption during the manufacture and transportation of biofuels does not lead to positive net carbon emissions. Generally biofuels currently offer decreased pollutant emissions but greater NO_x (NO_2 + NO) production from engines [20]. GHG savings compared to fossil fuel use were estimated to be 81% in the UK [17], and with legislation now passed committing to net zero emissions by 2050 in the UK [21], biofuels could make an important contribution moving forward.

Other alternatives to conventional transport fuels may have a role to play, such as hydrogen and electricity, however combustion is still an attractive proposition for powering transportation, due to the high energy density of fuels, a well-developed understanding of combustion, and the relative ease with which alternative combustion fuels could be ingratiated into existing infrastructure. This high energy density is a considerable advantage that biofuels still possess over other sources of renewable transport energy such as lithium-ion batteries, and hydrogen. Hydrogen has a very high energy density per mass, but its low mass density means liquid hydrogen has a low energy density for practical use in transport, of 8 MJ L^{-1} [22]. Similarly, the Panasonic 2170 cell used in the most recent Tesla vehicle equates to roughly 2.6 MJ L^{-1} [23]. These energy densities are much lower than for something like diethyl ether studied in this thesis, which possesses an energy density of approximately 26 MJ L^{-1} [24].

1.3 Bio-Ethers

Ether biofuels are emerging as a possible replacement for conventional fuels, or as a blending agent with petrol and diesel fuels [25]. Potential biofuel ethers include dimethyl ether (DME), and diethyl ether (DEE). They are not widely used as standalone fuels currently, but progress has been made, with gradual advancement towards commercial DME fuel use. Ford, in partnership with Oberon Fuels, announced a research project in 2015 that aims to develop the first cars to run on DME, along with oxymethylene ether (OME) (Table 1-1), citing lower particulate emissions than diesel and increased fuel efficiency as the primary advantages within reach [26]. Volvo are another large company that have demonstrated biofuel ethers' potential for commercial

use, utilising a fleet of heavy lorries running on DME fuel for two years starting in 2010 [27]. Field testing continued into 2015 and Volvo remain confident about DME as a fuel [28], pledging to continue to develop DME engines for commercial use in their subsequent Annual and Sustainability Report [29].

Aside from DME and DEE, other possible bio-ethers include di-*n*-butyl ether (DBE), methyl *tertiary*-butyl ether (MTBE), ethyl *tertiary*-butyl ether (ETBE), *tertiary*-amyl methyl ether (TAME), *tertiary*-amyl ethyl ether (TAEE), trimethyl orthoformate (TMOF), and di-*iso*-propyl ether (DIPE) (Table 1-1), which show more potential as conventional fuel additives [30, 31]. DME, DEE, DBE, MTBE and TMOF have all been studied in this thesis, and some of their properties are detailed Table 1-2, in comparison to conventional fuels, and gasoline.

Table 1-1: Molecular structure of various potential bio-ether fuels and additives.

Table 1-2: Properties of ethers studied in this thesis, and common fuels.

Property	DME	DEE	DBE	MTBE	TMOF	diesel	biodiesel	gasoline
Formula	C_2H_6O	$C_4H_{10}O$	$C_8H_{18}O$	$C_5H_{12}O$	$C_4H_{10}O$	C_8-C_{25}[a]	C_{12}-C_{22}[a,b]	C_4-C_{12}[a]
Energy density[c]	20.6[d]	26.3[e]	28.9[f]	28.2[g]	–	33.3[d]	32.3[g]	32.8[d]
b.p. / °C	-24.9[h]	34.6[e]	141[f]	55[i]	~101[j]	125-400[h]	330[e]	38-204[h]
Cetane rating	55-60[k]	>125[e]	100-115[e,l]	–	–	~55[k]	52[e]	–
Octane number	–	–	–	98-123[m]	–	–	–	80-100[g]
Self ignition T / °C	350[i]	363[e]	175[n]	374[i]	255[o]	316[a]	150[a]	247-280[g]
Flash point / °C	–41[i]	–49[g]	25[n]	–33[i]	9[j]	74[a]	100-170[a]	–43[g]
C / wt.%	52.1	64.9	72.2	68.1	45.3	87[o]	78[d]	85.5[o]
O / wt.%	34.7	21.6	13.1	18.2	45.2	trace	10[d]	<3.7[p]

[a]From ref [32]. [b]Methyl esters of C_4-C_{12} fatty acids. [c]Units of MJ L^{-1}. [d]From refs [33, 34]. [e]From ref [24]. [f]At 15 °C, from ref [14]. [g]From ref [35]. [h]From refs [34, 36]. [i]From Sigma Aldrich. [j]From ref [37]. [k]From refs [34, 38]. [l]From ref [39]. [m]From ref [40]. [n]From ref [41]. [o]From Fisher Scientific. [p]From ref [42].

1.3.1 Dimethyl Ether

Dimethyl ether is currently considered a potential alternative fuel to conventional fuels such as petrol and diesel, due to its promising properties and feasible production as a biofuel. Several production routes for DME are possible, with feedstocks including methane (via methanol), biomass, and coal [43]. For bio-DME, biomass can be gasified in order to produce syngas (mostly a mixture of hydrogen, carbon monoxide and carbon dioxide), which can then undergo copper catalytic conversion to produce methanol, before de-hydrogenation of the methanol to form DME, using zeolite- or alumina-based catalysts [38]. These two steps can be combined to occur simultaneously when using different catalysts.

Since 1996, between 100,000 and 150,000 tonnes of DME have been produced globally each year for various uses [38]. The Ghuangzhou Institute of Energy Conversion in China brought a DME-from-biomass demonstration plant to test phase in 2009, producing 1000 tonnes of DME per year by gasification of wood chips, achieving up to 38% total system efficiency, and self-sustaining electricity and steam use [44, 45]. Similarly, a 100 tonne per year pilot plant has been developed in China, synthesising DME through gasification of corn core [46]. More recently BASF and Linde have

announced plans to commercialise a process that achieves 50% CO_2 reductions in producing DME [47], and Oberon Fuels were awarded a grant to produce renewable DME in California [48].

Coal-based DME has also been shown by life cycle assessment to have fewer related greenhouse gas emissions than coal-based diesel [49], so even if DME were to be used as a fuel or fuel-additive having not been derived as a biofuel, it may still offer advantageous carbon savings. Production of DME by this route involves gasification of coal to produce synthesis gas (primarily H_2, CO, and some CO_2), which can be used to generate methanol, and ultimately DME.

DME overall shows favourable properties for fuel use. A cetane rating (an indicator of combustion speed for compression ignition) of approximately 55 – 60 is comparable to that of diesel (~55) [34, 38], where a higher number is indicative of desirable properties in a fuel, such as a shorter ignition delay time, and increased burning efficiency. The relatively high oxygen content of DME (1O:2C) and lack of any carbon-carbon bonds results in a clean-burning fuel that releases no [38] or little [50] soot, reducing its negative impact on tropospheric air quality. The zero sulphur content of DME, and other ether biofuels, shows another marked advantage over conventional fuels in terms of pollutant emissions.

Disadvantages are still present for dimethyl ether, primarily the lower energy density reported in Table 1-2, which is significantly lower than diesel and gasoline's, and is caused by the low carbon:oxygen ratio of atoms. As a result of the lower combustion enthalpy of the bioether, a greater volume of the fuel would have to be injected, over a longer period, in order to match the energy delivered by diesel [38]. Indeed, Volvo reported that due to the ~45% energy content drop of DME compared to diesel, larger fuel tanks were used in their lorry fleet in order to compensate, and common rail technology was used for biofuel injection so as to achieve high enough pressures to liquefy the dimethyl ether [27]. The lower viscosity of DME compared to diesel can also cause issues, due to resultant increased surface wear on engine parts, and the possibility of leakage from fuel supply system seals [38]. Existing as a gas under normal conditions also complicates the method of fuel injection used for DME [51].

Conversely, a low boiling point gives rise to fast evaporation if DME were to be delivered as a liquid into an engine cylinder [38]. Further advantages of DME that counteract the undesirable properties outlined above are its low combustion noise pollution [27, 50], and the potential for low NO_x release during combustion [38, 51] using

techniques such as pre-mixed combustion and exhaust gas recirculation (where a portion of exhaust gases is recycled back to the combustion cylinders, reducing peak temperatures via dilution of oxygen with inert gases).

Low temperature autoignition of dimethyl ether is important for its combustion in engines, due to the necessity for control over ignition timing. This control is important for the prevention of knocking [52], and in the event of leakages during transport, the prohibition of explosive organic peroxide formation [53]. As such, a full understanding of its autoignition mechanism is required.

1.3.2 Diethyl Ether

Diethyl ether is similar to DME, with the infrastructural advantage of being in liquid state at room temperature [54]. Where DME is derived from methanol dehydration, DEE is produced in the same way by ethanol dehydration, owing to the longer carbon chains either side of the oxygen. Much like DME, DEE is a suitable potential diesel replacement fuel due to its high cetane number (>125), high oxygen content, reasonably high energy density and low autoignition temperature (see Table 1-2). Due to the greater ratio of C:O, DEE should possess a greater energy density compared to DME. However, it is also a highly volatile fuel, undergoes peroxidation when stored, has low lubricity and has associated human health concerns as an anaesthetic [55]. Currently there have been fewer studies on DEE as a biofuel compared with DME, but some work has analysed its ability to operate when blended with other fuels such as liquified petroleum gas [56-58], and it is a known cold-start aid for engines.

As a fuel blend with diesel, DEE has been shown to reduce particulate matter (PM) emissions up to 24% with a 30% blend [59]. NO_x was also demonstrated to diminish with the addition of DEE to the fuel, but some increase in total hydrocarbon and CO was observed. Tree and Cooley [60] also saw reduced PM production when blending DEE with diesel. Lower CO and smoke emissions have been observed in several studies with the addition of DEE to diesel fuel [61-63].

1.3.3 Di-*n*-Butyl Ether

Di-*n*-butyl ether is the fourth of the straight chain symmetrical ethers (after DME, DEE, and di-*n*-propyl ether), and is of relatively recent interest as a potential replacement

fuel, where it can be produced from pulping of biomass and fermentation of cellulose [14], where dehydration of bio-butanol yields DBE [64]. DBE also has several desirable diesel-replacement fuel qualities, including reduced hydrocarbons, CO, and noise, when compared with diesel. An estimated cetane rating of 115 (Table 1-2) has led to its testing as an ignition enhancer in fuels, and it mixes well as a result of low viscosity, low boiling temperature, and low heat of vapourisation [39]. DBE has also demonstrated desirable spray characteristics [65]. Soot reduction has been observed through engine testing and laminar flame studies [66], sometimes up to 20% compared with diesel [67], or even near soot-free [39]. Conversely, Damyanov et al. [14] did not see a reduction in emissions from diesel engine testing. Ignition delay time studies [68, 69] demonstrated DBE fuel exhibits short ignition delay times, indicating higher reactivity than both DME and DEE.

Despite some of the favourable properties and potential DBE has shown for its application as a renewable fuel, as the early stage of the research conducted may suggest, it has not yet been used as a transport fuel commercially.

1.3.4 Methyl *tert*-Butyl Ether

Currently bio-MTBE is the most commercially available biofuel oxygenate used for petroleum blends, and can allow cleaner combustion and more efficient engine performance. It has been favoured for its compatibility with gasoline, with high miscibility, and good storage stability [70]. Synthesis from methanol and *iso*-butene [71] implies bio-methanol [72] can also be used to enable at least partially bio-derived MTBE. Despite its previous extensive use in the US, fears over contamination of groundwater due to its high solubility in water led to a ban and phasing-out of MTBE in the US. It is however still exported to, and used in, Central and South America.

MTBE has been added to fuels as an octane improver [73] (see octane number in Table 1-2), and has been shown to reduce petroleum exhaust gas emissions by 10 – 15%, 1.0 – 1.7%, and 10 – 20% for CO, NO_x and total hydrocarbons respectively with 15% v/v MTBE addition [74]. Conversely, other studies have shown no change in these emissions [75-77], and such studies depend heavily on the testing conditions used, such as temperature and blending ratios. Additionally, exhaust emissions as a result of MTBE addition have been demonstrated to exhibit increased ethanol and formaldehyde [78-80], known irritants and causes of respiratory problems. Its use as an octane enhancer (and

therefore anti-knock agent), may also suggest MTBE will not be well suited to a diesel-type fuel that undergoes autoignition via chain-branching (discussed in section 1.4.2).

1.3.5 Trimethyl Orthoformate

Trimethyl orthoformate (also known as trimethoxy methane) has the potential to be used as an alternative fuel, or fuel additive, owing to its production route from methanol, and therefore bio-methanol [81]. Its similarity to dimethyl ether in structure, with no carbon-carbon bonds, suggests it may be of similar use as an alternative fuel.

Currently there are no extensive studies on its use as a fuel, although it has been mixed with methanol in a test compression ignition engine, which ran successfully with 20% TMOF [82]. Potential has been shown, however, for its use in fuel cells [37, 83-85], where a great number of alternative fuels to those such as methanol are being investigated, in order to increase the likelihood that low-temperature fuel cells will penetrate the transport market. Although TMOF was seen to be less efficient when compared with methanol, it was also noted that its similar energy density, higher boiling point (Table 1-2), higher flash point, and lower toxicity in comparison with methanol were advantages [37, 83].

1.4 Hydrocarbon Combustion

Combustion involves the rate of reaction accelerating to a point where reactants are consumed, and in doing so, rises in temperature and pressure accompany a large release of energy, which can be harnessed for use in power generation, heating, explosive weapons, and transport fuels.

In typical transport fuel combustion, usually involving petroleum, or diesel, decomposition of the fuel to smaller species dominates the process, and it is more useful to use computational fluid dynamics to model the nature of combustion. Chemistry still occurs and can be important, but it is less fuel-specific, hence it may be more useful to study properties such as mixing, rather than understanding the detail of chemical reactions occurring. Low temperature combustion however, is much more sensitive to specific reactions occurring, thus knowledge of their rate coefficients becomes very important. Low temperature combustion mechanisms are important for alternative fuel combustion in novel engines that rely on autoignition of the fuel to start combustion, rather than a

spark. Additionally, the same autoignition mechanisms cause engine knock, where fuel in a typical gasoline engine ignites before the flame has reached it. This effect results in loss of power, and can damage the engine, meaning the understanding of low temperature combustion mechanisms for potential biofuels is important not only for their use as standalone fuels, but also fuel additives to gasoline.

1.4.1 High Temperature Combustion

At high temperatures above approximately 1000 K, combustion chemistry will still be somewhat influenced by the abstraction of H atoms from the parent fuel by small species (OH, H, and O). Rapid repetition of this reaction takes place until CO_2 remains. Soot precursors and other products will also remain.

Despite abstraction reactions still taking place, due to the extreme speed of higher hydrocarbon molecule and radical decomposition in this regime, only a small group of non-fuel-specific reactions bear any significant effect on the overall reaction rate. Primarily these are the reactions between H and O_2 to form O + OH, the equilibrium between CO + OH and H + CO_2, and the decomposition of HCO to H + CO. These are the main reactions controlling the concentration of H atoms and the total amount of radicals in the system. An example showing the sensitivity of a methane-air flame sensitivity to the H + O_2 reaction is presented in Figure 1-4.
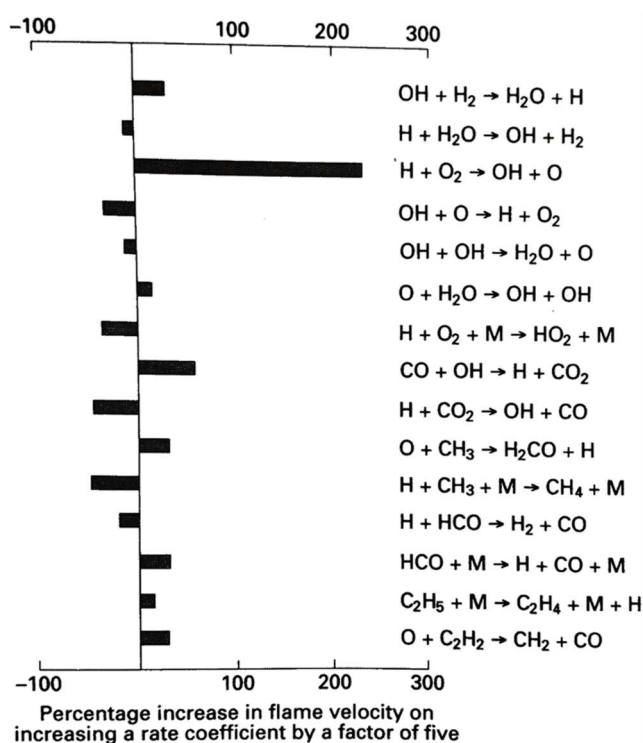
Figure 1-4: Typical sensitivity diagram for the effect on flame velocity of a stoichiometric methane-air mixture, where each rate coefficient is varied by a factor of five. Reproduced from [86].

1.4.2 Low Temperature Combustion

Low temperature combustion occurs below 1000 K, typically within the range 500 to 800 K, and is much more dependent on the hydrocarbon fuel used. Hydrogen abstraction from the parent fuel, RH, is again the initial step, where an R radical is formed (reaction R 1-1). The major initiating radical here (X) is typically a small species, such as OH, O or H, although other species can also abstract, such as O_2. Reaction R 1-1 is particularly relevant to the work in Chapter 3.

$$RH + X \rightarrow R + HX \qquad\qquad\qquad \text{R 1-1}$$

Addition of oxygen to the R radical forms a peroxy radical, RO_2 (reaction R 1-2) (studied in Chapter 4 and Chapter 5), which can undergo isomerisation via internal H-abstraction to form the QOOH radical (reaction R 1-3). The rate of RO_2 to QOOH isomerisation will depend on the structure of the radical involved, and the ring-structured transition state that is formed in the reaction. Smaller ring structures will have a larger pre-exponential factor, as the statistical likelihood of the correct orientation for internal

abstraction being achieved increases. However, larger rings will be favoured due to the decrease in ring strain of the transition state. Thermal decomposition of this QOOH radical to an OH radical and smaller stable species propagates the reaction (reaction R 1-4).

$$R + O_2 \rightarrow RO_2 \qquad\qquad\qquad \text{R 1-2}$$
$$RO_2 \leftrightarrow QOOH \qquad\qquad\qquad \text{R 1-3}$$
$$QOOH \rightarrow OH + \text{stable product} \qquad\qquad\qquad \text{R 1-4}$$

Alternatively, to undergo chain-branching of radicals, molecular oxygen can intercept the hydroperoxide radicals in reaction R 1-5, generating the QOOH-peroxy radical, O_2QOOH. This transient species is believed to be integral to the autoignition of fuels at low temperatures, where another isomerisation and decomposition provides the first of the two 'branching' OH radicals, along with a ketohydroperoxide product, $OQ'OOH$. Further dissociation of $OQ'OOH$ leads to the second of the branching OH radicals in reaction R 1-6.

$$O_2 + QOOH \rightarrow O_2QOOH \rightarrow HO_2Q'OOH \rightarrow OH + OQ'OOH \qquad \text{R 1-5}$$
$$OQ'OOH \rightarrow OH + \text{products} \qquad\qquad\qquad \text{R 1-6}$$
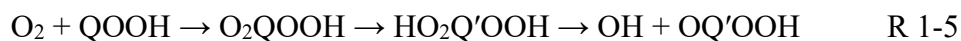
A potential energy surface (PES) showing the generic routes for low temperature oxidation of fuel, RH, including the reaction of O_2 with R and QOOH radicals, and the subsequent decomposition of species to yield OH radicals, is presented in Figure 1-5. Chapter 6 is concerned with the exploration of these later combustion steps.
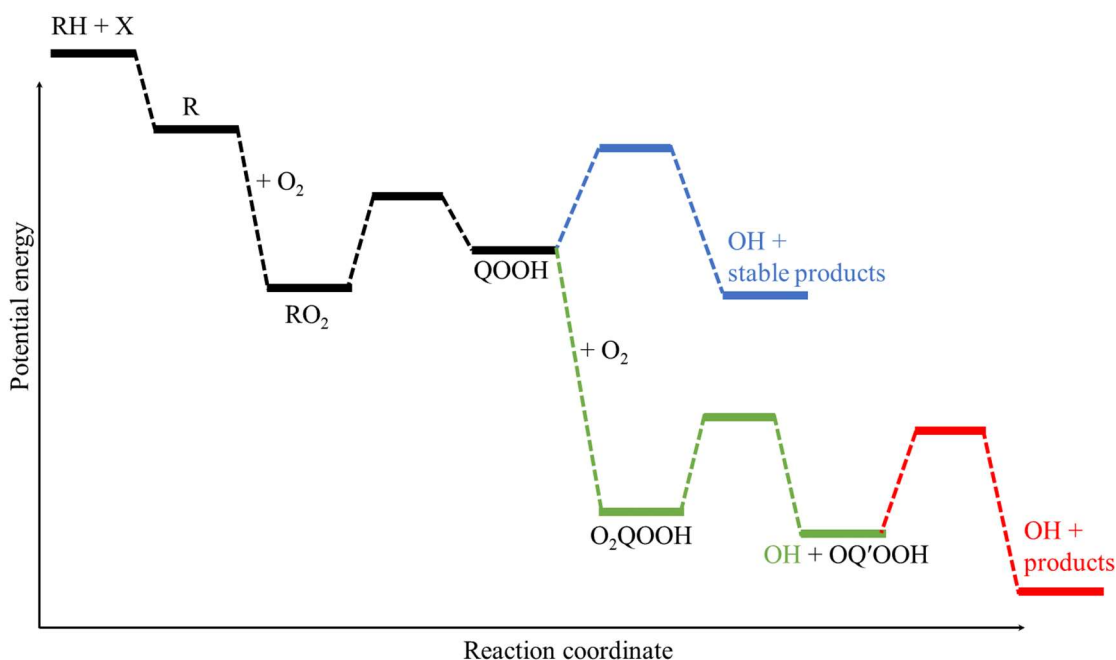
Figure 1-5: Generic low temperature combustion potential energy surface, showing propagation (blue and green) and chain-branching OH formation (green to red).

Additionally, ROOH species formed in reactions R 1-7 and R 1-8 undergo decomposition to RO and OH in reaction R 1-9, providing another chain-branching route.

$$QOOH + RH \rightarrow ROOH + R \qquad \text{R 1-7}$$
$$RO_2 + RH \rightarrow R + ROOH \qquad \text{R 1-8}$$
$$ROOH \rightarrow RO + OH \qquad \text{R 1-9}$$
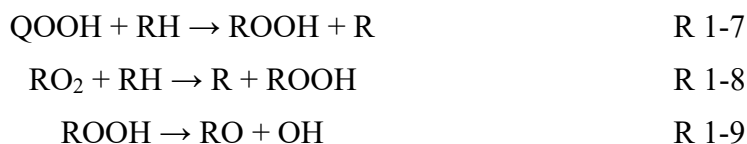
HO_2 formation on longer timescales can occur, and also through reaction between RH and O_2, but at these temperatures, HO_2 is not reactive and does not immediately contribute to the chain-branching mechanism.

Other reactions can compete with, or contribute to, the low temperature reaction scheme described here. Decomposition of R radicals can play a role at high temperatures, and where not enough oxygen is present to ensure the rate of R + O_2 reactions are competitive enough to inhibit the decomposition reaction. Decomposition of RO_2 to the reactants (in the reverse of reaction R 1-2) can also occur at high enough temperatures, where the C–O bond is broken, leading to a negative temperature dependence as the reactions following RO_2 formation that lead to chain-branching can no longer occur.

A great deal of the uncertainty surrounding the low temperature combustion mechanism arises from the lack of understanding of QOOH interception, and what happens to the products of this reaction. These transient species are very difficult to detect, but recent studies have begun to make progress in identifying such molecules. The product of O_2QOOH decomposition in the DME system, hydroperoxymethyl formate (HPMF), has now been detected [87] and quantified [88] by Moshammer and co-workers, using direct sampling of a jet-stirred reactor followed by detection with mass spectrometry. This offers an important insight into the key to autoignition.

1.5 Chemical Activation

The RO_2 radical formed in reaction R 1-2 is initially formed in an energetically excited state (reaction R 1-10). The RO_2* radical can undergo collisional deactivation to the relatively stable RO_2 molecular radical at higher pressures (reaction R 1-11).

$$R + O_2 \rightarrow RO_2* \qquad\qquad \text{R 1-10}$$
$$RO_2* + M \rightarrow RO_2 + M \qquad\qquad \text{R 1-11}$$

At lower pressures however, an excited species can undergo re-dissociation, or isomerisation to QOOH* species (reaction R 1-12) without undergoing thermalisation by M. This process is known as chemical activation, or 'well-skipping'.

$$RO_2* \rightarrow QOOH* \qquad\qquad \text{R 1-12}$$
$$RO_2* \leftarrow QOOH* \rightarrow OH + \text{stable products} \qquad\qquad \text{R 1-13}$$
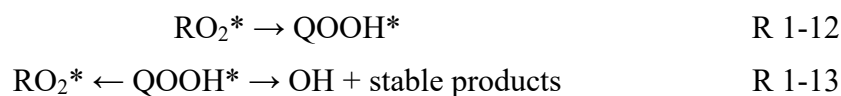
Similarly, QOOH* species can isomerise back to RO_2, or dissociate to the products (reaction R 1-13). This formally direct channel enables the generation of products, including OH, on fast timescales comparable to the decomposition of the R radical. This process is more efficient at lower pressures and higher temperatures, and will depend on the fuel molecule. Like the excited RO_2* radical, QOOH* can also undergo collisional stabilisation to QOOH, although this is less likely given the RO_2:QOOH equilibrium is shifted towards RO_2 as a result of their relative energy well-depths. A generic PES for this process is presented in Figure 1-6.
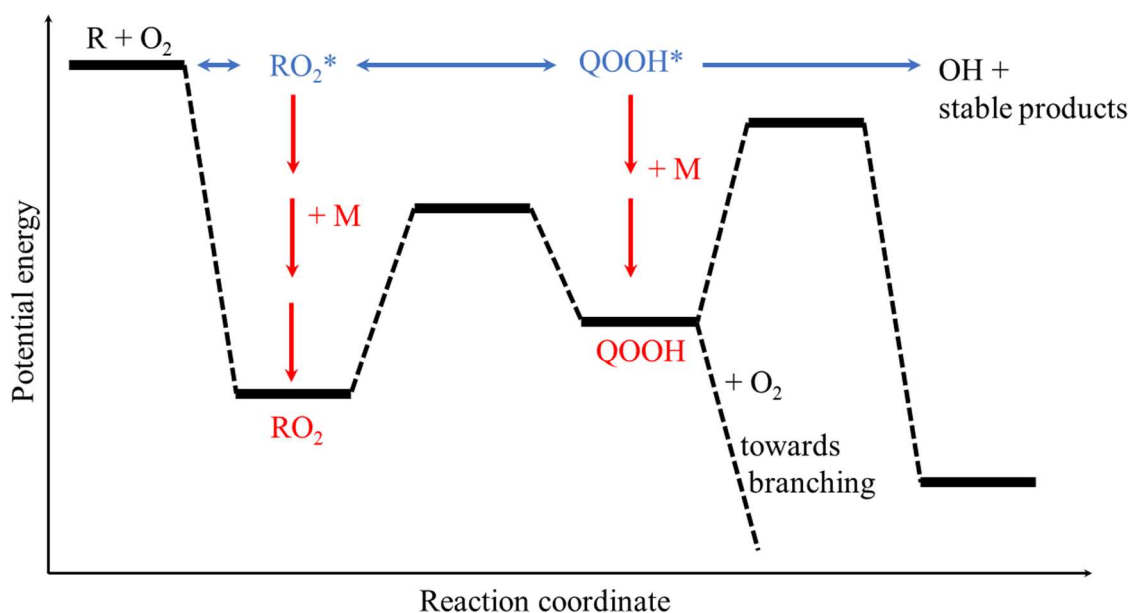
Figure 1-6: Generic potential energy surface showing the chemical activation process (blue), and thermalisation (red) by the bath gas.

The importance of chemical activation reactions for low temperature combustion has previously been demonstrated [89-93], but these formally direct reaction channels were generally missing in kinetic models developed previously [94-96] and therefore the fast yields of bimolecular products accessible at low pressures and high temperatures will not be present. Chemical activation has been shown to be of no consequence when modelling combustion chemistry at ~10 bar [89, 97], so will likely not play a significant role under engine combustion conditions at high pressures. However, these reactions often a play a role under laboratory conditions where rate coefficients relevant to combustion *are* determined, hence a full understanding of chemical activation parameters will be important for these determinations.

Eskola et al. [89] studied the importance of chemical activation in the DME system, making measurements of the $CH_3OCH_2 + O_2$ reaction kinetics and yields. The kinetic traces in Figure 1-7 show a sharp initial increase in OH detection arising from chemical activation, followed by a decay as OH production halts (left figure). At high enough temperatures (Figure 1-7, right), the initial OH signal increase is followed by gradual continued growth due to the propagation process described in section 1.4.2. Experiments in Chapter 4 will focus on an alternative method to measuring the initial fast rates and yields detected here, and the method will be applied to the DEE system in Chapter 5.
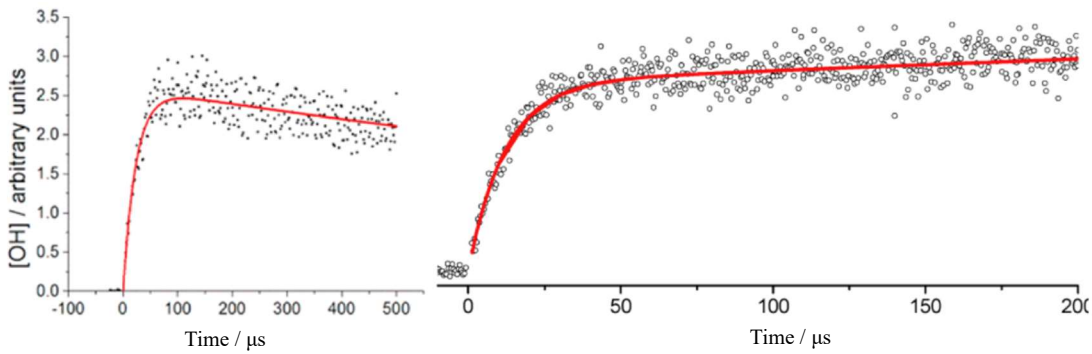
Figure 1-7: Temperature effect on OH production at low temperature (left) and high temperature (right). Figures taken from Eskola et al. [89].

1.6 Combustion Engines

Normal combustion for transport fuels generally takes place inside a diesel engine or a spark-ignition engine (SI), depending on the fuel (diesel or petroleum). Spark-ignition engines use pre-mixed fuel, whereas a diesel engine injects fuel directly into the cylinder for mixing, and relies on compression to initiate combustion, rather than relying on a spark initiator. A new type of engine has been developed, known as an HCCI (homogeneous charge compression ignition) engine, which is close to a hybrid of diesel and SI engines. HCCI engines use a pre-mixed fuel/air component as in SI, but the engine relies on autoignition as a result of the compressed gas heat, similar to a diesel engine [98] (Figure 1-8). Advantages of HCCI engines over conventional engines include increased thermal efficiency, and reduced emissions (such as NO_x) [99, 100]. Conventional engines combust at high temperatures (2000 – 2600 K) [101], which is the cause of NO_x formation. HCCI engines on the other hand, combust at less than 1900 K, which significantly reduces the formation of NO from the temperature-dependent reaction between N_2 and O_2 (the full Zeldovich mechanism involves multiple steps for molecular nitrogen and oxygen to indirectly produce NO).
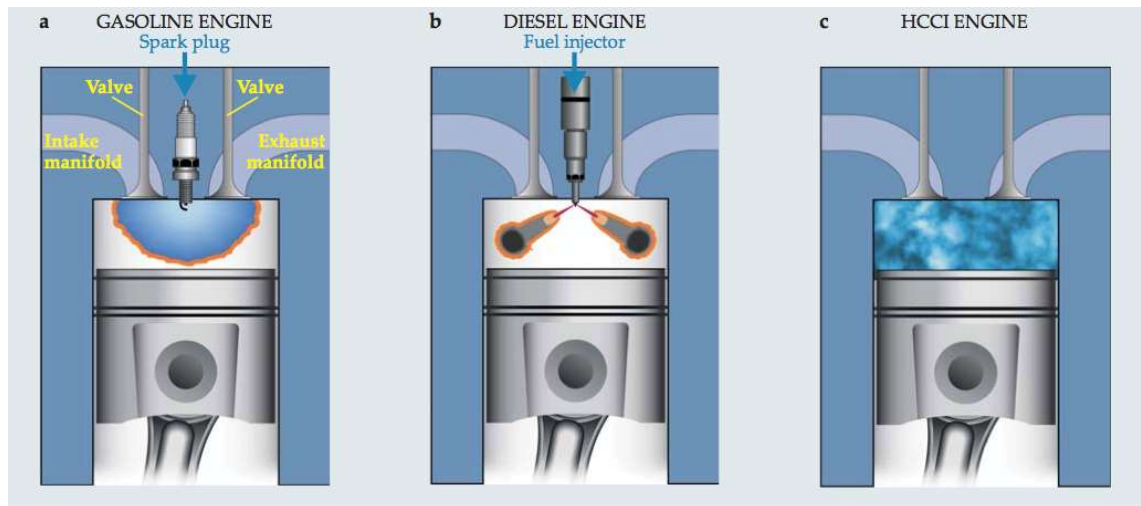
Figure 1-8: Diagram of three engine types, demonstrating the combined aspects from spark ignition and diesel engines used in HCCI engines, from [101].

The difficulty with novel engines like those of HCCI, is that the ignition timing is dependent on the inherent chemistry of the fuel mixture, rather than a spark [101]. Combustion in this case is caused by the chain-branching process, where products of a reaction are able to initiate new reactions in greater numbers (reactive radicals are produced at a rate greater than they are consumed). Combustion via chain-branching at low temperature is called autoignition, and the key to understanding autoignition is the kinetics of the reaction mechanism [102] discussed previously. Despite the high combustion temperatures discussed above, the actual temperature relevant to the initiation of the combustion at low temperature is generally accepted to be approximately 500 – 800 K. The low temperature of autoignition that many biofuels have make the HCCI engine better suited for their combustion. Without a detailed understanding of the chemistry that occurs during low temperature combustion, novel HCCI engines will not operate under optimal conditions for a specific fuel.

In an engine, the combustion mechanism is normally initiated by the fuel molecule undergoing a reaction with a small species, where O, H and OH are all important species, with the hydroxyl radical the most important, due to its much faster reaction with hydrocarbon fuels [103]. Hydroxyl radicals are present at the relatively high temperatures used in engines [102]. This well-known first step is relevant for all hydrocarbon fuels, and the subsequent reaction routes to autoignition are well-documented [104-108], albeit with limited evidence.

Extensive experimental techniques have been employed to study the potential of possible biofuel ethers, such as rapid compression machines [109, 110], shock tubes [111], jet-stirred reactors [111, 112], flow reactors [94], and laser photolysis – laser-induced fluorescence [113]. This research enables fuel characteristics of the ethers to be determined, such as ignition delay times, and should allow the temperature and pressure ranges for autoignition to be ascertained, often with the help of theoretical calculations [114-116].

1.7 Theories of Chemical Reactions

This section provides an outline of the basic kinetic theories applied to experimental observations, in order to extract the rate coefficients that are presented in this thesis.

1.7.1 Transition State Theory

Transition state theory (TST) is used to predict the rates of elementary chemical reactions, and explain to some extent, why the reactions take place. The theory operates on the assumption that a transition state, comprised of an activated complex of reactants, exists along the reaction coordinate (see $ABC^{\ddagger}$ in Figure 1-9).
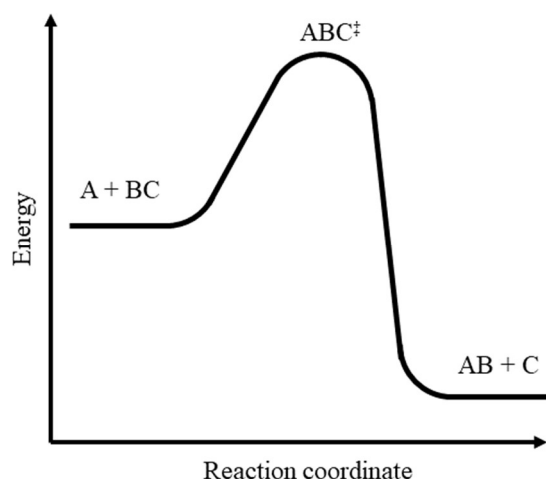
Figure 1-9: Typical energy profile of a reaction as described by transition state theory.

The transition state, $ABC^{\ddagger}$, lies along the reaction coordinate at the maximum of the minimum energy pathway, and ultimately falls apart to the products, AB + C. $ABC^{\ddagger}$

is assumed to be in equilibrium with the reactants, A + BC. The rate for the reaction can be given by equation E 1-1:

$$k_r[A][BC] = \frac{d[AB]}{dt} = k^{\ddagger}[ABC^{\ddagger}]$$

E 1-1

where k_r is the rate coefficient. The concentration of the transition state can be related to the equilibrium constant, $K^{\ddagger}$, in equation E 1-2:

$$[ABC^{\ddagger}] = K^{\ddagger}[A][BC]$$

E 1-2

and k_r to $K^{\ddagger}$ in equation E 1-3:

$$k_r = k^{\ddagger}K^{\ddagger}$$

E 1-3

$K^{\ddagger}$ is given by the statistical expression in equation E 1-4:

$$K^{\ddagger} = \frac{Q'_{ABC}}{Q'_A Q'_{BC}} \exp(-\varepsilon_c/RT)$$

E 1-4

where Q'_I refers to the molecular partition function per unit volume of species I, and ε_c is the potential energy difference between the reactants and the complex, or in other words, the height of the transition state saddle point. Statistical mechanics results in an expression of the rate coefficient in equation E 1-5:

$$k_r = \frac{k_B T}{h} \frac{Q'_{ABC}}{Q_A Q_{BC}} \exp(-\varepsilon_0/RT)$$

E 1-5

where, ε_0 is the sum of ε_c and $\Delta\varepsilon_z$ (the total difference in zero-point energies of the complex and reactants). A correction factor, κ, is inserted in equation E 1-6, where it will often be unity, but is included to account for the possibility that some activated complexes

may return to reactants, rather than the products. κ is known as the transmission coefficient.

$$k_r = \kappa \frac{k_B T}{h} \frac{Q^{\ddagger}_{ABC}}{Q_A Q_{BC}} \ \exp(-\varepsilon_0/RT) \qquad \text{E 1-6}$$

1.7.2 Unimolecular Reactions

The Lindemann mechanism provides a mechanism for the unimolecular decomposition of species A showing first order kinetics (equation E 1-7). Increasing rate with temperature suggests an energy barrier is being overcome, however first-order kinetics do not suggest there is collisional activation. The reaction sequence proposed by Lindemann explains this behaviour, where A is excited by collisional activation with a molecule such as the bath gas, M (reaction R 1-14). A* can react to form products, as in reaction R 1-15, or undergo collisional deactivation (see Figure 1-10).

$$\frac{d[A]}{dt} = -k[A] \qquad \text{E 1-7}$$

$$A + M \underset{k_{-1-14}}{\overset{k_{1-14}}{\rightleftarrows}} A^* + M \qquad \text{R 1-14}$$

$$A^* \overset{k_{1-15}}{\longrightarrow} \text{products} \qquad \text{R 1-15}$$
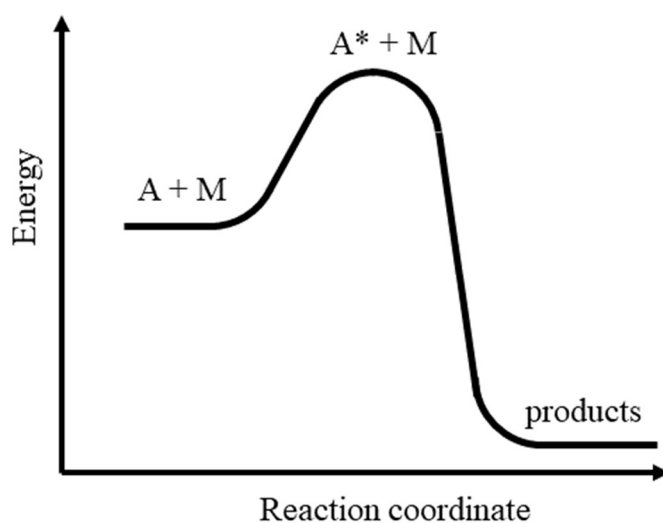
Figure 1-10: Potential energy surface for a unimolecular dissociation reaction.

Reaction R 1-15 shows that the overall rate of formation of products is equal to $k_{1\text{-}15}[A^*]$, and as such, $[A^*]$ must be calculated to obtain the formation rate. The steady-state approximation can be utilised to assume A^*, which has a short lifetime, maintains a steady concentration once built up. Equation E 1-8 equates the rate of formation and consumption for A^*.

$$k_{1\text{-}14}[A][M] = k_{-1\text{-}14}[A^*][M] + k_{1\text{-}15}[A^*] \qquad \text{E 1-8}$$

Rearrangement of equation E 1-8 for $[A^*]$, and substitution into the rate of formation of products gives equation E 1-9:

$$\frac{d[\text{products}]}{dt} = k_{1\text{-}15}[A^*] = \frac{k_{1\text{-}15}k_{1\text{-}14}[A][M]}{k_{-1\text{-}14}[M] + k_{1\text{-}15}} = k_{\text{uni}}[A] \qquad \text{E 1-9}$$

where k_{uni} represents the formal unimolecular rate coefficient; $k_{\text{uni}} = k_{1\text{-}15}k_{1\text{-}14}[M]/(k_{-1\text{-}14}[M] + k_{1\text{-}15})$. At high pressures k_{uni} is independent of pressure, as collisional deactivation is much faster than the unimolecular reaction of A^* ($k_{-1\text{-}14}[M] \gg k_{1\text{-}15}$), reducing the expression for k_{uni} to $k_{1\text{-}15}k_{1\text{-}14}/k_{-1\text{-}14}$ (independent of pressure). At low pressures, k_{uni} is directly proportional to pressure, as the rate determining step becomes the excitation reaction in reaction R 1-14. Here, collisional deactivation of A^* is less likely than reaction, and so $k_{-1\text{-}14}[M] \ll k_{1\text{-}15}$. This reduces k_{uni} to $k_{\text{uni}} = k_{1\text{-}14}[M]$ (dependent on pressure) (Figure 1-11).
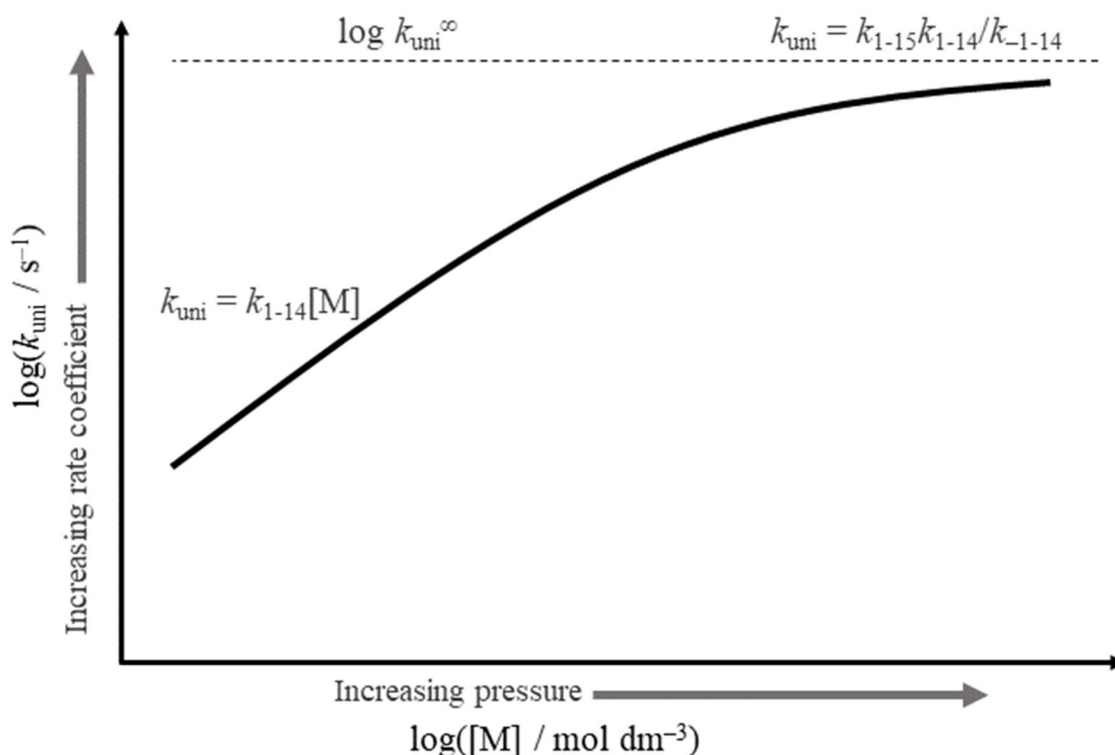
Figure 1-11: Example of the unimolecular rate coefficient fall-off at lower pressures.

The Lindemann mechanism does have some failures, and improvements made by Rice and Ramsperger, and later Kassel, and Marcus, have led to the development of this theory, which is referred to as RRKM (Rice-Ramsperger-Kassel-Marcus) theory, and will be used by software employed in Chapter 5. Lindemann theory does not take account of molecular structure in its assumptions, and as such underestimates the activation rate as a result of ignoring the number of degrees of freedom of a polyatomic molecule (such as its vibrational modes). Taking into account these degrees of freedom was required to improve the agreement between fall-off behaviour predicted by the Lindemann mechanism, and that shown by experimental observations.

Another failure of Lindemann theory arises where the excited molecule, A*, is energised, but it must also have sufficient energy localised into the relevant degree of freedom (i.e. a specific bond to be broken), before it can be converted into the products. This is termed the activated complex, $A^{\ddagger}$, and the rate of reaction from $A^* \rightarrow A^{\ddagger}$ (k^*), is typically much slower than $A^{\ddagger} \rightarrow$ products ($k^{\ddagger}$), thus it is the rate determining step. As k^* is much smaller than $k^{\ddagger}$, $A^{\ddagger}$ will be very small, and the steady state approximation $d[A^{\ddagger}]/dt = 0$ can be used to yield $k^* = k^{\ddagger}[A^{\ddagger}]/[A^*]$. This formed the basis of the theory by Rice and Ramsperger (and later developments by Kassel), who assumed energy can be

rapidly exchanged freely between vibrational modes, and were able to predict the fall-off behaviour well.

The final modification by Marcus took account of TST, where RRKM theory is a microcanonical transition state theory that assumes rate coefficients are a function of energy. $A^{\ddagger}$ is now treated as a transition state, and therefore transfer over $A^{\ddagger}$ to products is an irreversible process, and ultimately RRKM theory allows for a proper treatment of all internal modes.

1.7.3   Association Reactions

Association reactions are related to their counterpart unimolecular decomposition reactions (see example in reaction R 1-16) by an equilibrium constant, as in equation E 1-10. They will be important for the work carried out in Chapter 4 and Chapter 5.

$$A_2 + M \underset{k_{-1\text{-}16}}{\overset{k_{1\text{-}16}}{\rightleftarrows}} A + A + M \qquad\qquad \text{R 1-16}$$
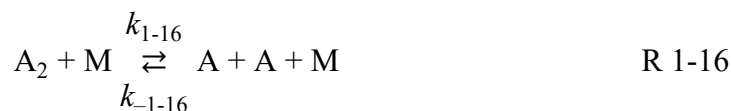
$$K_c = [A]^2/[A_2] = k_{1\text{-}16}/k_{-1\text{-}16} \qquad\qquad \text{E 1-10}$$

To maintain K_c, the pressure dependence of the association reaction must be the same as the unimolecular reaction. Decomposition reactions have high activation energies, and therefore temperature dependences, whereas an equivalent association reaction will have no activation energy and a weak temperature dependence.

Upon association of two species, the bond formed causes release of energy, which is conserved, and is distributed amongst the internal modes of the complex formed. An example for the $CH_3 + O_2$ reaction is shown in reaction R 1-17. If enough energy is located along the bond formed, then dissociation will occur, reforming the reactants. Collisional deactivation can remove this excess energy (reaction R 1-18), where it is transferred into the motion of a bath gas and the new species formed (a generic PES is presented in Figure 1-12).
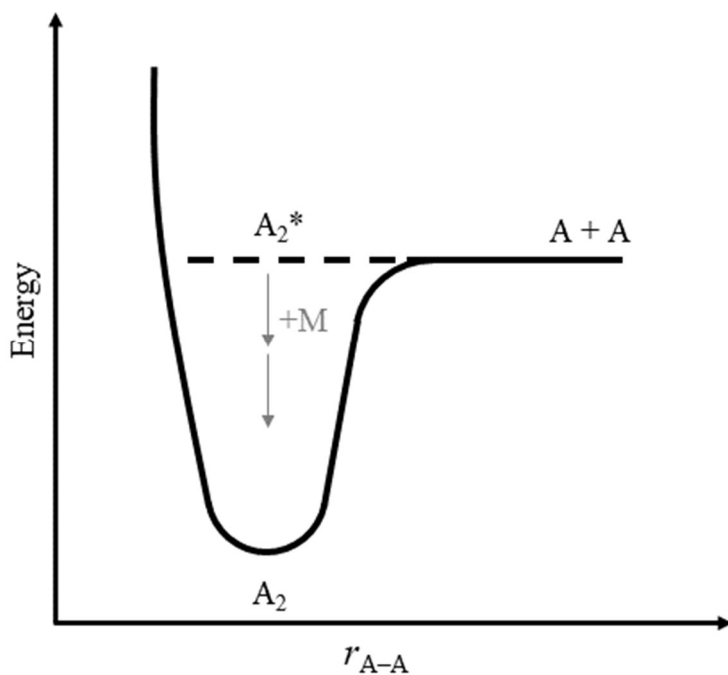
Figure 1-12: Potential energy surface for a generic association reaction, showing the routes to re-dissociation and collisional deactivation.

$$CH_3 + O_2 \rightleftarrows CH_3O_2^* \qquad\qquad \text{R 1-17}$$

$$CH_3O_2^* + M \rightarrow CH_3O_2 + M \qquad\qquad \text{R 1-18}$$
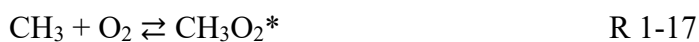
The steady state approximation can be applied to the energised molecule possessing a short lifetime, where the formation and removal rate are equal, as in equations E 1-11 and E 1-12:

$$k_{1\text{-}17}[CH_3][O_2] = k_{1\text{-}18}[CH_3O_2^*][M] + k_{-1\text{-}17}[CH_3O_2]^* \qquad \text{E 1-11}$$

$$[CH_3O_2^*] = k_{1\text{-}17}[CH_3][O_2] / (k_{1\text{-}18}[M] + k_{-1\text{-}17}) \qquad \text{E 1-12}$$

The formation rate for the stabilised CH_3O_2 species is $d[CH_3O_2]/dt = k_{1\text{-}18}[CH_3O_2^*][M]$. Substituting equation E 1-12 into this expression yields equation E 1-13:

$$d[CH_3O_2]/dt = k_{1\text{-}18}k_{1\text{-}17}[M][CH_3][O_2] / (k_{1\text{-}18}[M] + k_{-1\text{-}17}) \qquad \text{E 1-13}$$

At high pressures, $k_{-1\text{-}17} \ll k_{1\text{-}18}[M]$, reducing equation E 1-13 to $d[CH_3O_2]/dt = k_{1\text{-}17}[CH_3][O_2]$, Here, the rate-determining step is the bimolecular complex formation, where it will always be stabilised rather than dissociating. This leads to an overall second order reaction. At low pressures, stabilisation is slow and thus $k_{-1\text{-}17} \gg k_{1\text{-}18}[M]$, and $d[CH_3O_2]/dt = k_{1\text{-}18}k_{1\text{-}17}[M][CH_3][O_2]/k_{-1\text{-}17}$ (third order overall). Here, the rate-determining step is the deactivation of the energetically excited complex.

At higher temperatures, excited complexes will have a shorter lifetime as a result of the greater kinetic energy of collisions. Re-dissociation will be more likely under these conditions, and as such, negative temperature dependences are expected.

1.8   Thesis Overview

Chapter 2 provides an overview of the laser flash photolysis – laser-induced fluorescence technique used for the experiments in this thesis, and some characterisation of this instrumentation for the treatment of gas flow and temperature.

Chapter 3 covers the first reaction important for the low temperature oxidation mechanism of ethers, the reaction of the hydroxyl radical with TMOF, DEE, DBE, MTBE, and DME. Data are presented over a range from room temperature to approximately 740 K, and these data significantly extend the rate coefficients available for TMOF, DEE, and DBE.

Chapter 4 describes a generic technique for measuring rate parameters of the R + O_2 reaction that follows the OH + fuel reaction. A method applicable to any fuel that can undergo formally direct production of OH radicals at low pressures is presented, by analysis of biexponential kinetic decays. Numerical integration and simulation are used to analyse the method's efficiency for obtaining R + O_2 rate coefficients and experimental OH yields, and its sensitivity to experimental conditions. The CH_3OCH_2 + O_2 reaction relevant to the DME low temperature combustion mechanism was studied, and current measurements are compared to previous studies and alternate techniques.

Chapter 5 provides novel measurements of the $C_2H_5OC_2H_4$ + O_2 reaction rate coefficients and OH yields below 500 K, using a method analogous to the study of the CH_3OCH_2 + O_2 reaction, and an additional technique for obtaining OH yields. Comparison to *ab initio* calculations are provided using master equation methods.

Chapter 6 presents some observations of interesting, potentially unwanted, O atom chemistry occurring in the experimental setup at high temperatures and oxygen concentrations. Possible measurements of OH production from QOOH radical thermal decomposition, and O_2QOOH radical propagation/branching are presented for all five ethers.

Chapter 2 Experimental

This chapter gives an overview of the experimental setup used throughout this thesis to study the gas phase reactions of potential biofuel ethers. A description of the instruments used, such as lasers, temperature detectors, and the reaction cell, is provided. Some early results to characterise the set up are also provided, concerning gas flow calibration, and the calibration of temperature detection. Some other techniques that have been employed to measure gas phase kinetics relevant to this thesis are compared with the technique used in the current work.

2.1 Overview of Experimental Setup

In this work, laser flash photolysis – laser-induced fluorescence (LFP–LIF) was used to monitor OH, enabling the study of reactions between ether fuels with the hydroxyl radical over time, using gas phase reactants at low pressures ($< \sim$500 Torr). A schematic diagram of the typical experimental setup is presented in Figure 2-1.
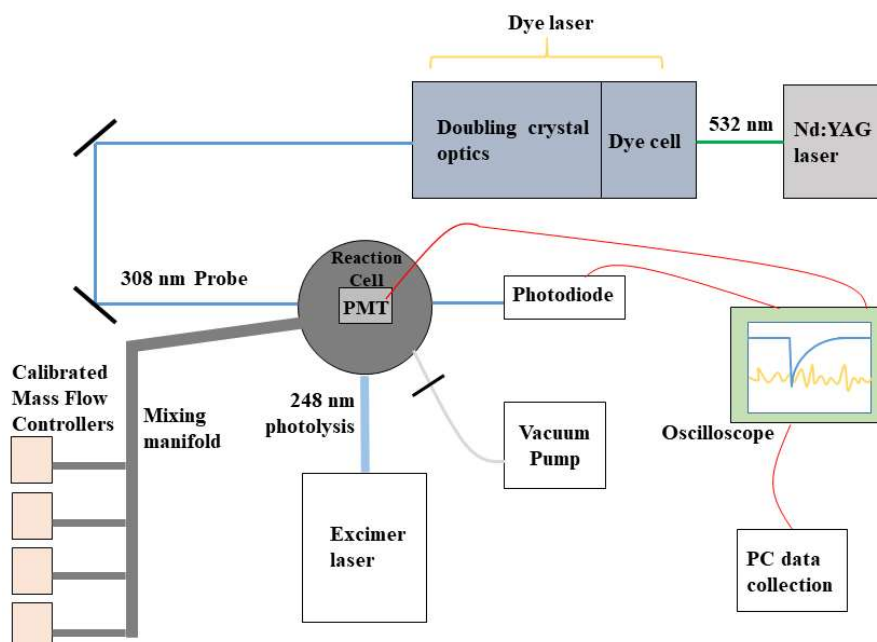
Figure 2-1: Schematic of laser flash photolysis – laser-induced fluorescence experimental setup used in this work.

Typically, initiation of the reaction was brought about by the first laser pulse from an excimer laser operating at 248 nm, in order to photolyse hydrogen peroxide (reaction

R 2-1), *t*-BuOOH (reaction R 2-2), or urea hydrogen peroxide (reaction R 2-3). The OH radicals formed during this photolysis initiate chemistry by reacting with the ether fuel. The photon density was approximately 7.5×10^{16} photons cm^{-2}, and the typical OH concentration was ~$(1 - 2) \times 10^{12}$ molecule cm^{-3} (a calculation to estimate this is provided in section 2.5.1).

$$H_2O_2 + h\nu \xrightarrow{\lambda=248 \text{ nm}} 2OH \qquad \text{R 2-1}$$

$$(CH_3)CO_2H + h\nu \xrightarrow{\lambda=248 \text{ nm}} OH + products \qquad \text{R 2-2}$$

$$(CO(NH_2)_2 \cdot H_2O_2) \xrightarrow{vap} H_2O_2 + h\nu \xrightarrow{\lambda=248 \text{ nm}} 2OH \qquad \text{R 2-3}$$
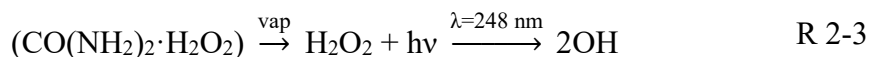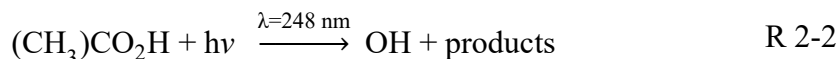
To monitor the progress of reactions and probe the OH radicals, on-resonance laser-induced fluorescence was used, probing at ~308 nm, corresponding to the energy of the OH $Q_1(2)$ rotational line of the $A^2\Sigma^+(v' = 0) \leftarrow X^2\Pi_i(v'' = 0)$ transition. The probe laser light was obtained from the output of an Nd:YAG-pumped dye. The lasers used in this thesis are described in the sections that follow.

Major differences between the experimental setup used for each chapter are outlined in their respective experimental sections. Briefly, the *t*-BuOOH precursor was only used for some OH + DEE experiments in Chapter 3, and the urea/H_2O_2 precursor was only used in Chapter 4. 266 nm wavelength light was used in Chapter 3 for some experiments on the OH + MTBE rate data. This was generated using the Quantel Nd:YAG laser described later. The majority of ethers were delivered from a bulb, as described in section 2.7.1, however some experiments requiring greater concentrations of ether used a bubbler delivery method, described in Chapter 3. Finally, Chapter 6 presents some experiments using a modified setup, which is described in detail in the experimental section.

2.2 Lasers

LASER is an acronym for Light Amplification by Stimulated Emission of Radiation, where a system of molecules is excited by a beam of light, with a frequency where the photon energy matches the gap between the excited state and lower energy state. A molecule can relax from the excited state, by emitting another photon at the same

frequency as the initial radiation. The direction of the applied light beam is also the favoured direction for emission, therefore amplifying the intensity.

Lasers are incredibly useful instruments for studying reaction kinetics, as they allow the study of premixed reactants and precursors, can be used to study reactions over a greater range of pressures when compared with traditional (liquid) flow methods, and the duration of a laser pulse is the only limitation on studying very fast reactions when using the flash photolysis method. Further, the laser-induced fluorescence technique allows highly selective monitoring of the relative concentration of products and/or reactants in a reaction.

This section aims to describe the principles of lasers, their use for kinetic studies, and the specific lasers used for the majority of this thesis' measurements.

2.3 Absorption and Emission of Radiation

Typically, the lowest discrete energy level, the ground state, is where a molecule exists, but in a laser medium, excited energy levels must be occupied before the lasing action can take place. Absorbing light can excite a molecule to a higher state. This process involves the energy of photons, E, transferring to the molecule, where $E = h\nu$. Here, h is Planck's constant, ν is the frequency of the photon, and E must be equal to the energy of the excitation gap between the lower and excited state of the molecule.

Emission of light is the reverse process of absorption, where a molecule in an excited state emits photons matching the energy gap between the excited state and the destination state of the molecule during relaxation. Photons are emitted in random directions. No external trigger is required for this process, hence the term spontaneous emission.

Finally, stimulated emission involves the emission of light from a molecule during relaxation from an excited state to a more stable state, but only after a light beam is directed toward the system, with the frequency corresponding to the photon energy matching the energy gap involved. The photon emitted also matches this energy. The amplification term in the definition of the laser acronym originates from the fact that emission prefers to occur in the same direction as the applied beam of light. Thus, the light intensity is amplified during the process of stimulated emission. An active medium

that can go undergo stimulated emission is the primary requirement for a laser, along with external stimulus.

Examples of the external stimulus that pumps the active medium are flashlamps, an electrical discharge, or a chemical reaction. In order to increase the intensity of the stimulated emission, a resonator is used within the optical cavity of the laser (Figure 2-2), to allow the multiple passage of light back and forth through the active medium, causing more stimulated emission with each passage. To arrange this process, two mirrors are placed either side of the active medium, one fully reflective, and a second partially reflective. The partially reflective mirror allows some passage of light through, to form the laser beam. Aiding the highly directional nature of lasers, any spontaneous emission not in the direction of the mirrors will not contribute to the intensifying stimulated emission.
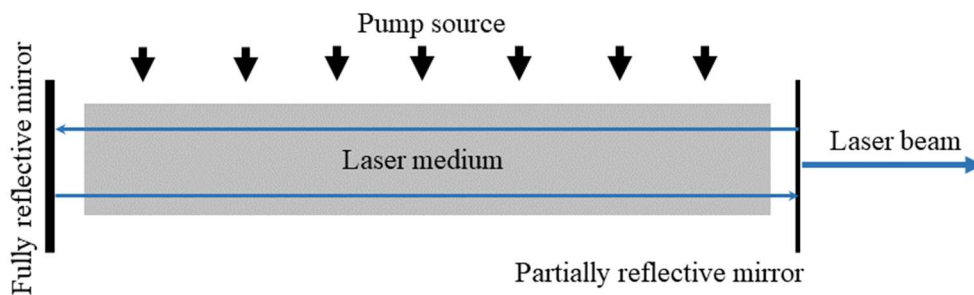
Figure 2-2: Schematic diagram of a laser cavity resonator.

2.4 Population Inversion

In a two-level system (Figure 2-3), with two non-degenerate energy levels, there are three radiative processes; absorption, spontaneous emission, and stimulated emission (see Figure 2-3). For lasing action to occur, a population inversion must be built up in the higher energy level in the laser system, otherwise the process of absorption will beat stimulated emission. Under equilibrium conditions, the Boltzmann relation stipulates that the lower energy level will always have the greater population. Energy is supplied to the system through 'pumping' in order to sustain a state of population inversion. Practically, a laser possesses more than two levels, in order to overcome the competition between absorption and stimulated emission.

In a three-level laser (Figure 2-3), E_3, a third level is present, at a higher energy than the two present in a two-level system. E_3 is the level populated by initial pumping of

the laser medium, which proceeds to decay non-radiatively to E_2. As long as this decay is slower than the emission from E_2 to E_1, the population in E_2 can continue to increase while E_1 loses population via the pumping process. For this to occur, E_2 must also be metastable, with a long lifetime compared to the other levels. Because the laser emission repopulates the ground state, it can be difficult to maintain the population inversion.
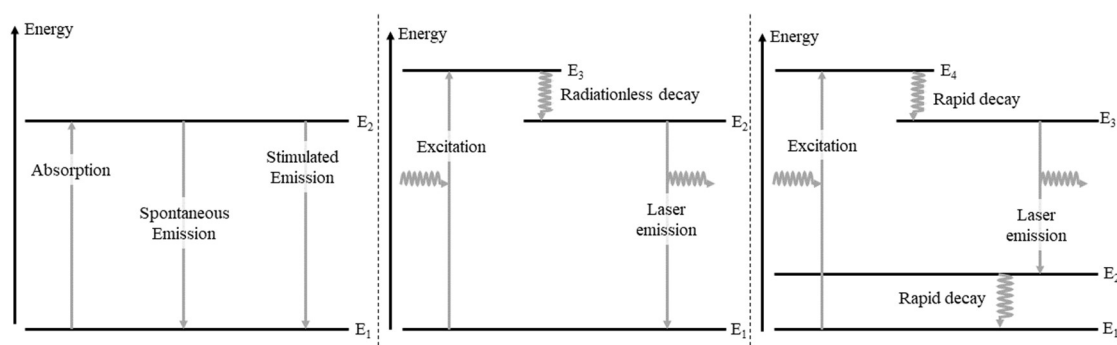
Figure 2-3: Schematics for the energy levels in a two-, three-, and four-level laser system, left to right.

A four-level laser is used to combat the repopulation of the lowest energy level, where the ground state (E_1) lies below the lower level of the laser emission process (E_2), ensuring that E_2 never builds up a significant population, as long as it decays rapidly to the ground state. This allows the population inversion to be maintained between the two relevant energy levels, regardless of the populations present in E_1 and E_4. The Nd:YAG and dye lasers described later are examples of four-level lasers that are employed in this thesis.

2.5 Laser Flash Photolysis

Norrish and Porter first developed the flash photolysis technique in the late 1940s, for which they were they were awarded the 1967 Nobel prize. Flash photolysis uses a light source, such as a flash lamp or laser, to photolyse molecules, where a specific bond is broken in order to produce a desired product species. The product species is generally a reactant in the reaction being studied [86]. In this work the product species was the OH radical. Flowing reactants and precursors together allows the reaction to take place once photolysis has occurred. Flash photolysis offers advantages over flow techniques with fewer limitations on pressure, and the possibility to remove mixing times. Generally, the

only limitation on reaction timescale imposed by flash photolysis, is the duration of the photolysis laser pulse, which can be faster than nanosecond durations. Unwanted reactions that may occur on the wall of an experimental cell can also be reduced, as photolysis light from the laser can be used to generate radical species in the centre of the cell and reaction occurs on a timescale faster than that of diffusion to and from the walls.

2.5.1   Excimer Laser

The light source most used in this work is an excimer (excited dimer), or more accurately an exciplex (excited diatomic complex) laser, which operate on a particular mixture of gases to achieve a certain wavelength of light. Some common excimer laser energies and the mixtures are listed below in Table 2-1. Excimer lasers have well-defined spatial profiles, a precise wavelength range, pulse durations of $10 - 20$ ns, and repetition rates from 1 Hz up to 500 Hz. High pulse energies, up to 1 J, also allow the photolysis of precursor molecules efficiently when using low concentrations.

Table 2-1: Excimer laser energies, wavelengths and the required gas compositions, from [86].

Gas mix	λ / nm	Photon energy / eV
$Ar/F_2/He$	193	6.44
$Kr/HCl/He$	222	5.60
$Kr/F_2/He$	248	5.01
$Xe/HCl/He$	308	4.04
$Xe/F_2/He$	351	3.54

When a pulsed electric discharge is passed through the mixture of gases in an excimer laser, ions are generated, which can form excited species when combined (for example KrF^*) within the helium buffer gas [117]. The excited complex emits photons, decaying rapidly to the lower energy state. This state never achieves a high population, due to the instantaneous dissociation of the molecule as a result of repulsive interatomic forces. The population inversion between excited and lower state that exists because of this is maintained in the laser cavity, where light of the appropriate wavelength is amplified upon passing through [86]. This is clearly an exception to the impossibility of achieving a population inversion in a two-level laser system. The energy gap between the

two states (Figure 2-4) dictates the wavelength of light, thus difference gas mixes have different energy separations and therefore wavelengths.

Other types of lasers that can be used for photolysis are dye-lasers (200 – 1000 nm), Nd:YAG (Yttrium Aluminium Garnet) lasers and Nd:glass lasers (both 1064 nm or sometimes 1319 nm), although these last two will operate not on the principal wavelength, but shorter wavelengths following frequency conversion (see section 2.6.1.1 on Frequency Conversion). Typically these lasers will output 10 – 50 mJ for a pulse width of 10 ns at 266 nm when frequency quadrupled, whereas an excimer laser can achieve energies of 200 – 300 mJ at the same pulse width, given the correct gas mixture. Dye lasers produce even lower pulse energies (1 – 5 mJ) in the wavelength range 260 – 320 nm, but have the advantage of tunability.
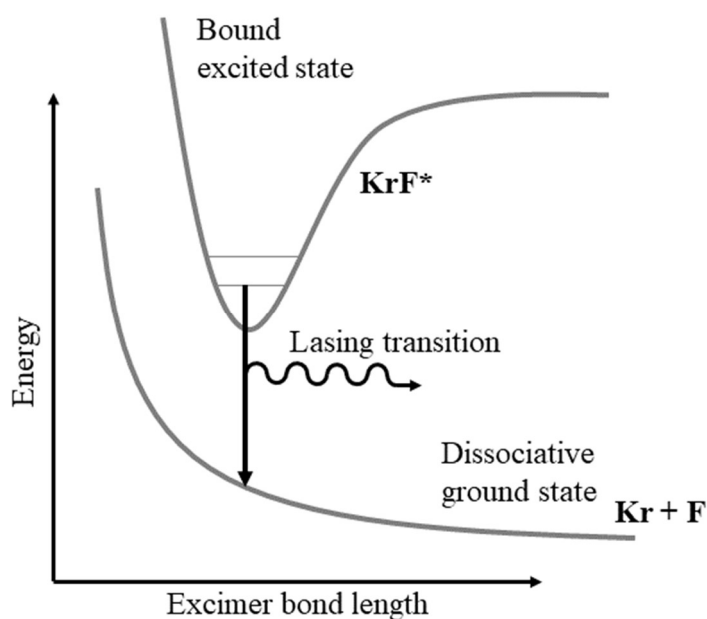
Figure 2-4: Potential energy curves for the states involved in a KrF exciplex laser transition.

In this thesis, the exciplex laser used was a Lambda Physik LPX 200 Excimer laser, operating on KrF at 248 nm. Typically a 10 Hz pulse repetition frequency was used for experiments, although 1, 2 and 5 Hz were also employed for repetition rate-dependent experiments. Typical pulse energies measured with a power meter were 40 – 100 mJ $pulse^{-1}$ cm^{-2}, and beam dimensions were 25 mm × 10 mm.

Measurements of the photolysis laser pulse energy can be used to estimate the concentration of OH radicals generated in the reaction cell at time zero. The energy of a photon, E, for an experiment using 248 nm laser light can be calculated using equation E 2-1, where h and c are Planck's constant and the speed of light respectively. Based on a typical laser energy of 0.06 J cm^{-2}, the number of photons, P, is estimated by equation E 2-2.

$$E = hc/\lambda = 8.01 \times 10^{-19} \text{ J} \qquad \text{E 2-1}$$
$$P = 0.06/(8.01 \times 10^{-19}) = 7.49 \times 10^{16} \text{ photons cm}^{-2} \qquad \text{E 2-2}$$

In order to calculate the concentration of [OH] radicals, the concentration of H_2O_2 must be known. This can be estimated based on the rate of decay of OH with no reactant present, only precursor (H_2O_2 and N_2). For a typical pseudo-first order rate coefficient of $k' = 200$ s^{-1}, [H_2O_2] can be estimated using equation E 2-3, where $k_{OH+H2O2}$ is estimated to be 1.70×10^{-12} cm^3 molecule^{-1} s^{-1} based on the Arrhenius parameterisation recommended by Atkinson et al. [118] at 298 K. An assumption about k' has been made here, where the entirety of the rate has been attributed to the reaction between OH and H_2O_2. In reality, some of this rate is likely to be as a result of diffusion, which would result in a lower [OH]$_0$. Finally, the estimated H_2O_2 concentration, number of photons, and cross section of [H_2O_2] (σ, estimated here as 1×10^{-19} cm^2 molecule^{-1} [119]) are used in equation E 2-4 to calculate the OH concentration at $t = 0$.

$$[H_2O_2] = 200/k_{OH+H2O2} = 1.18 \times 10^{14} \text{ molecule cm}^{-3} \qquad \text{E 2-3}$$
$$[OH]_0 = P.\sigma.2[H_2O_2] = 1.8 \times 10^{12} \text{ molecule cm}^{-3} \qquad \text{E 2-4}$$

2.5.2 Nd:YAG Laser

For a small number of experiments, a neodymium laser (described in detail below) was used to generate the radical species from the photolytic precursor. The Nd:YAG laser (Q-smart 850, Quantel) operated at 10 Hz, at a wavelength of 266 nm, with a beam diameter of 9 mm.

2.6 Laser-Induced Fluorescence

Laser-induced fluorescence is often used in conjunction with flash photolysis, and involves using a tunable laser source to excite a specific transition in target radicals, causing the molecule to emit fluorescence that can be detected as a reaction proceeds [86], thus monitoring relative concentration. This is used for the detection of OH radicals described in section 2.7.4.

After a photolysis laser is fired at $t = 0$, the probe laser used for laser-induced fluorescence can be fired at varying known times following the generation of radical species by the photolysis laser. In doing this, a time-resolved trace of fluorescence is generated, where the intensity of the fluorescence signal collected is proportional to the concentration of the target radical.
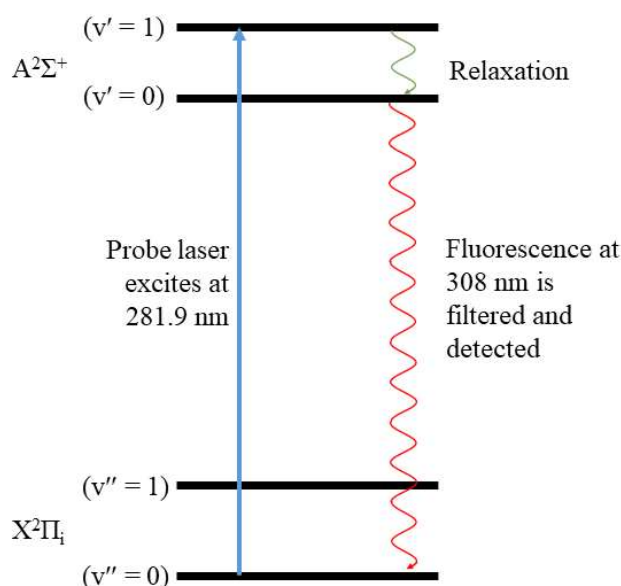
Figure 2-5: Example of off-resonance laser-induced fluorescence transitions in OH.

A probe laser is tuned to the wavelength necessary for the desired transition to excite the target molecule, for example ~282 nm laser light will excite an OH radical in the transition $(A^2\Sigma^+(v' = 1) \leftarrow X^2\Pi_i(v'' = 0), Q_1(1))$ [89]. The subsequent fluorescence emitted by the target molecule, as shown in Figure 2-5, can be filtered and detected by a photomultiplier tube, before a computer collects the signal to build up a kinetic trace. The main advantages of the LIF technique are its highly sensitive and selective nature, where unwanted wavelengths are not detected, and the ability to probe a wide range of species using tunable laser sources. One limitation is LIF's inability to detect species that do not

fluoresce, such as large molecules with enough vibrational modes to undergo radiationless transitions and intersystem crossing preferentially over fluorescence transitions, or molecules that do not have an accessible bound upper electronic state. Other processes possible are shown in Figure 2-6. Its inability to detect absolute concentrations is also a drawback when compared with absolute detection techniques such as absorption spectroscopy.
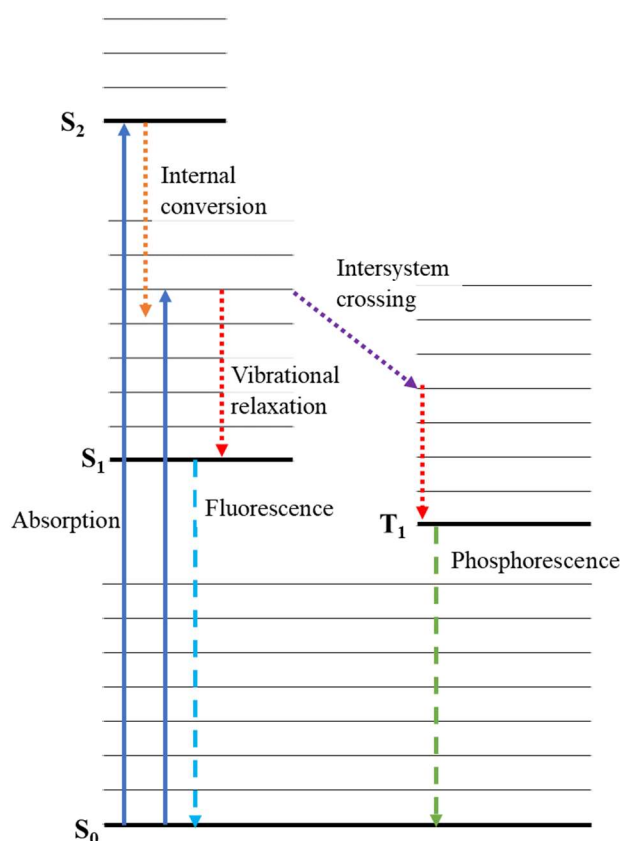
Figure 2-6: Jablonski diagram showing some possible fates of excited states.

In order to generate the light required for probing the desired transition, Nd:YAG lasers are often used in combination with dye lasers; both are described below.

2.6.1 Nd:YAG Laser

Nd:YAG lasers are comprised of neodymium ions (Nd^{3+}) hosted inside an yttrium aluminium garnet (YAG; $Y_3Al_5O_{12}$) crystal lattice. The host lattice influences the energy levels in the neodymium ions, where the laser action transitions take place. Originally degenerate, the energy levels are split by the influence of the crystal field, and laser

emission occurs after stimulated emission from the $^4F_{3/2}$ level to the $^4I_{11/2}$ level; a transition formally forbidden without the crystal lattice interaction. The active medium is located as a rod within the laser, with a flashlamp providing the initial excitation to higher energy levels than the $^4F_{3/2}$ level. Radiationless decay populates this level. The existence of a $^4I_{9/2}$ ground state below the lowest level of the lasing transition means the Nd:YAG level operates essentially as a four-level laser.

Nd:YAG lasers can operate with pulse energies up to 100 Joules, but also down to a fraction of 1 Joule. Frequency conversion can also enable access to wavelengths other than the typical 1064 nm, such as 532, 355 and 266 nm through harmonic generation.

In this thesis, a Nd:YAG-pumped dye laser was employed. The pump laser light was obtained from the output of a Continuum Precision II laser at 532 nm, after frequency doubling the fundamental 1064 nm output.

2.6.1.1   Frequency Conversion

The wavelength output characteristic of the active medium in the laser can be modified, and in this work, the Nd:YAG 1064 nm light underwent frequency doubling to 532 nm. Frequency doubling, also known as second harmonic generation, involves two photons of frequency v being absorbed by a substance in its ground state, and a photon of frequency $2v$ being emitted upon return to the ground state. Energy levels at hv or $2hv$ are not required, as there is no excited state with a measurable lifetime. Crystals are required for this process, as there must be no centre of symmetry in the medium. Third harmonic generation to produce 355 nm light from a Nd:YAG laser is also possible, as are using multiple doubling crystals in series to achieve even shorter wavelengths.

2.6.1.2   Q-Switching

Q-switching is used to achieve pulsed operation of a Nd:YAG with higher energies and shorter pulse durations. By placing a shutter within the optical cavity, the loss is increased, and a large population inversion can be established with very little stimulated emission occurring. Once the shutter is opened, the cavity releases the energy stored by the medium as a single pulse of intense light. The Q in Q-switching refers to quality, or Q-factor, where the process of Q-switching involves a sudden reversal in high loss (low Q-factor), to low loss (high Q-factor). Two common methods deployed to

achieve Q-switching involve using a high-speed rotating end-mirror to only briefly let out light or electro-optical shutter actions, such as a Pockels cell and polariser (Figure 2-7), where the light rotates 90º and is cut out by the polariser.
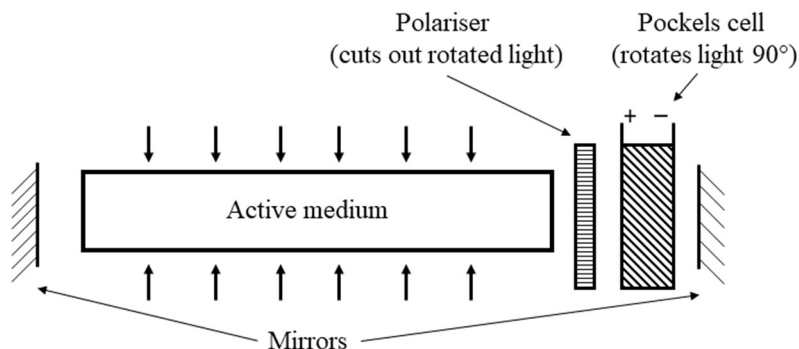
Figure 2-7: Schematic example of a Q-switch (Pockels cell type).

2.6.2 Dye Laser

Dye lasers operate using an organic dye solution which has a broad fluorescence spectrum and absorption in the visible region [117]. A common dye utilised is Rhodamine 6G, which is typical of dye molecules, where a large conjugated structure allows for considerable electron delocalisation, and a high number of distinct vibrational modes arising from the large number of atoms. As a liquid solution, the energy levels are broadened due to strong molecular interactions, and so for each electronic state, an energy continuum is formed where the broadened energy levels overlap.

Typically a dye will absorb visible light causing a transition from the ground singlet state S_0, transitioning to the S_1 first excited singlet state energy continuum. This state has a short lifetime, and rapidly undergoes radiationless decay to the lowest level of the S_1 continuum. Transitions down to S_0 continuum levels result in fluorescent emission, and are followed by further radiationless decay. A pseudo-four level system ensures a population inversion between the two levels involved in the lasing emission. Due to reduction in photon energy, fluorescence occurs at a longer wavelength than the initial excitation. For example, in this work, the frequency-doubled Nd:YAG laser light at 532 nm is retuned to 616 nm by the dye laser, before further frequency doubling to give the required probe light at 308 nm.

Laser efficiency is reduced (often to approximately 5%) within the dye as a result of processes such as intersystem crossing from a singlet state to a triplet state, where slow

phosphorescence can repopulate the lower S_0 levels. Intersystem crossing from the triplet states to S_0, or absorption of radiation to higher triplet states, also contribute to the process of reducing efficiency. Similarly, the S_1 state can undergo radiationless decay to S_0, or transition to S_2 states through absorption.

Diffraction gratings are used to tune the wavelength of the laser output, where rotation of the grating changes the monochromatic emission, and is placed between the two end mirrors of the cavity, where a cell is also placed containing the flowing dye liquid.

In this thesis, OH radicals were probed at ~308 nm, corresponding to the energy of the OH $Q_1(2)$ rotational line of the $A^2\Sigma^+(v' = 0) \leftarrow X^2\Pi_i(v'' = 0)$ transition. The Nd:YAG-pumped dye laser used (Sirah PRSC-DA-24) generally operated at 10 Hz, where the pulse energy was <0.1 mJ pulse^{-1}. The dye laser operated using DCM (4-(dicyanomethylene)-2-methyl-6-(4-dimethylaminostyryl)-4H-pyran) Special dye, the beam diameter was approximately 3 mm, and light output at ~616 nm was doubled to output ~308 nm light for the OH detection. Orientation of the tuning crystal used for frequency doubling was crucial, and the temperature dependence of the refractive index necessitated the use of a controlled heating cell held at a stable temperature to ensure maximum efficiency. When this heating cell was not reliable, manual tuning of the crystal was required, and regular checks were necessary, as the crystal was subject to temperature fluctuations in the laboratory.

2.7 Apparatus Used in this Work

This section describes the experimental setup (other than the lasers that have already been discussed) used for the majority of the experiments that comprise this thesis, and provides an example of typical data analysis, and some data used to calibrate the temperature of the reaction cell.

2.7.1 Gas Flow

Reactants were flowed using calibrated mass flow controllers (MFCs) in order to control and monitor the concentration of reagents (Figure 2-8). The fuel (DME, DEE, DBE, MTBE, or TMOF) was typically flowed from a bulb diluted with nitrogen, normally to 0.5 – 20% ether concentration. The exact concentration of a bulb was calculated using

the relative pressures after addition of ether and then nitrogen, and bulbs were left overnight before use, in order to ensure thorough mixing of the gases. Nitrogen (oxygen-free) was also flowed through a separate mass flow controller, as was oxygen (when required), and the hydroxyl radical precursor. Early experiments used t-BuOOH as an OH radical precursor, however this was later replaced by hydrogen peroxide (H_2O_2/H_2O). Both hydroxyl radical precursor compounds were delivered using a bubbler under nitrogen flow, with the bubbler situated upstream of the MFC. Slight variations in the delivery of reactants and precursors employed are outlined in the relevant chapters.
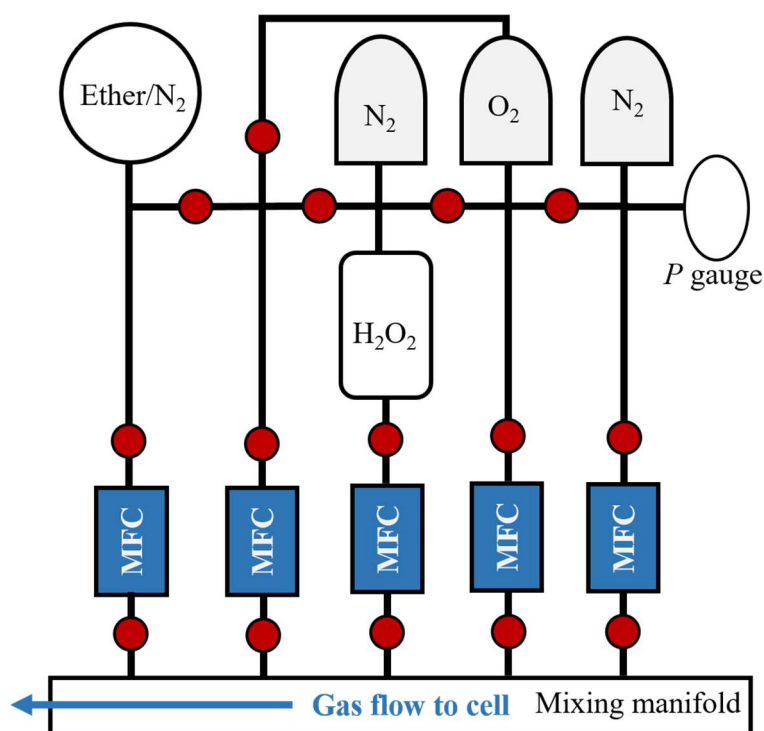
Figure 2-8: Gas delivery line used in the experimental setup. Red circles represent taps.

Taps were used to isolate the flow of different gases (red circles, Figure 2-8), and allow facile re-routing of gas flows where required (i.e. oxygen was sometimes delivered through a high flow MFC (~100 – 4000 sccm (standard cubic centimetre per minute)), or a MFC that allowed very low flows (~1 – 20 sccm), depending on the experiment being undertaken. Mass flow controllers were arranged so the larger volumes of gas were delivered at the rear of the mixing manifold, and small flows at the front of the mixing manifold, to encourage mixing and ensure low amounts of gases flowed were carried into the reaction cell efficiently.

Owing to the placement of a pressure gauge on the gas delivery line, bulbs were generally prepared on the same system used for experiments. Occasionally, for low concentration bulbs, or where ethers possessing low vapour pressures (such as DBE) were used, bulbs were made up on a separate, but similar line, that featured a wider range of pressure gauges, to enable more precise bulb concentration calculations. Leak testing was routinely carried out on the gas delivery line in Figure 2-8 to minimise loss of gases to the atmosphere, and the introduction of atmospheric O_2 into the mixing manifold. Generally this was carried out through systematic monitoring of gas line pressure changes when the system was sealed, or through identifying sudden pressure changes around loose joints or taps when the line was sprayed with ethanol. Joints were tightened, and tap o-rings replaced where necessary, and for leaks that were particularly difficult to identify, a Mass Spectrometer Leak Detector was used, with helium as the trace gas.

Two issues arising from the use of H_2O_2 and *t*-BuOOH precursors should be highlighted. The first, is a result of decomposition of H_2O_2 within the MFC and/or gas delivery lines, resulting in the presence of oxygen in the reaction cell at all times. The concentration of oxygen present varied depending on the total amount of hydrogen peroxide delivered, and the method used to ascertain this concentration is outlined in detail in Chapter 4. H_2O_2 is known to decompose at higher temperatures to H_2O and O_2 [120, 121], and iron (which will be present in the stainless steel pipes used to flow gases in experiments) acts as a catalyst for its decomposition. In general, knowing the amount of oxygen present allows experimental conditions to be set up to account for this in the best possible way, but its presence can make the extraction of kinetic parameters prone to greater uncertainty.

The second issue is decomposition of *t*-BuOOH, resulting in the formation of OH. Data for the OH + DEE reaction manifested itself as biexponential decays in Chapter 3 when using this precursor. Acting as a photolysis-independent precursor to OH radicals is unsurprising given the hydroperoxy group present in this molecule, and its instability at ~311 K [122] meant *t*-BuOOH was never used at higher temperatures (approximately 450 K) where it begins to interfere severely with kinetic decays, and ultimately wasn't relied on for the large majority of experiments in this thesis.

2.7.1.1 Flow Correction

For the fuel/N_2 bulbs, experiments were conducted that identified it was necessary to adjust flow rates using a correction factor (equation E 2-5), for a specific reactant molecule and bulb concentration. This was discovered after identifying a discrepancy between the flow of nitrogen through a MFC (used for the calibration of the MFCs), and the actual flow rates measured when an ether/N_2 bulb was used.

$$\frac{100}{\frac{[\text{ether}]}{\alpha} + \frac{100 - [\text{ether}]}{1}} \qquad \text{E 2-5}$$

The factor, α, in equation E 2-5 changes for each ether. For DME, $\alpha = 0.39$, and for DEE α was approximated to be 0.3, based on the correction factor for butanol. This was confirmed by calibrating the MFC with the actual DEE/N_2 mixed bulb, rather than pure nitrogen, to check that the α value corrected the pure nitrogen flow to match the measured bulb flow. The correction factor for nitrogen is 1. DBE, MTBE and TMOF were assigned approximate correction factors of 0.1, 0.20 and 0.15 based on their molecular masses. The correction factors are related to the specific heat capacity, and therefore mass, of the gas molecule in question, where a larger molecule can typically store more heat energy as a result of the greater number of degrees of freedom (vibrational and rotational modes). Heavier molecules will have lower α factors, and therefore a greater reduction in flow must be accounted for.

2.7.2 Reaction Cell

Reactants entered a mixing manifold, before the stainless steel reaction cell ($\sim$1000 cm^3 volume, Figure 2-9), where a needle valve before a vacuum pump (Edwards RV 5), and total gas flow rate, were used to control the pressure in the cell, and to control flow rates over a range of approximately 100 – 6000 sccm. Low pressures were used (generally 5 – 500 Torr) to minimise quenching of the fluorescence signal for detection.
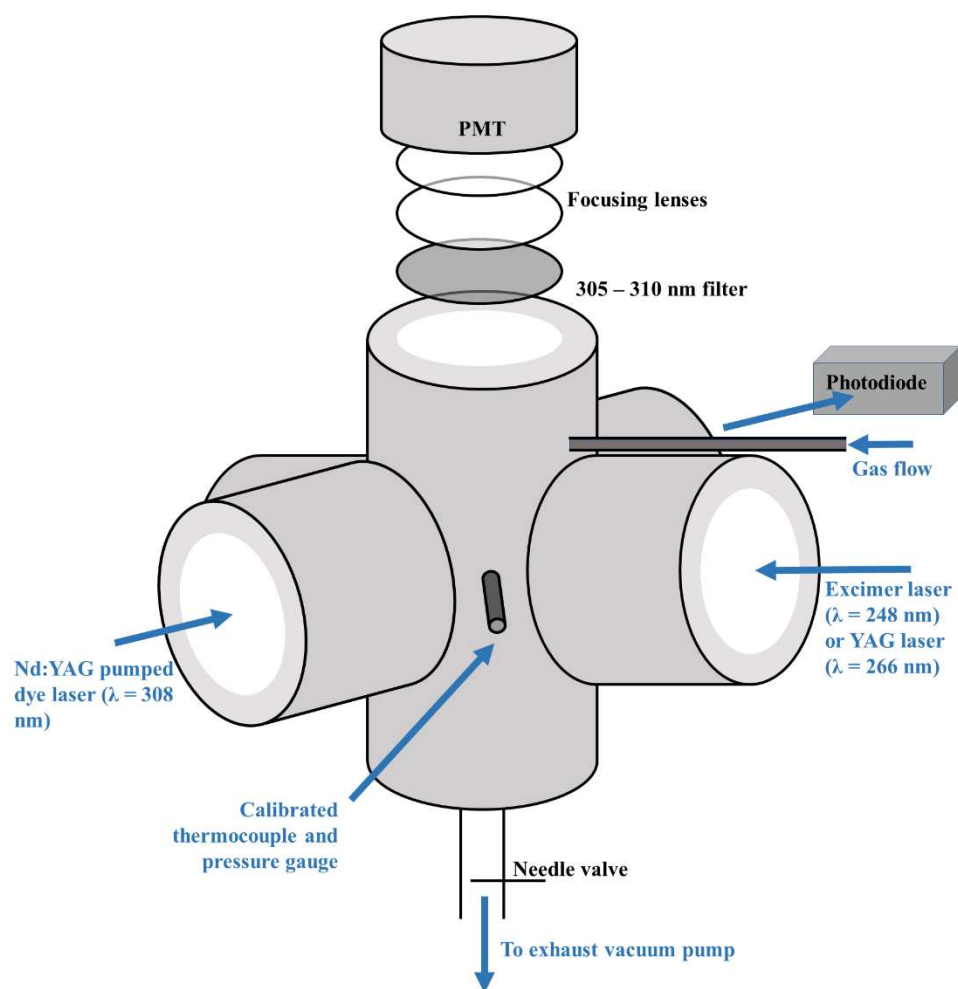
Figure 2-9: Schematic of the reaction cell used for the majority of experiments in this thesis.

Approximate flow rates can be calculated for a typical experiment at 298 K, 2000 sccm and 40 Torr as below in equation E 2-6:

$$Q_{actual} = Q_{standard} \frac{\rho_{standard}}{\rho_{actual}}$$

$$\text{E 2-6}$$

where Q = flow rate, and ρ = density. Typically over 95% of the flow is that of the bath gas (and the majority of the remainder would be O_2, which is of similar density to N_2), so the density is assumed to be equal to nitrogen's ($\rho_{standard}$ = 1.2506 kg m^{-3}). The ideal gas law (equation E 2-7) is used to calculate the actual density to be 0.0603 kg m^{-3}.

$$\frac{n}{V} = \frac{P}{RT}$$

$$\text{E 2-7}$$

From here, the actual flow rate can be calculated, and subsequent division by the volume of the cell in equation E 2-8 can be converted to give the total time required to flush the cell as 1.45 s. This is the total residence time within the entire cell, but the gas spends less time within the region where the two laser beams overlap.

$$\frac{41500 \text{ cm}^3 \text{ min}^{-1}}{1000 \text{ cm}^3} = 41.5 \text{ min}^{-1} \qquad\qquad \text{E 2-8}$$

By the time gas entering the cell has reached the observation zone, it should not have been subject to many repeated photolysis pulses, as the gas flow does not enter along the photolysis laser axis (see Figure 2-13). However, the flow is not laminar, and the reactor is not linear, so the flow of gas will be complex. Consequently experiments determining pseudo-first order rate coefficients at varying laser repetition rates can be used to rule out any interfering effects, and were often carried out (see Chapter 3).

2.7.3   Pressure Monitoring

Pressure in the reaction cell was monitored using a capacitance manometer (MKS Baratron, 0 – 1000 Torr) situated at the entrance to the reaction cell. Throttling of the rotary pump (Edwards RV 5) by a needle valve was used to control the pressure.

2.7.4   Detection of OH

Fluorescence from the OH radicals at ~308 nm was detected by a photomultiplier tube (Electron Tubes), after passing through a filter ((308 ± 5) nm, Barr Associates). A digital oscilloscope (LeCroy LT 372) integrated the fluorescence signal, before transferring the output to the personal computer for collection and analysis, where the fluorescence signal was normalised for probe laser power. Probing on-resonance necessitated the use of a delay (~30 ns) before analysing the fluorescence, to avoid detecting the scatter pulse from the probe laser.

Photomultiplier tubes (PMTs) used in this thesis operate on the photoelectric effect, where photons from the detectable light source hit a photosensitive cathode within a vacuum tube, releasing electrons. These electrons are received by the anode, and, using a series of electrodes (metal channel dynodes), multiplied by up to a factor of 10^9,

achieving great sensitivity to weak fluorescence signals. The PMT was situated at a right angle to the reaction cell in order to reduce the amount of scattered light hitting the cathode, and the filter was used to ensure only light of the target wavelength was collected.

To build up a time-dependent trace of OH fluorescence signal, the delay time between the photolysis and probe lasers was varied using a delay generator, with a typical decay trace consisting 220 points, each averaged 3 – 30 times, over approximately 0.1 – 25 ms, depending on the experiment.

2.7.5 Typical Data Analysis

During experiments, pseudo-first order conditions were used, where the concentration of the ether was in excess of the OH radicals (typical OH concentrations of 1×10^{12} molecule cm^{-3} and typical ether concentrations of 5×10^{14} molecule cm^{-3}). Using rate laws, it can be shown that an excess of ether allowed the reaction between OH and ether to be studied. Additionally, the high concentration of ether ensured that the reaction between ether and hydroxyl radical dominated, rather than the reaction between OH and the peroxide precursor in reaction R 2-4. OH self-reactions were also negligible due to the even lower concentration of OH radicals compared with H_2O_2.

$$OH + H_2O_2 \rightarrow HO_2 + H_2O \qquad\qquad R\ 2\text{-}4$$

After the collection of the fluorescence signal, the data were transferred to a personal computer, and normalised for probe laser power measured by a photodiode placed behind the exit window of the cell. An example of this is shown in Figure 2-10. There is no statistical difference between the pseudo-first order rate coefficients returned before and after normalisation, and only a marginal reduction in the rate coefficient uncertainty (there is not a great deal of fluctuation in laser power).
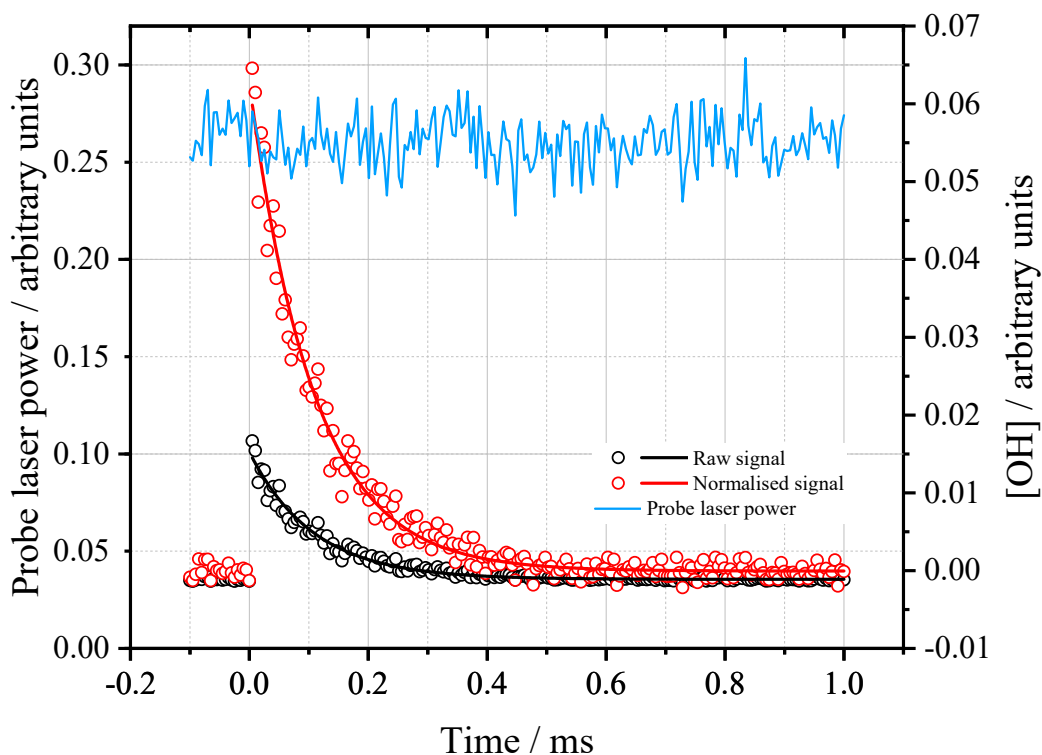
Figure 2-10: Typical OH decay trace showing pre- and post-normalisation for probe laser power. Pseudo-first order parameters for raw signal and normalised signal respectively: $k' = (9290 \pm 370)$ s^{-1} and (9280 ± 330) s^{-1}. Uncertainties are statistical at the 2σ level.

For a typical OH + ether kinetic single exponential decay, the following rate equations were used to analyse the data based on reaction R 2-5, in order to obtain the bimolecular rate coefficient. More complex analysis required for biexponential traces as a result of more convoluted reaction schemes was often necessary, and these analyses are described in their relevant chapters.

$$OH + ROR'H \rightarrow ROR' + H_2O \qquad\qquad R\ 2\text{-}5$$

The rate of reaction R 2-5 can be expressed as the rate of removal of a species (OH in this case) with time. This is equal to the product of the concentration of both reactants (ether and hydroxyl radical) multiplied by a rate coefficient for a specific temperature (equation E 2-9). The reaction between OH and the photolytic precursor (reaction R 2-4, k_{OH}) will also contribute. This is measured as a kinetic decay in the absence of ether, although diffusion (k_{diff}) likely also contributes to the rate in this case.

$$\frac{-d[OH]}{dt} = k_{\text{bim}}[OH][\text{ether}] + k_{OH}[OH][H_2O_2] + k_{\text{diff}}[OH] \qquad \text{E 2-9}$$

By keeping the ether in large excess of the hydroxyl radicals, it can be assumed that the ether concentration remains constant throughout the reaction time. Now the rate law can be approximated as equation E 2-10, where k' is referred to as the pseudo-first order rate coefficient (equation E 2-11).

$$\frac{-d[OH]}{dt} = k'[OH] \qquad \text{E 2-10}$$

$$k' = k_{\text{bim}}[\text{ether}] + k_{OH}[H_2O_2] + k_{\text{diff}} \qquad \text{E 2-11}$$

From the relationship between the parameters in equation E 2-11, it can be seen that a plot of the observed pseudo-first order rate coefficient against ether concentration will yield the bimolecular rate coefficient as the gradient of the plot, with the intercept = $k_{OH}[H_2O_2] + k_{\text{diff}}$. In order to extract the pseudo-first order rate coefficient from a kinetic trace, the integrated rate law is used [123]. Equation E 2-10 can be rearranged to equation E 2-12, which in turn can be integrated between $t = 0$, and the final time, t, as in equation E 2-13, yielding equation E 2-14.

$$\frac{d[OH]}{[OH]} = -k'dt \qquad \text{E 2-12}$$

$$\int_{[OH]_0}^{[OH]} \frac{d[OH]}{[OH]} = -k' \int_0^t dt \qquad \text{E 2-13}$$

$$\ln[OH] - \ln[OH]_0 = -k't \qquad \text{E 2-14}$$

$$[OH] = [OH]_0 e^{-k't} \qquad \text{E 2-15}$$

Equation E 2-15 is obtained from equation E 2-14. This equation allowed analysis of single exponential kinetic traces obtained from the laser flash photolysis – laser-induced fluorescence experiments conducted in this work. The actual equation used does not rely on [OH], but I_f, which is the intensity of the OH fluorescence. Pseudo-first order conditions do not require absolute concentrations to be known, as I_f is proportional to [OH], and the pseudo-first order rate coefficient determined is dependent on time, and the relative change in the fluorescence intensity.

$$I_{f,t} = I_{f,0}e^{-k't} \qquad\qquad \text{E 2-16}$$

An example of a typical kinetic decay is shown in Figure 2-11. Data points present pre-time zero were recorded before the photolysis laser fire, in order to establish a baseline of fluorescence signal. This average baseline could be incorporated into the exponential equation, or the trace could be corrected to have a baseline of zero. In this example case, the decay has been corrected so the pre-trigger baseline has a mean value of zero.
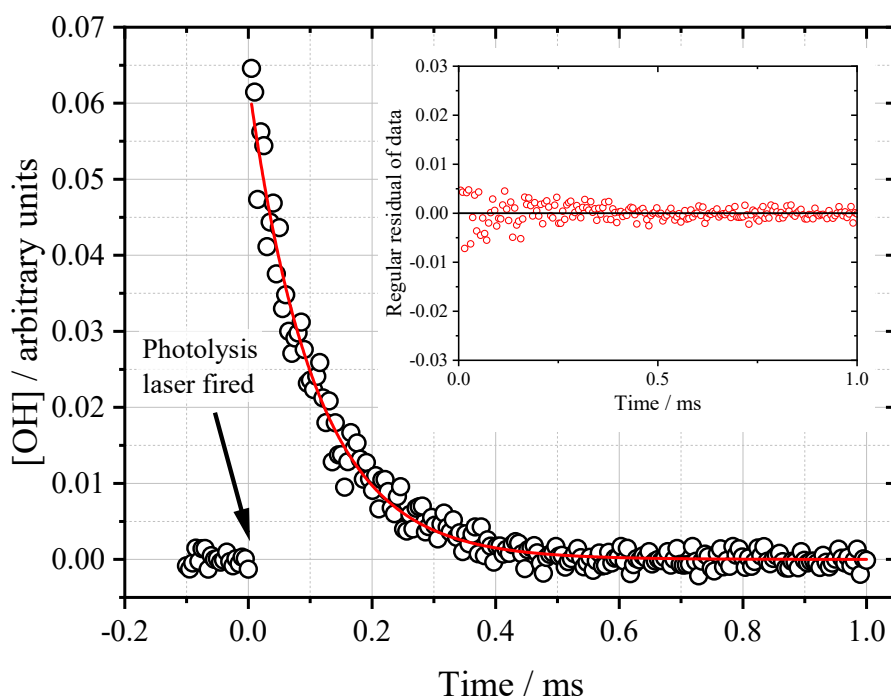
Figure 2-11: Typical single exponential kinetic decay trace for the OH + DEE reaction, with a fit of single exponential decay (red line). Trace was obtained at 298 K, in 47 Torr N_2, where [DEE] = 7.7 × 10^{14} molecule cm^{-3}. The exponential fit yielded $k' = (9320 \pm 340)$ s^{-1} where the error was statistical, calculated at the 2σ level. The inset shows the residuals of the fit to the data.

The bimolecular rate coefficients were obtained from the slope of the plot of the phenomenological rate coefficient k' as a function of [ether], where the intercept, k_d, was the rate coefficient for loss of OH in the absence of ether, primarily from the OH + H_2O_2 reaction. An example bimolecular plot for the OH + DBE reaction is shown in Figure 2-12.
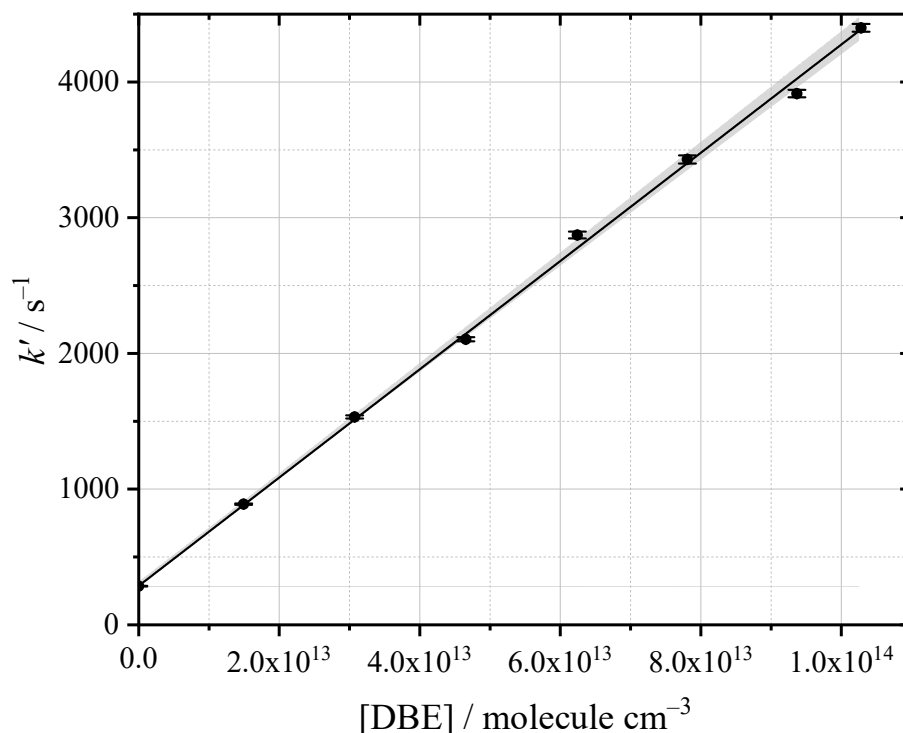
Figure 2-12: Example bimolecular plot to determine the OH + DBE bimolecular rate coefficient at T = 298 K and 29 Torr N_2. Slope, k_{bim} = (3.99 ± 0.09) × 10^{-11} cm^3 $molecule^{-1}$ s^{-1}, where the error is statistical, calculated at the 2σ level. The grey shaded area represents the bounds of the 95% confidence limits.

2.7.5.1 Treatment of Data and Weighting

Not all the data collected were of equal precision, due to varied signal quality as a result of laser alignment, excimer power, temperature, pressure, and hydrogen peroxide purity. These factors often led to a difference in the quality of a kinetic trace. To weight the values of pseudo-first order rate coefficients used in bimolecular determinations, instrumental weighting in OriginPro was used. This weight factor, w_i, is defined in equation E 2-17:

$$w_i = \frac{1}{\sigma_i^2} \qquad \text{E 2-17}$$

here, σ_i refers to the size of the uncertainty on the data point. Instrumental weighting was also used for other data fitting regimes, such as Arrhenius parameterisations (Chapter 3), and mean OH yield calculations (Chapter 6).

One exception, where an instrumental weighting factor was not used, was in the use of globally analysed data. Global analysis uses multiple kinetic traces at once, sharing

some parameters (i.e. k_{bim} for a set of traces at a given pressure and temperature), and not sharing other parameters (i.e. k' and [ether] will be unique to each trace across a set for bimolecular determination). This technique allows a more robust determination of kinetic parameters, but does not allow for suitable weighting factors. Uncertainties on each data point in a kinetic decay were not readily available, and a weighting factor based on the magnitude of the signal will only serve to weight each trace in favour of the early or later points in a trace.

Global determinations of rate parameters typically returns much smaller uncertainties than single trace analysis (shown above in Figure 2-11 and Figure 2-12), and so uncertainties from global analysis, such as those for the determination of $k_{OH+MTBE}$ in Chapter 3, were often propagated with an extra uncertainty factor if the errors appeared unreasonably small. Further discussion of the global fitting method can be found in Chapter 4.

2.7.6   Temperature Control and Monitoring

The reactor was heated up to maximum temperatures of approximately 750 K, using a ceramic oven. A variable autotransformer was used to control the voltage of the heater, and calibration curves were constructed, allowing the prediction of the voltage setting required to give the desired cell temperature, for a given flow rate. For early experiments, one Type K thermocouple was situated near the inlet of reactant gas, and for later experiments two more thermocouples were inserted at different positions, as it became apparent there was a discrepancy between the thermocouple readout and the true temperature of the reaction region.

2.7.6.1   Temperature Calibration

Placement of three Type K thermocouples within the reaction cell (Figure 2-13) showed there was some disagreement between the temperatures recorded in each of the positions. The difference between these temperatures was sometimes greater than 50 K, and varied greatly with different flow rates of gas. Kinetic parameters measured in this work were often temperature dependent, and thus required accurate knowledge of the temperature of the gases where the reactions took place. Characterisation of the experimental setup was necessary to achieve this.
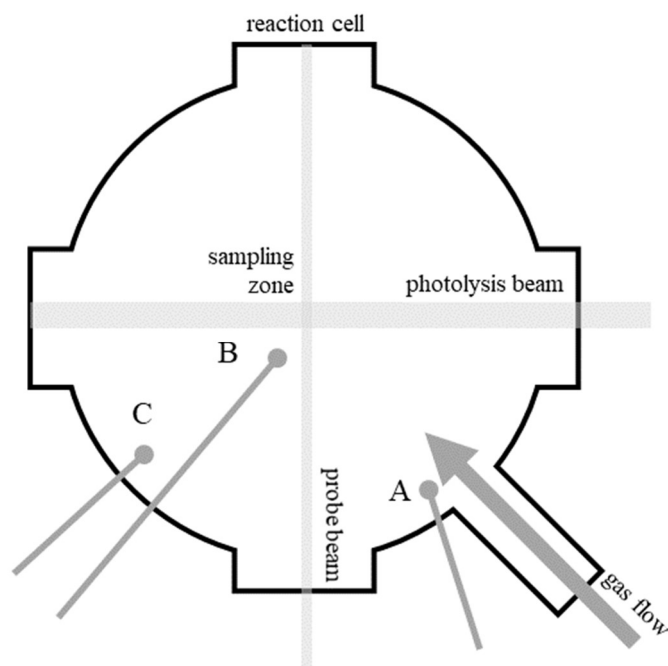
Figure 2-13: Diagram of approximate thermocouple placement in reaction cell. Round-headed arrows indicate the ends of the thermocouples.

In order to ascertain the temperature of the reaction cell when heated, the well-known reaction between methane and the hydroxyl radical was used (reaction R 2-6). This reaction was suitable due to its particularly strong dependence on temperature, and therefore sensitivity as a chemical thermometer.
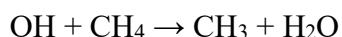
$$OH + CH_4 \rightarrow CH_3 + H_2O \qquad\qquad R\ 2\text{-}6$$

Bimolecular plots were produced by measuring the decay of OH in the presence of methane, and using the Arrhenius parameters reported by Dunlop and Tully [124], an implied temperature could be determined. A bimolecular rate coefficient for OH + CH$_4$ in a given experiment was initially calculated using the temperature reading given by the thermocouple. The true temperature was implied by the measured k_{OH+CH4} value. However, calculated reactant concentrations were changed when the temperature was corrected, which in turn adjusted the value of the experimental bimolecular plot, leading to a new implied true temperature (Figure 2-14 demonstrates this iterative process).
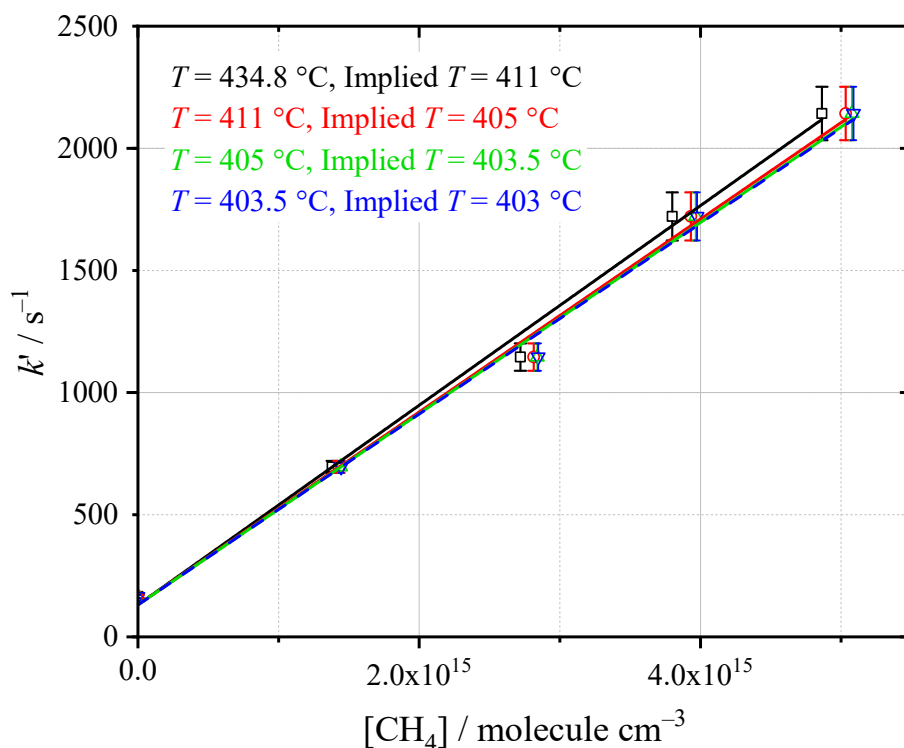
Figure 2-14: OH + CH₄ bimolecular determination plot, iterating towards the final calibrated temperature, 403 °C. This temperature would be assigned an uncertainty of 8.2 °C (twice the 4.1% uncertainty of the bimolecular plot slope, discussed in the text).

To iterate towards the solution efficiently, a simple command within the experimental spreadsheet can be set up, which calculates the difference between the rate coefficient predicted by Dunlop and Tully [124], and the experimental k_{OH+CH4}. The difference between the two can then be minimised using the 'goal seek' command in Microsoft Excel, by adjusting the temperature used in both the calculation for Dunlop and Tully's expression, and the experimental measurement.
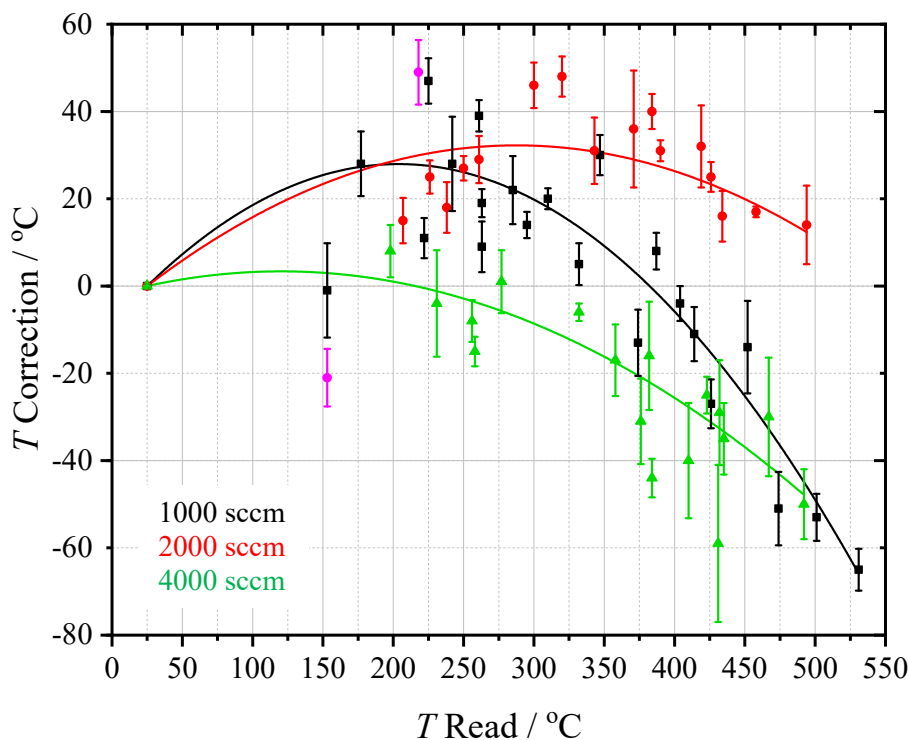
Figure 2-15: Correction curves for temperature, based on the Dunlop and Tully [124] study of the OH + CH$_4$ reaction. Corrections at flow rates of 1000, 2000 and 4000 sccm N$_2$ (black, red, green respectively). Fits are second order polynomials. Anomalous data points (purple data) in 2000 sccm flow calibration curve were omitted from the polynomial fitting expression. All corrections are based on the measurements using thermocouple A.

A significant number of experiments have been conducted so that the temperature can be assigned with reasonable confidence for reactions at flow rates of 1000, 2000 and 4000 sccm, at temperatures between approximately 150 and 550 °C (as measured by the thermocouple). These experiments were conducted over a period of months, rather than back-to-back in a short time period, resulting in greater scatter. Degrees Celsius are used here (Kelvin are generally used in the rest of this thesis), simply as a result of the units used by the thermocouple readouts. Simple second order polynomial equations were used to fit the correction curves (Figure 2-15), in the form $y = ax + bx^2$.

Error bars were assigned simply by doubling the percentage error of the OH + methane rate coefficient measured. For example, the 4.1% uncertainty in the bimolecular plot in Figure 2-14, would result in an uncertainty value of 8.2 °C for the corresponding correction factor. The uncertainties' absolute values, and magnitudes, are not that important, they are primarily used to weight the parameterisation towards the better quality bimolecular determinations, based on statistical uncertainties. Doubling of the percentage uncertainty was used so all error bars could be clearly seen. Calibrations are

shown in Figure 2-16 for both 2000 sccm and 4000 sccm flow rates, where the total pressures of the measurements are specified. No significant effect on the temperature correction calculated was caused by varying total pressure, reinforcing the theory that the temperature deviations arose from changes in the gas flow rate.
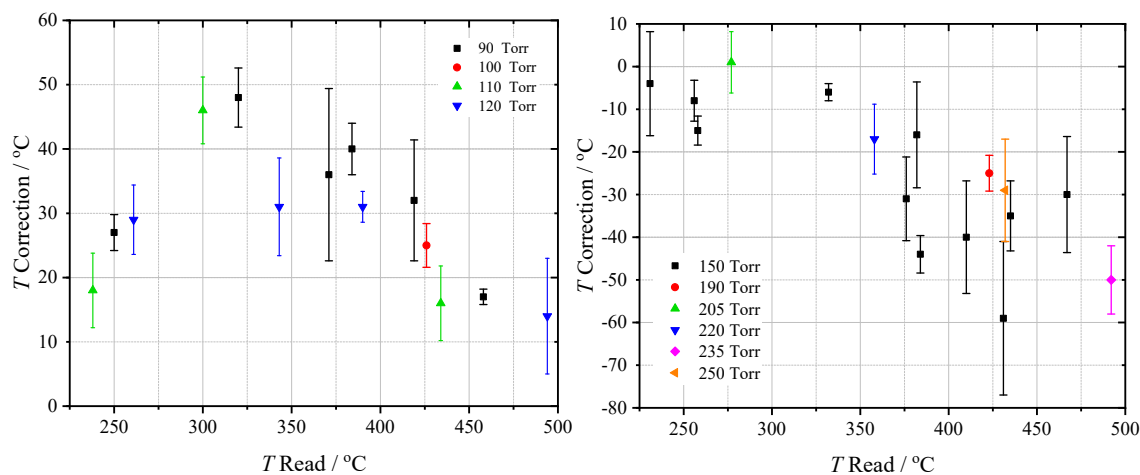
Figure 2-16: Temperature correction measurements as a function of total pressure. 2000 sccm (left) and 4000 sccm (right).

The three thermocouples placed in the system were positioned in different locations (Figure 2-13), and though the reasons behind their different readings is not fully understood, the positions likely account for the observed behaviour. For example, thermocouple A is located very close to the inlet of reactant gases entering the cell, so at higher flow rates is likely to feel a greater decrease in temperature due to gas rapidly passing across the thermocouple. Thermocouple C may read higher temperatures due to its location next to the wall, where it is ultimately closer to heaters, and should experience the flow of better-heated gases. Placement of thermocouple B is closest to the centre of the cell, where the photolysis and probe lasers intersect, however thermocouple A was used to generate the calibration curves. In practice it shouldn't matter which thermocouple is used, but measurements carried out prior to all three thermocouples being present were measured using thermocouple A, so basing the temperature corrections on this thermocouple allowed the same correction factors to be applied to all experiments, maintaining relative consistency.

Below 150 °C, no OH + CH$_4$ rate coefficient measurements were made in this work, as the reaction becomes too slow for the experimental method to measure accurately. The calibration curves cannot necessarily be extrapolated directly back to

room temperature, as the difference between measured and implied temperatures should be zero at 298 K, but it is clear to see the polynomial curve extrapolations could give extreme corrections close to room temperature if not constrained (1000 sccm curve, Figure 2-15). A suitably sensitive and fast reaction that can be studied at temperatures below 200 °C would enable future measurements to identify accurate correction factors closer to room temperature. For this reason, reactions close to room temperature were not corrected. Flows approaching 500 sccm and below were also not corrected, as it was assumed the slower-flowing gas had less of an effect on the system. As the flow rate was reduced, the three thermocouples gave closer temperature readings to one another, supporting this theory.

Figure 2-15 shows significant scatter in the measurements at all flow rates, and as such, it is clear that there is always a degree of uncertainty when assigning temperatures to heated reactions, even when using a calibrated thermocouple. Ideally, further experiments would use a thermocouple that behaves as expected at all flow rates; essentially following the shape of the 4000 sccm calibration graph (green curve, Figure 2-15), where the temperature correction required does not switch from positive to negative (black and red curves, Figure 2-15). It is not clear what causes this behaviour, and the extreme difference between the calibration curve shape at different flow rates. A wider range of flow rate calibrations, and a thermocouple with more predictable measurement behaviour, would allow a parameterisation that interpolates the correction for any given flow rate.

Ultimately, calibration of the experimental setup allowed kinetic studies of biofuel ethers to be carried out with greater certainty, and was necessary to ensure the true temperature was known, where previously the thermocouple was able to give an incorrect reading of up to 60 °C above or below the true temperature at the location of the reaction. In this thesis, typically all data above room temperature that require a temperature correction (i.e. flow rates ≥1000 sccm) are subject to approximately an uncertainty of ±10 °C as a result of the calibrations presented here. This work highlights a need to rigorously check the experimental setup used for laser-based kinetic studies, and demonstrates that trust in one thermocouple may be misplaced. Furthermore, an incorrect temperature reading would be difficult to notice if a reaction that is not particularly temperature dependent was being studied, although this would likely mean a well-characterised temperature reading is not crucial. Experiments using thermocouples to

measure temperatures of fast flowing gases, particularly at higher temperatures, are likely to be subject to greater correction factors.

2.8 Other Experimental Techniques

This section outlines some techniques used to study the kinetics of gas phase reactions, and they are contrasted with the methods employed throughout this thesis. Most of these techniques have been used to study the reactions of OH + hydrocarbons, but some are relevant to the detection of intermediate species in low temperature combustion.

2.8.1 Shock Tubes

In a shock tube experiment, an inert gas shock wave is passed through a pierced diaphragm along a metal tube, which contains a well-mixed reaction mixture, raising the temperature of the reactants as it passes [86, 125]. Precursor dissociation takes place inside and behind the shock wave, before the transient species goes on to react. Normally the shock front is detected by observation of the large change in pressure, temperature, or density. The reaction within this front can be followed by observation of a reactants' absorption spectrum in order to monitor its concentration. Mass spectrometry has also been used, which allows several species to be monitored at once.
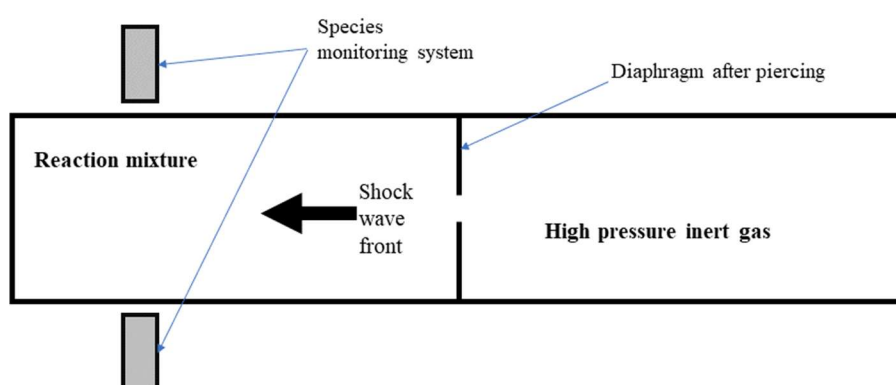
Figure 2-17: Schematic of a typical shock tube experiment setup.

Shock tubes allow the study of reactions at high temperatures (800 – 2500 K), and have become more sensitive with advances in detection techniques, however disadvantages to this technique include dissociation of undesired reactants, which will

lead to unexpected reactions perturbing the measured kinetics, although decomposition of precursors at high temperatures is also an issue for the flash photolysis technique. Additionally, only one decay trace is obtained for each experiment, which leads to many measurements being required in order to improve the signal-to-noise ratio satisfactorily. The laser flash photolysis – laser-induced fluorescence technique employed in this thesis can obtain many measurements in a short space of time in comparison. The high temperatures accessible using shock tubes are well complemented by the lower temperatures (<800 K) that are typically studied using the technique in this thesis, and the technique has been used to study the reactions of OH with MTBE and DME [126, 127].

Developments improving shock tube experiments have allowed lower temperature studies by using a tailored shock wave mixture to minimise the heating effect caused by backward propagating waves after wall contact, and by using longer driver sections in order to increase the test times accessible [128]. This is necessary as a result of the slower reactions in low temperature chemistry when compared with higher temperatures. Aerosol shock tubes have also been developed to allow the study of fuels with low vapour pressures.

2.8.2 Relative Rate Determinations

When isolation of an elementary reaction is not possible, relative rate methods can be used to study the reaction, and have been used to report rate coefficients for many of the OH + ether reactions studied in this thesis [129-132]. Known concentrations of two reactants, one a reference compound with a known bimolecular rate (RH), and the other the compound of interest where the rate coefficient is unknown (SH), are introduced to a reaction vessel with a photolytic precursor (in this example a precursor to OH). When photolysis lamps are turned on, a small constant concentration of OH radicals is generated. Reactions R 2-7 and R 2-8 will be taking place in the vessel.

$$OH + RH \rightarrow H_2O + R \qquad\qquad R\ 2\text{-}7$$
$$OH + SH \rightarrow H_2O + S \qquad\qquad R\ 2\text{-}8$$
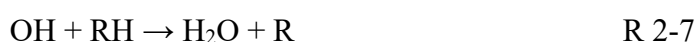
At multiple times, gas samples are taken from the reaction cell and analysed by a technique such as gas chromatography (GC), to determine $[RH]_t$ and $[SH]_t$. Initial concentrations of RH and SH can be low to allow plenty of time to sample over a long

reaction time. Rate laws for reactions R 2-8 and R 2-7 can be expressed as equations E 2-18 and E 2-19 respectively.

$$\frac{d[SH]}{dt} = k_s[OH][SH] \qquad\qquad \text{E 2-18}$$

$$\frac{d[RH]}{dt} = k_r[OH][RH] \qquad\qquad \text{E 2-19}$$

Integrating equations E 2-18 and E 2-19 under the assumption [OH] is constant ($[OH]_{ss}$, steady-state), yields equations E 2-20 and E 2-21, which when combined, give equation E 2-22.

$$\ln\left(\frac{[SH]_t}{[SH]_0}\right) = k_s[OH]_{ss}t \qquad\qquad \text{E 2-20}$$

$$\ln\left(\frac{[RH]_t}{[RH]_0}\right) = k_r[OH]_{ss}t \qquad\qquad \text{E 2-21}$$

$$\ln\left(\frac{[SH]_t}{[SH]_0}\right) = \frac{k_s}{k_r}\ln\left(\frac{[RH]_t}{[RH]_0}\right) \qquad\qquad \text{E 2-22}$$

Plotting $\ln([SH]_t/[SH]_0)$ against $\ln([RH]_t/[RH]_0)$ should produce a straight line, where the gradient $= k_s/k_r$. Disadvantages of this analytical method are the requirement for a well-known reference reaction rate coefficient, which will rely on other experimental techniques. Should this rate coefficient change, previous relative rate measurements will adjust, giving new results, although this could also be regarded as an advantage. It is less likely that a measurement using an absolute method will be able to undergo readjustment. Impurities in the compound of interest do not necessarily matter in a relative rate experiment, as long as the removal of the compound is measured. However, if impurities reacted with SH, this would affect the measured concentration of the compound with time. SH must only be removed by OH. Flash photolysis may be subject to issues arising from impurities if they react with OH, whereas the reaction of impurities with the compound of interest is less important (as it is likely to cause a negligible change in the compound concentration). Efficient detection of OH can be difficult, and this can make flash photolysis difficult, but is not a consideration for a relative rate experiment.

2.8.3 Discharge Flow

Discharge flow is a fast experimental method that allows study of gas phase reaction kinetics. It works on the principle that the time between initiation of a reaction and the detection can be calculated, and is varied across an experiment [86].

Microwave discharge of molecular hydrogen in helium produces H atoms, which are injected into a flow tube. In the flow tube is an excess of NO_2, which reacts with all H atoms to produce OH and NO. At a known point along the flow tube, at which point all H has been converted, a movable injector introduces the reactant to be studied. This reactant is in excess of the OH atoms, and thus the relative concentration of OH atoms can be detected at a known point by a technique such as LIF. Due to knowledge of the flow velocity (V), and distance (X) between initiation and detection, the reaction time (t) can be calculated (equation E 2-23), so as to obtain relative OH concentration over time as an exponential decay.

$$t = X/V \qquad\qquad \text{E 2-23}$$

Mixing time is an issue in discharge flow experiments, as an ideal uniform concentration of reactants after injection is not instantly achieved. Faster reactions are affected more adversely by slow mixing times, as more of the reaction will have taken place before the uniform concentration is reached. As a result of this, discharge flow is limited to reactions that take place on the order of milliseconds. Flash photolysis experiments specifically enable well-mixed reactants as a result of the photolysis technique, hence much faster reactions can be studied. The upper limit of pressure is also around 1000 Pa, as uniform flow requires lower pressures. Wall reactions are a consideration, and often the walls require a coating such as Teflon to deactivate the surface the reactants will contact. The main advantage of discharge flow is that, provided the distances between injector and detector are measured accurately enough, it can be an effective technique coupled to a variety of detectors. Previously, this technique has been coupled to LIF in order to study $R + O_2$ reactions [133], relevant to the material in Chapter 4 and Chapter 5.

2.8.4 Detection Techniques

2.8.4.1 Resonance Fluorescence

Resonance fluorescence involves passing helium gas with a trace of atomic precursor (e.g. H_2, O_2 or Br_2) through a microwave discharge, where a portion of the molecules are dissociated. Collisional excitation of some of the atoms formed, by He or electrons, is followed by fluorescence when they return to the ground state. The frequency of the light is specific to the atoms in the discharge lamp, and the light is filtered and passed into the reaction cell. The light is absorbed in the reactor by atoms of the same species, and these undergo the same process of excitation and fluorescence. A PMT positioned at a right angle to the lamp collects the fluorescence, which is proportional to the small atomic concentration, and rises rapidly after photolysis, before decaying as the reactant is removed.

This technique can be used to monitor the relative concentration of atomic species, but only a few molecular species. It is very specific, and low cost, but LIF is predominantly used to monitor reactions where molecular species are targeted. Resonance fluorescence has been used to monitor the reaction of OH with DEE, DBE, MTBE, and DME [134-136].

2.8.4.2 Absorption Spectroscopy

Absorption spectroscopy can be used to follow transient species in a flash photolysis experiment by probing the reaction cell with light of a frequency corresponding to a vibrational or electronic absorption for the species. The radical's absorption signal increases immediately then decays away as it undergoes reaction, and this signal is recorded by a detector. The Beer-Lambert Law relates absorption to concentration in equation E 2-24:

$$I = I_0\exp(-\varepsilon cl) \hspace{3cm} \text{E 2-24}$$

where I = light intensity, I_0 = initial intensity, c = species concentration, l = path length, and ε is the absorption coefficient. If εcl is very small, the equation becomes equation E 2-25, where I_{abs} is the change in light intensity measured. Under pseudo-first order conditions, the absorption coefficient does not need to be known.

$$I_{abs}/I_0 = -\varepsilon cl \qquad\qquad\qquad \text{E 2-25}$$

The possibility for monitoring direct concentrations of reactants using absorption spectroscopy is a major advantage over the LIF technique, and an entire trace is recorded for every time the photolysis laser initiates the reaction, which is particularly efficient. Potential issues arise where multiple species may absorb at the wavelength used to monitor the reaction, however tunable lasers do help alleviate this problem by allowing selection of a specific transition in the reactant molecule. Nelson et al. [137] used absorption spectroscopy to monitor the reactions of OH with DEE, DBE, and DME.

2.8.4.3   Proton Transfer Reaction-Mass Spectrometry

Proton transfer reaction-mass spectrometry (PTR-MS) is a technique developed by Hansel et al. [138] which enables the detection of species at very low concentrations. The sensitivity of the technique has improved from as low as one ppb (parts per billion) [139], to a few ppt (parts per trillion) [140], up to its current state where it can detect analyte at concentrations <1 ppt [141].

PTR-MS uses soft ionisation to detect species present, by employing H_3O^+ to transfer protons to analyte compounds which have a higher affinity for protons than water [142]. General air components (N_2, O_2, Ar and CO_2) do not get ionised by the beam as they have proton affinities lower than water. It will, however, ionise volatile organic compounds without causing fragmentation. The only source of H_3O^+ ion loss is the association reaction, forming $H_3O^+.H_2O$, after collisional stabilisation of the excited $(H_3O^+.H_2O)^*$ complex [138]. The use of H_3O^+ ions is the key to achieving such high sensitivity, as a higher ion count rate per unit density can be achieved when using air, rather than diluting with a buffer gas [140].

The hydronium beam is generated by a hollow cathode glow discharge, which is injected into a transfer reactor at approximately 1 mbar pressure [142]. Under the influence of an electric field and viscous gas flow, the ions travel through the reactor. Once the analyte is injected into this reactor, they will collide with the hydronium ions (reaction R 2-9 from [138], where M can be C, O, N or S atoms). Ionised molecules leave the reactor, into a 1×10^{-4} mbar low pressure region, where flow becomes molecular, and is no longer viscous [142]. Here, conventional electrostatic ion optics are used to extract the divergent ion beam, focussing the ions into the mass spectrometer. The continuous

ion beam is converted into a pulse of ions, suitable for the time of flight MS method. A high performance time-to-digital converter initiates extraction pulses, where the pulse travels in and out of a reflectron analyser to an ion detector, and arrival time is converted to mass/charge ratio to generate spectra.

$$H_3O^+ + M_iH_j \rightarrow M_iH_{j+1}^+ + H_2O \qquad\qquad\qquad R\ 2\text{-}9$$
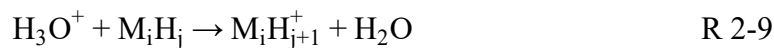
Further advantages of PTR-MS over other detection techniques, such as gas chromatography, are the lack of sample preparation required, no pre-separation necessary, and trace gas analysis being possible *in situ* [141]. Other mass spectrometry techniques exist, and one major advantage they possess over LIF, is the ability to detect any species (in theory). This has been put to good use for detecting important combustion intermediates in the DME oxidation system [87, 88], and mass spectrometry has been used to aid the study of gas phase kinetics previously [143-146].

Chapter 3 Kinetic Study of OH + Ether Reactions

3.1 Abstract

The reactions of OH with five potential biofuel ethers (dimethyl-, diethyl-, methyl *tert*-butyl-, and di-*n*-butyl- ether, and trimethyl orthoformate) have been studied from 298 to 744 K, in 13 – 190 Torr N_2 using laser flash photolysis and laser-induced fluorescence detection of the OH radical.

This represents the first study of the temperature dependence of OH + trimethyl orthoformate (($CH_3O)_3CH$), and extended temperature dependences for di-*n*-butyl ether ($C_4H_9OC_4H_9$) and diethyl ether ($C_2H_5OC_2H_5$). For dimethyl ether (CH_3OCH_3) and methyl *tert*-butyl ether ($CH_3OC(CH_3)_3$), the studies were primarily used to validate the measurements, thereby ensuring any observations of more complex chemistry (OH regeneration, observed in Chapter 4, Chapter 5, and Chapter 6) were reliable, and not subject to any major issues. Thus, the focus of this chapter is on the novel measurements, and less so on the measurements of OH + DME, where significant previous work has been conducted.

The temperature dependences of the rate coefficients for OH + ether (all in units of cm^3 $molecule^{-1}$ s^{-1}) can be parameterised by:

$$k_{OH+TMOF}(298–744 \text{ K}) = (8.0 \pm 12.2) \times 10^{-13} [(T/298)^{(2.6\pm1.2)} + (T/298)^{(-8.1\pm4.6)}] \times e^{(2.7\pm3.9)/RT},$$

$$k_{OH+DEE}(298–727 \text{ K}) = (1.28 \pm 0.21) \times 10^{-11} \times e^{(-0.11\pm0.59)/RT},$$

$$k_{OH+DBE}(298–732 \text{ K}) = (3.05 \pm 7.13) \times 10^{-12} (T/298)^{1.3\pm1.6} \times e^{(6.4\pm5.8)/RT},$$

$$k_{OH+MTBE}(298–680 \text{ K}) = (9.8 \pm 21.6) \times 10^{-13} (T/298)^{2.7\pm1.5} \times e^{(2.5\pm5.6)/RT}, \text{ and}$$

$$k_{OH+DME}(298–656 \text{ K}) = (1.22 \pm 2.83) \times 10^{-15} (T/298)^{6.9\pm0.5} \times e^{(19.1\pm3.8)/RT}.$$

3.2 Introduction

OH + ether reactions (reaction R 3-1) are the important first steps in the low temperature combustion of ethers as potential biofuels, and in order to best understand the conditions required for novel engines, and generate accurate kinetic models, accurate measurements of these reaction rate coefficients are required below 1500 K. Often, there exists gaps in the knowledge of rate coefficients, $k_{OH+ether}$, over this temperature range, particularly between approximately 450 K (the upper temperature of many literature

relative rate and flash photolysis experiments) and approximately 900 K (the lower limit of many higher temperature shock tube studies).

$$ROR'H + OH \rightarrow ROR' + H_2O \qquad\qquad R\ 3\text{-}1$$

For simple hydrocarbon fuels, the preliminary reactions for their low temperature combustion are well-documented [147], with the initial propagation step consisting of hydrogen atom abstraction by a small radical, such as O or H. Here, OH is the example used; it is generally considered the most important abstraction agent, as it exhibits a much faster reaction with hydrocarbon fuels [103] than O and H, and is present at the high temperatures used in engines [102]. The reactions of the OH radical with TMOF, DEE, DBE, MTBE, and DME are presented in this chapter and compared with previous literature measurements in the discussions.

3.3   Experimental

The typical slow flow laser flash photolysis instrumentation used throughout this thesis was combined with laser-induced fluorescence to monitor OH. The reactants used are listed in Table 3-1. Also used were OH precursors (hydrogen peroxide, H_2O_2, Sigma-Aldrich, 50% or 70% (w/w) in H_2O; some early DEE experiments used t-BuOOH (Sigma-Aldrich, 70% (w/w) in H_2O)), and a buffer gas (N_2, BOC, oxygen-free).

Generally experiments in this work were carried out at an approximate flow rate of 1000 sccm and 30 – 60 Torr of nitrogen, or 2000 sccm and 120 Torr, and as such, temperatures above 298 K are subject to an uncertainty of ± 10 K, based on the calibration discussed in Chapter 2. The full range of flow rates and pressures explored was 100 – 4000 sccm and 13 – 208 Torr. Photolysis was carried out using 248 nm or 266 nm laser light, and OH radicals were probed by on-resonance LIF at 308 nm.

Table 3-1: Reactants used, with concentration ranges.

TMOF	Sigma-Aldrich, 99.8%	$(0.3 - 7.9) \times 10^{14}$ molecule cm^{-3}
DEE	Sigma-Aldrich, ≥99%	$(0.8 - 30.4) \times 10^{14}$ molecule cm^{-3}
DBE	Sigma-Aldrich, 99.3%	$(0.5 - 41.8) \times 10^{13}$ molecule cm^{-3}
MTBE	Sigma-Aldrich, 99%	$(1.6 - 11.6) \times 10^{14}$ molecule cm^{-3}
DME	Argo International Ltd, 99.8%	$(1.1 - 14.2) \times 10^{14}$ molecule cm^{-3}

Hydrogen peroxide (or t-BuOOH when used) was delivered with N_2 using a bubbler placed before a MFC, to ensure the amount of gas being delivered was known. Contact of hydrogen peroxide with the metal in the MFC and consequent decomposition results in some oxygen always being delivered to the system, which was estimated to be approximately 10^{15} molecule cm^{-3}, but this varied depending on pressure and flow. Under typical conditions of 298 K, 30 Torr N_2, 1000 sccm flow, the estimated amount of H_2O (from the hydrogen peroxide precursor) delivered was approximately 1.5% of the total gas density ($\sim 10^{18}$ molecule cm^{-3}), and thus we expect H_2O to make a negligible contribution to the total gas density, acting as a carrier gas.

A bubbler delivery method was also used for the reactant in the di-n-butyl ether experiments, as a result of the low vapour pressure exerted by DBE in comparison to the other ether fuels (approximately 4 – 6 Torr at room temperature) [148, 149]. The result of this was particularly low bulb concentrations, and therefore slow pseudo-first order rate coefficients in comparison to other losses of OH. Some experiments showed recycling of OH due to O_2 present in the system, which also contributed to the need for a faster OH + DBE pseudo-first order loss (see section 4.5 in Chapter 4). For these experiments, the bubbler was placed before a calibrated mass flow controller, and nitrogen was flowed across the surface of DBE in the bubbler. The concentration of ether delivered by the bubbler was estimated using the measured bath gas (N_2) pressure within the bubbler, and the estimated vapour pressure of DBE. Antoine parameters were used to determine the vapour pressure of the DBE, where the bubbler was surrounded by a Dewar flask filled with room temperature water to reduce temperature fluctuations. The water was kept in the flask overnight before use, to stabilise at room temperature, and a thermometer was used during experiments to measure the water temperature. The Antoine equation used is shown below (equation E 3-1) [150].

$$\log(P \,/\, \text{Torr}) = A - \frac{B}{((T \,/\, \degree\text{C}) + C)} \qquad\qquad \text{E 3-1}$$

Here A = 6.92032, B = 1064.07 and C = 228.8 for the temperature range 212.15 – 293.15 K [151], therefore the equation has been extrapolated in this work, and may explain the need for a reasonable correction between bubbler and bulb experiments. The correction factor for mass flow was still applied (described in Chapter 2). A correction factor between bubbler and bulb experiments was required, and determined at room temperature (described in full in section 3.6.1).

Generally, OH kinetic traces exhibited single exponential behaviour, and were analysed as described in Chapter 2. An example for OH + dimethyl ether is presented in Figure 3-1.
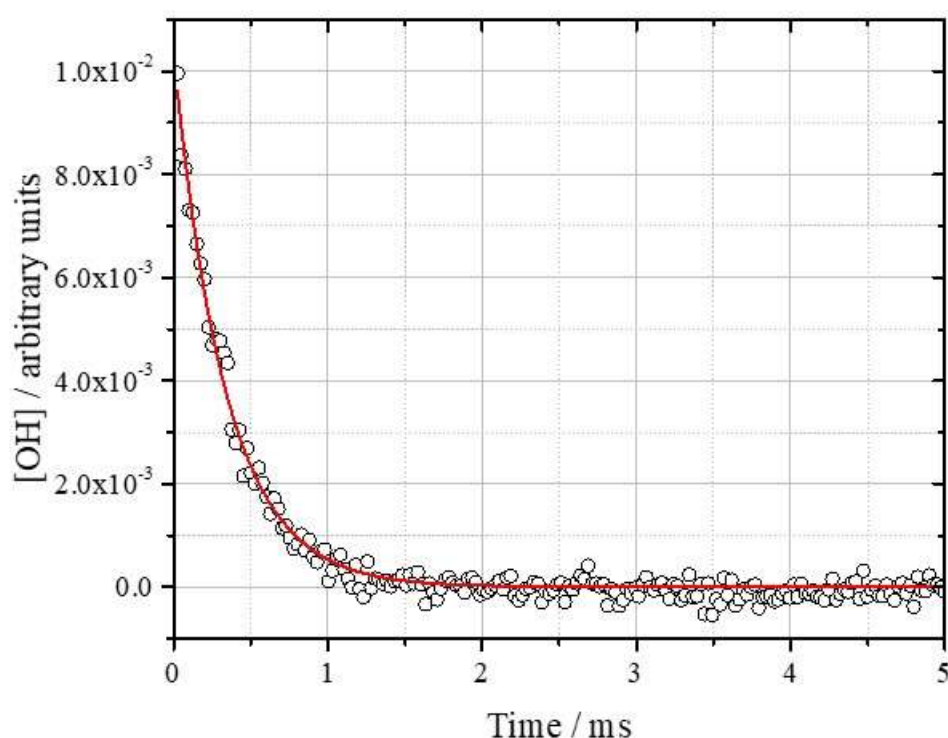
Figure 3-1: Single exponential decay, [DME] = 1.0 × 10^{15} molecule cm^{-3}. The exponential fit yielded $k' = (2970 \pm 100)$ s^{-1}. The uncertainty on the returned parameter is 2σ and purely statistical. The experimental conditions were 298 K, in 59 Torr N$_2$.

Kinetic traces measured at higher temperatures in the presence of O$_2$ often exhibited biexponential behaviour (examples are presented for each ether in Appendix A), rather than a single exponential decay. Diethyl ether experiments using the

t-BuOOH precursor also resulted in biexponential kinetic traces. The initial fast decay in the biexponential traces is the reaction between OH and the ether (k_a'), and the second, tail portion of the decay, contains information about the regeneration of OH (k_b and k_c) (thus the decay is slower in the tail). These more complex traces were analysed by fitting to an equation derived from the scheme shown in Scheme 3-1.

$$RH + OH \xrightarrow{k_a'} R\cdot \xrightarrow{+O_2} RO_2 \xrightarrow{k_b} OH$$

$$\downarrow k_d \qquad\qquad\qquad \downarrow k_c$$

$$loss \qquad\qquad\qquad loss$$
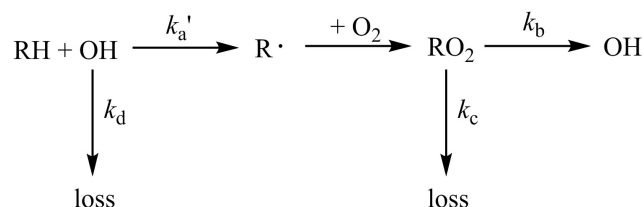
Scheme 3-1: Simplified reaction scheme for biexponential analysis equation parameters.

The OH traces were fitted with the following equation (E 3-2) derived from Scheme 3-1:

$$[OH] = [OH]_0 \times \left[\left(\frac{-(k_d + k_a') - \lambda_2}{\lambda_1 - \lambda_2} \right) \times \left(e^{\lambda_1 \times t} - e^{\lambda_2 \times t} \right) + e^{\lambda_2 \times t} \right] \qquad \text{E 3-2}$$

here, k_a' = pseudo first-order rate coefficient for OH + ether reactions, k_d = rate coefficient for OH loss in the absence of ether, and the terms λ_1 and λ_2 are expanded fully in equations E 3-3 to E 3-6:

$$\lambda_1 = \frac{\left(-M1 + \sqrt{M1^2 - 4M2} \right)}{2} \qquad \text{E 3-3}$$

$$\lambda_2 = \frac{\left(-M1 - \sqrt{M1^2 - 4M2} \right)}{2} \qquad \text{E 3-4}$$

$$M1 = k_d + k_a' + k_b + k_c \qquad \text{E 3-5}$$

$$M2 = (k_d + k_a') \times (k_b + k_c) - (k_a' k_b) \qquad \text{E 3-6}$$

The terms k_b (first order rate coefficient for OH regeneration from the R radical) and k_c (first order rate coefficient for R radical reacting without producing OH) are both

present in the λ_1 and λ_2 terms. This equation can be used to determine the parameters from single trace analysis, where parameters are best defined when [ether] is sufficiently high that k_a' is faster than the sum of k_c and k_b. Parameters are even better defined/more robust when using global analysis, as the information is taken from many traces. The equation will be referred to as a biexponential equation (despite there being three exponential terms present), because of the two distinct portions of the biexponential traces (the initial fast decay, and the slow tail).

For robust parameter retrieval, global fitting was used to analyse several biexponential traces at once ($k_a' = k_{OH+ether}$[ether] for each trace), and share the bimolecular rate coefficient between decays. In this process the initial signal intensity, k_a', k_b and k_c are local parameters for each trace and rate coefficient $k_{OH+ether}$ is shared globally across all traces in the fit. This allows a well-defined, robust bimolecular rate coefficient for each temperature to be obtained from kinetic traces, which contain information on k_a' in the earlier part of the trace.

Global analysis was used for the bimolecular rate coefficients obtained for OH + DEE, MTBE, and TMOF, and single trace (non-global) analysis was used for measurements using DME and DBE.

3.4   OH + Trimethyl Orthoformate

Trimethyl orthoformate bears structural similarities to DME (Scheme 3-2), and can be synthesised using methanol (and therefore bio-methanol) [81], making it a potential alternative bio-derived fuel or fuel additive. TMOF has been investigated for its use in fuel cells [37, 83-85]. Few studies exist on the low temperature oxidation mechanism of TMOF. TMOF possesses two distinct sites that the hydroxyl radical can abstract from; primary (reaction R 3-2) and tertiary (reaction R 3-3) α sites shown in Scheme 3-2. The products of these reactions are H_2O and a radical, R. This first step has been measured in this work, with a non-site-specific approach, thus reported values $k_{OH+TMOF}$ refer to the sum of the rate coefficients for reactions R 3-2 and R 3-3.
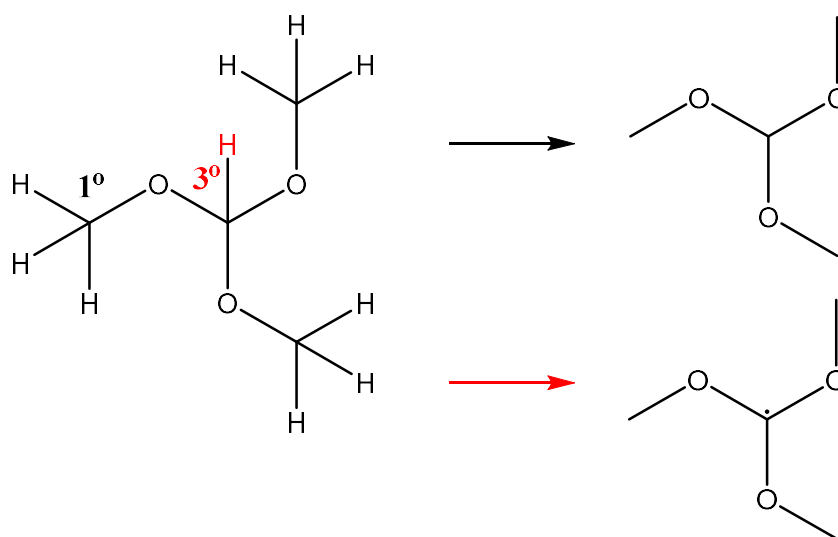
Scheme 3-2: Potential abstraction sites in the OH + trimethyl orthoformate reaction, and R radical products formed.

$$(CH_3O)_3CH + OH \rightarrow CH_2O(CH_3O)_2CH + H_2O \qquad\qquad R\ 3\text{-}2$$

$$(CH_3O)_3CH + OH \rightarrow (CH_3O)_3C + H_2O \qquad\qquad R\ 3\text{-}3$$
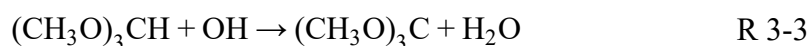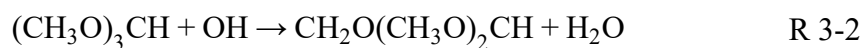
Trimethyl orthoformate and hydroxyl radical kinetics have only been studied once prior to the experiments presented here, by Platz et al. [152] using pulse radiolysis and UV absorption, finding $k_{OH+TMOF} = (6.0 \pm 0.5) \times 10^{-12}$ cm^3 molecule^{-1} s^{-1} at 295 K, which they compared to OH + DMM (dimethoxymethane, CH$_3$OCH$_2$OCH$_3$), a similarly structured molecule, where $k_{OH+DMM} = 5.2 \times 10^{-12}$ cm^3 molecule^{-1} s^{-1} as an average of two measurements [153, 154]. No measurements were made above room temperature.

Since the measurements in this work were published in Potter et al. [155], a theoretical study of OH + TMOF has been carried out by Du and Zhang [116], including *ab initio* calculations of the extended TMOF low temperature oxidation system, with a focus on the agreement between their calculated $k_{OH+TMOF}$ and the measurements from this thesis that were presented in Potter et al. At room temperature, 71% of the abstraction is predicted to occur on the tertiary site (reaction R 3-3), and the remaining 29% at the primary sites (reaction R 3-2).

3.4.1 OH + (CH₃O)₃CH Temperature Dependence

The bimolecular rate coefficient for the reaction between trimethyl orthoformate and the hydroxyl radical has been measured under pseudo-first order conditions, where

the concentration of OH was controlled by reaction R 3-4. Analysis of the OH decay rate at varying concentrations of trimethyl orthoformate to give $k'_{OH+TMOF}$, and least squares linear fitting of these pseudo-first order rate coefficients as a function of [TMOF], for a given temperature and pressure, provides the bimolecular rate coefficient $k_{OH+TMOF}$. Three example bimolecular plots are displayed in Figure 3-2. An example single exponential decay is shown in Appendix A.

$$C_4H_{10}O_3 + OH \rightarrow C_4H_9O_3 + H_2O \qquad\qquad \text{R 3-4}$$
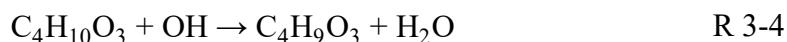
Rate coefficients for the abstraction of hydrogen by OH, from trimethyl orthoformate ($k_{OH+TMOF}$), were measured as a function of temperature using hydrogen peroxide as the OH photolytic precursor, in the ranges 298 – 744 K and 37 – 68 Torr (Table 3-2). The uncertainties in the rate coefficients in this work are 2σ with an extra 10% of the measured rate coefficient propagated, to allow for the systematic errors associated with the experimental method, and avoid weighting the data towards the small errors produced by global analysis of biexponential decays. Measured rate coefficients did not vary significantly with laser power or laser repetition rate (7.0% maximum variation between 10, 5 and 2 Hz, and no variation within uncertainties).

The reaction of OH with TMOF showed similar behaviour to most ethers in this chapter, in that low temperature OH decays were single exponential, and higher temperature decays were biexponential. The OH + TMOF reaction exhibited biexponential behaviour at a relatively low temperature, where the nature of the decays changed at ~489 K, indicating recycling of OH radicals, where the initial fast portion of a decay contains information about the initial hydrogen abstraction (reaction R 3-4) and the tail of the decay contains information about OH recycling and yields. Oxygen present in the system due to decomposition of hydrogen peroxide (discussed in Chapter 4, and Potter et al. [156]) is the probable source of this OH, where it combines with TMOF-derived R radicals (reaction R 3-5).
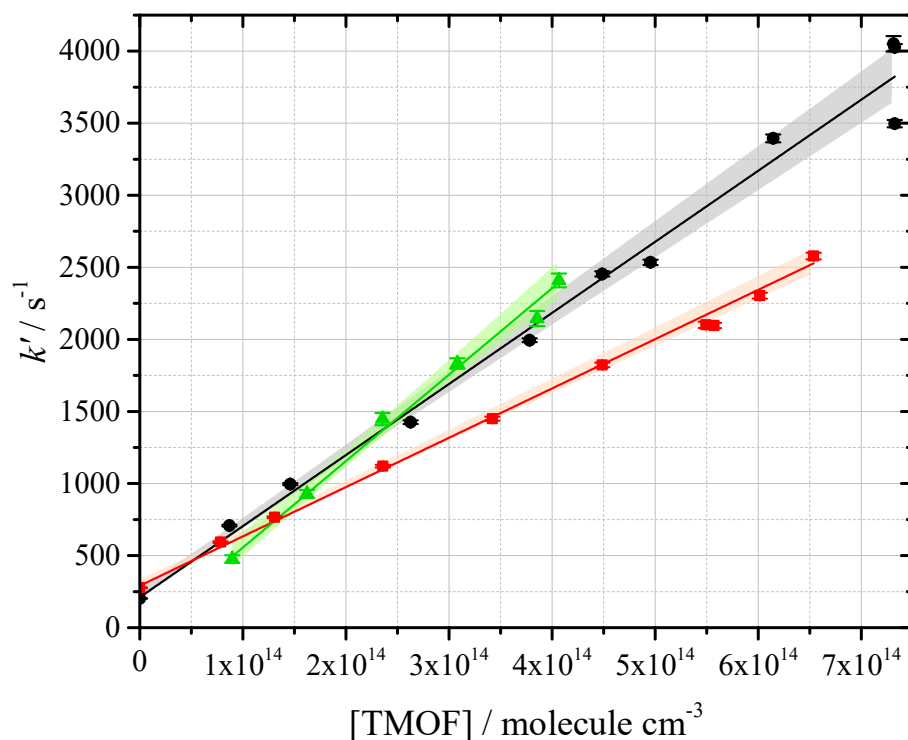
Figure 3-2: Example bimolecular plots for OH + TMOF at 298 K and 68 Torr N₂ (black), 336 K and 68 Torr N₂ (red), and 489 K and 64 Torr N₂ (green). $k_{OH+TMOF}$ = $(4.73 \pm 0.84) \times 10^{-12}$ cm³ molecule⁻¹ s⁻¹, $(3.34 \pm 0.15) \times 10^{-12}$ cm³ molecule⁻¹ s⁻¹, and $(6.00 \pm 0.57) \times 10^{-12}$ cm³ molecule⁻¹ s⁻¹ respectively. **Shaded areas represent the 95% confidence limits, and error bars are statistical at the 1σ level. Uncertainties on rate coefficients are statistical at the 2σ level. The intercepts are (–210 ± 30) s⁻¹ (black), (–290 ± 20) s⁻¹ (red), and (–40 ± 100) s⁻¹ (green).**
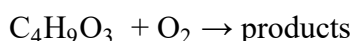
$$C_4H_9O_3 + O_2 \rightarrow products \qquad\qquad R\ 3\text{-}5$$

Observations discussed later (Chapter 6) demonstrate the potential for TMOF to act as a precursor for OH even when isolated from other reactants or precursors (reaction R 3-6), so it is possible this is the sole cause of OH regeneration in the TMOF system, rather than the R + O₂ reaction (reaction R 3-5).
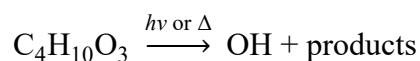
$$C_4H_{10}O_3 \xrightarrow{hv\ or\ \Delta} OH + products \qquad\qquad R\ 3\text{-}6$$

Table 3-2: Bimolecular rate coefficients obtained for OH + TMOF. Uncertainties are 2σ with an additional 10% of the measurement value added to account for systematic errors.

T / K	$10^{12}\, k_{OH+TMOF}{}^{a}$	n	$10^{-14}\, [TMOF]^{b}$	P / Torr
298	4.69 ± 0.83	9	$0.8 - 7.9$	37
298	4.73 ± 0.84	10	$0.9 - 7.3$	68
298	4.53 ± 0.92	7	$1.4 - 6.3$	61
336	3.34 ± 0.49	10	$0.8 - 6.5$	68
338	3.75 ± 0.56	8	$1.2 - 5.6$	61
380	4.65 ± 0.98	7	$1.1 - 5.2$	64
451	5.26 ± 0.70	12	$0.3 - 3.5$	37
489	5.71 ± 0.67^{c}	6	$0.9 - 4.1$	64
540	7.05 ± 0.82^{c}	10	$0.8 - 3.9$	61
598	7.75 ± 0.97^{c}	5	$0.6 - 2.2$	60
642	9.88 ± 1.14^{c}	6	$0.6 - 2.5$	61
675	10.45 ± 1.20^{c}	7	$0.5 - 2.3$	60
704	11.88 ± 1.33^{c}	4	$0.5 - 1.8$	60
734	14.01 ± 1.67^{c}	4	$0.5 - 1.6$	59
744	14.67 ± 1.86^{c}	4	$0.5 - 1.7$	62

^{a}Units of cm^{3} molecule^{-1} s^{-1}. ^{b}Units of molecule cm^{-3}. ^{c}From global analysis. n refers to the number of experiments comprising a bimolecular determination.

Biexponential decays were fit by the biexponential equation rather than the single exponential equation. An example biexponential decay with fitting is shown in Figure 3-3, and the green data in Figure 3-2 demonstrate the extraction of $k_{OH+TMOF}$ from biexponential analysis. Biexponential traces were analysed globally, where several traces generated at a given temperature and pressure were analysed simultaneously to obtain a $k_{OH+TMOF}$ shared across the traces (and other parameters analysed in Chapter 6, such as OH yield). As a result of the well-defined nature global fitting possesses, uncertainty ranges on these data are particularly small.
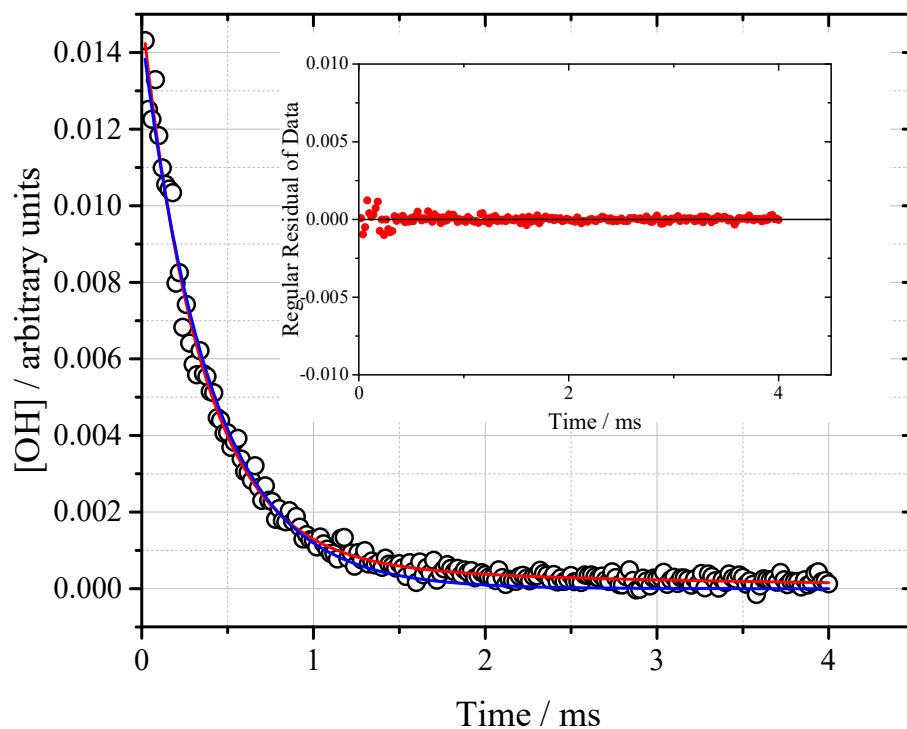
Figure 3-3: Example OH + TMOF biexponential decay with a good fit to the biexponential equation (red line), and a poor fit to the single exponential equation (blue line), measured at 675 K and 60 Torr N₂. The inset shows the residuals for the biexponential fit. Parameters from the biexponential fit: $k_a' = (2560 \pm 100)$ s^{-1}, $k_b = (110 \pm 50)$ s^{-1}, $k_c = (380 \pm 240)$ s^{-1}, and k_d was fixed at 200 s^{-1}. Parameters from the single exponential fit: $k' = (2500 \pm 70)$ s^{-1}. [TMOF] $= 2.28 \times 10^{14}$ cm^3 molecule^{-1} s^{-1}. Uncertainties are statistical at the 2σ level.

Examining the temperature dependence of the bimolecular rate coefficient for the OH + TMOF reaction (Figure 3-4), there is a clear positive temperature dependence above approximately 340 K, and a small negative temperature dependence region below this temperature. The temperature dependence of the data can be parameterised by

$$k_{\text{OH+TMOF}}(298-744\,\text{K}) = (8.0 \pm 12.2) \times 10^{-13} \left[\left(\frac{T}{298}\right)^{2.6 \pm 1.2} + \left(\frac{T}{298}\right)^{-8.1 \pm 4.6} \right] \times \exp\left[\frac{2.7 \pm 3.9}{RT}\right] \text{cm}^3$$

molecule^{-1} s^{-1}, where a weighted fit was used, and the uncertainty in the parameterisation is 12%, taken as the maximum magnitude of the 95% confidence limit.
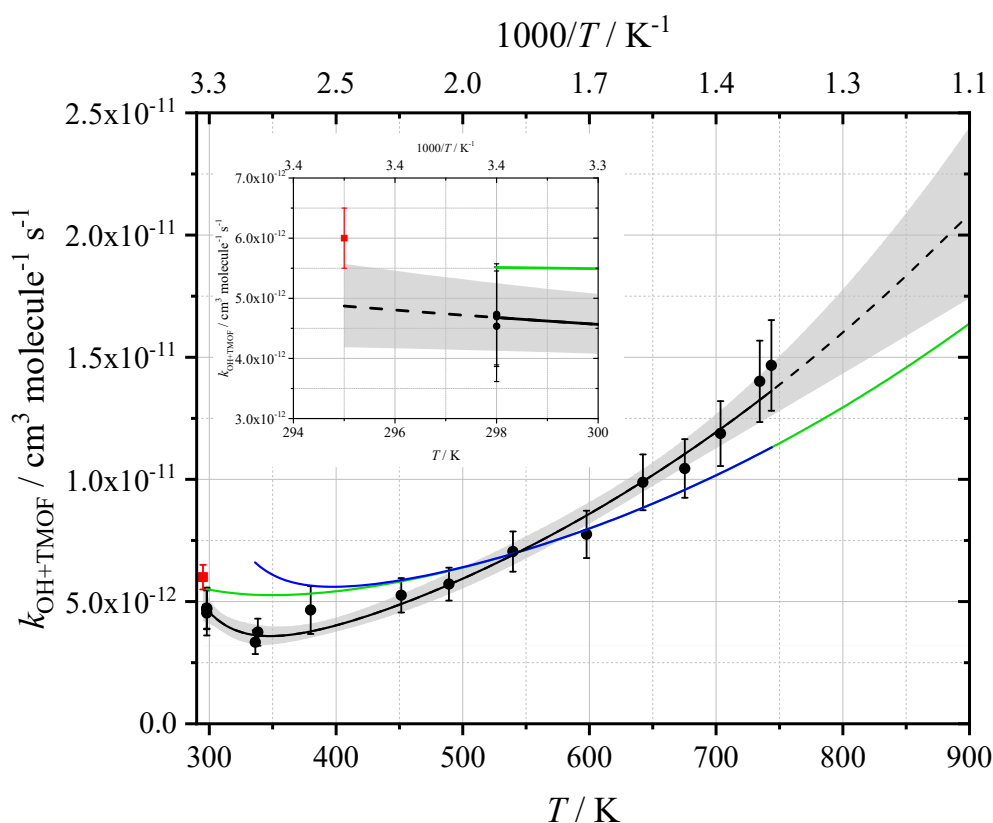
Figure 3-4: $k_{OH+TMOF}$ **measured in this work (●), as a function of temperature. Errors are 2σ with an additional 10% of the value to account for systematic errors. The only available literature measurement, by Platz et al. [152], is included (■). The temperature dependence of** $k_{OH+TMOF}$ **from this work can be described by** $k_{OH+TMOF}(298-744\text{ K}) = (8.0 \pm 12.2) \times 10^{-13} [(T/298)^{(2.6\pm1.2)} + (T/298)^{(-8.1\pm4.6)}] e^{(2.7\pm3.9)/RT}$ **cm^3 molecule^{-1} s^{-1}, where the 95% confidence bounds are shown in grey shading. Two theoretical Arrhenius parameterisations by Du and Zhang [116] are shown; blue line:** $k_{OH+TMOF}(336-744\text{ K}) = 4.2 \times 10^{-13} [(T/298)^{2.6} + (T/298)^{-8.1}] e^{5.7/RT}$ **cm^3 molecule^{-1} s^{-1}, and the green line is described in Table 3-3.**

Comparison with experimental measurements is only possible at room temperature, where we measure an average $k_{OH+TMOF} = (4.65 \pm 0.50) \times 10^{-12}$ cm^3 molecule^{-1} s^{-1}, approximately 25% slower than the only reported rate coefficient, by Platz et al. [152] (Figure 3-4 and Table 3-3), who found $k_{OH+TMOF} = (6.0 \pm 0.5) \times 10^{-12}$ cm^3 molecule^{-1} s^{-1} at 295 K using pulsed radiolysis. The uncertainty on the measurement in this work is the propagated 2σ+10% uncertainty. There is no overlap of the two values' uncertainty ranges. Pulsed radiolysis can involve much higher radical concentrations, and hence fast radical-radical reactions, causing increased OH loss, may have affected the Platz et al. measurements.

Figure 3-4 shows what is possibly the onset of a negative temperature dependence region for $k_{OH+TMOF}$, at temperatures below approximately 340 K. Low temperature

studies have shown that a negative temperature dependence of the rate coefficient for OH + hydrocarbon reactions can occur below ~200 K. DME and acetone have both demonstrated this behaviour arising from the formation of a hydrogen-bonded pre-reaction complex, in which an H atom can subsequently quantum tunnel through the reaction barrier to form water [157, 158]. The result is a rapid increase in rate at low temperatures. Measurements of $k_{OH+TMOF}$ at ~340 K and room temperature were both repeated to ensure the exhibited temperature dependence was unlikely to be the result of anomalous measurements. Further studies of ethers at sub-ambient temperatures would be of mechanistic interest, and potentially relevant to planetary atmospheres.

Since the publication of the data presented here in Potter et al. [155], Du and Zhang [116] undertook a theoretical study of the reaction between trimethyl orthoformate and the hydroxyl radical, carrying out *ab initio* calculations for the extended low temperature oxidation surface of TMOF, and compared their data to our results. Molecular structures for the OH + TMOF surface were optimised at the M06-2X-GD3/6-311++G(d,p) level, with vibrational frequencies computed using the same method and basis set. The single point energies of each optimised structure were calculated using the QCISD(T)/6-311++G(d,p) method, and conventional transition state theory was used to calculate the OH + TMOF rate coefficients for each abstraction site, allowing the total bimolecular rate coefficient to be calculated at different temperatures. The reported 298 K calculated $k_{OH+TMOF}$ was 5.48×10^{-12} cm^3 molecule^{-1} s^{-1}, 6% faster than the upper limit of our measurement when considering the uncertainty range ($4.65 \pm 0.50 \times 10^{-12}$ cm^3 molecule^{-1} s^{-1}), however this assumes there is no uncertainty associated with the *ab initio* calculation method, and overall shows a good level of agreement.

Table 3-3: Comparison of the rate coefficient obtained for $k_{OH+TMOF}$ with literature measurements and calculations.

Reference	Technique	k(298 K)[a]	T / K	$k(T)$[b]
Platz et al.	Pulsed radiolysis	6.0 ± 0.5[c]	295	–
Du and Zhang	Theory (QCISD(T))	5.48	298 – 1500	1.02×10^{-13} $(T/298)^{3.4}$ $e^{9.89/RT}$
This work	PLP–LIF	4.65 ± 0.50	298 – 744	$(8.0 \pm 12.2) \times 10^{-13}$ $((T/298)^{2.6 \pm 1.2} + (T/298)^{-8.1 \pm 4.6}) e^{(2.7 \pm 3.9)/RT}$

[a]Units are 10^{-12} cm^3 molecule^{-1} s^{-1}. [b]Units of A are cm^3 molecule^{-1} s^{-1} and E_a are kJ mol^{-1}. [c]Measured at 295 K.

The Arrhenius parameterisation calculated by Du and Zhang is displayed in Table 3-3, along with their calculated room temperature rate coefficient for OH + TMOF. Figure 3-4 displays two fits reported by Du and Zhang, where the green line represents a full fit to the temperature range 298 – 1500 K, and the blue line a less extensive parameterisation from 336 to 744 K. Across the reduced range in the blue fit, Du and Zhang used the temperature dependence exponential terms (2.6 and –8.1) from this study, and found a pre-exponential factor approximately 50% lower (4.2 × 10^{-13} cm^3 molecule^{-1} s^{-1} compared to 8.0 × 10^{-13} cm^3 molecule^{-1} s^{-1}), and an activation energy twice as low (–5.7 kJ mol^{-1} in comparison to –2.7 kJ mol^{-1}). As a result, their fit underestimates the rate coefficient we observe at high temperatures, and over-predicts $k_{OH+TMOF}$ below approximately 400 K. It is not clear why a temperature of 336 K was chosen as a lower limit for this fit. The authors note their calculated rate coefficients fit to the full temperature range using a linear least squares analysis, giving the modified Arrhenius parameterisation $k_{OH+TMOF}$(298 – 1500 K) $= 1.02 \times 10^{-13} \left(\frac{T}{298}\right)^{3.4} \times \exp\left[\frac{9885}{RT}\right]$ cm^3 molecule^{-1} s^{-1}. This full expression is just within the uncertainty range of the room temperature data reported here, but underestimates the measured rate coefficient above approximately 700 K by ~20%. From the upper limit of our data, it is not clear whether the extrapolation up to 1500 K would greatly deviate from the calculated fit by Du and Zhang. The reversal in the temperature-dependent behaviour at approximately 350 K is reproduced reasonably well by the *ab initio* study reported by Du and Zhang, but has not been extrapolated below room temperature, so the extent to which low temperature complex formation will affect the rate coefficient is not explored.

3.5 OH + Diethyl Ether

Bio-derived diethyl ether is synthesised from bioethanol dehydration, and has already been used as a cold-start aid in engines [55]. Its similarity to DME, high cetane number (>125), good energy density (26.3 MJ L^{-1}) and low self-ignition temperature (363 °C) [24], make DEE a suitable candidate for diesel replacement. The reaction between OH and diethyl ether is the most probable first step in the low temperature combustion mechanism.

Waddington et al. [159] proposed a likely mechanism for the low temperature gaseous oxidation of DEE. Initially the mechanism follows the same route as other organic compounds, where abstraction of a hydrogen atom occurs. As the second most

simple symmetrical ether, diethyl ether is slightly more complex than dimethyl ether, as there are two unique abstraction sites (Scheme 3-3). Abstraction can occur at either the α- or β-carbon, and was found to take place primarily on the α-carbon (reaction R 3-7), based on products formed. Abstraction from the β site is the minor channel (reaction R 3-8). Di Tommaso et al. [115] later postulated the same abstraction split, due to the more stable product that is formed when the radical is centred on the secondary carbon. This radical should be stabilised as a result of electron density donated by the neighbouring methyl group, and the lone electrons situated on the adjacent oxygen atom. Oxygen was the suggested abstraction agent, and is significant for initiation processes, however in low temperature combustion, it is likely to be O, H or OH from propagation reactions that will initiate the chemistry with DEE.

$$CH_3CH_2OCH_2CH_3 + OH \rightarrow CH_3CH_2OCHCH_3 + H_2O \qquad \text{R 3-7}$$
$$CH_3CH_2OCH_2CH_3 + OH \rightarrow CH_3CH_2OCH_2CH_2 + H_2O \qquad \text{R 3-8}$$

Orlando [160] predicted that >80% of abstractions occurred at the secondary carbon (α position) when the abstraction agent was a Cl atom, and Eberhard et al. [161] found that previous studies showed 95% of alkane hydrogen abstraction undergone by OH initiated photo-oxidation will occur on the secondary carbon. In the measurements here, k_{OH+DEE} refers to the bimolecular rate coefficient for the total abstraction taking place in reactions R 3-7 and R 3-8, where the measurements made were non-site-specific.
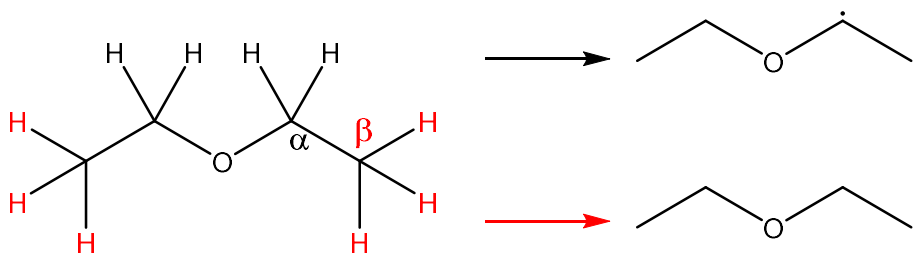
Scheme 3-3: Possible hydrogen abstraction sites, and subsequent R radicals formed for the reaction between OH and diethyl ether.

Kinetics of the OH + DEE reaction have been investigated experimentally since 1976, initially by Lloyd et al. [162], with various techniques being employed [113, 129, 132, 136, 163-165], including flow reactors, smog chambers, and pulsed laser photolysis

– laser-induced fluorescence. Results of the rate coefficient studies of this reaction previously are summarised in Table 3-5. No pressure dependence is expected for this reaction [163], and also for the reaction of Cl + DEE [166], which should show the same pressure dependence as OH + DEE. Room temperature values are well-documented, and up to approximately 440 K, the kinetics have been explored, however there is a large gap between 440 K and the single relative rate measurement at 753 K, and no current studies at temperatures above this. The work presented here measures k_{OH+DEE} within this void of experimental measurements.

3.5.1   OH + $C_2H_5OC_2H_5$ Temperature Dependence

The bimolecular rate coefficient for the reaction between diethyl ether and the hydroxyl radical has been measured under pseudo-first order conditions, where the concentration of OH was controlled by reaction R 3-9. Analysis of the OH decay rate at varying concentrations of diethyl ether to give k'_{OH+DEE}, and least squares linear fitting of these pseudo-first order rate coefficients as a function of [DEE], for a given temperature and pressure, provides the bimolecular rate coefficient k_{OH+DEE}. An example single exponential decay can be found in Appendix A.

$$C_2H_5OC_2H_5 + OH \rightarrow C_2H_5OC_2H_4 + H_2O \qquad \text{R 3-9}$$

An example of a bimolecular plot is displayed in Appendix A. It should be noted that the analysis presented here is for illustrative purposes, and the actual values reported were obtained from a global analysis of multiple traces at once for a given temperature and pressure (more details of this method are given in Chapter 4 and Chapter 2).

Above room temperature (357 – 532 K) decays produced using the t-BuOOH photolytic precursor exhibited biexponential behaviour. This behaviour was not seen when using the hydrogen peroxide precursor, so is likely as a result of t-BuOOH decomposition (discussed in Chapter 2). For this reason, above 532 K OH radicals were solely generated using the H_2O_2 precursor. Biexponential decays were fit using the biexponential expression in equation E 3-2, and an example biexponential decay with fitting is shown in Appendix A. It is worth noting the loss of OH in the absence of DEE in this figure (k_d) is much higher than for the H_2O_2 precursor, due to faster reaction with t-BuOOH.

Rate coefficients for the abstraction of hydrogen by OH, from diethyl ether (reaction R 3-9), have been measured as a function of temperature, using hydrogen peroxide or *tert*-butyl hydroperoxide as photolytic precursors, in the ranges 298 – 727 K and 13 – 190 Torr N_2. The measured rate coefficients did not vary significantly with laser power. A plot of the rate coefficient as a function of temperature is shown in Figure 3-5, and all values of k_{OH+DEE} are displayed in Table 3-4, where total uncertainties are estimated as 2σ with an extra 10% of the rate coefficient value propagated, to account for the unrealistically small statistical errors on parameters returned by global analysis of multiple traces.

Data obtained from different OH precursors have been identified in Figure 3-5, where no significant difference between the rates measured using H_2O_2 or *t*-BuOOH precursors was identified. At room temperature, the average measurement using H_2O_2 is 15% lower than that of *t*-BuOOH, however, considering the uncertainty ranges (~10% for each measurement), the two values are in agreement. The mean values were calculated from four hydrogen peroxide experiments, and eight *t*-BuOOH experiments. The reported uncertainties are statistical at the 2σ level.

Table 3-4: Bimolecular rate coefficients obtained for OH + DEE. Uncertainties are 2σ +10% to account for estimated systematic errors.

T / K	$10^{11} k_{OH+DEE}$[a]	n	10^{-14} [DEE] range[b]	P / Torr	Precursor
298	1.23 ± 0.14	5	$5.8 - 27.6$	29	^{t}BuOOH
298	1.42 ± 0.16	11	$8.2 - 28.1$	29	^{t}BuOOH
298	1.30 ± 0.15	17	$5.8 - 27.7$	30	^{t}BuOOH
298	1.19 ± 0.17	5	$4.6 - 17.8$	38	H_2O_2
298	1.14 ± 0.17	5	$7.3 - 28.5$	38	H_2O_2
298	1.16 ± 0.14	5	$1.5 - 7.4$	47	H_2O_2
298	0.96 ± 0.10	7	$6.2 - 24.1$	48	H_2O_2
298	1.30 ± 0.17	6	$4.3 - 16.4$	59	^{t}BuOOH
298	1.15 ± 0.17	4	$4.3 - 16.7$	60	^{t}BuOOH
298	1.34 ± 0.17	4	$4.3 - 16.7$	60	^{t}BuOOH
298	1.25 ± 0.17	5	$7.8 - 15.4$	60	^{t}BuOOH
298	1.37 ± 0.18	7	$4.0 - 30.4$	60	^{t}BuOOH
357	1.29 ± 0.16	5	$4.1 - 19.7$	30	^{t}BuOOH
361	1.24 ± 0.26	17	$3.9 - 19.0$	30	^{t}BuOOH
367	1.42 ± 0.16	6	$6.9 - 19.8$	13	^{t}BuOOH
415	1.19 ± 0.26	9	$3.4 - 16.6$	30	^{t}BuOOH
494	1.21 ± 0.14	7	$4.8 - 13.6$	60	^{t}BuOOH
500	1.25 ± 0.15	14	$3.3 - 12.9$	35	^{t}BuOOH
531	1.47 ± 0.18	8	$3.2 - 12.7$	30	^{t}BuOOH
532	1.24 ± 0.17	15	$3.8 - 14.7$	29	^{t}BuOOH
620	0.96 ± 0.12	5	$3.8 - 15.1$	47	H_2O_2
632	1.25 ± 0.14	8	$3.3 - 13.2$	40	H_2O_2
642	1.18 ± 0.13	4	$1.7 - 6.6$	57	H_2O_2
663	1.31 ± 0.20	5	$1.4 - 5.3$	190	H_2O_2
669	1.32 ± 0.16	7	$1.6 - 6.5$	57	H_2O_2
670	1.29 ± 0.19	4	$1.1 - 4.1$	150	H_2O_2
682	1.77 ± 0.21	4	$1.7 - 6.5$	59	H_2O_2
686	1.30 ± 0.16	4	$1.6 - 6.3$	57	H_2O_2
691	1.21 ± 0.15	5	$1.6 - 6.1$	57	H_2O_2
714	1.33 ± 0.16	5	$1.5 - 6.1$	57	H_2O_2
727	1.25 ± 0.15	5	$0.8 - 5.9$	57	H_2O_2

[a]Units of cm^3 molecule^{-1} s^{-1}. [b]Units of molecule cm^{-3}. n refers to the number of experiments comprising a bimolecular determination.
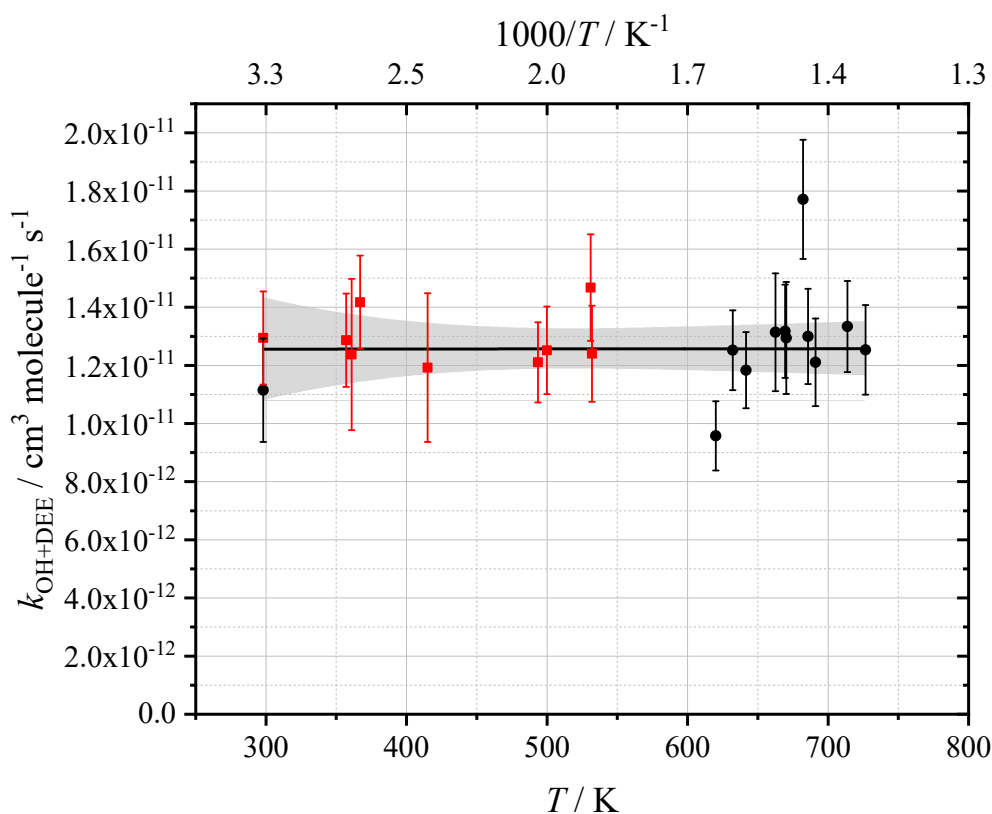
Figure 3-5: Measured $k_{OH+DEE}(298 - 727\ K) = (1.26 \pm 0.11) \times 10^{-11} \times e^{(0.01\pm0.80/RT)}$ cm³ molecule⁻¹ s⁻¹, uncertainties are 2σ and statistical, and the grey shaded area represents the bounds of the 95% confidence limits. Precursors were H_2O_2 (●) and *t*-BuOOH (■). Note the room temperature data are averages with propagated 2σ uncertainties (H_2O_2, *n*=4; *t*-BuOOH, *n*=8).

Plotting k_{OH+DEE} against temperature, shown in Figure 3-5, shows a clear lack of temperature dependence, where the rate coefficient is statistically invariant from room temperature to approximately 730 K. An Arrhenius fit has been performed, where the data can be described by $k_{OH+DEE}(298 - 727\ K) = (1.26 \pm 0.11) \times 10^{-11} \times \exp\left[\frac{0.01\pm0.80}{RT}\right]$ cm³ molecule⁻¹ s⁻¹. The uncertainties reported are statistical at the 2σ level, and the maximum uncertainty of the 95% confidence limits across the temperature range valid for this parameterisation is 14%. Given the uncertainty in the activation energy, a temperature independent value of $(1.26 \pm 0.11) \times 10^{-11}$ cm³ molecule⁻¹ s⁻¹ is recommended. A weaker temperature dependence compared with DME (see section 3.8.1) can be rationalised by the more facile abstraction from the α C–H bond in DEE, where the adjacent CH₃– group weakens the bond by donating electron density. DME lacks this adjacent methyl group.
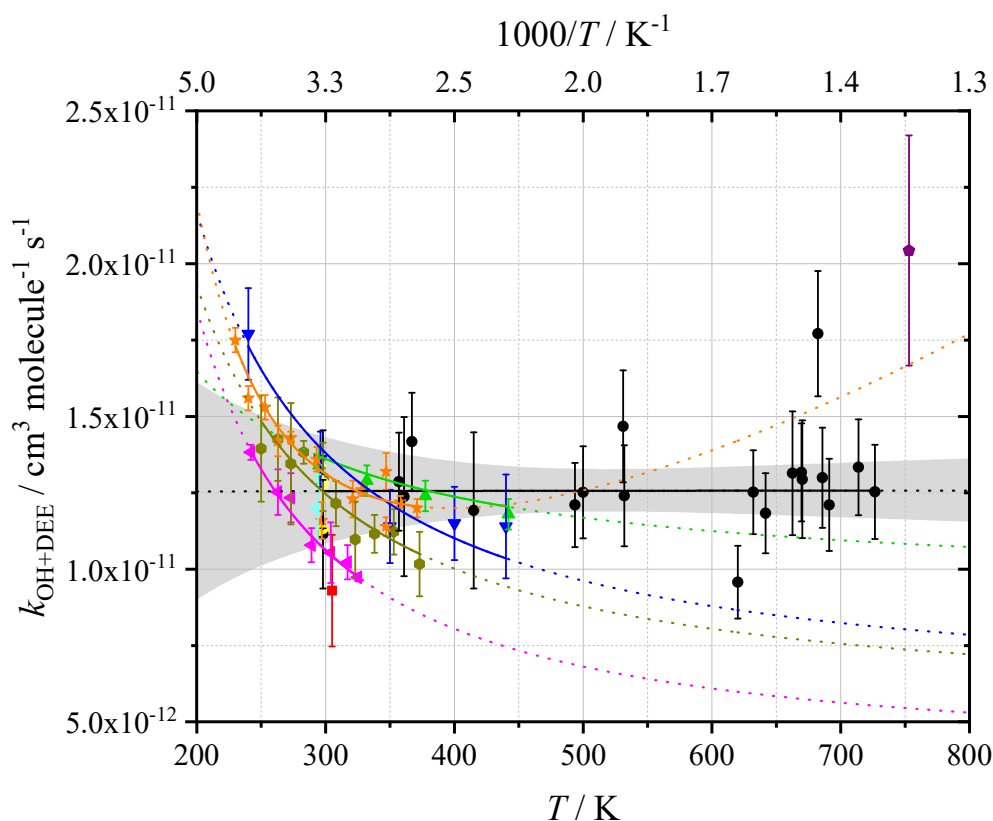
Figure 3-6: k_{OH+DEE} measured in this work (●) as a function of temperature, with the modified Arrhenius fit described in the text, where the bounds of the 95% confidence limits are shaded grey. Error bars are 2σ with another 10% of the measured value added to account for estimated systematic errors. Dashed lines represent the respective Arrhenius parameterisations extrapolated past the experimental data. Literature measurements and their temperature dependences are shown for Tranter and Walker (2001) (⬟), Mellouki et al. (1995) (★), Semadeni et al. (1993) (●), Bennett and Kerr (1990) (◀), Nelson et al. absolute (1990) (▶), Nelson et al. relative (1990) (◯), Bennett and Kerr (1989) (◆), Wallington et al. (1989) (▼), Tully and Droege (1987) (▲), and Lloyd et al. (1976) (■).

Measurements of k_{OH+DEE} made in this work occupy the gap previously present in the literature between those made by Tully and Droege [165] and Tranter and Walker [147]. Agreement within uncertainty ranges with all other studies at room temperature is seen here, although there is variability of ~15% in our data given the two photolytic precursors used at this temperature, and the previous room temperature values range from $(0.93 – 1.36) × 10^{-11}$ cm^3 molecule^{-1} s^{-1}, all details of previous studies are displayed in Table 3-5. The majority of previous studies used relative rate techniques. Bennett and Kerr [129] initially studied the reaction in a smog chamber, relative to the reaction between OH and *iso*-butene, using 350 – 450 nm photolysis of nitrous acid vapour. There is no significant difference in the updated reference rate coefficient recommended by IUPAC (international union of pure and applied chemistry) [167]

($k_{OH+iso\text{-}butene} = 5.24 \times 10^{-11}$ cm^3 molecule^{-1} s^{-1} compared to the authors' value $k_{OH+iso\text{-}butene}$ = 5.26×10^{-11} cm^3 molecule^{-1} s^{-1}).

A later study by Bennett and Kerr [163] used methyl nitrite photolysis and a reference compound of 2,3-dimethyl butane, where their data are in agreement with our measurements. An update to the temperature-independent reference rate coefficient used ($k_{OH+DMB} = 6.20 \times 10^{-12}$ cm^3 molecule^{-1} s^{-1}) to the latest recommended by Atkinson [168] ($k_{OH+DMB} = 5.78 \times 10^{-12}$ cm^3 molecule^{-1} s^{-1} at 298 K) which is dependent on temperature, reduces the rate coefficients by approximately 15% at the lower temperatures, and ~1% at the highest temperatures reported.

Agreement was found with the relative rate study by Semadeni et al. [164], where 2,3-dimethyl butane was the reference compound used, after ethyl or methyl nitrite photolysis using a Xe arc lamp. The same adjustment to the reference reaction rate coefficient as described above reduces the lowest temperature rate coefficients by approximately 15%, and increases the highest temperature rate coefficients by 11%, giving a less pronounced temperature dependence, which is in better agreement with this work.

Lloyd et al. [162] used a similar technique, with OH + iso-butene as the reference reaction, and photolysis of HONO in a smog chamber to measure $k_{OH+DEE} = (9.30 \pm 1.83)$ $\times 10^{-12}$ cm^3 molecule^{-1} s^{-1}, just in agreement with our 298 K measurement. Updating the $k_{OH+iso\text{-}butene}$ value used (4.99×10^{-11} cm^3 molecule^{-1} s^{-1}) to the most recent IUPAC recommendation [167] (4.92×10^{-11} cm^3 molecule^{-1} s^{-1} at 305 K) yields a corrected value of $k_{OH+DEE} = (9.17 \pm 1.83) \times 10^{-12}$ cm^3 molecule^{-1} s^{-1}, marginally lower than our value when considering uncertainty ranges.

Table 3-5: Comparison of the rate coefficient obtained for k_{OH+DEE} with previous measurements.

Reference	Technique	$k(298\ K)^a$	$T\ /\ K$	$k(T)^b$
Mellouki et al. (1995)	LFP-LIF	1.36 ± 0.11^c	230 – 371	$9.07\times10^{-13}\ (T/298)^{2.0}\ e^{6.63/RT}$
Semadeni et al. (1993)	Relative rate	1.3 ± 0.11 *(1.21 ± 0.11)*	250 – 373	$5.2\times10^{-12} \times e^{2.18/RT}$
Nelson et al. (1990)	Pulse radiolysis – UV spec.	1.13 ± 0.01	298	–
Nelson et al. (1990)	Relative rate	1.28 ± 0.06 *(1.19 ± 0.36)*	298	–
Bennett and Kerr (1990)	Relative rate	1.05 ± 0.10^g *(1.00 ± 0.10)*	242 – 328	$3.5\times10^{-12} \times e^{2.77/RT}$
Bennett and Kerr (1989)	Relative rate	1.20 ± 0.11	294	–
Wallington et al. (1988)	UV photolysis – OH RF	1.36 ± 0.09^d	240 – 440	$5.6\times10^{-12} \times e^{2.25/RT}$
Lloyd et al. (1976)	Relative rate	0.93 ± 0.18^e *(0.92 ± 0.18)*	305	–
Tully and Droege (1987)	LFP-LIF	1.34 ± 0.06^f	295 – 442	$9.3\times10^{-12} \times e^{0.95/RT}$
Tranter and Walker (2001)	Relative rate	na	753	2.04 ± 0.38
This work	LFP-LIF	1.25 ± 0.13	298 – 727	$(1.28\pm0.21) \times 10^{-11} \times e^{(-0.11 \pm 0.59)/RT}$

^{a}Units are 10^{-11} cm^3 molecule^{-1} s^{-1}. ^{b}Units of A are cm^3 molecule^{-1} s^{-1} and E_a are kJ mol^{-1}. ^{c}Measured at 293 K. ^{d}Measured at 296 K. ^{e}Measured at 305 K. ^{f}Measured at 295 K. ^{g}Measured at 304 K. ^{h}Measured at 294 K. RF = resonance fluorescence discharge lamp. Rate coefficients in italics are based on updated reference reaction rates from references [167, 168].

Nelson et al. [137] measured a relative rate value using a photolytic method, where methyl nitrite was photolysed at wavelengths longer than 300 nm, or H$_2$O$_2$ ($\lambda = 254$ nm), to act as the OH precursor. OH + cyclohexane was used as the reference reaction. The reported rate ($(1.28 \pm 0.06) \times 10^{-11}$ cm^3 molecule^{-1} s^{-1}) lies within the uncertainty ranges of the average room temperature measurement made here, as does their rate coefficient from an absolute determination. For the absolute determination, pulse radiolysis–UV spectroscopy of H$_2$O/Ar mixtures was used to generate OH radicals, and it was found that $k_{OH+DEE} = (1.13 \pm 0.01) \times 10^{-11}$ cm^3 molecule^{-1} s^{-1}. The small errors here account purely

for statistical 2σ uncertainties, and the authors suggest an estimated total uncertainty for the absolute measurements of 20%, based on reactant concentration accuracies. Relative rate experiments would be subject to 25% of the value propagated into the error, to account for the OH + c-C_6H_{12} reference reaction. With an updated value for the reference reaction to the latest value recommended by Atkinson [168] ($k_{OH+cyclohexane}$ value used = 7.49 × 10^{-12} cm^3 molecule^{-1} s^{-1}, corrected $k_{OH+cyclohexane}$ = 6.97 × 10^{-12} cm^3 molecule^{-1} s^{-1}), k_{OH+DEE} at 298 K = (1.19 ± 0.36) × 10^{-11} cm^3 molecule^{-1} s^{-1}, in good agreement with the measurement in this chapter.

Flash photolysis – laser-induced fluorescence studies by Mellouki et al. [113] and Tully and Droege [165] are both in agreement with this work at room temperature. Mellouki et al. used 248 nm photolysis of H_2O_2, whereas Tully and Droege photolysed N_2O at 193 nm to produce O(^{1}D) atoms, which produced OH radicals in the presence of H_2O. Finally, the study by Wallington et al. [136] also used flash photolysis, coupled to resonance fluorescence with photolysis of H_2O at 165 nm, which produced a result in agreement with the other room temperature studies here. Previous work by Wallington et al. [136], Mellouki et al. [113], Tully and Droege [165], Bennett and Kerr [163] and Semadeni et al. [164] all undertook temperature-dependent measurements of the reaction between diethyl ether and the hydroxyl radical, where the ranges explored were, in Kelvin, 240 – 440, 230 – 370, 294 – 442, 242 – 328 and 247 – 373 respectively. At lower temperatures, virtually all of these more extensive studies overlap with our work, within error. Figure 3-7 shows the 95% confidence limits of all temperature dependent study fits, where the only significant deviation from this work is the behaviour of k_{OH+DEE} with temperature observed by Bennett and Kerr [163] above 300 K. Above ~360 K, the Arrhenius parameterisation by Semadeni et al. [164] also starts to fall outside the 95% confidence limits of the rate coefficients measured in this work. This trend is similarly seen for the data fits by Wallington et al. [136] and Tully and Droege [165] above approximately 450 K, although it could be argued the data show signs of plateauing, similar to the behaviour observed in this work. It is possible that the upper limit of previous studies (~440 K) can account for this, where the studies simply did not extend to high enough temperatures to observe the plateau of the rate coefficient. Additionally, there was no hint of the strong negative temperature dependence seen by previous studies in the data obtained here. Once again, these may be as a result of the 298 K lower limit on temperature explored here, where the temperature dependence only becomes particularly strong below this threshold. Furthermore, it is feasible that certain

experiments may have been subject to photolysis of DEE, such as those by Tully and Droege, and Wallington et al., where wavelengths as short as 193 nm and 165 nm were used to initiate chemistry, potentially resulting in interfering reactions. This effect would become more pronounced at higher temperatures where the cross section of diethyl ether (at 165 nm and 193 nm, 295 K, 8.5×10^{-18} and 3.9×10^{-19} cm^2 molecule^{-1} respectively [169]) would typically be expected to increase, resulting in greater loss of reactant. Tully and Droege did observe non-exponential decays at high temperatures, where the initial decay portions were weakly dependent on laser energy. These decays were not reported however, but the dependence on laser energy suggests some photolysis may have occurred. This explanation would not account for the discrepancy with the negative temperature dependence for OH + DEE seen in studies using smog chambers or longer flash photolysis wavelengths.
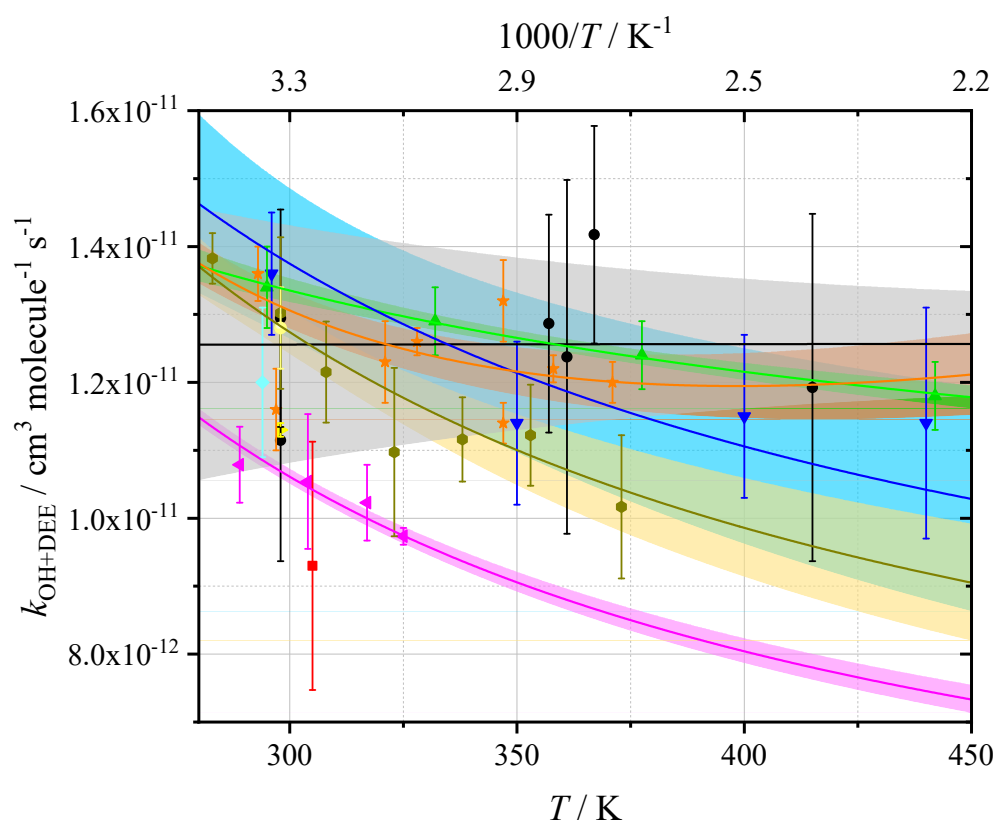
Figure 3-7: k_{OH+DEE} comparison with literature determinations showing the 95% confidence bounds of the studies. Black data represent this work's fit and 95% limits. Literature studies are Mellouki et al. (1995) (★), Semadeni et al. (1993) (●), Bennett and Kerr (1990) (◀), Nelson et al. (1990) absolute (▶), Nelson et al. relative (1990) (○), Bennett and Kerr (1989) (◆), Wallington et al. (1989) (▼), Tully and Droege (1987) (▲), and Lloyd et al. (1976) (■).

At higher temperatures, the modified Arrhenius parameterisation by Mellouki et al. [113] predicts a positive temperature dependence above approximately 400 K (Figure 3-6), however this is an extreme extrapolation beyond their experimental conditions, and as such shouldn't be held to any degree of certainty.

There is only one study that suggests there may be a positive temperature dependence above 400 K, by Tranter and Walker [132], who used a relative rate technique, where the reaction between H_2 and OH was the reference used. Although measurements in this work are not in agreement with theirs, considering the extremes of the uncertainty bounds, there is only a ~20% difference in the rate measurement. The most comparable temperature to Tranter and Walker's measurement in this work is 727 K, which is 26 K lower than theirs. A strong positive temperature dependence would need to appear between 727 and 753 K for the gap between measurements here and the highest temperature literature measurement to be consistent, which is unreasonable given the lack of temperature dependence seen throughout the study of k_{OH+DEE} presented here. We note the presence of one data point at 682 K, where a rate coefficient measured was in agreement with Tranter and Walker's value, however we consider this to be an anomalous result, potentially as a result of a mis-reported bulb composition.

Because of the considerable uncertainty between previous literature measurements, negative temperature dependences, and the fast rate coefficient previously observed at 753 K, a combined modified Arrhenius parameterisation was performed, fitting to all available data in the literature and this work. The data can be described by

$$k_{OH+DEE}(230-753 \text{ K}) = (5.8 \pm 5.4) \times 10^{-13} \times \left(\frac{T}{298}\right)^{2.3\pm0.8} \exp\left[\frac{7.5\pm2.3}{RT}\right] \text{ cm}^3 \text{ molecule}^{-1} \text{ s}^{-1},$$

where the uncertainties quoted are the bounds of the 95% confidence limits from the fit. The maximum percentage uncertainty of the 95% confidence limits is 23%, at the highest temperature.
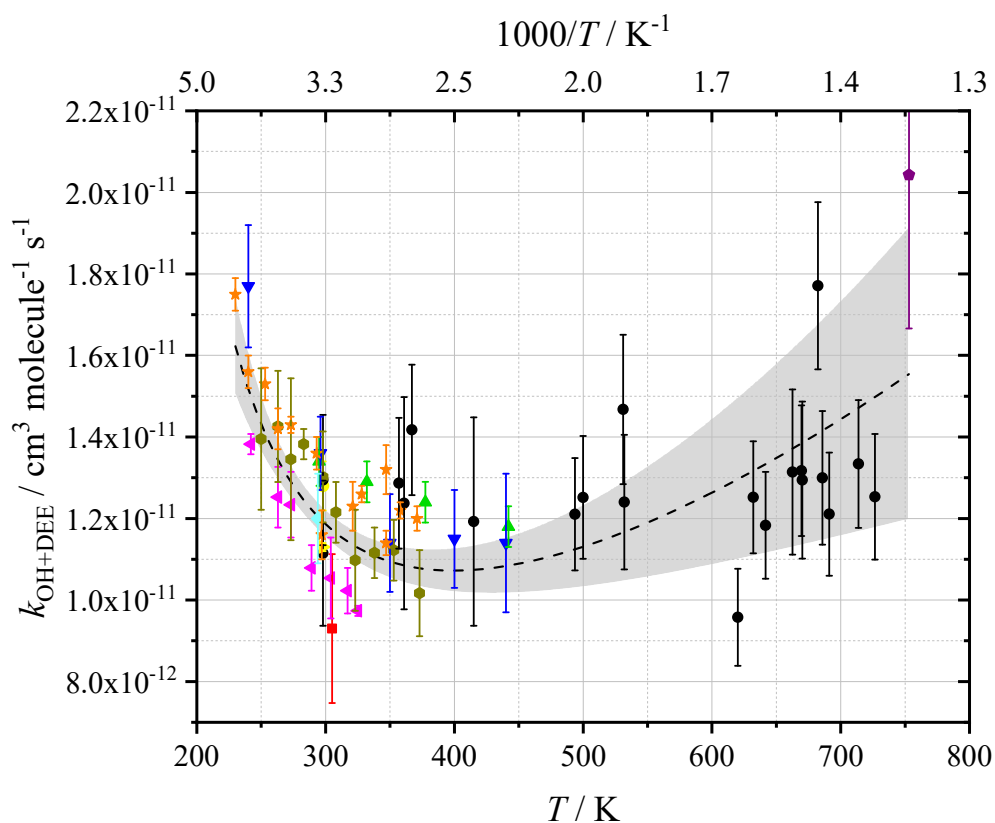
Figure 3-8: OH + DEE modified Arrhenius combined fit, described by = k_{OH+DEE}(230 – 753 K) = (5.8 ± 5.4) × 10^{-13} × (T/298)$^{2.3±0.8}$ e$^{(7.5±2.3)/RT}$ cm^3 molecule^{-1} s^{-1}. The grey shaded area represents the 95% confidence limits of the fit.

3.6 OH + Di-*n*-butyl Ether

Di-*n*-butyl ether is a straight chain symmetrical ether, with four saturated carbons on both sides of the oxygen atom. It is of relatively recent interest as a potential replacement fuel, where it can be produced from pulping of biomass [14]. Desirable properties such as reduced soot [39, 66, 67], good spray characteristics [65], high cetane rating (100 – 115) [14, 39], and short ignition delay times [68], suggest it may be a suitable alternative fuel for low temperature combustion.

Laminar flow studies have been carried out using DBE [170, 171], and radical chain branching was shown to dominate the low temperature ignition of DBE, suggesting that a similar reaction mechanism to that of DME and DEE, and typical low temperature hydrocarbon combustion, should be expected. In contrast to the two smaller linear ethers, DBE has four potential unique sites for the OH abstraction reaction. As a result of its proximity to the oxygen atom, the α site has been shown to be the dominant location for H abstraction to take place [170, 172]. All possible sites are shown in Scheme 3-4 and reactions R 3-10 to R 3-13.
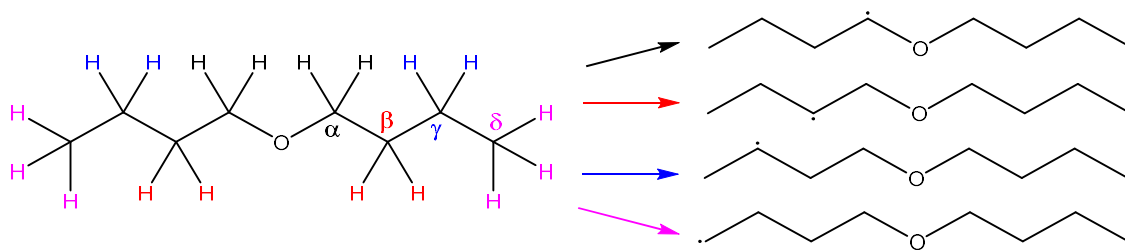
Scheme 3-4: Potential hydrogen abstraction sites on di-*n*-butyl ether for its reaction with the OH radical, and the R radicals formed.

$$C_4H_9OCH_2CH_2CH_2CH_3 + OH \rightarrow C_4H_9OCHCH_2CH_2CH_3 + H_2O \qquad \text{R 3-10}$$

$$C_4H_9OCH_2CH_2CH_2CH_3 + OH \rightarrow C_4H_9OCH_2CHCH_2CH_3 + H_2O \qquad \text{R 3-11}$$

$$C_4H_9OCH_2CH_2CH_2CH_3 + OH \rightarrow C_4H_9OCH_2CH_2CHCH_3 + H_2O \qquad \text{R 3-12}$$

$$C_4H_9OCH_2CH_2CH_2CH_3 + OH \rightarrow C_4H_9OCH_2CH_2CH_2CH_2 + H_2O \qquad \text{R 3-13}$$

In this work, a non-site-specific approach has been used to measure the bimolecular rate coefficient, and as such, values for k_{OH+DBE} reported refer to the total rate coefficient for OH + DBE in reaction R 3-14.

$$C_4H_9OC_4H_9 + OH \rightarrow C_4H_9OC_4H_8 + H_2O \qquad \text{R 3-14}$$

In this chapter, reaction R 3-14 has been studied, and generally found to be in qualitative agreement with the negative temperature-dependent behaviour observed in other studies over the temperature range 298 – 372 K, but with some disagreement over the absolute values of the rate coefficient. Beyond 500 K, no temperature dependence was seen. Such a lack of temperature dependence has not been seen before. Previous studies on the kinetics of reaction R 3-14 have employed the use of various techniques, the majority of which were relative rate studies within smog chambers, but there have been other studies using flash photolysis initiation methods coupled to fluorescence detection [113, 129, 130, 135, 137, 164, 173, 174].

3.6.1 OH + C₄H₉OC₄H₉ Temperature Dependence

The bimolecular rate coefficient for the reaction between di-*n*-butyl ether and the hydroxyl radical has been measured under pseudo-first order conditions, where the concentration of OH was controlled by reaction R 3-14. An example single exponential

decay is included in Appendix A. Analysis of the OH decay rate at varying concentrations of di-*n*-butyl ether to give k'_{OH+DBE}, and least squares linear fitting of these pseudo-first order rate coefficients as a function of [DBE], for a given temperature and pressure, provides the bimolecular rate coefficient k_{OH+DBE}. Two example bimolecular plots are included in Appendix A.

At higher temperatures, where the rate coefficient became slower, the low vapour pressure (and therefore low DBE/N_2 concentration bulbs) became a prohibiting factor in measuring accurate rate coefficients, where pseudo-first order conditions would become harder to maintain. To circumvent this issue, a different method was used, where a glass bubbler was used to deliver higher quantities of fuel, by flow of nitrogen carrying DBE vapour into the mixing manifold. At room temperature, several measurements using both a bulb and a bubbler allowed the bubbler measurements to be multiplied by a correction factor to account for any discrepancies between the estimated [DBE] delivered by the bubbler and the actual amount delivered. Full discussion of this method is presented in section 3.3. An estimated 10% uncertainty was applied to all bubbler measurements after correction.

At 483 K and higher temperatures, some decays exhibited biexponential behaviour, indicating recycling of OH radicals. Oxygen present in the system due to decomposition of H_2O_2 is likely the source of this OH, combining with *n*-butyl butoxy radicals (reaction R 3-15).
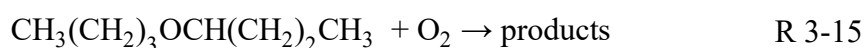
$$CH_3(CH_2)_3OCH(CH_2)_2CH_3 + O_2 \rightarrow products \qquad\qquad R\ 3\text{-}15$$

Observation of biexponential decays is highly dependent on temperature and concentrations of oxygen and fuel. As such, biexponential decays were subtle, and not seen when the bubbler delivery method was employed (a very slow recycling rate is well hidden when the initial decay is too fast), as a result of the more concentrated amounts of DBE delivered. Despite their subtlety, biexponential decays were fit marginally better by the biexponential equation (Scheme 3-1) compared to the single exponential equation. An example biexponential decay with fitting is shown in Appendix A.

Table 3-6: Bimolecular rate coefficients obtained for OH + DBE. Uncertainties are 2σ for bulb measurements, and 10% of the k_{OH+DBE} value for corrected bubbler measurements

T / K	$10^{11}\, k_{OH+DBE}$[a]	n	10^{-13} [DBE] range[b]	P / Torr
298	3.86 ± 0.33	6	4.5 – 9.3	29
298	3.99 ± 0.09	7	1.5 – 10.3	29
298	3.57 ± 0.47 [c]	4	8.2 – 41.8	30
298	4.34 ± 0.42 [c]	9	7.9 – 26.2	30
298	3.87 ± 0.37 [c]	7	4.8 – 14.8	30
363	3.12 ± 0.45 [c]	5	4.3 – 13.3	29
483	2.91 ± 0.63	7	2.3 – 9.5	28
550	2.75 ± 0.38 [c]	7	2.5 – 8.1	29
572	2.70 ± 0.27	8	0.5 – 4.0	28
613	2.77 ± 0.36 [c]	6	2.5 – 8.2	29
663	2.68 ± 0.26 [c]	5	3.4 – 12.8	30
704	3.31 ± 0.35 [c]	10	2.7 – 11.3	30
732	2.54 ± 0.29 [c]	11	2.6 – 9.9	30

[a]Units cm^3 molecule^{-1} s^{-1}. [b]Units molecule cm^{-3}. [c]Value obtained and corrected using the bubbler delivery method. n refers to the number of experiments comprising a bimolecular determination.

The temperature dependence of reaction R 3-14 has been investigated, with rate coefficients measured between 28 and 30 Torr of pure nitrogen, and between 298 and 732 K. Hydrogen peroxide was the photolytic precursor, and the measured rate coefficients did not vary significantly with laser power. A plot of the rate coefficient as a function of temperature is shown in Figure 3-9, and all values of k_{OH+DBE} are displayed in Table 3-6. Previous measurements by other studies are included in Figure 3-10. The mean room temperature rate coefficient taken from two bulb measurements was (3.92 ± 0.13) × 10^{-11} cm^3 molecule^{-1} s^{-1}, where the uncertainty in the measurement refers to a purely statistical range at the 2σ level. This average value is shown in Figure 3-10, but the two individual bulb measurements, and three measurements made with the bubbler, at room temperature, are all displayed separately in Figure 3-9.
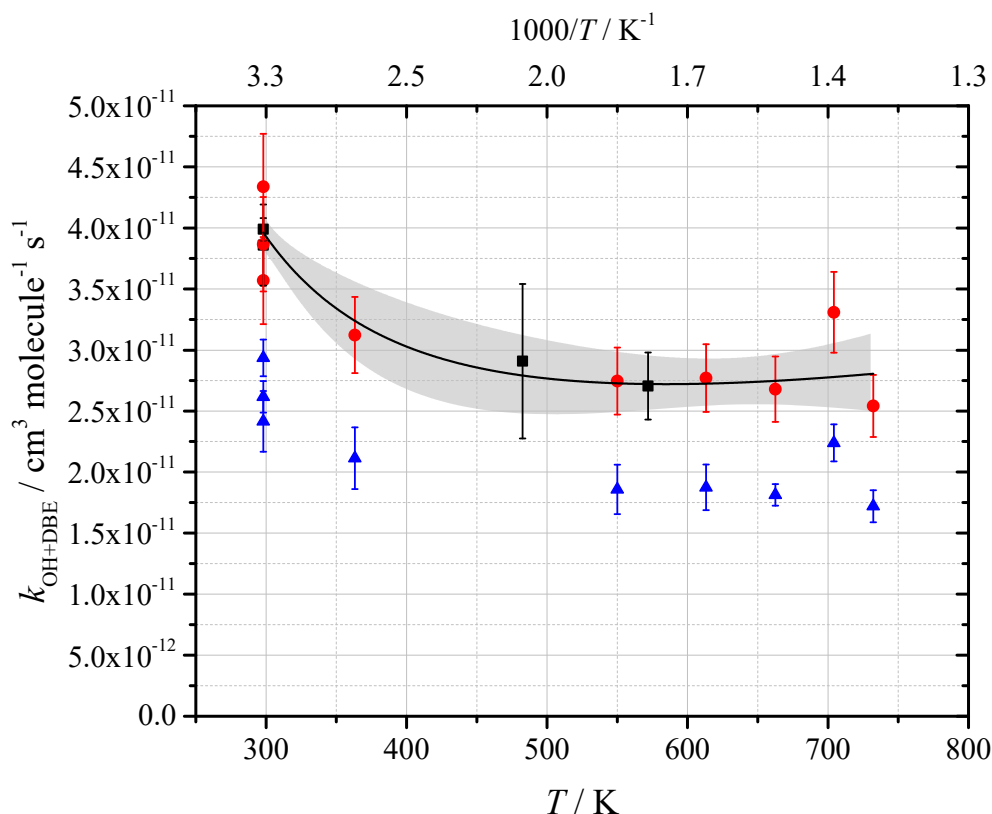
Figure 3-9: Bimolecular rate coefficient k_{OH+DBE} measured in this work as a function of temperature. Data shown are rate coefficients measured using the bulb delivery method (■), bubbler delivery method corrected (●), and the uncorrected values obtained with a bubbler (▲). Uncertainties on bulb and original bubbler data are statistical at the 2σ level. Corrected bubbler error bars represent 10% of the value to account for uncertainty in the correction factor. The shaded area represents the 95% confidence limits of the fit to the data (uncorrected bubbler values not included). The data can be parameterised as $(3.05 \pm 7.13) \times 10^{-12}$ $(T/298)^{(1.31\pm1.62)}$ $e^{(6.35\pm5.83)/RT}$ cm^3 molecule^{-1} s^{-1}. All measurements at 298 K are shown here, rather than the mean reported in the text.

The modified Arrhenius fit to the data can be described by $k_{OH+DBE}(298 - 732$ K$)$

$= (3.05 \pm 7.13) \times 10^{-12} \left(\dfrac{T}{298}\right)^{(1.31\pm1.62)} \times e^{\frac{(6.35\pm5.83)}{RT}}$ cm^3 molecule^{-1} s^{-1}. The uncertainties

reported are statistical at the 2σ level, and the maximum uncertainty of the 95% confidence limits across the temperature range valid for this parameterisation is 12%, at approximately 450 K. A weighted fit to the bulb and corrected bubbler measurements was used to describe the temperature dependence of the rate coefficient.
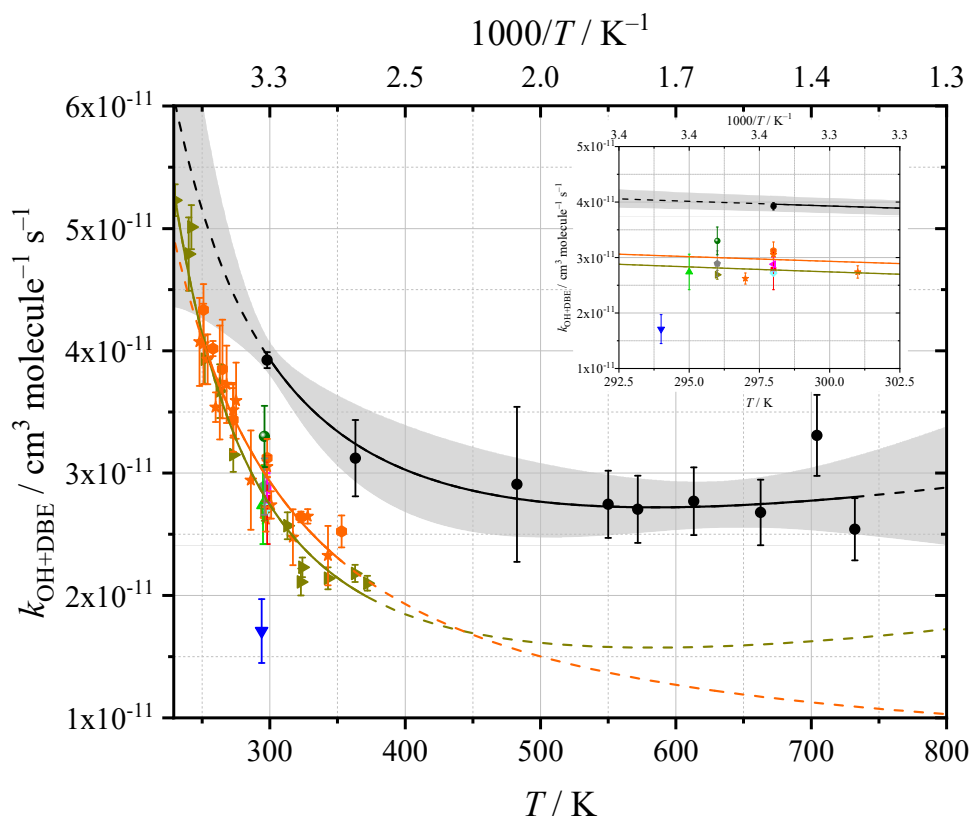
Figure 3-10: Comparison of k_{OH+DBE} measured in this work (●) with previous studies. Literature studies are Wallington et al. (1988) (■), Bennett and Kerr (1989) (▼), Wallington et al. (1989) (▲), Nelson et al. absolute (1990) (◆), Nelson et al. relative (1990) (◄), Mellouki et al. (1995) (►), Semadeni et al. (1993) (DMB ref.) (●), Semadeni et al. (1993) (DEE ref.) (★), Kramp and Paulson (1998) (⬟), and Harry et al. (1999) (●). Orange fit is from Semadeni Arrhenius parameters, reported as an average of the DMB- and DEE-relative rate measurements.

At room temperature (Figure 3-10 inset), the majority of the previous measurements in the literature are approximately 25 – 30% slower than the measured rate coefficient in this work (Table 3-7). Bennett and Kerr [129] used a relative rate technique to measure k_{OH+DBE} with *iso*-butene as the reference compound within a smog chamber, employing photolysis of nitrous acid as the OH precursor (λ = 350 – 450 nm). Their reported rate and suggested 2σ+10% error, $(1.71 \pm 0.26) \times 10^{-11}$ cm^3 molecule^{-1} s^{-1}, is significantly lower than the values reported in this work and the remainder of the literature. The latest recommended rate coefficient by IUPAC [167] for $k_{OH+iso\text{-butene}}$ makes no significant change to the rate coefficient. In general, the smog-chamber approach is less precise, and this is acknowledged by the authors.

Room temperature measurements reported by Wallington et al. [136], Nelson et al. [137], Wallington et al. [174], and Kramp and Paulson [173] are slower than the mean

measured rate coefficient at room temperature in this work ($(3.92 \pm 0.13) \times 10^{-11}$ cm^3 molecule^{-1} s^{-1}), by approximately $(17 - 27)\%$ when uncertainties are considered.

The first study conducted by Wallington et al. [136] used flash photolysis – resonance fluorescence to study reaction R 3-14, where the source of OH was photolysis of H_2O at wavelengths greater than 165 nm. Their reported rate coefficient for the reaction between OH and di-*n*-butyl ether was $(2.78 \pm 0.36) \times 10^{-11}$ cm^3 molecule^{-1} s^{-1}. As such, their experiments may have been subject to reagent photolysis at such short wavelengths, potentially introducing unwanted radical-radical reactions, or simply resulting in less DBE delivered than expected. No absorption cross-sections for DBE have been reported, but a comparable value to those of DME and DEE at 165 nm already discussed could be expected. Despite this, the later room temperature study by Wallington et al. [174] measured the rate coefficient again, to an almost identical value $(2.74 \pm 0.32) \times 10^{-11}$ cm^3 molecule^{-1} s^{-1} via a relative rate study using OH + diethyl ether as the reference reaction. There, photolysis of methyl nitrite in synthetic air would have used longer wavelengths, and therefore would not have subjected the ether fuel to any photolysis effects. There is no new recommended rate coefficient for the reference, k_{OH+DEE}, to update their reported rate coefficient.

Measurements made by Nelson et al. [137] provide both a relative rate value, and an absolute determination ($(2.88 \pm 0.12) \times 10^{-11}$ cm^3 molecule^{-1} s^{-1} and $(2.72 \pm 0.03) \times 10^{-11}$ cm^3 molecule^{-1} s^{-1}) which are only just outside agreement of each other's uncertainty ranges. The relative rate determination employed a photolytic method, using methyl nitrite ($\lambda \geq 300$ nm) or H_2O_2 ($\lambda = 254$ nm) as hydroxyl radical precursors. The reference reaction rate coefficient used, $k_{OH+cyclohexane} = 7.49 \times 10^{-12}$ cm^3 molecule^{-1} s^{-1}, when updated to the latest recommendation by Atkinson [168] ($k_{OH+cyclohexane} = 6.97 \times 10^{-12}$ cm^3 molecule^{-1} s^{-1}) provides a corrected measurement of, $k_{OH+DBE} = (2.68 \pm 0.79) \times 10^{-11}$ cm^3 molecule^{-1} s^{-1}, in worse agreement with the rate coefficient observed in this work. Pulse radiolysis coupled to UV spectroscopy was used to make the absolute measurement, where mixtures of H_2O and Ar were irradiated (2 MeV) to induce reaction between Ar* and H_2O, producing OH. The authors note that the absolute measurements only report the statistical uncertainties at the 2σ level, but a realistic estimate of the total uncertainty from reactant concentrations would be 20%. Similarly, for the relative rate experiments, a further 25% of the value would be a reasonable estimate to add to the statistical uncertainties, as a result of the uncertainty in the cyclohexane + hydroxyl reaction rate coefficient. With these considerations, the absolute and update relative

values reported by Nelson et al. would put their measurements 14% and 8% slower than k_{OH+DBE} in this work respectively.

Further relative rate measurements were made using UV photolysis of methyl nitrite and NO in a smog chamber, by Kramp and Paulson [173] who determined a mean bimolecular rate coefficient = $(2.89 \pm 0.23) \times 10^{-11}$ cm^3 molecule^{-1} s^{-1} at 296 K, using n-nonane, methylcyclohexane and butadiene as reference compounds for the three contributing measurements. Newer recommended rate coefficients are available for n-nonane (at 296 K), and methylcyclohexane (at 298 K) from Atkinson [168], but no update exists for butadiene. Taking into account the updates possible, a new mean rate coefficient $k_{OH+DBE} = (2.73 \pm 0.23) \times 10^{-11}$ cm^3 molecule^{-1} s^{-1} is in slightly worse agreement with this work.

Of the previous work carried out, the room temperature measurement by Harry et al. [130] is the most recent, and closest to the value in this work, reporting $k_{OH+DBE} = (3.30 \pm 0.25) \times 10^{-11}$ cm^3 molecule^{-1} s^{-1} (~6% slower when considering the quoted uncertainty ranges). Methyl vinyl ketone was employed as the reference compound in their relative rate experiment, using a smog chamber and photolysis of methyl nitrite and NO at >300 nm. The value $k_{OH+MV\text{-}ketone} = 2.06 \times 10^{-11}$ cm^3 molecule^{-1} s^{-1} used can be updated to the latest recommendation by IUPAC [167] where $k_{OH+MV\text{-}ketone} = 2.04 \times 10^{-11}$ cm^3 molecule^{-1} s^{-1}. This makes the updated rate coefficient of $k_{OH+DBE} = (3.27 \pm 0.25) \times 10^{-11}$ cm^3 molecule^{-1} s^{-1} in marginally worse agreement with rate coefficient measured in this work.

Table 3-7: Comparison of the rate coefficient obtained for k_{OH+DBE} with previous measurements. Uncertainties for this work are 2σ.

Reference	Technique	$k(298\text{ K})^a$	T / K	$k(T)^b$
Wallington et al. (1988)	FP–resonance fluorescence	2.78 ± 0.36	298	–
Wallington et al. (1989)	Relative rate	2.74 ± 0.32^c	295	–
Bennett and Kerr (1989)	Relative rate	1.71 ± 0.26^d	294	–
Nelson et al. (1990)	Relative rate	2.88 ± 0.12 *(2.68 ± 0.79)*	298	–
Nelson et al. (1990)	Pulse radiolysis	2.72 ± 0.03	298	–
Mellouki et al. (1995)	PLP–LIF	2.69 ± 0.08^e	230–372	$6.3\times10^{-18} \times T^{2.0} \times e^{9.7/RT}$
Semadeni et al. (1993)	Relative rate^f	3.09 ± 0.09 *(2.91 ± 0.09)*	251–353	$5.5\times10^{-12} \times e^{4.17/RT}$
Kramp and Paulson (1998)	Relative rate	2.89 ± 0.23^e *(2.73 ± 0.23)*	296	–
Harry et al. (1999)	Relative rate	3.30 ± 0.25^e *(3.27 ± 0.25)*	296	–
This work	PLP–LIF	3.92 ± 0.13	298–732	$(3.1\pm7.1)\times10^{-12} (T/298)^{1.3\pm1.6} e^{(6.4\pm5.8)/RT}$

^{a}Units are 10^{-11} cm^3 molecule^{-1} s^{-1}. ^{b}Units of A are cm^3 molecule^{-1} s^{-1} and E_a are kJ mol^{-1}. ^{c}Measured at 295 K. ^{d}Measured at 294 K. ^{e}Measured at 296 K. ^{f}Arrhenius parameterisation and $k(298\text{ K})$ are both the averages of experiments using OH + diethyl ether and OH + 2,3-dimethyl butane as reference reactions. Rate coefficients in italics are based on updated reference reaction rates from references [167, 168].

Two temperature-dependent investigations of the OH + di-*n*-butyl ether rate coefficient exist (Figure 3-10), and as with the single room temperature measurement studies, their reported rate coefficients are lower than this work's. Semadeni et al. [164] made measurements using a relative rate method using 2,3-dimethyl butane and diethyl ether as reference compounds, and the photolysis of ethyl or methyl nitrite in the presence of NO provided the hydroxyl radicals required for the reactions. A Xe arc lamp was used as a solar simulator for photolysis. Mellouki et al. [113] employed pulse flash photolysis – laser-induced fluorescence to study the reaction using 248 nm photolysis of H$_2$O$_2$, similar to the work carried out here. The reported room temperature values for k_{OH+DBE} are (2.69 ± 0.08), (3.12 ± 0.16), and $(3.05 \pm 0.09) \times 10^{-11}$ cm^3 molecule^{-1} s^{-1} respectively

for Mellouki et al., and Semadeni et al. using DMB and DEE. Semadeni et al. used a modified Arrhenius expression to yield an average parameterisation of all their relative rate experiments where $k_{OH+DBE}(248 - 353 \text{ K}) = (6.3 \pm 0.74) \times 10^{-18} \times T^2 \times e^{\frac{9.7 \pm 0.3}{RT}}$ cm^3 molecule^{-1} s^{-1}. The fit to the data by Mellouki et al. yielded the expression $k_{OH+DBE}(248 - 353 \text{ K}) = 5.5 \times 10^{-12} \times e^{\frac{4.2 \pm 1.2}{RT}}$ cm^3 molecule^{-1} s^{-1}. In comparison with the modified Arrhenius expression in this work, $k_{OH+DBE}(298 - 732 \text{ K}) = \times (3.05 \pm 7.13) \times 10^{-12} \left(\frac{T}{298}\right)^{(1.31 \pm 1.62)} \times e^{\frac{(6.35 \pm 5.83)}{RT}}$, the fit by Semadeni et al. predicts a shallow negative temperature dependence when extrapolated past their experimental temperature range, whereas the data in this study shows a lack of temperature dependence above approximately 500 K. Extrapolating the fit by Mellouki et al. past their experimental conditions almost identically predicts the temperature dependence we observe. An update to the temperature-independent reference rate coefficient used by Semadeni et al. ($k_{OH+DMB} = 6.20 \times 10^{-12}$ cm^3 molecule^{-1} s^{-1}) to the latest recommended by Atkinson [168] ($k_{OH+DMB} = 5.78 \times 10^{-12}$ cm^3 molecule^{-1} s^{-1} at 298 K) which is dependent on temperature, reduces the rate coefficients by approximately 15% at the lower temperatures, and results in an increase of ~6% at the highest temperatures reported. No update to the recommended OH + DEE rate coefficient exists.

Given the disagreement with the majority of the literature by approximately 25% across all temperatures, it is possible there is a systematic error associated with the preparation of the di-*n*-butyl ether bulbs that the bubbler experiments were calibrated with. The low vapour pressure of DBE results in a more difficult bulb composition process, and inherently increases the percentage error of any discrepancy between the pressure of DBE in the bulb, and that of the pressure read from the manometer. Similarly, any slight leaks on the vacuum line will contribute to the uncertainty, however these were negligible. Loss of DBE to the walls will be greater over time, as a result of the low vapour pressure. It is possible that these issues affect the ability to deliver the reactant in this work, but also in the previous literature studies. Nelson et al. [137] also noted the discrepancy between their work and Bennett and Kerr and Wallington was not clear, as they were in agreement on shorter chain ethers. This suggests there can be systematic issues with higher member ethers.

The negative temperature dependence seen for the reaction between OH and DBE in this work, and previous literature, may indicate similar behaviour to that observed for the OH + TMOF reaction in section 3.4.1. Occurring at approximately 350 K for the OH

+ DBE reaction indicates that the complex formation may become more facile with a larger molecule, where the larger number of degrees of freedom makes the configuration required to form a complex between the ether molecule and OH more probable. Similarly, the temperature where this behaviour has been observed to begin in previous studies for OH + DEE is between that for DME and for DBE.

Despite the overall disagreement, qualitatively this work has corroborated the temperature dependence seen in other studies from room temperature to approximately 370 K, and therefore confidence should be afforded in the higher temperature ($\leq$732 K) behaviour of k_{OH+DBE}, where a lack of temperature dependence is clear.

3.7   OH + Methyl *Tertiary* Butyl Ether

MTBE bears structural similarities to DME, and can be synthesised using methanol (and therefore bio-methanol) [72]. MTBE has been used as an additive to improve the octane rating of fuels [73], but few studies exist on the low temperature oxidation mechanism of MTBE relevant to its use as a biofuel additive. MTBE possesses two distinct sites that the hydroxyl radical can abstract from; α (reaction R 3-16) and β (reaction R 3-17) primary sites (Scheme 3-5). The products of these reactions are H_2O and a radical, R. This first step has been measured in this work, with a non-site-specific approach, thus reported values for $k_{OH+MTBE}$ refer to the sum of the rate coefficients for reactions R 3-16 and R 3-17.

$$(CH_3)_3COCH_3 + OH \rightarrow (CH_3)_3COCH_2 + H_2O \qquad \text{R 3-16}$$

$$(CH_3)_3COCH_3 + OH \rightarrow H_2C(CH_3)_2COCH_3 + H_2O \qquad \text{R 3-17}$$
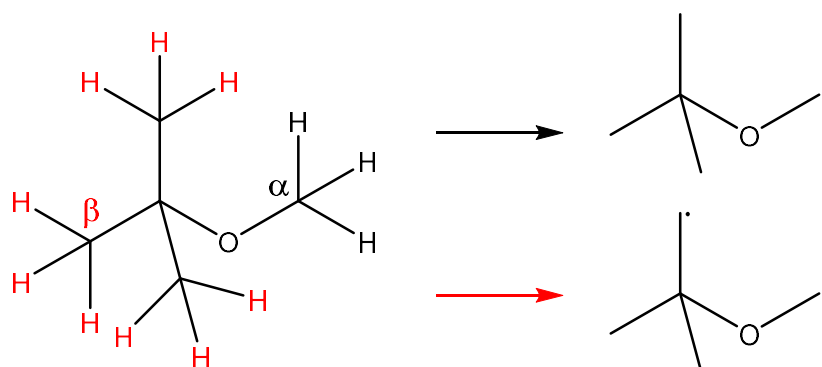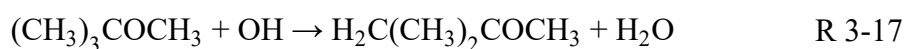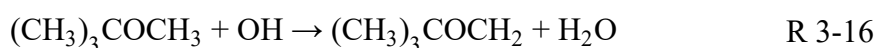
Scheme 3-5: Possible hydrogen abstraction sites for MTBE, and the resulting R radicals formed.

Previous research has not covered $k_{OH+MTBE}$ comprehensively, with few extensive temperature dependent studies conducted. The majority of studies focused on lower temperatures, often using relative rate or flash photolysis methods [131, 132, 135, 163, 174-179]. A full summary of past work on $k_{OH+MTBE}$ is presented in Table 3-9. Only two studies have been undertaken across large temperature ranges comparable to our measurements [175, 176]. All other studies were carried out at 440 K and below. There has been some discussion in the literature of the two possible MTBE sites for hydrogen abstraction, but no direct experimental measurements of the site-specific rate coefficients. Arif et al. [175] predicted ~80% and ~20% abstraction from the α and β sites respectively, based on previous product analysis from smog chamber experiments [180, 181]. The dominance of abstraction from the methyl site rather than the *t*-butyl site was expected due to the weaker C-H bonds on the α carbon. Theoretical studies by Iuga et al. [182], Zavala-Oseguera et al. [183] and Atadinc et al. [184] have all indicated similar branching ratios for H abstraction (~75%, 74% and 63% abstraction from the α site respectively).

3.7.1   OH + (CH$_3$)$_3$COCH$_3$ Temperature Dependence

The bimolecular rate coefficient for the reaction between methyl *tertiary*-butyl ether and the hydroxyl radical has been measured under pseudo-first order conditions, where the concentration of OH was controlled by reaction R 3-18. Appendix A includes a typical single exponential decay. Analysis of the OH decay rate at varying concentrations of MTBE to give $k'_{OH+MTBE}$, and least squares linear fitting of these pseudo-first order rate coefficients as a function of [MTBE], for a given temperature and pressure, provides the bimolecular rate coefficient $k_{OH+MTBE}$. Three example bimolecular plots are displayed Appendix A.

$$C_5H_{12}O + OH \rightarrow C_5H_{11}O + H_2O \qquad\qquad R\ 3\text{-}18$$
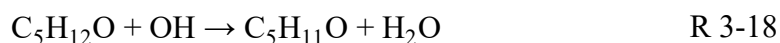
Rate coefficients for the abstraction of hydrogen by OH from methyl *tert*-butyl ether ($k_{OH+MTBE}$) were measured as a function of temperature, using hydrogen peroxide as a photolytic precursor, in the ranges 298 – 727 K and 29 – 67 Torr N$_2$. The details of all rate coefficients measured are displayed in Table 3-8. The measured rate coefficients did not vary significantly with laser power or laser repetition rate (5.9% maximum variation between 10, 5 and 2 Hz, and no variation within uncertainties). Additionally,

varying the photolysis wavelength between 248 and 266 nm produced no significant variation in the bimolecular rate coefficient. Although there are no reported UV cross sections for MTBE, this lack of variation with photolysis wavelength is consistent with the insignificant cross-sections for smaller ethers at 248 nm and 266 nm [169].

Table 3-8: Bimolecular rate coefficients obtained for OH + MTBE. Uncertainties are 2σ with an additional 10% of the measurement value added to account for systematic errors.

T / K	$10^{12}\,k_{OH+MTBE}$[a]	n	10^{-14} [MTBE][b]	P / Torr
298	2.81 ± 0.37	6	$1.6 - 7.7$	29
298	2.80 ± 0.53	5	$2.7 - 10.8$	39
354	3.00 ± 0.70	5	$2.8 - 9.6$	37
395	4.18 ± 0.76	6	$2.5 - 8.5$	37
441	6.15 ± 1.19	5	$2.2 - 7.7$	37
495	7.27 ± 1.68	6	$2.1 - 10.2$	63
510	8.43 ± 1.45	6	$2.3 - 9.9$	45
568	10.62 ± 1.18[c]	6	$2.4 - 10.2$	52
604	10.42 ± 1.23[c]	11	$1.7 - 8.3$	62
605	10.76 ± 1.22[c]	6	$2.0 - 8.3$	45
624	11.18 ± 1.32[c]	8	$1.6 - 6.9$	38
646	12.55 ± 1.45[c]	6	$1.9 - 7.9$	45
653	13.46 ± 1.57[c]	5	$2.7 - 11.6$	67
680	14.35 ± 1.71[c]	5	$1.8 - 7.5$	45
707	13.13 ± 2.13[c]	7	$1.7 - 9.8$	46
727	12.44 ± 1.57[c]	5	$1.6 - 6.9$	46

[a]Units of cm^3 molecule^{-1} s^{-1}. [b]Units of molecule cm^{-3}. [c]From global analysis. n refers to the number of experiments comprising a bimolecular determination.

At temperatures greater or equal to 568 K, the OH signal could no longer be represented as a single exponential, rather, the OH signal decay was biexponential. The presence of some oxygen when delivering hydrogen peroxide by a mass flow controller, allowed OH regeneration to occur via reaction R 3-19, where the O$_2$ combines with the MTBE-derived R radicals.
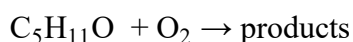
$$C_5H_{11}O + O_2 \rightarrow products \qquad\qquad R\ 3\text{-}19$$

The biexponential decay in Appendix A (Figure A 10) demonstrates the poor fit of a single exponential decay equation to the data obtained at 568 K and above, and the good fit by the biexponential equation. Biexponential traces were analysed globally, where several traces generated at a given temperature and pressure were analysed simultaneously to obtain a $k_{OH+MTBE}$ shared across the traces (and other parameters important for Chapter 6). As a result of the well-defined nature global fitting possesses, uncertainty ranges on these data are particularly small. A bimolecular plot derived from biexponential data is shown for illustrative purposes only in Appendix A.

The Arrhenius plot for $k_{OH+MTBE}$ is shown in Figure 3-11 and $k_{OH+MTBE}(T)$ can be described by $k_{OH+MTBE}(298\text{–}680\text{ K}) = (9.8 \pm 21.6) \times 10^{-13} \left(\frac{T}{298}\right)^{2.7\pm1.5} \times \exp\left[\frac{2.52\pm5.63}{RT}\right] cm^3$ molecule^{-1} s^{-1}. Across the temperature range relevant to this work (298 – 680 K), the uncertainty of the Arrhenius parameterisation is 13% – the maximum size of the 95% confidence limits. A weighted fit was used to describe the temperature dependence of the data obtained, and the highest two temperature measurements were omitted, as a result of the apparent decrease in rate coefficient, which was attributed to decomposition of the MTBE at high temperatures.

The mean room temperature value for the bimolecular rate coefficient for reaction R 3-18 measured in this work is shown in Table 3-9, along with a summary of literature measurements and their room temperature measurements. The uncertainty in the room temperature rate coefficient from this work is 2σ with an extra 10% of the measured rate coefficient propagated, to allow for the systematic errors associated with the experimental method, and avoid weighting the data towards the small errors produced by global analysis of biexponential decays. Our value for $k_{OH+MTBE}$ ((2.81 $\pm$ 0.32) $\times$ 10^{-12} cm^3 molecule^{-1} s^{-1}) is in good agreement with previous measurements. Considering only the statistical uncertainty ($\pm$ 0.12 at the 2σ level), we measured a slightly lower rate than the majority of the literature values, but are in agreement (within errors) with measurements made by Arif et al. [175], Picquet et al. [178], Teton et al. [179], Smith et al. [131], Cox and Goldstone [177], and Bennett and Kerr [163].
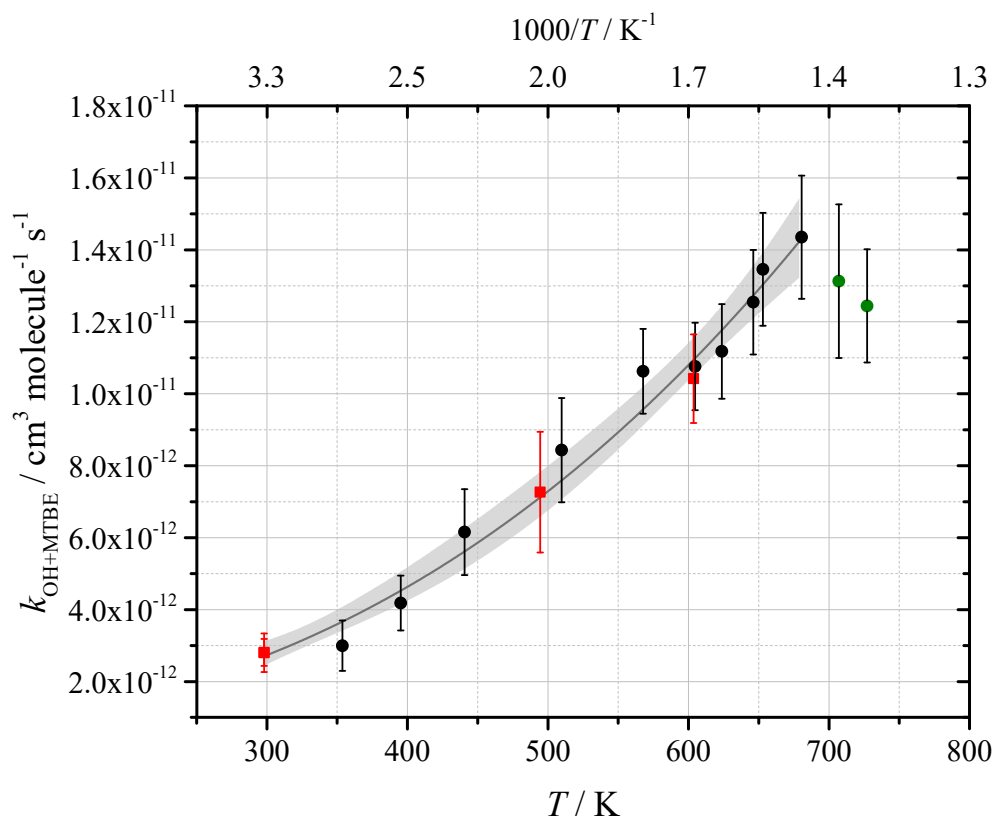
Figure 3-11: This work $k_{OH+MTBE}$ dependence on temperature. Red = 266 nm, black = 248 nm, green data are also 248 nm, but omitted from the Arrhenius parameterisation. $k_{OH+MTBE}(298-680\ K) = (9.8 \pm 21.6) \times 10^{-13}\ (T/298)^{2.7\pm1.5}\ e^{(2.52\pm5.63)/RT}$ cm^3 molecule^{-1} s^{-1}.

The studies by Picquet et al. [178], Smith et al. [131], Cox and Goldstone [177], and Bennett and Kerr [163] all used relative rate techniques, employing reference reactions of the hydroxyl radical with *n*-pentane, *n*-butane, *n*-hexane, and *iso*-butene respectively. Smog chambers were used by Picquet et al., Smith et al., and Bennett and Kerr, where methyl nitrite photolysis was the precursor for OH in the studies by Picquet et al. and Smith et al. Photolysis of hydrogen peroxide at 254 nm and 310 nm was also used by Picquet et al., and Bennett and Kerr photolysed nitrous acid at wavelengths ranging from 350 to 450 nm. Teton et al. [179] reported a bimolecular rate coefficient of $(3.13 \pm 0.36) \times 10^{-12}$ cm^3 molecule^{-1} s^{-1}, measured using flash photolysis – laser-induced fluorescence, where H_2O_2 was the photolytic precursor, and 248 nm the wavelength used. Given the similarity to the technique used in this work, agreement is to be expected, although their absolute value is 11% higher. An updated rate coefficient for the study by Picquet et al. can be calculated based on the latest recommendation for $k_{OH+n\text{-pentane}}$ by Atkinson [168] ($k_{OH+n\text{-pentane}}$ used = 3.96×10^{-12} cm^3 molecule^{-1} s^{-1}, updated $k_{OH+n\text{-pentane}}$ = 3.80×10^{-12} cm^3 molecule^{-1} s^{-1}), where the new room temperature rate coefficient

$k_{OH+MTBE} = (2.86 \pm 0.06) \times 10^{-12}$ cm^3 molecule^{-1} s^{-1}, is in better agreement with this work. The relative rate study by Smith et al. also sees improved agreement after updating their measurements. The value for $k_{OH+n\text{-butane}}$ used was 2.54×10^{-12} cm^3 molecule^{-1} s^{-1}. The latest recommendation by Atkinson [168] yields an updated rate coefficient of $k_{OH+n\text{-butane}}$ $= 2.36 \times 10^{-12}$ cm^3 molecule^{-1} s^{-1}, giving an updated measurement of $k_{OH+MTBE} = (2.78 \pm 0.12) \times 10^{-12}$ cm^3 molecule^{-1} s^{-1}. Bennett and Kerr's work sees slightly worse agreement with the measurements in this chapter, where the temperature-independent reference rate coefficient $k_{OH+DMB} = 6.20 \times 10^{-12}$ cm^3 molecule^{-1} s^{-1} is updated to the temperature dependent recommendation by Atkinson [168], seeing a decrease in OH + MTBE rate coefficients of approximately 15% at the lowest temperatures, and 5% at the highest.

A relative rate study by Wallington et al. [174] does not agree with our measured $k_{OH+MTBE}$ when considering only the statistical uncertainties, and is just outside agreement of the full uncertainty range estimated here. Methyl nitrite photolysis was used to generate the OH radicals, and MTBE was measured relative to the reaction between OH and n-butane. Using the updated value for $k_{OH+n\text{-butane}}$(295 K) recommended by Atkinson [168] since, a value of $k_{OH+MTBE} = (2.97 \pm 0.08) \times 10^{-12}$ cm^3 molecule^{-1} s^{-1} puts the relative rate measurement by Wallington et al. in good agreement with this work. The earlier study by Wallington and co-workers [135] used UV photolysis of H$_2$O at 165 nm coupled to microwave OH resonance to study the reaction, and their reported rate coefficient $k_{OH+MTBE} = (3.09 \pm 0.15) \times 10^{-12}$ cm^3 molecule^{-1} s^{-1} is less than 1% away from our value when statistical uncertainties are accounted for.

Figure 3-12 shows a comparison between $k_{OH+MTBE}$ as a function of temperature in this work, with previous studies. Below approximately 400 K, the values of $k_{OH+MTBE}$ from this work overlap with the measurements of Arif et al. [175] and Bonard et al. [176], however above this temperature higher rate coefficients were measured. Biexponential decays were not observed prior to this work, despite Bonard et al. using H$_2$O$_2$ as their OH precursor, meaning their experiment potentially contained oxygen. The small number of data points (~8 per trace), may have been insufficient to reveal biexponential behaviour. Any unaccounted biexponential behaviour would have resulted in extraction of their pseudo-first order rate coefficients lower than the actual values. An example of the lower value of k' extracted from a single exponential fit to biexponential data can be seen in the reported k' and k_a' values in Appendix A.

Table 3-9: Comparison of the rate coefficient obtained for $k_{\text{OH+MTBE}}$ with previous measurements.

Reference	Technique	$k(298\ \text{K})^a$	$T\ /\ \text{K}$	$k(T)^b$
Bonard et al. (2002)	PLP–LIF	3.05 ± 0.03^c	$297 - 616$	$5.7\times10^{-13}\ (T/298)^{2.4}\ e^{4.15/RT}$
Picquet et al. (1998)	Relative rate	2.98 ± 0.06 *(2.86 ± 0.06)*	298	–
Arif et al. (1997)	LP–LIF	2.98 ± 0.11^d	$293 - 750$	$1.3\times10^{-12}\ (T/298)^{2.0}\ e^{2.21/RT}$
Teton et al. (1996)	PLP–LIF	3.13 ± 0.36	$230 - 371$	$5.0\times10^{-12} \times e^{-1.1/RT}$
Smith et al. (1991)	Relative rate	2.99 ± 0.12 *(2.78 ± 0.12)*	298	–
Bennett and Kerr (1990)	Relative rate	2.84 ± 0.28 *(2.64 ± 0.28)*	$242 - 328$	$4.0\times10^{-12} \times e^{-0.85/RT}$
Wallington et al. (1989)	Relative rate	3.24 ± 0.08^e *(2.97 ± 0.08)*	295	–
Wallington et al. (1988)	UV photolysis–microwave OH resonance	3.09 ± 0.15	$240 - 440$	$5.1\times10^{-12} \times e^{-1.29/RT}$
Cox and Goldstone (1982)	Relative rate	2.51 ± 0.50^e	295	–
Tranter and Walker (2001)	Relative Rate	na	753	$(1.48 \pm 0.22) \times 10^{-11}$
This work	PLP–LIF	2.81 ± 0.32	$298 - 727$	$(9.8\pm21.6)\times10^{-13}\ (T/298)^{2.7\pm1.5}\ e^{2.5\pm5.6/RT}$

^{a}Units are 10^{-12} cm^3 molecule^{-1} s^{-1}. ^{b}Units of A are cm^3 molecule^{-1} s^{-1} and E_a are kJ mol^{-1}. ^{c}Measured at 297 K. ^{d}Measured at 293 K. ^{e}Measured at 295 K. Rate coefficients in italics are based on updated reference reaction rates from reference [168].

Measurements made by Arif et al. [175] were made using photodissociation of N$_2$O at 193 nm, and subsequent reaction of O(^{1}D) with H$_2$O to generate OH radicals. Lower rate coefficients measured by Arif et al. in comparison with this work may be as a result of photolysis of their reactant at the lower wavelength used, or relaxation of excited OH radicals over the duration of a kinetic decay. On the basis of the absorption cross-section of diethyl ether, at room temperature and 193 nm (3.9×10^{-19} cm^2 molecule^{-1} [169]), the estimate of 10^{-21} cm^2 molecule^{-1} for the cross-section of MTBE used by Arif et al. may underestimate the degree of reagent photolysis, particularly at

high temperatures, as cross-sections generally increase with temperature. The degree of MTBE photolysis (<0.5% for a cross-section of 3.9×10^{-19} cm^2 molecule^{-1}) will not cause significant MTBE depletion in a single photolysis pulse. However, if the reaction mixture is subject to several photolysis pulses and/or the cross-section is larger at higher temperatures, then MTBE depletion could be significant. Additionally, there would be a significant extra radical pool from MTBE photolysis and there may therefore have been radical-radical reactions present that could have affected the OH kinetics. However, Arif et al. reported no variation in rate coefficients as the photolysis laser intensity was changed, suggesting that such effects were not present, although the temperatures at which such checks were made was not stated.
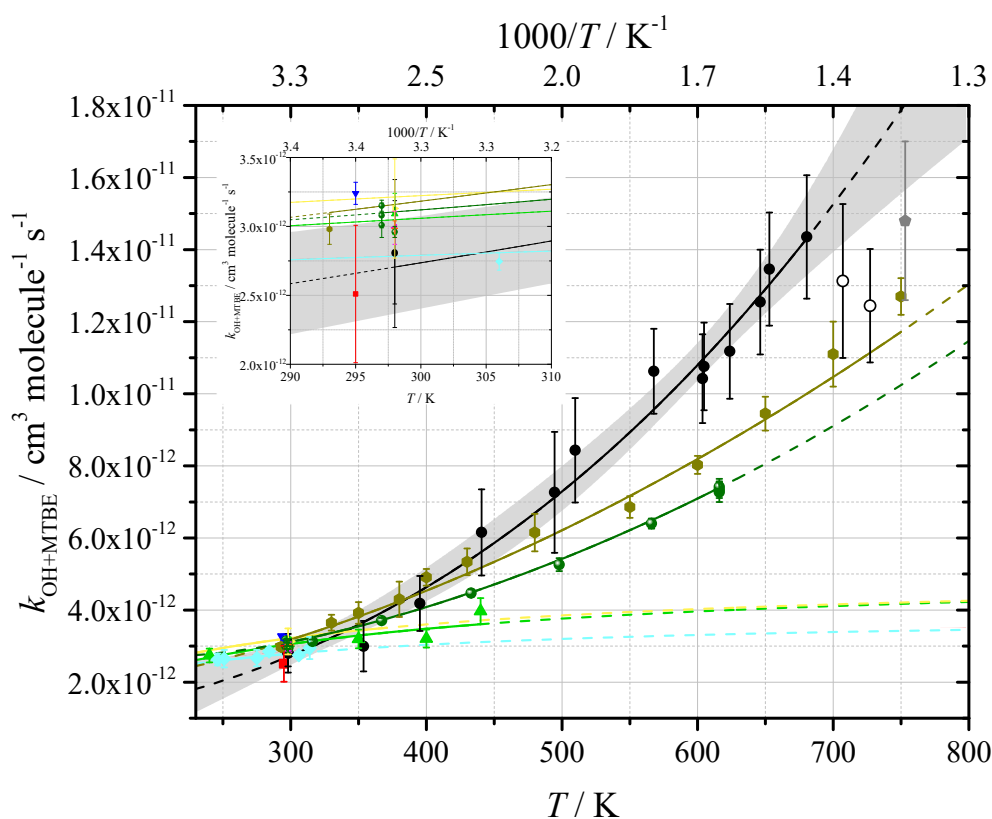
Figure 3-12: $k_{OH+MTBE}$ **measured in this work (●, hollow=masked in fit), with a modified Arrhenius fit (excluding the highest two temperatures), where the 95% confidence bounds are shown in grey shading. The black dashed line shows the Arrhenius parameterisation extrapolated past the experimental conditions of this work. Uncertainties are 2σ with an additional 10% of the value to account for systematic errors. The literature studies, and their Arrhenius parameterisations where relevant, are Cox and Goldstone (1982) (■), Wallington et al. (1988) (▲), Wallington et al. (1989) (▼), Bennett and Kerr (1990) (◆), Smith et al. (1991) (◄), Teton and Mellouki (1996) (►) (only fit and room temperature data provided in paper/SI, no temperature dependent data), Arif et al. (1997) (●), Picquet et al. (1998) (★), Tranter and Walker (2001) (●), and Bonard (2002) (●).**

Explorations of the temperature-dependent behaviour of the OH + MTBE reaction over ranges less comparable to this work were presented in the studies already described by Teton et al. [179], Wallington et al. [135], and Bennett and Kerr [163]. Figure 3-12 shows the Arrhenius parameterisations of these studies, extrapolated to higher temperature comparable with this study. All three temperature dependences exhibit remarkably similar behaviours, where the rate coefficient is under predicted as a result of the lack of a modified exponential temperature term (Table 3-9). This is not surprising given the limited temperature ranges explored (230 – 371, 240 – 440, and 242 – 328 K respectively).

A value of $k_{OH+MTBE}$ = (1.48 ± 0.22) × 10^{-11} cm^3 molecule^{-1} s^{-1} at 753 K was determined by Tranter and Walker [132] using relative rate methods, with the OH + H_2 reaction as a reference. This value is in good agreement with the current work.

There is slight evidence of a negative temperature dependence around room temperature for $k_{OH+MTBE}$ measured here, but not so pronounced as for the DBE and TMOF systems. Bennett and Kerr [163] studied reaction R 3-18 using a relative rate technique from 246 – 314 K finding a slight positive temperature dependence (E_a = 0.85 ± 0.59 kJ mol^{-1}) although for diethyl ether and several other larger ethers, a negative temperature dependence was observed.

Presented in Figure 3-13 is the modified Arrhenius expression for OH + MTBE hydrogen abstraction employed by Yasunaga et al. [127] to validate data on MTBE oxidation from their shock tube measurements. To our knowledge, these are the only data on reaction R 3-18 above ~750 K. Yasunaga et al. used group additivity rate coefficient estimates based on H abstraction from other molecules, such as DME, ethyl methyl ether, *iso*-propyl methyl ether, and methyl cyclohexane. Although this expression was only used to validate experiments over the range 900 – 1600 K, when it is extrapolated back over a relatively short temperature range to the highest temperatures of this work and Arif et al. [175], the extrapolated values are approximately a factor 2 lower (Figure 3-13). Yasunaga et al. report that unimolecular decomposition reactions of MTBE dominate the chemistry and hence an underestimation of $k_{OH+MTBE}$ will have a limited effect on their model:measurement comparison.
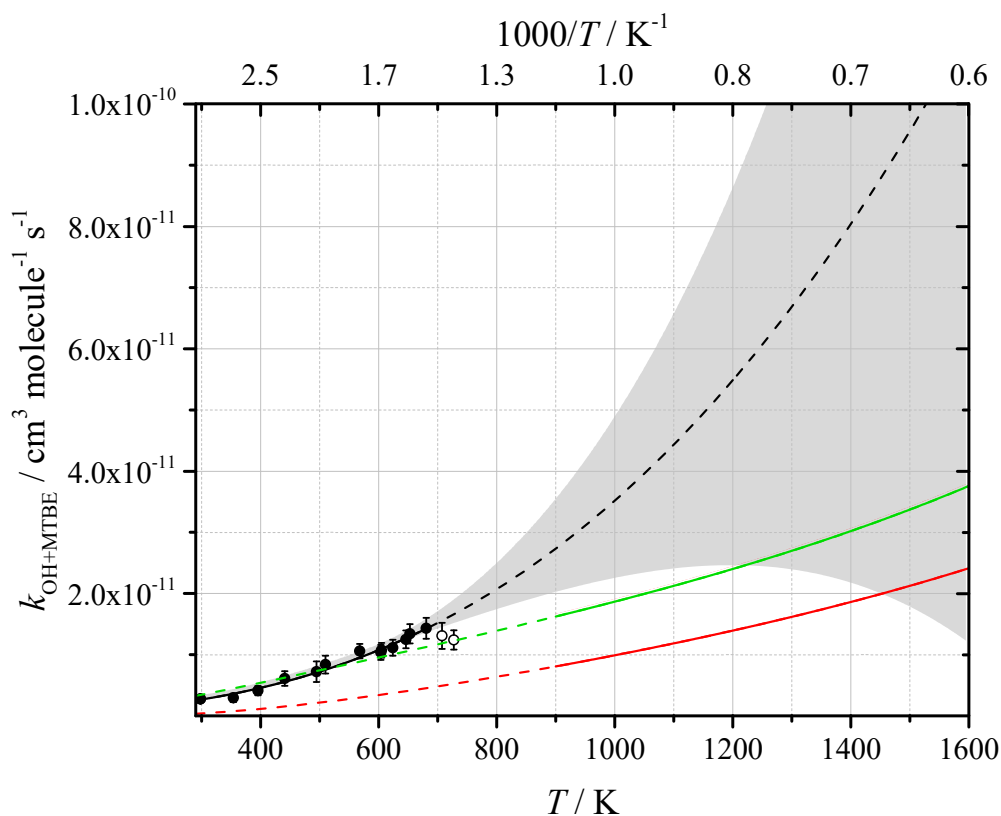
Figure 3-13: Comparison of measured $k_{OH+MTBE}$ with Yasunaga et al. [127], red line as they report their Arrhenius parameterisation. The modelled modified Arrhenius expression used by Yasunaga et al. is shown for their validated temperature range (red) and extrapolated to lower temperatures (red dashed). The green line represents the Arrhenius expression if the gas constant used in the fit is J mol^{-1} K^{-1} rather than cal mol^{-1} K^{-1}.

A second Arrhenius expression is present in Figure 3-13, where the green line represents the fit reported by Yasunaga et al. [127] if the gas constant used in the fit is expressed in J mol^{-1} K^{-1}, rather than the units of cal mol^{-1} K^{-1} suggested in their model. This correction causes their expression to line up remarkably well with our data and other studies, so it is possible this was intended. It is not certain whether this is the case, or it is merely coincidental.

3.8   OH + Dimethyl Ether

There has been considerable interest in the use of dimethyl ether as a biofuel additive and standalone fuel, owing to its good cetane rating [34, 38] and lack of soot emissions [38]. The reaction between the hydroxyl radical and DME (reaction R 3-20) is the initial step in its low temperature combustion mechanism (when initiated by OH, rather than another small molecule) which gives rise to the autoignition of the fuel in a

low temperature engine. Further reactions involving the addition of O_2 will ultimately lead to chain-branching and combustion (see Chapter 6 for further details and experiments).

$$CH_3OCH_3 + OH \rightarrow CH_3OCH_2 + H_2O \qquad\qquad R\ 3\text{-}20$$
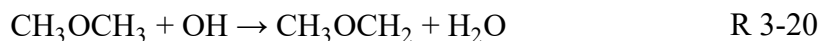
As the simplest ether, possessing only one unique abstraction site (Scheme 3-6), two methyl groups, and one oxygen, OH + DME was a good reaction to study initially, for later comparison with higher ethers. Reaction R 3-20 has been studied over an extensive temperature range previously in the literature, where techniques, the majority of which are flash photolysis or relative rate studies [113, 132, 134, 136, 137, 165, 174-176, 185-187], have characterised the temperature dependence up to 800 K, and a shock tube study has been used to observe the reaction at higher temperatures (923 – 1523 K) [126]. All previous studies are summarised in Table 3-11. In this chapter, reaction R 3-20 has been measured, and is generally in reasonable agreement with the previous studies. Thus, work in this section was able to verify that the experimental setup possessed no major issues, allowing the study to proceed with reactions involving higher, lesser studied, ethers, and more complex reactions.
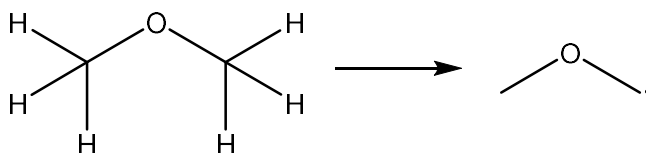
Scheme 3-6: Identical hydrogen abstraction sites possible for dimethyl ether reaction with OH, and the R radical formed.

3.8.1 OH + CH$_3$OCH$_3$ Temperature Dependence

The bimolecular rate coefficient for the reaction between dimethyl ether and the hydroxyl radical has been measured under pseudo-first order conditions, where the concentration of OH was controlled by reaction R 3-20. A typical pseudo-first order decay was presented in the kinetic trace in section 3.3 in Figure 3-1. Analysis of the OH decay rate at varying concentrations of dimethyl ether to give k'_{OH+DME}, and least squares linear fitting of these pseudo-first order rate coefficients as a function of [DME], for a given

temperature and pressure, provides the bimolecular rate coefficient k_{OH+DME}. Three examples of typical bimolecular plots are displayed in Appendix A (Figure A 11).

At 523 K to 634 K, kinetic decays exhibited biexponential behaviour, indicating recycling of OH radicals. Oxygen present in the system due to decomposition of H_2O_2 is likely the source of this OH, combining with methyl methoxy radicals in reaction R 3-21.
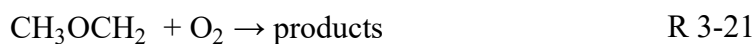
$$CH_3OCH_2 + O_2 \rightarrow products \qquad\qquad R\ 3\text{-}21$$

Observation of biexponential decays is highly dependent on temperature and concentrations of oxygen and fuel. As such, there were occasionally traces within the temperature range quoted above that exhibited normal exponential behaviour, rather than biexponential. Similarly, the highest two temperatures explored in this study – 671 K and 673 K – were single exponential decays. Regardless, this should have no effect on the ability to extract the pseudo-first order rate coefficient from a kinetic trace. An example biexponential decay with fitting is shown in Appendix A.

The temperature dependence of reaction R 3-20 has been investigated, with rate coefficients measured between 25 and 57 Torr of pure N_2, between 298 and 673 K, and hydrogen peroxide was the photolytic precursor. A plot of the rate coefficient as a function of temperature is shown in Figure 3-14, and all values of k_{OH+DME} are displayed in Table 3-10. Previous measurements by other studies are included in Figure 3-15.

The mean room temperature rate coefficient taken from three measurements was $(2.66 \pm 0.09) \times 10^{-12}$ cm^3 molecule^{-1} s^{-1}, where the error quoted in the measurement refers to a purely statistical uncertainty at the 2σ level. The fit to the data as a function of temperature in Figure 3-14 used the three individual room temperature k_{OH+DME} values, rather than the calculated mean.

Table 3-10: Bimolecular rate coefficients obtained for OH + DME. Uncertainties are purely statistical at the 2σ level.

T / K	$10^{12}\,k_{\text{OH+DME}}{}^{a}$	n	10^{-14} [DME] range^{b}	P / Torr
298	2.63 ± 0.13	6	3.6 – 14.2	50
298	2.71 ± 0.09	5	3.4 – 11.8	57
298	2.65 ± 0.23	5	2.7 – 12.0	57
419	3.18 ± 0.15	6	2.1 – 10.1	57
475	3.46 ± 0.19	6	1.8 – 8.7	57
523	5.19 ± 1.49	4	1.7 – 6.8	57
543	5.36 ± 0.72	5	1.7 – 6.7	57
545	5.86 ± 0.85	7	2.3 – 8.9	38
546	6.73 ± 1.14	4	1.9 – 7.2	57
574	6.28 ± 1.24	4	1.6 – 6.4	57
590	6.41 ± 0.30	4	2.9 – 10.8	57
590	7.06 ± 0.93	4	1.7 – 6.5	57
594	6.41 ± 0.11	6	1.6 – 6.4	57
605	7.22 ± 0.50	4	1.1 – 8.1	25
629	8.64 ± 1.3	4	1.6 – 6.0	57
634	8.11 ± 0.72	4	1.4 – 5.6	57
656	8.41 ± 2.19	4	1.4 – 5.5	57
671	6.47 ± 0.54	8	1.4 – 5.4	57
673	6.89 ± 0.70	6	1.5 – 5.3	57

^{a}Units of cm^{3} molecule^{-1} s^{-1}. ^{b}Units of molecule cm^{-3}. n refers to the number of experiments comprising a bimolecular determination.

Plotting the obtained bimolecular rate coefficients for the reaction between DME and the hydroxyl radical as a function of temperature shows a strong positive temperature dependence above approximately 450 K. The modified Arrhenius fit to the data in Figure 3-14 can be described by $k_{\text{OH+DME}}(298-656\text{ K}) = (1.22 \pm 1.83) \times 10^{-15} \left(\frac{T}{298}\right)^{(6.88\pm1.08)} \times$

$e^{\frac{(19.07\pm3.82)}{RT}}$ cm^{3} molecule^{-1} s^{-1}. The uncertainties reported are statistical at the 2σ level, and the maximum uncertainty of the 95% confidence limits across the temperature range valid for this parameterisation is 7%. The two hollow data points in Figure 3-14 were omitted from the fit to the data, where unusually slow rate coefficients were measured. It is possible this was a result of decomposition of the fuel in the reaction cell at high temperatures, resulting in lower DME concentrations than calculated, and therefore a

slower observed removal rate of OH radicals. This was seen by Arif et al. [175] studying the same reaction, at approximately the same temperature, and their suggestion was also decomposition of their fuel.
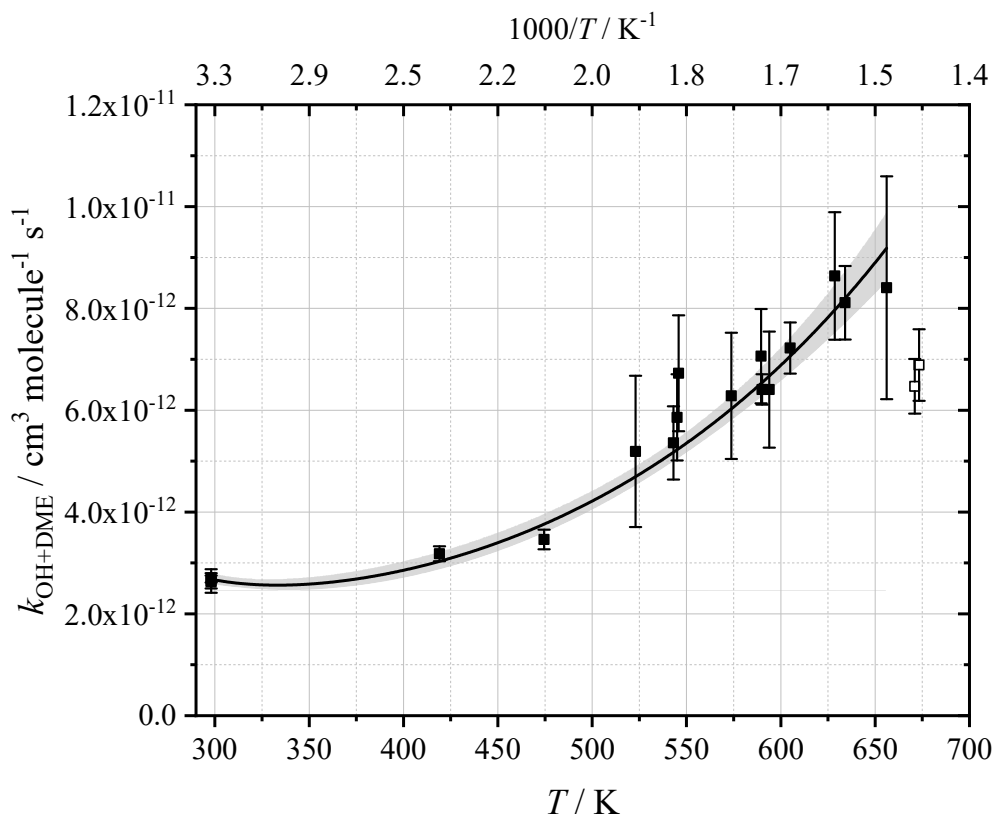
Figure 3-14: Measured bimolecular rate coefficient (●) for the OH + DME reaction as a function of temperature. The black line represents the best fit of a modified Arrhenius parameterisation where k_{OH+DME}(298 − 656 K) = (1.22 ± 1.83) × 10⁻¹⁵ $(T/298)^{6.88±1.08}$ $e^{(19.07±3.82)/RT}$ cm³ molecule⁻¹ s⁻¹. Hollow data at high temperature are omitted from the fit, the grey boundaries are the 95% confidence limits, and error bars represent statistical uncertainties at the 2σ level.

Figure 3-15 compares the temperature dependence of the OH + DME rate coefficient measured in this work with previous studies, and all previous works are summarised in Table 3-11. Relative rate studies by Wallington et al. [174] and Nelson et al. [137] found room temperature rate coefficients (highlighted in Figure 3-16) k_{OH+DME} = (2.32 ± 0.23) and (3.19 ± 0.70) × 10⁻¹² cm³ molecule⁻¹ s⁻¹ respectively, both in, or very close to, agreement with the rate coefficient measured in this work. Wallington et al. used methyl nitrite photolysis, and made measurements relative to the reaction between OH and n-butane. Updating the reference rate coefficient used ($k_{OH+n\text{-butane}}$ = 2.53 × 10⁻¹² cm³ molecule⁻¹ s⁻¹) to the latest recommended by Atkinson [168] ($k_{OH+n\text{-butane}}$ = 2.32 × 10⁻¹²

cm^3 molecule^{-1} s^{-1}), gives a new value of $k_{OH+DME} = (2.13 \pm 0.23) \times 10^{-12}$ cm^3 molecule^{-1} s^{-1} placing their measurement further from agreement with this work's. Nelson et al. used the same photolytic precursor, as well as H_2O_2 ($\lambda = 254$ nm), and employed OH + cyclohexane as the reference reaction. The uncertainty quoted and included in Figure 3-15 includes the extra 25% suggested by the authors. An update to the reference rate coefficient used ($k_{OH+cyclohexane} = 7.49 \times 10^{-12}$ cm^3 molecule^{-1} s^{-1}) to the latest recommended by Atkinson [168] ($k_{OH+cyclohexane} = 6.97 \times 10^{-12}$ cm^3 molecule^{-1} s^{-1}), gives a new value of $k_{OH+DME} = (2.97 \pm 1.44) \times 10^{-12}$ cm^3 molecule^{-1} s^{-1}, still in agreement with this work. Nelson et al. also made an absolute measurement of k_{OH+DME} ($(2.35 \pm 0.24) \times 10^{-12}$ cm^3 molecule^{-1} s^{-1}) using pulse radiolysis of Ar/H$_2$O mixtures coupled to UV spectroscopy.
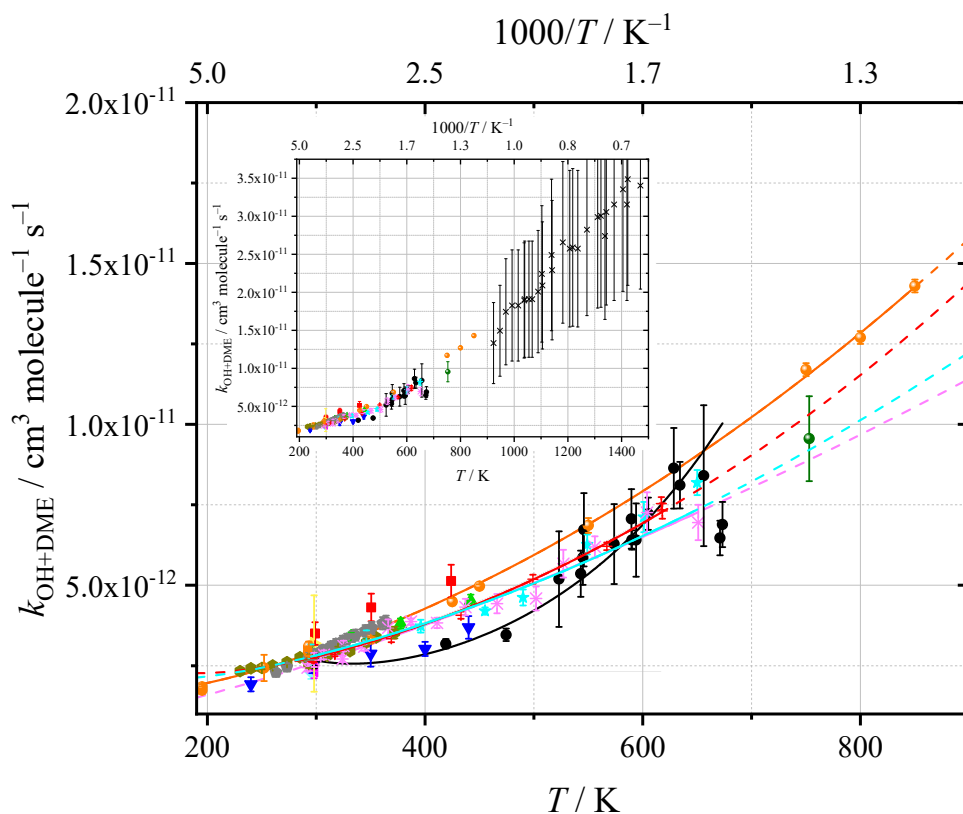
Figure 3-15: Comparison of k_{OH+DME} measured in this work (●) with previous literature measurements. Symbols represent Perry et al. (1977) (■), Tully and Droege (1987) (▲), Wallington et al. (1988) (▼), Wallington et al. (1989) (◆), Nelson et al. (1990) absolute (◄), Nelson et al. (1990) relative (►), Mellouki and Teton (1995) (●), Arif et al. (1997) (★), DeMore and Bayes (1999) (⬠), Tranter and Walker (2001) (●), Bonard et al. (2002) (+), Bansch and Olzmann (2013) (✳), Carr et al. (2013) (●). The inset shows the full range at high temperature including Cook et al. 2009 (×). Uncertainties in this work represent statistical errors at the 2σ level, and literature uncertainties are as reported/suggested by the authors.
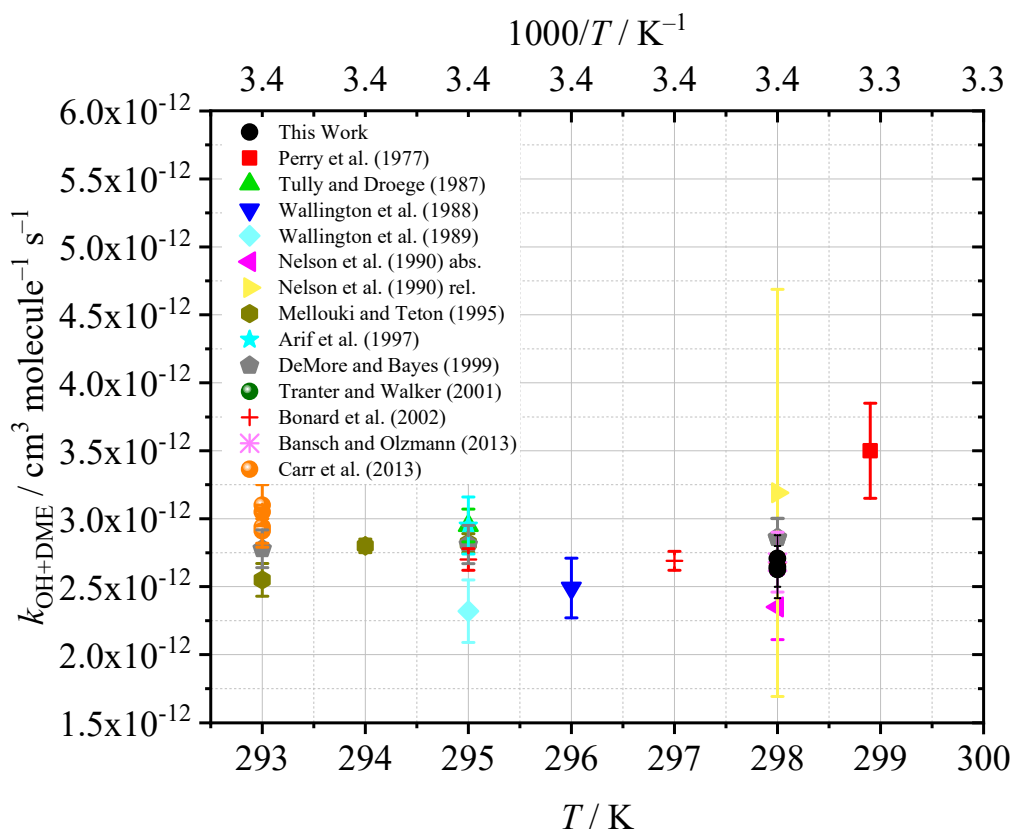
Figure 3-16: Comparison of k_{OH+DME} rate coefficients measured in the literature (legend) with this work (●), ~298 K. Uncertainties in this work represent statistical errors at the 2σ level, and literature uncertainties are as suggested by the authors.

Narrow temperature ranges up to approximately 440 K were explored in studies by Perry et al. [134], Tully and Droege [165], Wallington et al. [136], Mellouki et al. [113] and DeMore and Bayes [187]. The flash photolysis – resonance fluorescence technique used by Wallington et al. involved photolysis of H_2O to generated OH radicals, where the wavelength used was >165 nm. The room temperature measurement reported in their study was $k_{OH+DME} = (2.49 \pm 0.22) \times 10^{-12}$ cm^3 molecule^{-1} s^{-1}, in good agreement with this work's, and the positive temperature dependent behaviour appears to align well with that reported here. These studies by Perry et al., Tully and Droege, Mellouki et al. and DeMore and Bayes all exhibited higher rate coefficients across their studied temperature ranges in comparison to our study, barring the room temperature k_{OH+DME} reported by Mellouki et al. which shows agreement within uncertainties. Perry et al. used flash photolysis – resonance fluorescence with photolysis of H_2O ($\lambda > 105$ nm) to study the reaction across the temperature range 299 – 427 K. Wavelengths this short could certainly subject dimethyl ether to some degree of photolysis, particularly at high temperatures, (DME $\sigma = 5 \times 10^{-17}$ cm^2 molecule^{-1} at 105 nm [188], 9.8×10^{-18} cm^2 molecule^{-1} at 165 nm [169], both at room temperature. Typically absorption cross

sections increase with temperature), which may have been the source of unwanted radical-radical reactions interfering with the removal of OH. However, Perry et al. reported no variation in rate coefficients when the photolysis laser energy was varied by a factor of two. Similarly, the photolysis of N_2O to $O(^1D)$ in the presence of water was employed as the photolytic OH generation method by Tully and Droege, where the laser wavelength needed was 193 nm. In the flash photolysis – laser-induced fluorescence experiment used, this likely also contributed to reactant photolysis and potential extraneous reactions, resulting in a faster rate coefficient. At higher temperatures, the authors saw non-exponential decays, where the initial decay portions were weakly dependent on laser energy. These decays were not reported, but the dependence on laser energy may suggest some photolysis took place.

Despite the potential for issues with the studies described above, the work by Mellouki et al. [113] also observed a faster rate coefficient than reported here above room temperature, however the technique used was identical to this work; pulsed laser photolysis – laser-induced fluorescence, with 248 nm photolysis of the hydrogen peroxide photolytic precursor. As such, there is no obvious reason for a discrepancy between the two studies. Finally, DeMore and Bayes [187] studied reaction R 3-20 from 263 K to 364 K, using a relative rate technique where n-butane, n-pentane and cyclohexane were all employed as reference compounds, and ethane was the ultimate reference used for those. Photolysis of H_2O at 254 nm provided the source of OH radicals at temperatures comparable to this chapter, so no significant photolysis of DME is expected to have occurred. Adjustment of the reference rate coefficient used (at 298 K $k_{OH+ethane} = 2.54 \times 10^{-13}$ cm^3 molecule^{-1} s^{-1}) to the latest recommended by Atkinson [168] (at 298 K $k_{OH+ethane} = 2.48 \times 10^{-13}$ cm^3 molecule^{-1} s^{-1}), yields a new value of $k_{OH+DME} = (2.79 \pm 0.14) \times 10^{-12}$ cm^3 molecule^{-1} s^{-1} placing their measurement just in agreement with this work's. The updated values make only a minor adjustment across the entire temperature range.

Between 400 and 500 K, the limited number of rate coefficients measured in this work are noticeably slower than the data available in the literature. It is possible that a significant recycling of OH could yield single exponential decays (rather than biexponential), where the returned pseudo-first order rate coefficient is significantly slower, and the difference between the true rate and the measured rate would give the OH yield (see section 5.4 in Chapter 5 for a detailed description of this method). However, it is not immediately clear why such an extreme recycling rate would occur at such temperatures and low oxygen concentrations, so this is unlikely.

Table 3-11: Comparison of the rate coefficient obtained for k_{OH+DME} with previous measurements.

Reference	Technique	k(298 K)^a	T / K	$k(T)^b$
Mellouki et al. (1995)	LFP-LIF	2.82 ± 0.07^e	230 – 372	$6.38 \times 10^{-12} \times e^{-1.95/RT}$
Arif et al. (1997)	LP-LIF	2.95 ± 0.21^e	295 – 650	$1.05 \times 10^{-17} \times T^2 \times e^{2.73/RT}$
Nelson et al. (1990)	Pulse radiolysis – UV spec.	2.35 ± 0.24	298	–
Nelson et al. (1990)	Relative rate	3.19 ± 0.70 *(2.97 ± 1.44)*	298	–
Wallington et al. (1989)	Relative rate	2.32 ± 0.23^e *(2.13 ± 0.23)*	295	–
Wallington et al. (1988)	UV photolysis-microwave OH resonance	2.49 ± 0.22^c	296 – 440	$6.7 \times 10^{-12} \times e^{-2.49/RT}$
Perry et al. (1977)	Flash photolysis-resonance fluorescence	2.95 ± 0.12^d	299 – 424	$1.29 \times 10^{-11} \times e^{-0.77/RT}$
Tully and Droege (1987)	LFP-LIF	2.95 ± 0.06^e	295 – 442	$1.04 \times 10^{-11} \times e^{-3.09/RT}$
Tranter and Walker (2001)	Relative rate	na	753	$(9.56 \pm 1.32) \times 10^{-12}$
DeMore and Bayes (1999)	Relative rate	2.86 ± 0.14 *(2.79 ± 0.13)*	263 – 364	$1.51 \times 10^{-11} \times e^{-4.12/RT}$
Bonard et al. (2002)	PLP-LIF	2.67 ± 0.07	295 – 618	$4.59 \times 10^{-19} T^{2.46} \times e^{3.96/RT}$
Cook et al. (2009)	Shock tube	na	923 – 1523	na
Carr et al. (2013)	LFP-LIF	3.00 ± 0.06^f	195 – 800	$1.23 \times 10^{-12} (T/298)^{2.05} \times e^{-2.14/RT}$
Bansch and Olzmann (2013)	LFP-LIF	2.68 ± 0.22	292 – 651	$4.50 \times 10^{-16} T^{1.48} \times e^{0.55/RT}$
This work	LFP-LIF	2.66 ± 0.09	298 –656	$(1.22 \pm 2.83) \times 10^{-15} (T/298)^{(6.88 \pm 0.50)} \times e^{(19.07 \pm 3.82)/RT}$

^{a}Units are 10^{-12} cm^3 molecule^{-1} s^{-1}. ^{b}Units of A are cm^3 molecule^{-1} s^{-1} and E_a are kJ mol^{-1}. ^{c}Measured at 296 K. ^{d}Measured at 299 K. ^{e}Measured at 295 K. ^{f}Measured at 293 K. Measurements in italics are based on updated reference reaction rates from reference [168].

Most pertinent for comparison to our measurements are the studies with fitted Arrhenius parameterisations included in Figure 3-15, where the full temperature ranges

explored were similar to that of this work. Fits to the narrower previous temperature explorations discussed above were not included, for clarity's sake in the figure. The following studies all used laser flash photolysis – laser-induced fluorescence to explore a wide range of temperatures. In these studies, Bansch and Olzmann [185] employed photolysis of HNO_2 at 248 nm to generate OH radicals at 292 – 651 K. Arif et al. [175] photolysed N_2O at 193 nm in the presence of H_2O from 295 – 650 K. Bonard et al. [176] used photolysis of H_2O_2 across the temperature range 295 – 618 K, where the photolysis wavelength was 266 nm. Carr et al. [186] previously studied OH + DME at the University of Leeds from 195 to 850 K, and made use of three photolytic precursors: t-BuOOH (λ = 248 nm), acetone/O_2 (λ = 248 nm), and N_2O/H_2O (λ = 193 nm). All studies described here are in qualitative agreement with the positive temperature dependence of k_{OH+DME} reported in this work, but generally exhibited a faster rate coefficient below ~500 K. Bonard et al. and Bansch and Olzmann, however, were both in agreement with our measurement at room temperature, whereas Carr et al. and Arif et al. both measured approximately 10% faster rate coefficients. Between this temperature and approximately 500 K, the two rate coefficients reported here underestimated all four extensive literature studies, but above this temperature, agreement is found again when considering the error bars. Higher than 650 K, this work's modified Arrhenius parameterisation appears to begin exhibiting a much more pronounced positive temperature dependence than the previous studies, however, it is not unreasonable to envisage how our fit could follow the same trend observed by Bonard et al. and Carr et al., and an extrapolation would be subject to large uncertainties. There is likely to be some error in the measurement of temperature, particularly with the experiments conducted by Carr et al., where a very similar setup was used to that in this work. Since their study, we have demonstrated that correction factors are required to compensate thermocouple readings for flow within the reaction cell (see Chapter 2). However, the flow rates used are not known, and their experiments were carried out in He, so a temperature correction may not be significant.

Tranter and Walker [132] used a relative rate method, with H_2 + OH as the reference reaction to study k_{OH+DME} at 753 K, measuring $(9.56 \pm 1.32) \times 10^{-12}$ cm^3 molecule^{-1} s^{-1}. There is no updated recommended rate coefficient for the H_2 + OH reaction at the relevant temperature. Considering the error bars, an extrapolation of this work (Figure 3-15) would be approximately 15% faster at this temperature. One shock tube study has been carried out by Cook et al. [126], where t-BuOOH was used as the source of OH radicals, and the reaction was monitored at 307 nm from 947 – 1423 K. The

data from this study are shown in the inset to Figure 3-15. The error bars represent 40% of the values, which was estimated by the authors to be a reasonable consideration of the overall uncertainty in the measurements. As a result, all studies could conceivably pass through the data reported by Cook et al. at these temperatures, and no real confidence could be placed in an extrapolation of the measurements made in this work to such high temperatures.

3.9 Comparison of Ethers

Comparisons between the five ethers studied in this chapter can be drawn, where Figure 3-17 displays the behaviour of all OH + ether rate coefficients as a function of temperature. A straightforward comparison for the different molecules, are the rate coefficients at room temperature. As expected, with increasing chain length, the three straight-chained symmetrical ethers exhibit an increasing OH + ether rate coefficient as more sites are available for hydrogen abstraction. Thus, the slowest rate coefficient is that of OH + DME; OH + DEE is approximately five times faster, and DBE is three times as fast again ($k_{OH+ether}$ = (2.66 ± 0.09), (12.6 ± 1.1) and (39.2 ± 1.3) × 10^{-12} cm^3 molecule^{-1} s^{-1} respectively). Evidently, the increase in rate coefficient magnitude is not proportional to the changing number of potential abstraction sites, where they double from DME to DEE, and again to DBE. An extension of the activation effect the ether –O– group exhibits over at least three –CH$_2$– groups likely gives rise to this behaviour [189].

MTBE and TMOF show different behaviour, with more marginal increases on the OH + DME rate coefficient being apparent. Despite possessing the same number of carbon abstraction sites as diethyl ether (4), MTBE's *t*-butyl groups' hydrogens are not activated through close proximity to the oxygen. Only the single methyl site adjacent to the oxygen will benefit from the donated electron density. As a result, the rate coefficient for OH + MTBE at 298 K is very similar to that of the dimethyl ether system (2.81 ± 0.32) × 10^{-12} cm^3 molecule^{-1} s^{-1}. Trimethyl orthoformate has the same number of abstraction sites available, but exhibits a faster reaction rate coefficient ((4.65 ± 0.50) × 10^{-12} cm^3 molecule^{-1} s^{-1}) as a result of the increased number of oxygen atoms. Three methyl groups are adjacent to O atoms, and the lone hydrogen attached to the central carbon is activated through proximity to all three O atoms.

A comparison of the temperature dependence of the straight chain ethers shows the progression of a positive dependence, to flat, to negative, from DME to DEE to DBE

respectively. Mellouki et al. [189] noted that the temperature dependence of mono ethers becomes negative as the reactivity increases. The positive temperature dependence of the more complex MTBE and TMOF molecules is possibly as a result of the sites not favoured at room temperature (the $(CH_3)_3$ and $(CH_3O)_3$ groups respectively) becoming more reactive as the temperature is increased.
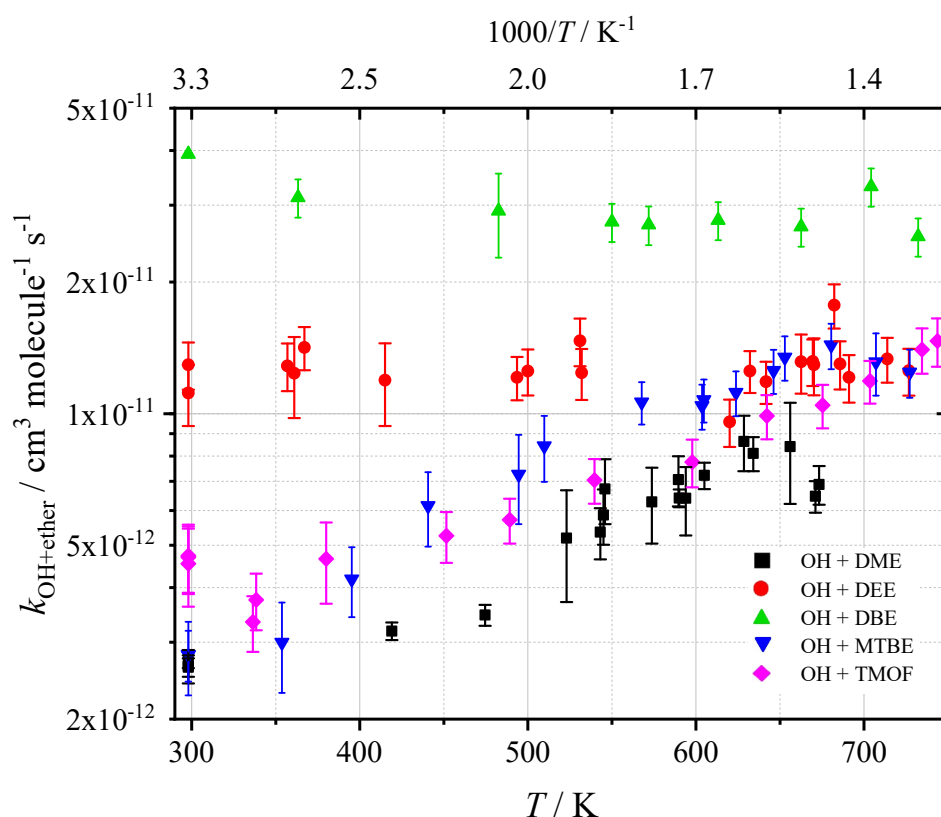
Figure 3-17: Temperature dependent behaviour of the reactions between the hydroxyl radical and DME (■), DEE (●), DBE (▲), MTBE (▼), and TMOF (◆).

Figure 3-18 presents a comparison of the data presented in this chapter with temperature dependent predictions of $k_{OH+ether}$ using the structure-activity relationship (SAR) parameters reported by Kwok and Atkinson [190] to predict the reactivity of gas-phase organic compounds. For DME and MTBE the SAR calculated rate coefficients reproduce the qualitative behaviour of the temperature dependences well, and for DEE there is a slight negative and positive temperature dependence which were not seen in this work's measurements. The prediction for DBE under-predicts the rate coefficient measured here close to room temperature, and then over-predicts k_{OH+DBE} above 550 K as a result of the positive temperature dependence arising from the calculations, which should be valid from 250 – 1000 K. Porter et al. [153] attributed the deviations of OH +

ether reactions from a simple SAR to the long-range activating effects that ether groups exhibit. The largest discrepancy between the SAR parameterisation and the experimental measurements is for the reaction between OH and TMOF, where the inset to Figure 3-18 shows a large over-estimation of $k_{OH+TMOF}$ at room temperature, and the opposite temperature dependence to that observed here. The presence of three oxygen atoms causes this poor agreement, where Kwok and Atkinson noted poly-ethers have particularly bad agreement, and poor agreement for di-ethers has also been observed previously by Porter et al. [153] through the study of dimethoxy methane. As a tri-ether, the issue is exacerbated with TMOF.
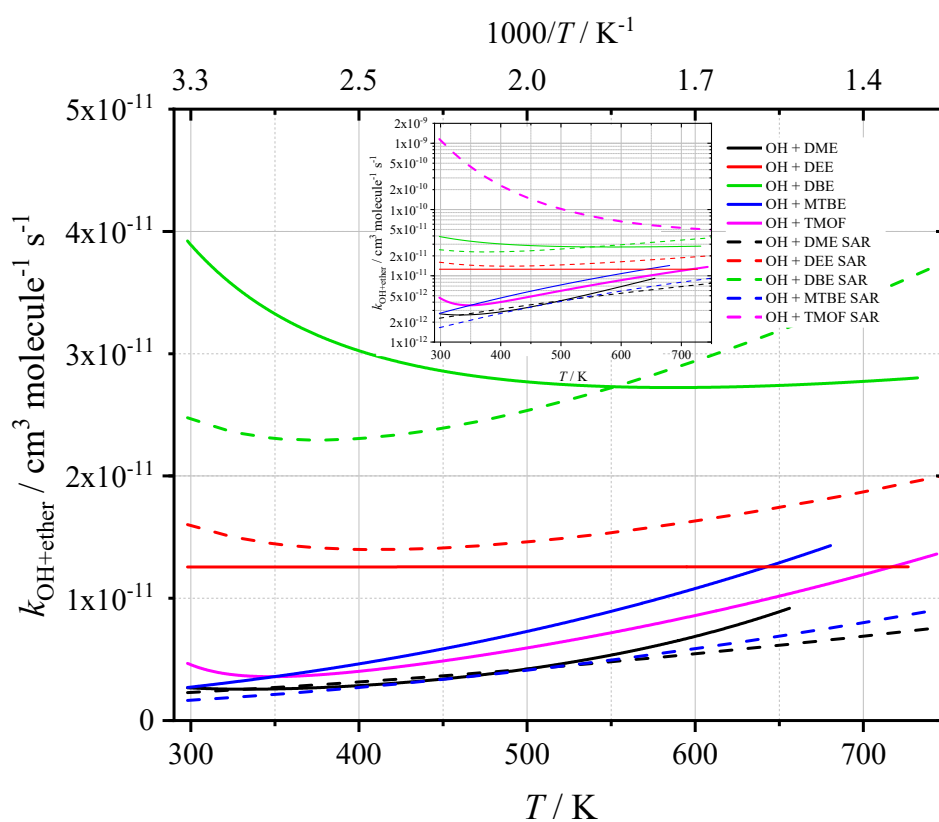
Figure 3-18: Comparison of OH + ether temperature dependences measured in this work with SAR predictions by Kwok and Atkinson [190]. Inset shows the full range of $k_{OH+ether}$ to incorporate the SAR prediction for OH + TMOF.

3.10 Conclusions

The first temperature-dependent study of the rate coefficient for OH + TMOF has been carried out between 298 and 744 K. A similar study between 298 and 727 K was conducted for OH + MTBE, and OH + DEE, where the study of DEE provided new measurements of the rate coefficient between approximately 450 to 750 K. Similarly, new rate coefficients were provided for the reaction between OH and DBE at temperatures from ~370 to 732 K. A study of the simplest ether, DME, and its reaction with OH, was also carried out from 298 – 673 K, and validated through comparison with previous studies, where reasonable overall agreement was found. For DEE, reasonable agreement with the literature was observed, although no temperature dependence was measured over the temperature range studied, whereas previous studies carried out over lower temperature ranges reported a negative temperature dependence. Measurements carried out at an early stage of this thesis, for the DME and DEE reactions, were subject to a less well-optimised experimental setup, where lower quality signal and a less leak-tight experiment all likely contributed to lower quality data. These experiments were not deemed important enough to revisit at the time, rather, chemistry that is more complex was explored (in later chapters). Future work revisiting these reactions, in particular the novel temperature range explored for DEE, may be of interest.

In general, the rate coefficients measured for OH + MTBE displayed reasonable agreement with previous studies, although they were slightly faster at higher temperatures, for which a rationale was provided. Across the whole temperature range for which the reaction between OH and DBE was studied, the rate coefficients reported here were faster than those previously measured, and this was attributed to possible difficulties with bulb composition accuracies as a result of the ether's low vapour pressure. Finally, the study of OH + TMOF displayed good agreement with the limited data available for comparison.

Signs of increasing rate coefficient at lower temperatures were also observed for TMOF, and possibly the onset of this for MTBE, where these effects have already been measured for DME and DEE, indicating pre-reaction complex formation. OH + DBE displayed this behaviour very clearly below ~350 K.

Chapter 4 A Generic Method for Determining R + O$_2$ Rate Parameters via Measurements of OH Regeneration using the CH$_3$OCH$_2$ + O$_2$ Reaction

4.1 Abstract

This chapter reports a new method for determining rate parameters from chemical activation using an OH precursor and the fuel, circumventing the need for a photolytic R radical precursor. Using analysis of the biexponential decays generated by OH regeneration that follows initiation via OH + RH, rate coefficients and OH yields are determined for the R + O$_2$ reaction, where the CH$_3$OCH$_2$ + O$_2$ reaction in the DME low temperature oxidation mechanism is the example studied here.

The rate coefficient $k_{CH3OCH2+O2}$ is reported at 291 – 483 K, in 4.1 – 32.6 Torr of nitrogen. At room temperature, $k_{CH3OCH2+O2}$ = (0.94 ± 0.04) × 10^{-11} cm^3 molecule^{-1} s^{-1}, where the errors represent the statistical uncertainty at the 2σ level. The rate coefficients and OH yields obtained are validated through comparison with other methods, and previous measurements. Numerical integration simulations have also been used to demonstrate the sensitivity of the new method to experimental conditions, and the limitations of the method are discussed.

4.2 Introduction

Fuel derived radicals, R, produced by abstraction of a hydrogen by a radical species, X (X = OH, O, H, HO$_2$ etc), are an integral species in low temperature combustion chemistry (reaction R 4-1). In a typical low temperature oxidation mechanism, the reaction of R with molecular oxygen leads to formation of the RO$_2$ radical (reaction R 4-2), which can undergo internal rearrangement to form the QOOH radical (reaction R 4-3) where the radical centre is now located on a carbon atom. Decomposition of this QOOH radical (reaction R 4-4) in a chain-propagating reaction, is in competition with a second oxygen addition, to form a QOOH-peroxy species (reaction R 4-5). Under the appropriate conditions, this O$_2$QOOH species can undergo internal rearrangement, followed by decomposition to ultimately produce two OH radicals (reaction R 4-6). This chain-branching step is believed to be key to the autoignition of fuels [90, 191, 192].

$$X + RH \rightarrow HX + R \qquad\qquad \text{R 4-1}$$
$$R + O_2 \leftrightarrow RO_2 \qquad\qquad \text{R 4-2}$$
$$RO_2 \leftrightarrow QOOH \qquad\qquad \text{R 4-3}$$
$$QOOH \rightarrow OH + \text{carbonyl} \qquad\qquad \text{R 4-4}$$
$$QOOH + O_2 \rightarrow O_2QOOH \qquad\qquad \text{R 4-5}$$
$$O_2QOOH \rightarrow HO_2Q'OOH \rightarrow OH + OQ'OOH \rightarrow \text{chain branching} \qquad \text{R 4-6}$$
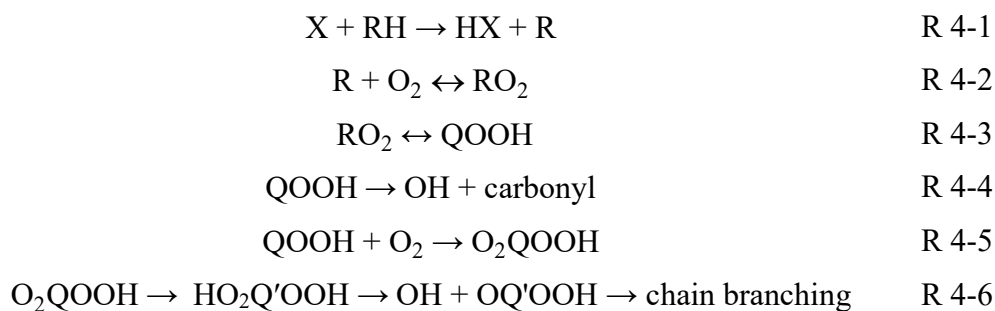
Understanding the details of this mechanism is important in determining the autoignition properties of a fuel. The recent development of HCCI and related engines, whose operation depends on autoignition, provides added impetus for unravelling the chemical details of these mechanisms for both fossil fuels and biofuels [193, 194].

As the next step towards autoigniton after reaction R 4-1 studied in Chapter 3, reaction R 4-2 is similarly important, and has been studied for the R radicals generated in the DME system in this chapter. Without measurements of this rate coefficient, and the OH yields arising from the reaction, any measurements of chain-branching OH recycling would be very difficult to analyse.

Studies on $R + O_2$ reactions have been conducted previously, such as $CH_3 + O_2$ by Pilling and Smith [195] using flash photolysis and absorption spectroscopy, and several $R + O_2$ reactions via photoionisation mass spectrometry (PIMS) [196-198], and a correlation between k_{R+O2} and the ionisation potential of the R radical has been demonstrated [199], showing that rate coefficients for reaction R 4-2 decrease with ionisation potential.

Here, a method for measuring both $R + O_2$ rate coefficients and OH yields using an OH precursor is presented. This is universal for all fuels, provided they possess the ability to well-skip sufficiently at low pressures (previous studies show this technique should be applicable for systems such as OH + ketones [200], aldehydes [133, 200-205], dialdehydes [206, 207], and esters [208]).

4.2.1 The Dimethyl Ether System

The methoxy methyl radical (CH_3OCH_2), is the R radical formed in the low temperature oxidation system for DME (CH_3OCH_3) (reaction R 4-7), a potential biofuel, and a comprehensive understanding of its reactivity is therefore crucial for the elucidation of DME's combustion behaviour. Its reaction with O_2 (reaction R 4-8) ultimately leads to

chain-branching, by reformation of OH through various routes. The integral role R + O_2 chemistry plays in DME low temperature oxidation is evidenced by the various fates of its product (Figure 4-1). Oxygen addition in reaction R 4-8 leads to an energetically excited RO_2^* peroxy radical, which can undergo pressure-dependent stabilisation to the relatively stable RO_2 radical (reaction R 4-9). Alternatively, the RO_2^* radical has two other competing pathways. These are re-dissociation to reactants (competitive at high temperatures), or formation of QOOH* (via an internal hydrogen abstraction) followed rapidly by decomposition to OH and formaldehyde (reaction R 4-10), the process referred to as well-skipping. Stabilisation of QOOH* is not considered, as the QOOH energy well is significantly higher than that of RO_2, thus the equilibrium of reaction R 4-10's initial step is shifted towards the RO_2^* species.

$$CH_3OCH_3 + OH \rightarrow CH_3OCH_2 + H_2O \qquad \text{R 4-7}$$

$$CH_3OCH_2 + O_2 \leftrightarrow CH_3OCH_2O_2^* \qquad \text{R 4-8}$$

$$CH_3OCH_2O_2^* \xrightarrow{M} CH_3OCH_2O_2 \qquad \text{R 4-9}$$

$$CH_3OCH_2O_2^* \leftrightarrow CH_2OCH_2OOH^* \rightarrow 2CH_2O + OH \qquad \text{R 4-10}$$
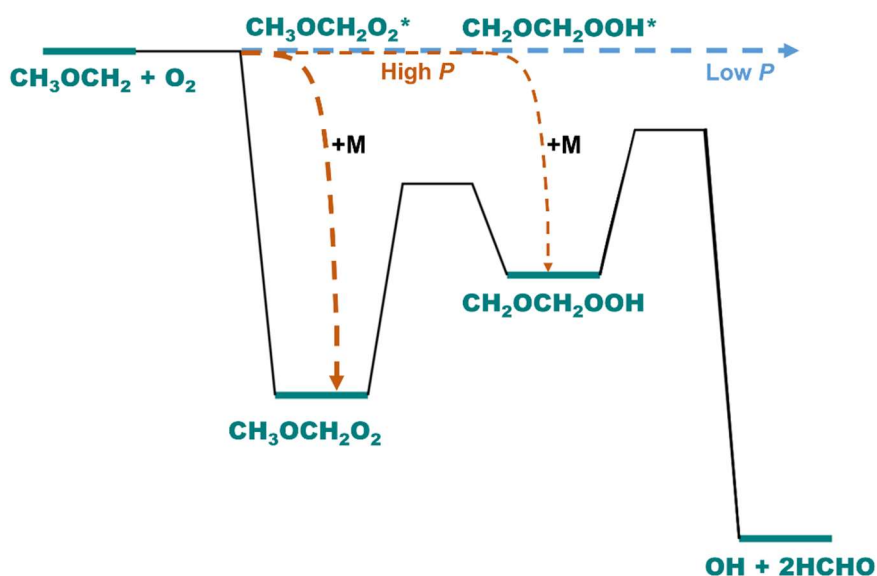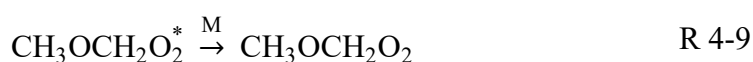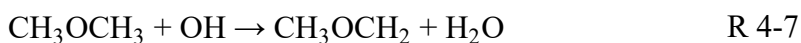
Figure 4-1: Potential energy surface showing the competition between RO_2^* stabilisation into RO_2/QOOH wells at high pressures (orange thick/thin line), and formation of OH at low pressures (blue line) for dimethyl ether.

Previously, in order to measure the rate coefficient for reaction R 4-8 ($k_{CH3OCH2+O2}$), a brominated molecule of DME was used [209]. Using this method to

measure the R + O$_2$ rate coefficient and OH yields from chemical activation is not possible for other potentially important fuels, such as diethyl ether, where the brominated version of the dominant DEE-derived R radical is not readily available. Eskola et al. [89, 209] studied the kinetics of reaction R 4-8 using this method, and LFP–LIF, obtaining $k_{CH3OCH2+O2}$ and OH yields in nitrogen and helium, by an absolute and relative method. Generation of the R radical by Cl + DME was also used, but subsequent reactions of (COCl)$_2$ photolysis products can interfere with measurements. A similar problem exists when using t-butyl hydroperoxide to generate OH radicals, a precursor Eskola et al. used. More importantly, the absolute determinations of the OH yield using Cl + DME or OH + DME previously conducted in this laboratory offer no information on the R + O$_2$ rate coefficient.

Other studies on CH$_3$OCH$_2$ + O$_2$ rate parameters have been carried out by Sehested et al. [210] (Fourier transform infrared smog chamber, FTIR), Maricq et al. [211] (transient infrared and UV), Masaki et al. [212] (laser photolysis – mass spectrometry), and Rosado-Reyes et al. [213] (transient infrared), yielding a combination of branching ratios, product yields, and rate coefficients. The data measured in this section are validated by comparison with the previous method employed in the work of Eskola et al. [89].

4.3   Experimental

The experimental setup used in this chapter is largely the same as the throughout the rest of this work, with the major difference being the experimental conditions required. The same conventional slow flow laser flash photolysis setup was combined with laser-induced fluorescence to monitor OH. The reactants were DME (Argo International Ltd, 99.8%); CH$_3$OCH$_2$Br (Sigma-Aldrich, technical grade 90%); DBE (Sigma-Aldrich, 99.3%); MTBE (Sigma-Aldrich, 99%); and TMOF (Sigma-Aldrich, 99.8%), OH precursor (generally hydrogen peroxide, H$_2$O$_2$ (Sigma-Aldrich, 50% (w/w) in H$_2$O)). Urea hydrogen peroxide (CO(NH$_2$)$_2$·H$_2$O$_2$) was also used for comparison (Sigma-Aldrich, 97%), buffer gas (N$_2$, BOC, oxygen-free), and O$_2$ (BOC, 99.5%).

On average, experiments were carried out at lower pressures than the majority of the work in this thesis, between 4 and 33 Torr of nitrogen. At even lower pressures, diffusion became so pronounced as to interfere with experiments, and at higher pressures chemical activation OH yields were too insignificant to be measured with any true

certainty. In order to achieve low pressures, in combination with more efficient vacuum pumping of the reaction cell, lower flows were often used. For the extensive investigation using DME, the flows were typically 100 – 1000 sccm, and temperatures reported above room temperature have an associated uncertainty of approximately ±10 K, due to the calibrations presented in Chapter 2. Only preliminary checks were conducted using the MTBE, TMOF, and DBE compounds.

Contact of hydrogen peroxide with the metal pipes and consequent decomposition results in some oxygen always being delivered to the system, which was estimated to be approximately $(0.6 - 2.9) \times 10^{14}$ molecule cm^{-3} (the method for estimating O$_2$ concentration is discussed in section 4.4), and varies depending on pressure, flow and precursor. Photolysis of the hydrogen peroxide at 248 nm was used to generate the hydroxyl radicals, as described previously, and was the source of OH for the majority of experiments in this work. Urea hydrogen peroxide $(CO(NH_2)_2 \cdot H_2O_2)$ (reaction R 4-11) was also used as a known OH precursor [214, 215] for comparison. Reactions were studied under pseudo-first order conditions where [ether] >> [OH], and extensive details of the analyses of kinetic traces in this chapter are presented in section 4.4.

$$(CO(NH_2)_2 \cdot H_2O_2) \xrightarrow{\text{vap}} H_2O_2 + h\nu \ (\lambda=248 \text{ nm}) \rightarrow 2OH \qquad \text{R 4-11}$$
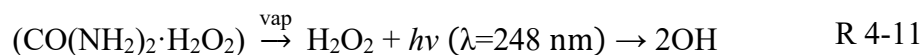
CH$_3$OCH$_2$Br (reaction R 4-12) was employed as a photolytic precursor to measure CH$_3$OCH$_2$ + O$_2$ rate coefficients using the same method as Eskola et al. [89] for the DME system. Photolysis of this compound generates the DME R radical directly, and the rate of formation of OH can be used to measure $k_{CH3OCH2+O2}$.

$$CH_3OCH_2Br + h\nu \ (\lambda=248 \text{ nm}) \rightarrow CH_3OCH_2 + Br \qquad \text{R 4-12}$$
$$CH_3OCH_2Br + h\nu \ (\lambda=248 \text{ nm}) \rightarrow \text{other products} \qquad \text{R 4-13}$$
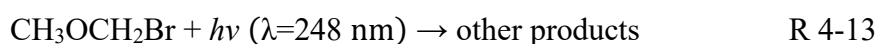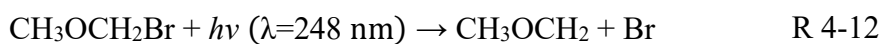
This method was used as further validation of the experimental setup used to measure rate coefficients of the reaction between O$_2$ and R radicals in this chapter. Equation E 4-1 was used to analyse kinetic traces, an example of which is presented in Figure 4-2, and a plot the OH growth pseudo-first order rate coefficient as a function of oxygen concentration (Figure 4-3) yields the bimolecular rate coefficient.

$$[OH] = [OH]_0 \left(\frac{k'_{grow}}{k'_{grow} - k'_{decay}} \times \left(e^{-k'_{decay} \times t} - e^{-k'_{grow} \times t} \right) + e^{-k'_{decay} \times t} \right) \qquad \text{E 4-1}$$
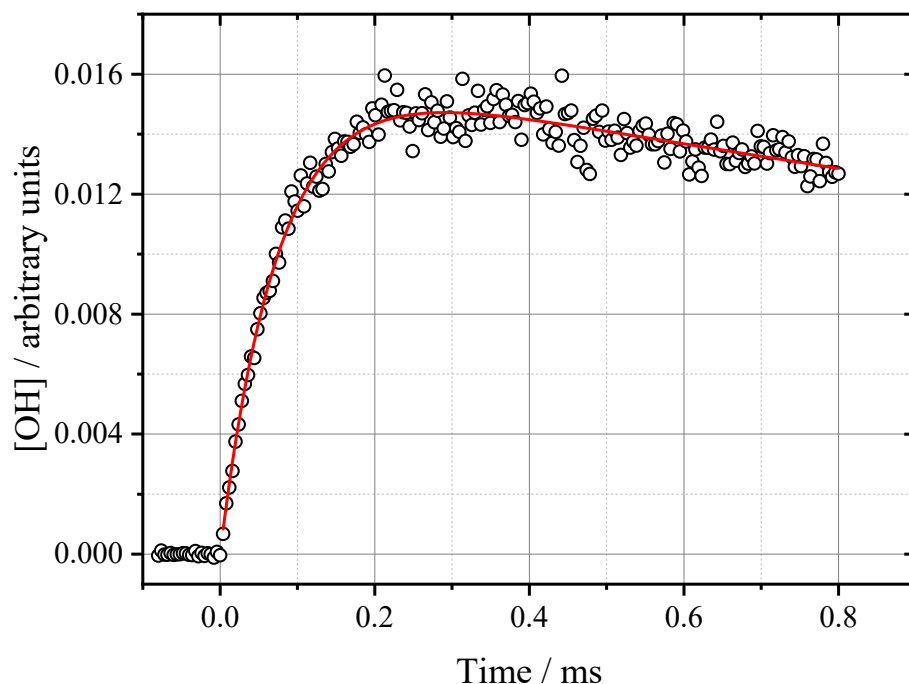
Figure 4-2: Example trace obtained using the CH3OCH2Br precursor. [CH3OCH2Br] ≈ 1.1 × 10^14 molecule cm^−3. Parameters were k'_{grow} = (13230 ± 660) s^−1, k'_{decay} = (310 ± 40) s^−1, where uncertainties are statistical at the 2σ level.
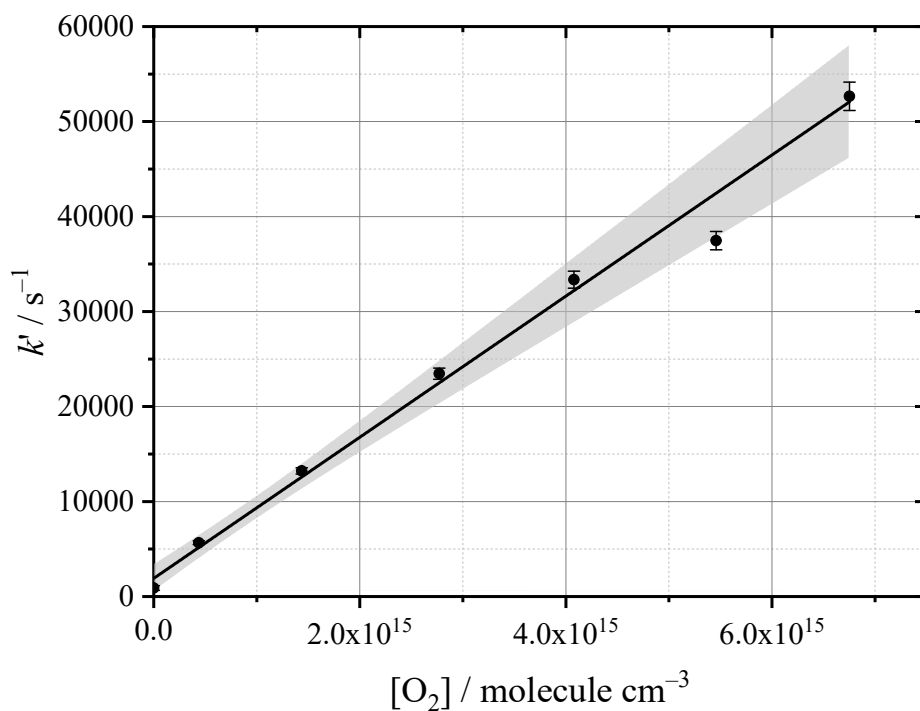
Figure 4-3: Example bimolecular using the bromo precursor method at 294 K, in 7 Torr N2, and $k_{CH3OCH2+O2}$ = (7.43 ± 0.98) × 10^−12 cm^3 molecule^−1 s^−1. Uncertainty on the bimolecular rate coefficient is statistical at the 2σ level. Here k' is equivalent to the k'_{grow} parameter in equation E 4-1.

4.4   Treatment of Chemical Activation Data

Decays showing chemical activation in the presence of low oxygen ($[O_2] \approx (0.2 -$ 26) $\times 10^{14}$ molecule cm^{-3}) require complex analysis. Regeneration of OH results in biexponential kinetic decays, where the initial fast decay is the reaction between OH and the ether, and the tail portion of the decay contains information about the OH formation. An equation derived from Scheme 4-1 was used to analyse these traces. DME is used as the example system for the purpose of explaining the complex data analyses. For the DEE experiments presented in Chapter 5, the same will apply for the equivalent radicals (i.e. R, RO$_2$ etc., see Scheme 4-1).
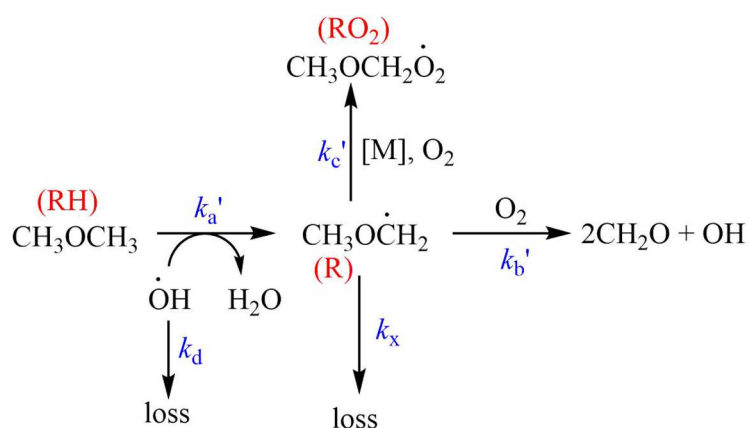
Scheme 4-1: Reaction scheme for analysis of OH regeneration traces. This scheme represents the route following initial H abstraction from DME. Parameters used in the biexponential equation are in blue. Bracketed red species show the generic equivalent.

Here, the only routes considered for the fate of the R radical are reaction with O$_2$ followed by stabilisation to RO$_2$ (reaction R 4-9), reaction with O$_2$ followed by formation of OH (chemical activation) (reaction R 4-10), and another minor loss process for the R radical, potentially self-reaction. The total rate for R + O$_2$ is the sum of reaction R 4-9 and reaction R 4-10, and can be generalised as reaction R 4-14.
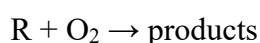
$$R + O_2 \rightarrow products \qquad\qquad R\ 4\text{-}14$$

The following equations (equation E 4-2 – E 3-6) were used to fit the traces:

$$\text{OH} = \text{OH}_0 \times \left[\left(\frac{-(k_d + k_a') - \lambda_2}{\lambda_1 - \lambda_2} \right) \times \left(e^{\lambda_1 \times t} - e^{\lambda_2 \times t} \right) + e^{\lambda_2 \times t} \right] \qquad \text{E 4-2}$$

$$\lambda_1 = \frac{\left(-\text{M1} + \sqrt{\text{M1}^2 - 4\text{M2}} \right)}{2} \qquad \text{E 4-3}$$

$$\lambda_1 = \frac{\left(-\text{M1} - \sqrt{\text{M1}^2 - 4\text{M2}} \right)}{2} \qquad \text{E 4-4}$$

$$\text{M1} = k_d + k_a' + k_b' + k_c' \qquad \text{E 4-5}$$

$$\text{M2} = (k_d + k_a') \times (k_b' + k_c') - (k_a' k_b') \qquad \text{E 4-6}$$

here, k_a' = pseudo-first order rate coefficient for reaction R 4-7, k_d = rate coefficient for OH loss in the absence of ether (fixed to the value measured when only OH precursor is present), and the terms λ_1 and λ_2 are expanded fully in equations E 4-3 – E 4-6. The terms k_b' (pseudo-first order rate coefficient for OH regeneration from R + O$_2$) and k_c' (pseudo-first order rate coefficient for R radical reacting with O$_2$ and not producing OH) are both present in λ_1 and λ_2. Reactions were studied under pseudo-first order conditions where [ether] >> [OH].

For robust parameter retrieval, global fitting was used to analyse several kinetic traces as a function of [ether] at once ($k_a' = k_{OH+ether}$[ether] for each trace), and share the bimolecular rate coefficient for OH + ether ($k_{OH+ether}$) and R + O$_2$ ($k_{CH3OCH2+O2}$ or $k_{C2H5OC2H4+O2}$ in Chapter 5) between decays. Similarly, the k_b' and k_c' parameters have been related to their bimolecular rate coefficient counterparts to globally share these parameters across all traces. Additionally, O$_2$x (O$_2$x refers to unavoidable O$_2$ arising from hydrogen peroxide decomposition) has been accounted for, and k_x was introduced as a small loss of the R radical to achieve good fits at the very lowest [O$_2$] traces, where O$_2$ addition was in competition with other possible processes (loss of R, R + R, R decomposition). For single trace analysis using equation E 4-2, k_x is not present, or even obtainable, but this does not affect the measured value for k_{R+O2}, as the straight line in Figure 4-6 would simply be translated down if k_x was accounted for (k_x is constant across a range of [O$_2$]). The intercepts, and therefore [O$_2$x] will be slightly affected by the exclusion of k_x for single trace analysis, but these are compared to those from global analysis in Figure 4-4. Ultimately, multiple traces are required to yield information about k_x. All parameters are listed below in Table 4-1.

Table 4-1: Description of parameters used in the global analysis treatment of data. Details on whether these parameters are fixed (input), and shared (across multiple traces where pressure and temperature is constant) or local are included. The full Origin C code is included in Appendix B.

Parameter	Definition	Relationship	Share	Fix
k_a'	Pseudo-first order rate coefficient for OH + ether	$= k_{OH+ether}[ether]$	No	No
$k_{OH+ether}$	OH + ether bimolecular rate coefficient		Yes	No
[ether]	ether concentration		No	Yes
k_b'	Pseudo-first order rate coefficient for OH formation	$= k_b([O_2]+[O_2x])$	No	No
k_b	R + O$_2$ → OH bimolecular rate coefficient		Yes	No
[O$_2$]	Oxygen concentration added		No	Yes
[O$_2$x]	Oxygen concentration always present in system		Yes	No
k_c'	Pseudo-first order rate coefficient for R + O$_2$ not yielding OH	$= k_c([O_2]+[O_2x])$ $+ k_x$	No	No
k_c	R + O$_2$ → RO$_2$ bimolecular rate coefficient		Yes	No
k_x	First order rate coefficient for loss of R radical		Yes	No
OH yield	Yield of OH formed from R + O$_2$	$= k_b/k_{R+O2}$	Yes	No
k_{R+O2}	R + O$_2$ bimolecular rate coefficient	$= \dfrac{(k_b'+k_c'-k_x)}{([O_2]+[O_2x])}$	Yes	No
OH$_0$	Initial signal intensity		No	No
k_d	First order rate coefficient for loss of OH		Yes	Yes
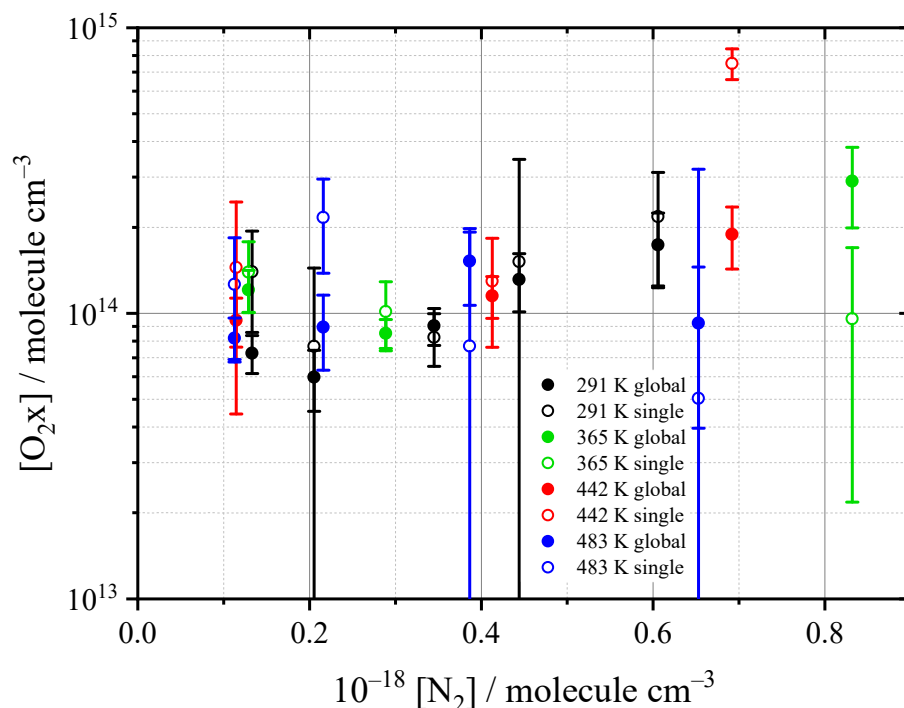
Figure 4-4: Comparison of O₂x obtained from single trace analysis and global analysis of H₂O₂/H₂O experiments for the DME system.

Data analysis using equation E 4-2 allows the total rate coefficient for reaction R 4-14 (k_{R+O2}) to be measured using a pseudo-first order bimolecular treatment of the total removal of the RO_2 radical ($k_b' + k_c'$) as a function of $[O_2]$. After the initial abstraction (reaction R 4-7) occurs, the CH_3OCH_2 radical concentration can be no higher than $[OH]_0$ $\approx 10^{12}$ molecule cm^{-3}, thus the addition of $[O_2] \approx (0.2 - 26) \times 10^{14}$ molecule cm^{-3} allows k_{R+O2} to be measured under pseudo-first order conditions, where R + O_2 is the rate determining step. Figure 4-5 shows an example biexponential decay, and a bimolecular plot determining $k_{CH3OCH2+O2}$ is presented in Figure 4-6.
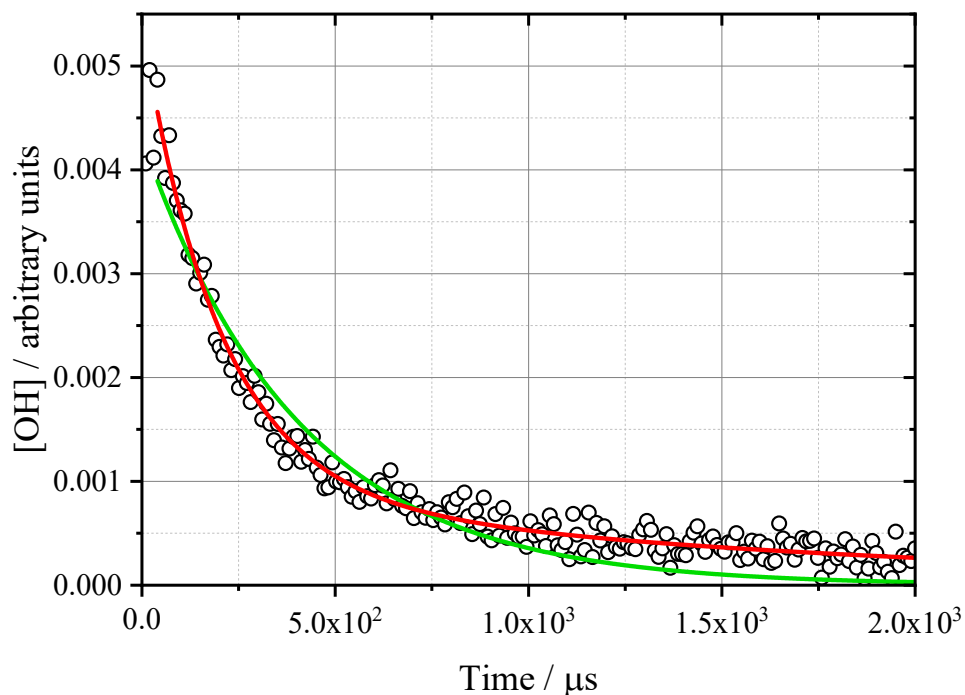
Figure 4-5: Biexponential decay for determination of k_b' and k_c'. The parameters recovered were $k_b' = (870 \pm 190)$ s^{-1}, $k_c' = (820 \pm 200)$ s^{-1}, $k_d = 400$ s^{-1} (fixed based on [DME] = 0 decay), and $k_a' = (4170 \pm 340)$ s^{-1}, at [O$_2$] = 1.8×10^{14} molecule cm^{-3}, [DME] = 6.8×10^{14} molecule cm^{-3}, and experimental conditions were the same as for the bimolecular plot. The green line compares a single exponential decay fit where $k_a' = (2490 \pm 150)$ s^{-1}. Uncertainties are statistical at the 2σ level.
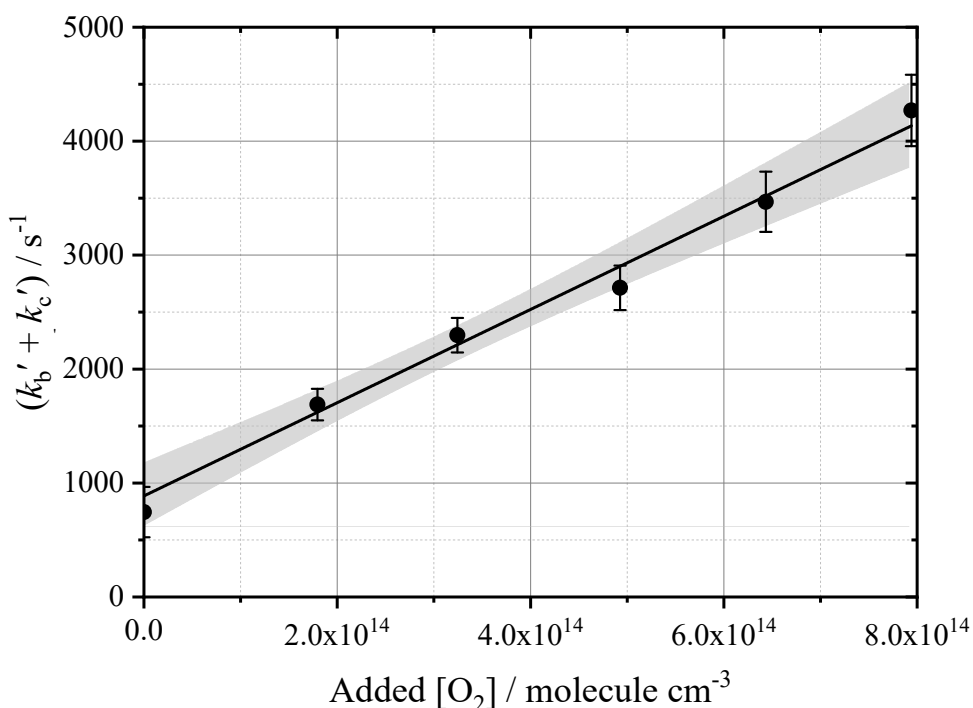
Figure 4-6: Bimolecular plot for the determination of the CH$_3$OCH$_2$ + O$_2$ rate coefficient, at (483 ± 5) K, 10.8 Torr N$_2$, [DME] = $(0.67 - 1.01) \times 10^{15}$ molecule cm^{-3}. $k_{CH3OCH2+O2} = (4.09 \pm 0.73) \times 10^{-12}$ cm^3 molecule^{-1} s^{-1}. The shaded area represents the bounds of the 95% confidence limits. All errors represent 2σ statistical uncertainties.

The intercept for a bimolecular plot of this nature can be related to the amount of oxygen in the system by default (O_2x) (H_2O_2 decomposes in the MFC to deliver some O_2). Equation E 4-7 shows that $[O_2x] = \text{intercept}/k(R+O_2)$.

$$(k_b'+k_c') = k(R+O_2)[O_2] + (k(R+O_2)\,[O_2x]) \qquad \text{E 4-7}$$

Furthermore, from the biexponential analysis (using equation E 4-2), the OH yield can be obtained through a relationship between k_b' and k_c' (equation E 4-8), that is, the ratio between $R + O_2$ leading to OH, and the total removal of R by O_2 (see Scheme 4-1). Loss of R is also accounted for.

$$\text{OH yield \%} = \frac{k_b'}{k_b' + k_c' - k_x} \times 100 \qquad \text{E 4-8}$$

For this biexponential analysis method to work as precisely as possible, the separation of the two time constants for the equation (λ_1 and λ_2 (containing the information on OH + ether and removal of R respectively)) should be pronounced, with $\lambda_1 > \lambda_2$. Experimentally, a clear separation can be achieved by keeping [ether] as high as possible (and thus k_a' fast), and [O_2] low, in order to keep the total rate of removal of the RO_2 radical ($k_b' + k_c'$) slow in comparison to k_a'. As λ_1 and λ_2 become closer together, or λ_2 becomes larger than λ_1, the OH decay becomes a less clear biexponential trace, and tends towards a single exponential decay. Additionally, under high oxygen conditions, it is possible that $R + O_2$ is no longer the rate-determining step. Under non-ideal conditions, analysing the data biexponentially yields poorer-defined parameters, with larger uncertainties. This is especially problematic under conditions where [O_2x] is high initially, and therefore a reduced range of [O_2] is available for determination of $k_{CH3OCH2+O2}$ using a bimolecular plot. Kinetic parameters obtained using the H_2O_2/urea precursor are presented, where the background O_2 was much higher compared with the H_2O_2/H_2O precursor (Figure 4-7).

Oxygen has been detected as a major decomposition product of urea hydrogen peroxide previously [214]. The concentration of O_2 delivered to the system by decomposition of the H_2O_2/H_2O precursor in this work is reasonably consistently ~0.03% of the total gas density delivered to the cell from the hydrogen peroxide bubbler (Figure 4-8).
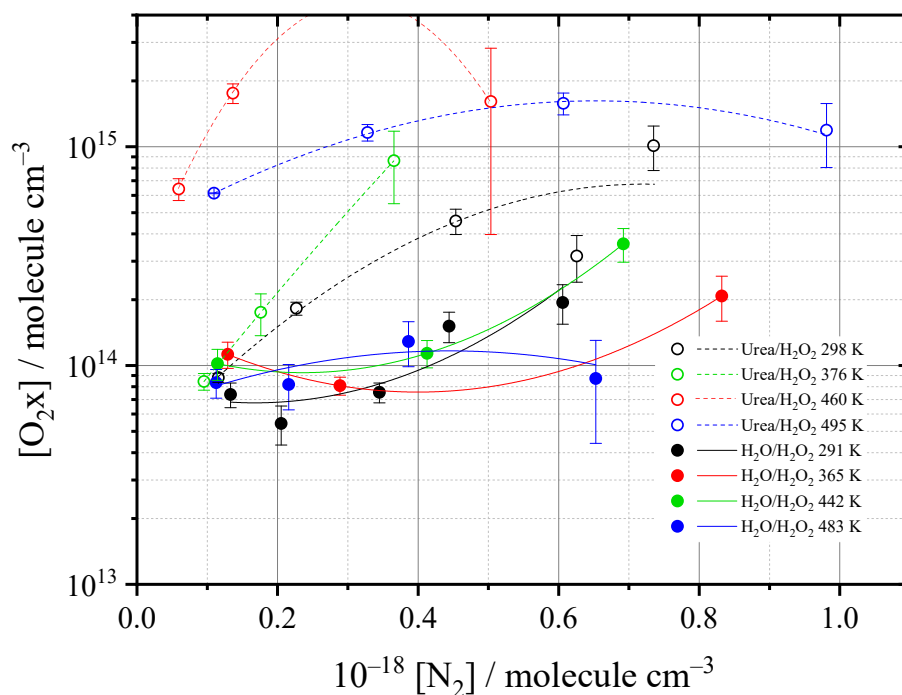
Figure 4-7: Comparison of O₂x present in H₂O₂/H₂O experiments and H₂O₂/urea experiments for the DME system. Lines represent second order polynomial fits, purely to aid visualisation of the overall trends – the fits themselves are meaningless.
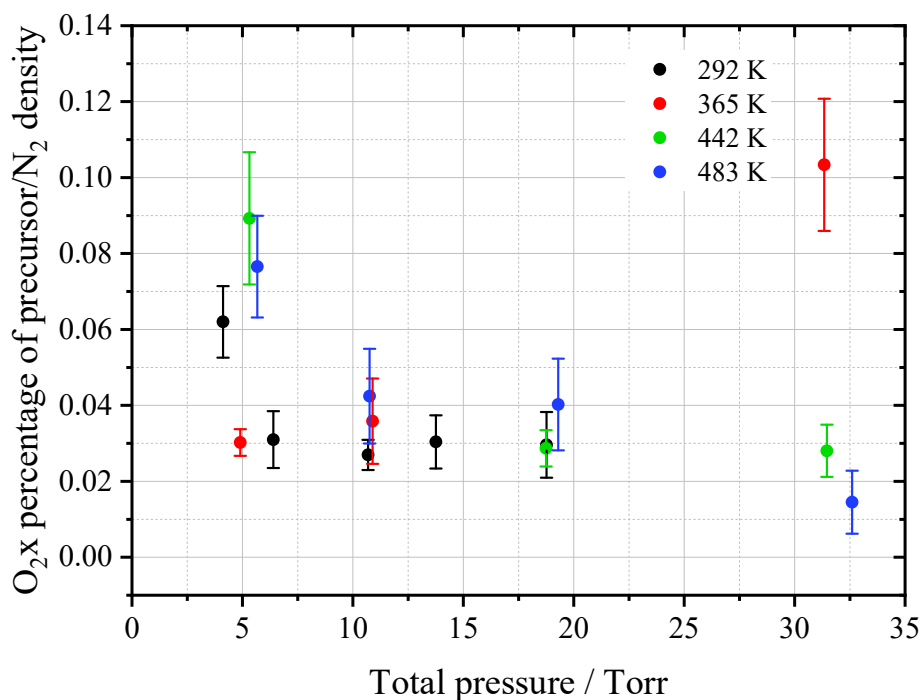
Figure 4-8: O₂x from DME experiments as a percentage of total gas density delivered from the H₂O₂/H₂O, given as a function of pressure and temperature.

The uncertainties on $k_{CH3OCH2+O2}$ measured from urea experiments were larger, and $k_{CH3OCH2+O2}$ itself generally faster (Figure 4-9), even when the time constants did not overlap, possibly indicating R + O₂ was no longer the rate determining step in OH

regeneration (once the rate of OH regeneration becomes fast compared to OH loss via reaction with ether, the decays will again become exponential). OH yields were always measured reliably regardless of the photolytic precursor used (Figure 4-10).
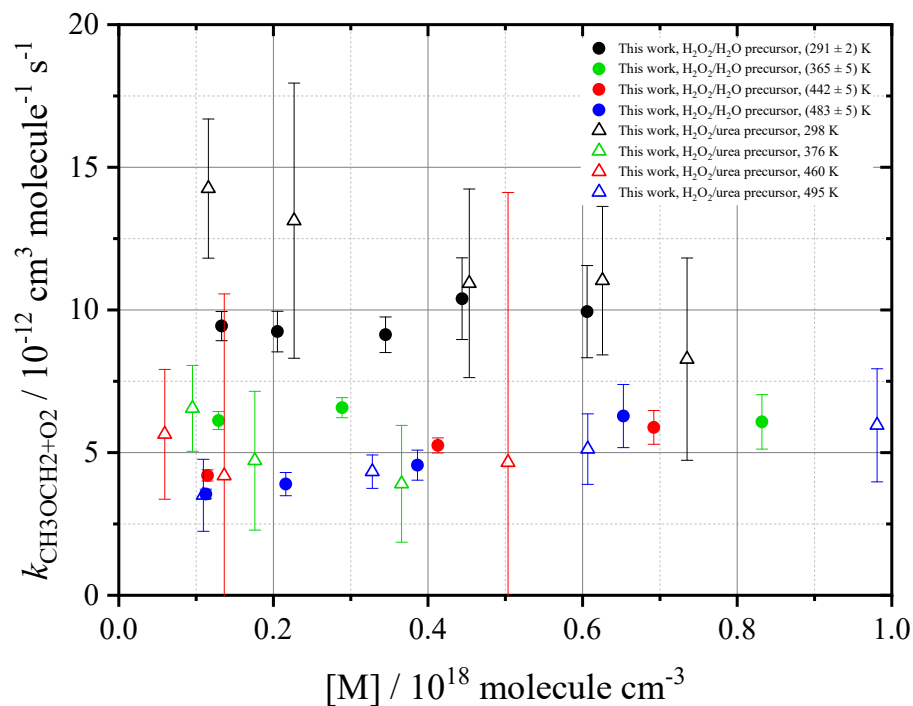
Figure 4-9: Comparison of $k_{CH3OCH2+O2}$ measured in H_2O_2/H_2O experiments and $H_2O_2/urea$ experiments. M = N_2.
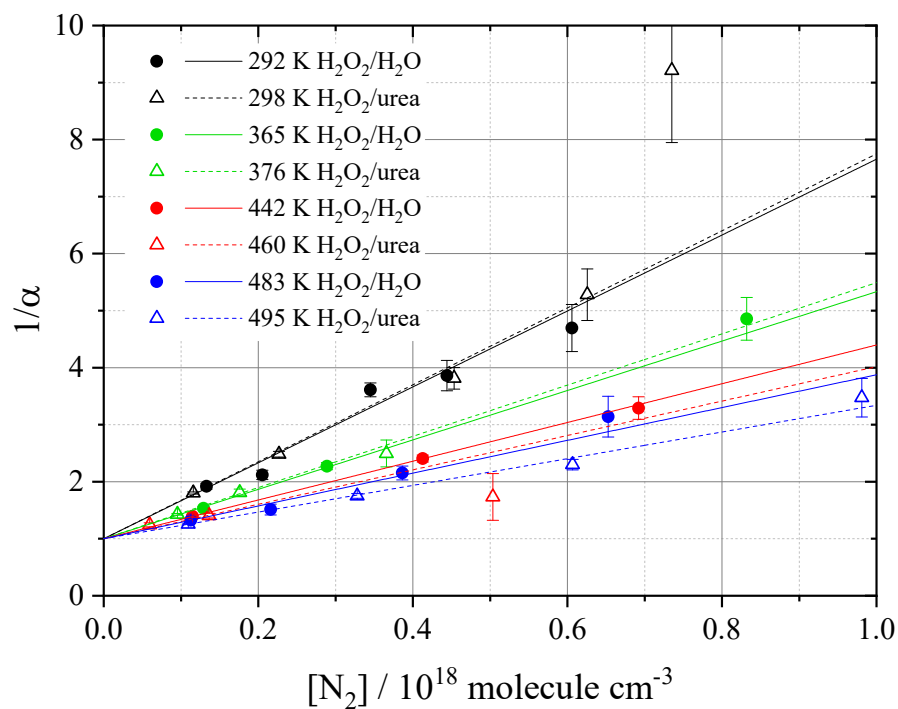
Figure 4-10: Comparison of OH yields measured in H_2O_2/H_2O experiments and $H_2O_2/urea$ experiments for the DME system.

The bimolecular plots (Figure 4-6) are weighted fits to the data, to account for the uncertainty in values of $(k_b' + k_c')$. All values reported in this work are from global analysis, including $k_{CH3OCH2+O2}$; Figure 4-6 is purely for illustrative purposes. For values of $k_{CH3OCH2+O2}$ measured using the H_2O_2/urea precursor presented in Figure 4-9, $k_{CH3OCH2+O2}$ was obtained using the single trace analysis method in Figure 4-6, and then fixed in the global determination of other parameters.

4.5 Analysis Simulations in Kintecus

A simple chemical model generated in the numerical integrator package Kintecus [216] was used to demonstrate the poor ability to retrieve k_{R+O2} from data under less-than-ideal conditions, using the DME system as an example. Here, the only parameters simulated were $k_{OH+DME} = 2.93 \times 10^{-12}$ cm^3 molecule^{-1} s^{-1} (based on room temperature k_{OH+DME} Arrhenius parameterisation by Carr et al. [186]), $k_{CH3OCH2+O2} = 1 \times 10^{-11}$ cm^3 molecule^{-1} s^{-1} and OH yield = 70%. Kintecus was used to generate traces over a range of $[O_2] = (0$ and $10^{13} - 10^{16})$ molecule cm^{-3}, for $[DME] = 5 \times 10^{13}$ molecule cm^{-3} and $[DME] = 5 \times 10^{14}$ molecule cm^{-3}, in order to simulate a set of data under ideal (high [DME]), and non-ideal (low [DME]) conditions. Figure 4-11 shows the bimolecular determinations of $k_{CH3OCH2+O2}$ from both sets of simulated experiments, where the rate coefficient returned at high [DME] was closer to the true value used for the simulated data, and the uncertainty in the low [DME] determination is much greater.

Figure 4-12 and Figure 4-13 show the individual fits to each trace analysed in Figure 4-11, where all fits appear good, and the low [DME] traces only demonstrate one good biexponential decay (at $[O_2] = 10^{13}$ molecule cm^{-3}). Even at high [DME] conditions, the trace becomes single exponential at the highest concentration of O_2. In order to extract the parameters properly from these single exponential traces, a shorter timescale is required, to reveal the two time constants of the decay (Figure 4-14). It is noted however, that at timescales these short, there is a minimal change in [OH], and as such, noise ($\pm(0 - 1)$%) generated randomly in Figure 4-15, or experimentally) will greatly perturb the ability to analyse the decay.
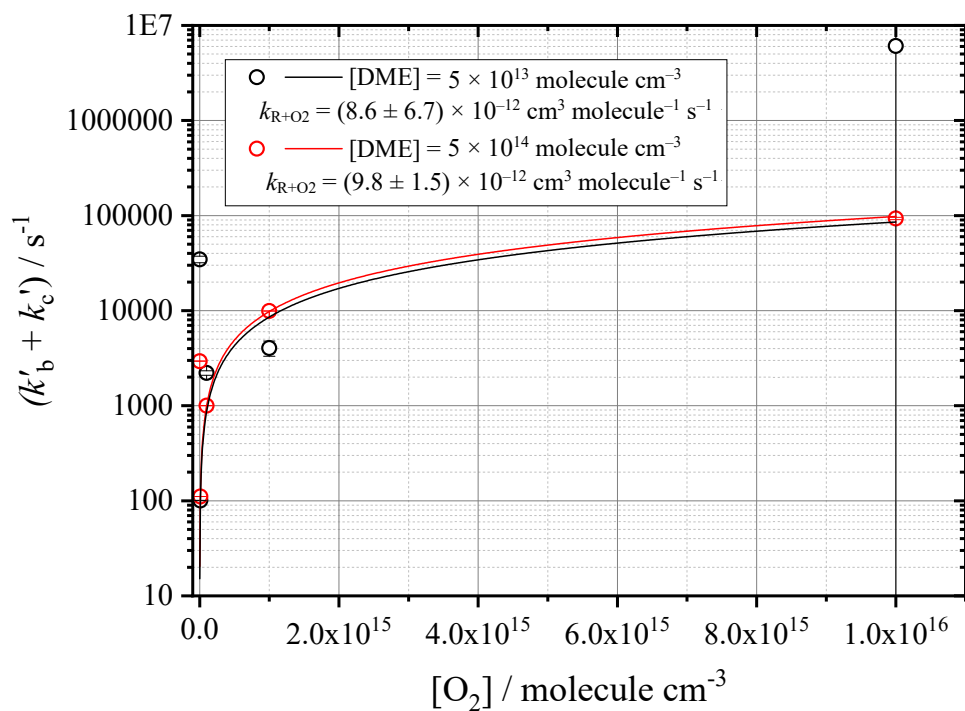
Figure 4-11: Weighted linear least squares fitting to bimolecular determinations of R + O₂ from data generated in Kintecus. Note the y-axis is log scale. True $k_{CH3OCH2+O2}$ = 1 × 10⁻¹¹ cm³ molecule⁻¹ s⁻¹.
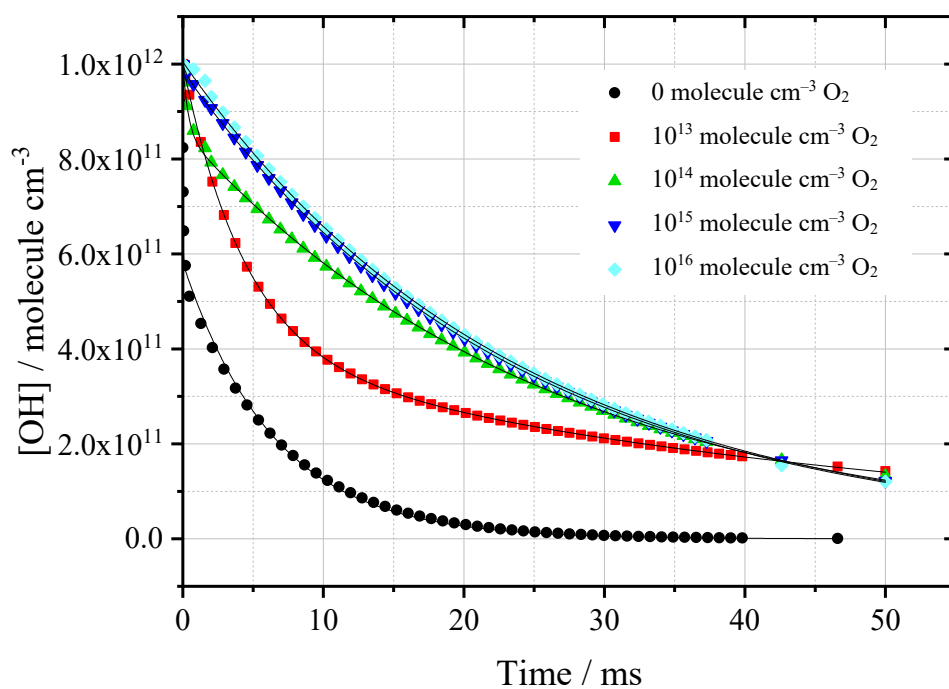
Figure 4-12: Biexponential fits to low [DME] OH decays generated in Kintecus. [O₂] increasing from black through light blue.
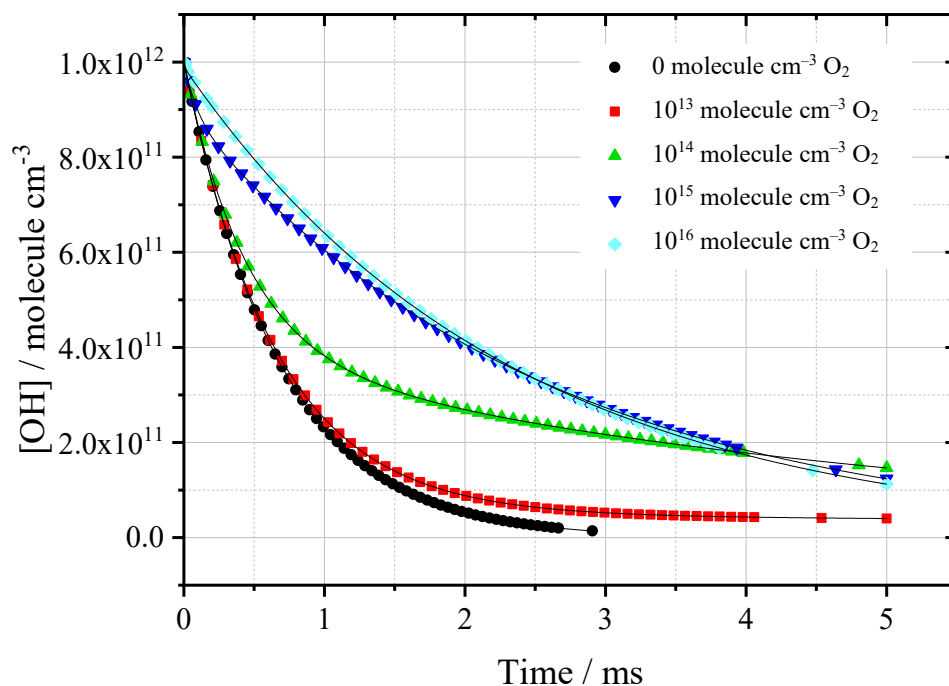
Figure 4-13: Biexponential fits to high [DME] OH decays generated in Kintecus. [O$_2$] increasing from black through light blue.
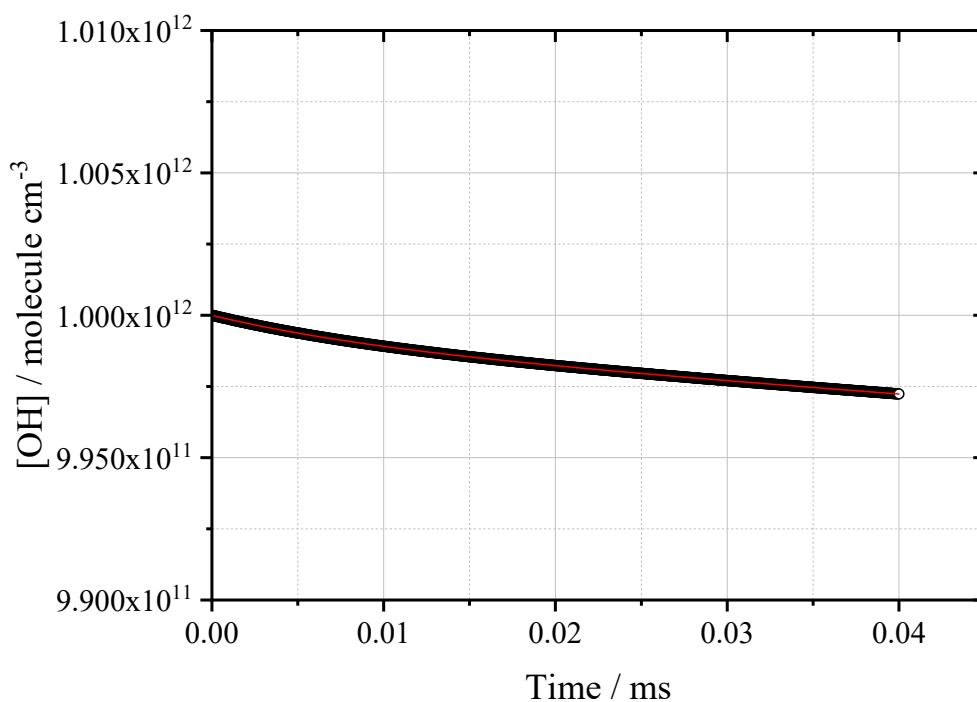
Figure 4-14: Short timescale OH decay generated in Kintecus for low [DME] (5 × 10^{13} molecule cm^{-3}), high [O$_2$] (10^{16} molecule cm^{-3}) conditions, on a very short timescale to properly retrieve parameters: $k_a' = (147 \pm 1)$ s^{-1}, $k_b' = (70005 \pm 19)$ s^{-1}, $k_c' = (29995 \pm 9)$ s^{-1}.
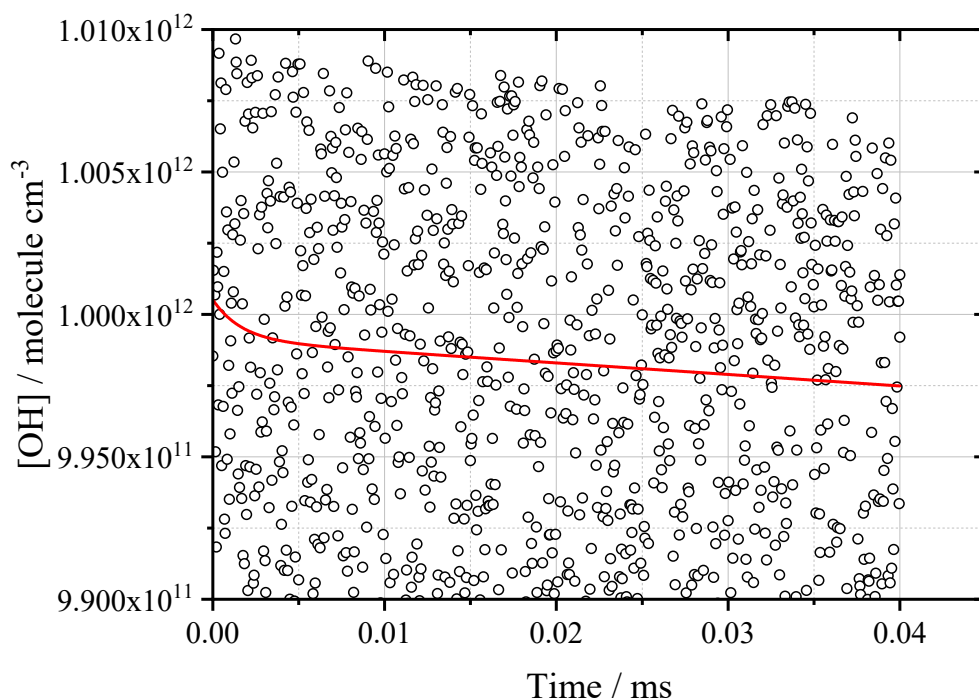
Figure 4-15: Short timescale OH decay generated in Kintecus for low [DME] (5 × 10^{13} molecule cm^{-3}), high [O$_2$] (10^{16} molecule cm^{-3}) conditions, on a very short timescale, with ±(0 − 1)% random noise generated. Parameters are not properly retrieved: $k_a' = (900 \pm 2600)$ s^{-1}, $k_b' = (576000 \pm 1335000)$ s^{-1}, $k_c' = (27500 \pm 36300)$ s^{-1}.

The Kintecus model was also used to investigate possible complexities from radical-radical reactions. In our experiments, no variations in the kinetics or yields (based on single trace analysis) were observed as laser power was varied by 50% (between approximately 28 and 42 mJ cm^{-2}), suggesting a limited role for radical-radical reactions. In the model, secondary chemistry such as $CH_3OCH_2O_2$ + OH was included with an approximate rate coefficient of 10^{-10} cm^3 molecule^{-1} s^{-1} [217], but no significant change was observed in the returned kinetic parameters when these reactions were included in the model (Figure 4-16).
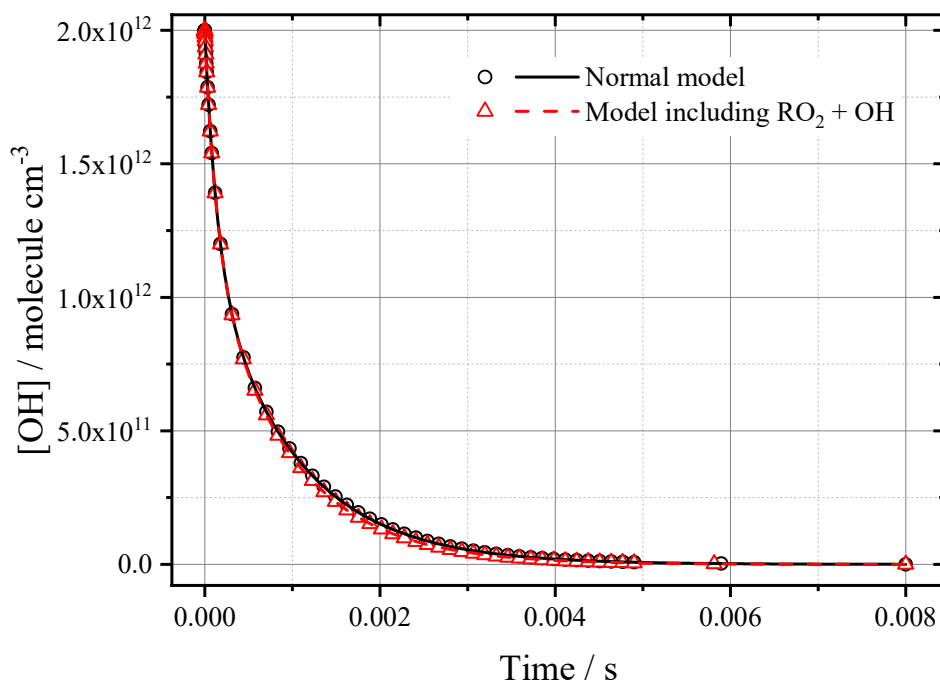
Figure 4-16: Effect on modelled OH decays when the CH₃OCH₂O₂ + OH reaction is included in the simulations. Parameters returned from the original model $k_a' = (3560 \pm 10)$ s⁻¹, $k_b' = (2490 \pm 10)$ s⁻¹, $k_c' = (2010 \pm 10)$ s⁻¹, when RO₂ + OH is included $k_a' = (3580 \pm 10)$ s⁻¹, $k_b' = (2570 \pm 20)$ s⁻¹, $k_c' = (2220 \pm 10)$ s⁻¹. Uncertainties are statistical at the 2σ level.

Further Kintecus simulations were used to demonstrate the deviation in returned parameters from the true values as λ_2/λ_1 increases (Figure 4-17). Here, the same rate parameters were simulated, but [O₂] was constant at 10^{15} molecule cm⁻³, while a range of [DME] ($(1 - 2000) \times 10^{13}$ molecule cm⁻³) was used to alter the degree of biexponential behaviour the traces exhibited. To achieve a deviation in the removal of the R radical rate comparable to those observed experimentally (~30 – 50%), λ_2 needed to be approximately ten times larger than the true value of λ_1 (dashed orange line, Figure 4-17), however, experimentally we see large deviations in time constant ratios much smaller than this (closer to 1:1). These data were generated with ± (0 – 10)% random signal noise. With no noise, parameter retrieval was significantly better, and an even larger value of λ_2/λ_1 was required to mimic experimental deviation from true parameters (Figure 4-18).
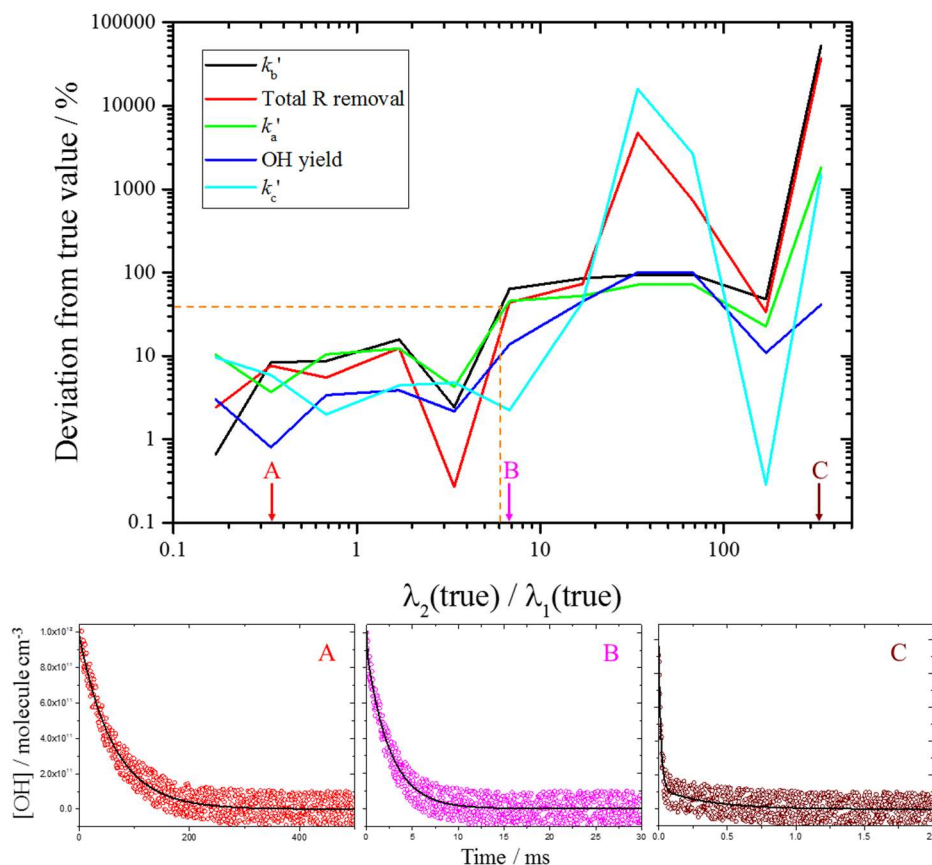
Figure 4-17: Deviation of returned parameters from true values as the ratio of λ₂ to λ₁ increases (% deviations here are sometimes negative, but the modulus of the values are presented). Traces generated using Kintecus (three examples shown, note the varying timescales), with ± (0 – 10)% random noise generated.
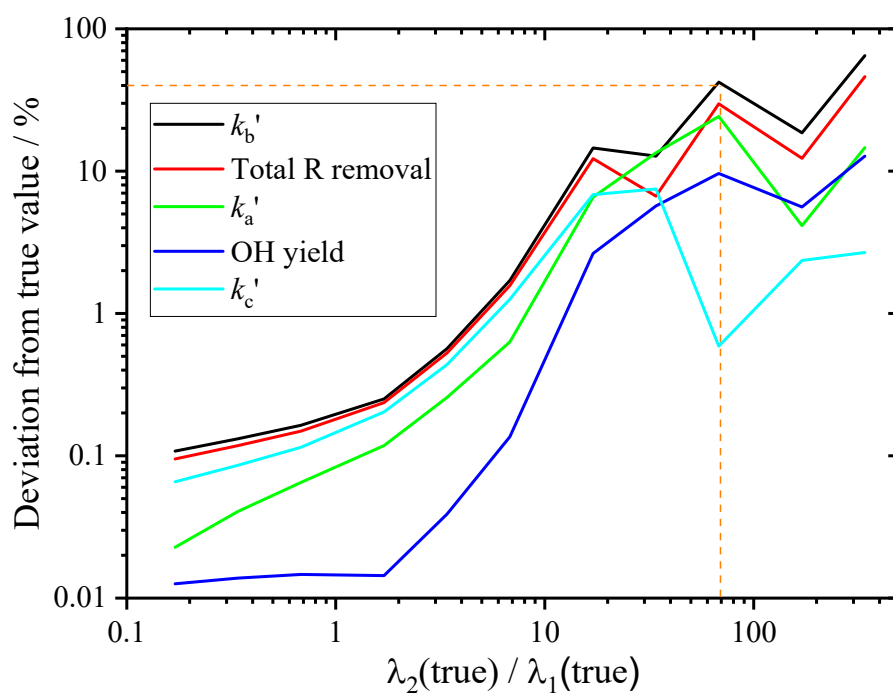
Figure 4-18: λ₂:λ₁ ratio effect on deviation of returned parameters from true values, based on retrieval from traces simulated in Kintecus, with no noise generated.

More accurate parameter recovery may be as a result of the perfect data produced in Kintecus, compared to experimental data which is subject to signal noise, other processes occurring (removal of R radical by other reactions, k_x), and [O_2x] present in the system, which limits the effective range of oxygen concentrations explorable over a bimolecular plot. OH loss in experimental data may also complicate parameter retrieval further, particularly at the lowest pressures, where diffusion plays more of a role. The same principle is demonstrated experimentally by consideration of the percentage uncertainty of ($k_b' + k_c'$) increasing as a function of [O_2] (Figure 4-19 and Figure 4-20) in H_2O_2/urea precursor measurements.
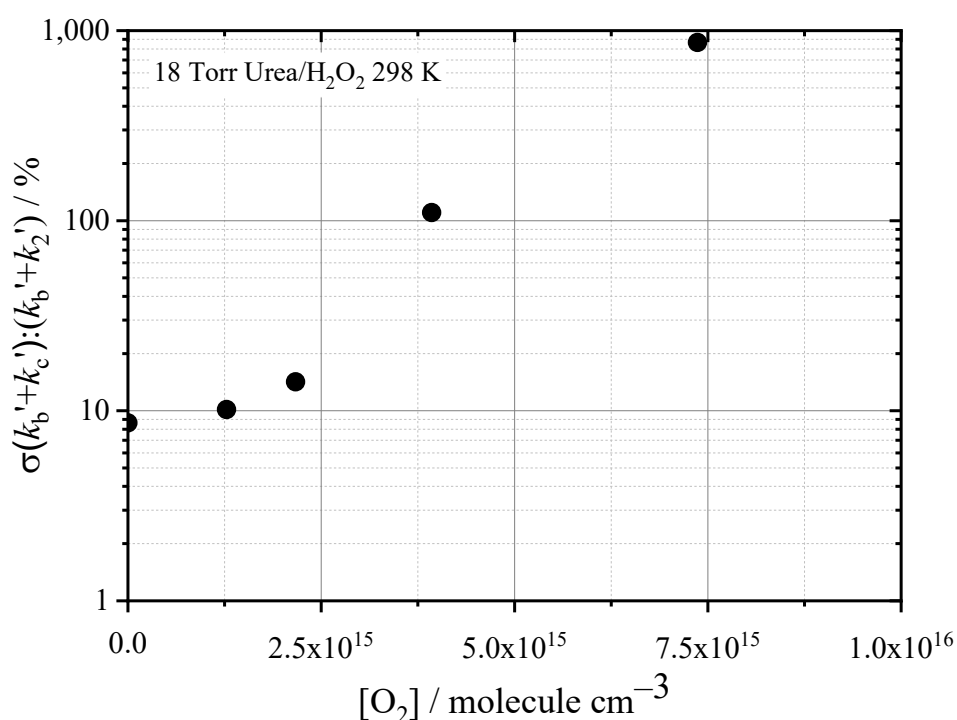
Figure 4-19: Increasing percentage uncertainty of ($k_b' + k_c'$) from experimental data at room temperature and 18 Torr N_2 H_2O_2/urea experiment.
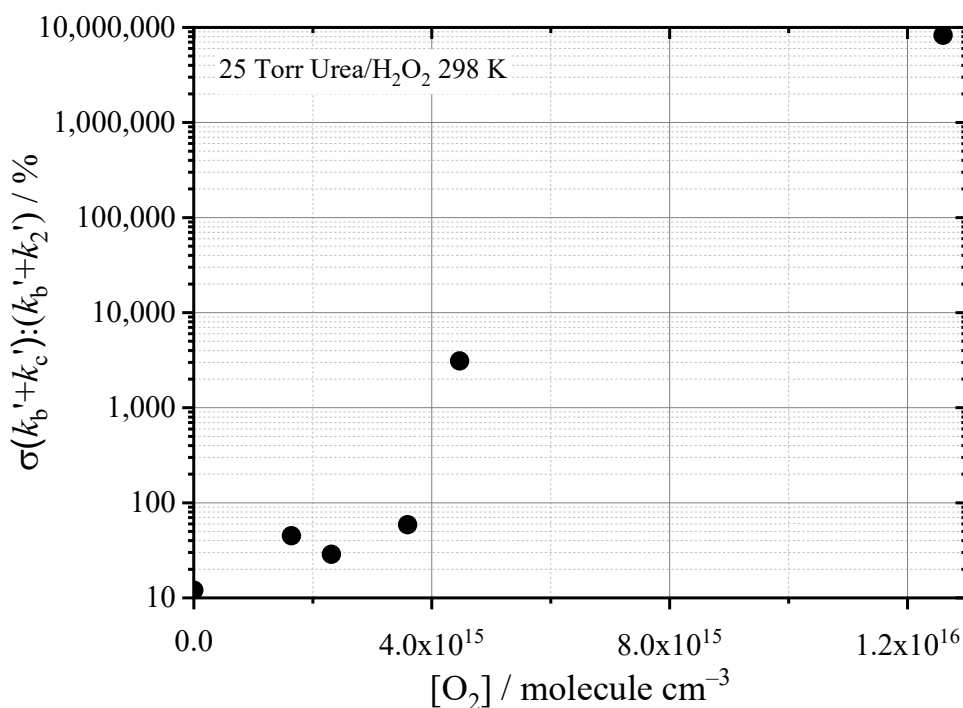
Figure 4-20: Increasing percentage uncertainty of (k_b' + k_c') from experimental data at room temperature and 25 Torr N₂ H₂O₂/urea experiment.

4.6 Temperature Dependent Measurements of the CH₃OCH₂ + O₂ Reaction

Measurements of the R + O₂ rate coefficient for DME made in this work (Figure 4-21), which are comparable to those made by Eskola et al. [89] in He, and Maricq et al. [211] in N₂, are presented in Figure 4-22. Additionally, $k_{CH3OCH2+O2}$ at all temperatures studied here are reported in Table 4-2. It was observed that $k_{CH3OCH2+O2}$ in the current work exhibits a negative temperature dependence, which is qualitatively consistent with what would be expected from a barrierless addition reaction, and was seen in the previous work. The Arrhenius parameterisation of this work's measurements is shown in Figure 4-21 and can be described by $k_{CH3OCH2+O2}$(290 − 482 K) = (1.70 ± 0.39) × 10^{-12} × $e^{((4.09±0.66)/RT)}$ cm³ molecule^{-1} s^{-1}. It should be noted this fit omits measurements at the lowest pressure for ~440 K, and rate coefficients at the lowest two pressures at ~480 K, where measurements appear not to be at the high pressure limit.
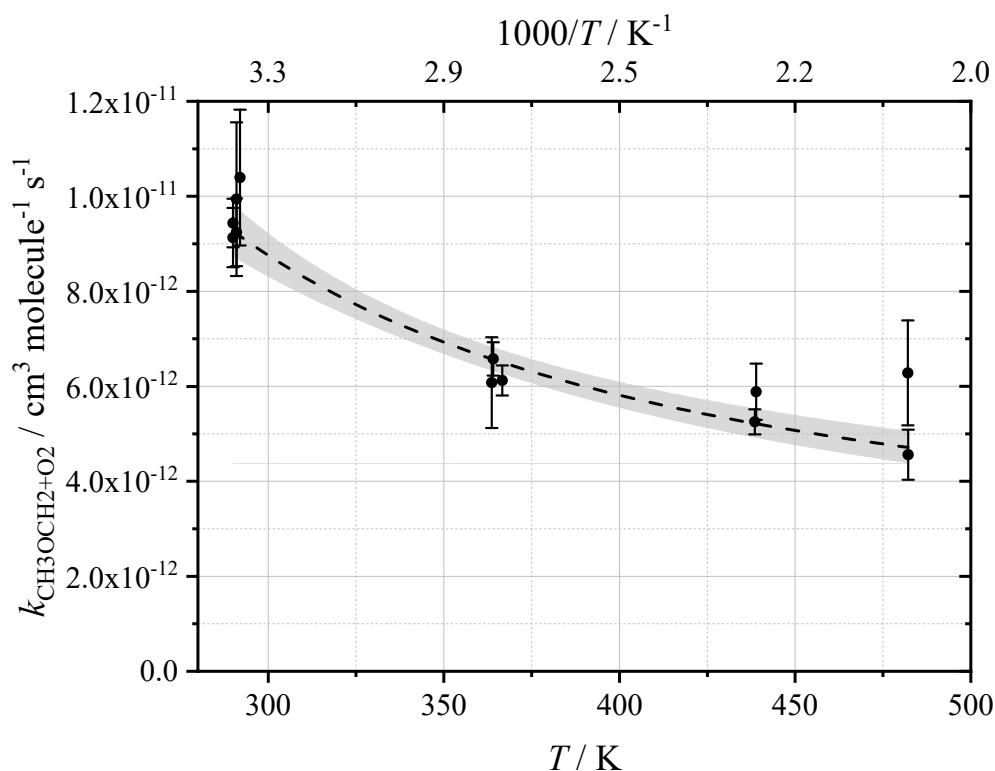
Figure 4-21: CH₃OCH₂ + O₂ rate coefficient measured as a function of temperature. The fit to the data yields $A = (1.70 \pm 0.39) \times 10^{-12}$ cm³ molecule⁻¹ s⁻¹ and $E_a = (-4.09 \pm 0.66)$ kJ mol⁻¹. The total pressure range explored was 4.1 – 32.6 Torr of N_2.

The lack of significant dependence on pressure at the lowest two temperatures suggests the reaction is at the high pressure limit. Within uncertainties, measurements of $k_{CH3OCH2+O2}$ are in agreement with those of Eskola et al. [89] at 295 K. Room temperature measurements in the current work using the CH_3OCH_2Br precursor (solid black triangles in Figure 4-22) agreed within uncertainties with those reported by Eskola et al., but were generally (10 – 20)% slower than the method presented here. The lowest pressure $k_{CH3OCH2+O2}$ measured at ~10^{17} molecule cm⁻³ using CH_3OCH_2Br was significantly lower than the most comparable H_2O_2/H_2O measurement (~35%). The study by Maricq et al. [211] primarily covered higher pressures, but the lowest two pressure measurements are included in Figure 4-22. The two room temperature measurements made using transient infrared detection of formaldehyde and UV detection of OH, have reasonably large uncertainties, but fall within the range of measurements made in this work (~6–10⁻¹² cm³ molecule⁻¹ s⁻¹).
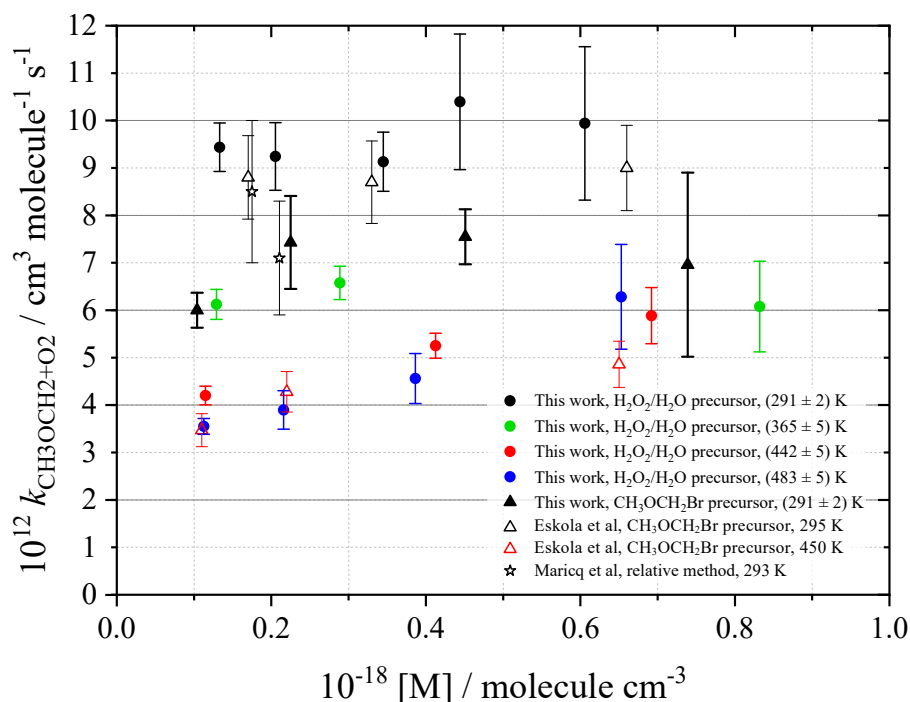
Figure 4-22: Comparison of R + O₂ rate coefficients measured in this work (filled symbols) with Eskola et al. [89] (open triangles) and Maricq et al. [211] (upturned triangles) as a function of pressure and temperature. For this work and Maricq et al., M = N₂, for data from Eskola et al., M = He. Error bars for this work are statistical at the 2σ level. Uncertainties on measurements by Eskola et al. were estimated to be 10% to take account of systematic errors (based on this work's approximate 2σ uncertainties using the same CH₃OCH₂Br precursor method).

At 450 K, where Eskola et al. [89] made measurements in the fall-off region using He as the bath gas, we also report a positive pressure dependence (442 K data, and 483 K) in N₂. Compared to the literature measurements at 450 K, we measure approximately 5% faster at 442 K, but are in agreement within error at the highest total pressure.

Both this study and previous studies observe a negative temperature dependence for $k_{CH3OCH2+O2}$, and positive pressure dependence at higher temperatures over the pressure range tested. The average room temperature $k_{CH3OCH2+O2} = (0.94 \pm 0.04) \times 10^{-11}$ cm³ molecule⁻¹ s⁻¹, is in agreement with previous measurements, and significantly faster than other R + O₂ reactions, such as acetyl + O₂ (~$(0.5 - 0.6) \times 10^{-11}$ cm³ molecule⁻¹ s⁻¹) [200, 205] and propionyl + O₂ (0.54×10^{-11} cm³ molecule⁻¹ s⁻¹) [200]. Previously, the ionisation potential of the R radical has been correlated with the rate coefficient for R + O₂, where an approximate ionisation potential for CH₃OCH₂ of 7 eV [218, 219] would predict ~3×10^{-11} cm³ molecule⁻¹ s⁻¹ for $k_{CH3OCH2+O2}$ [199]. This estimation is three times higher than $k_{CH3OCH2+O2}$ observed here, but is qualitatively in agreement with DME's system exhibiting a much faster rate coefficient than other R + O₂ reactions.
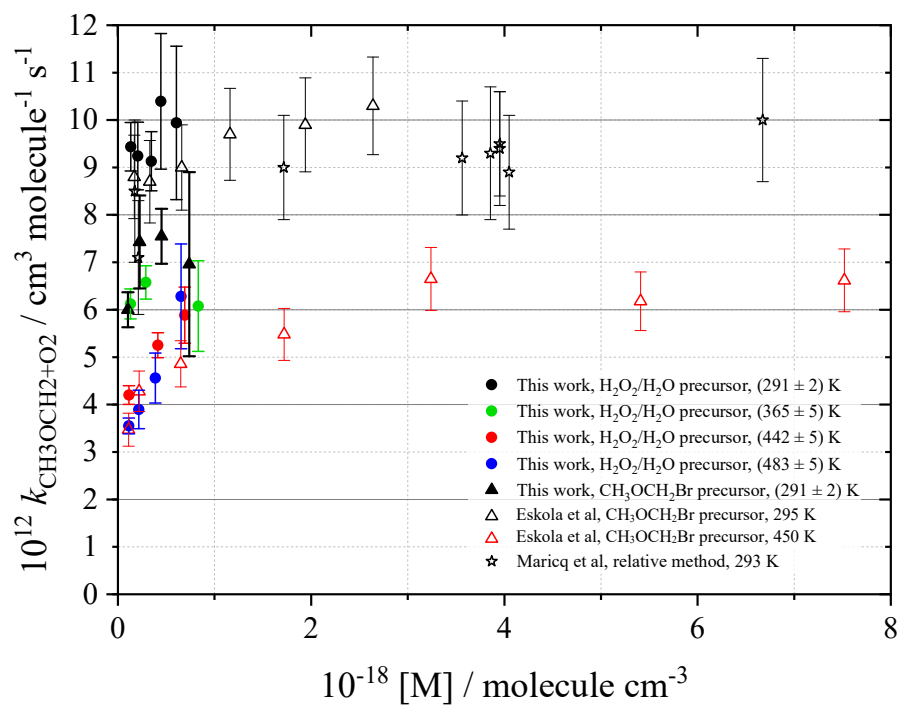
Figure 4-23: The same as Figure 4-22 above, but with an extended total pressure axis.

Table 4-2: Rate coefficients for the CH₃OCH₂ + O₂ reaction measured in this work using H₂O₂/H₂O, H₂O₂/urea and CH₃OCH₂Br precursors. Uncertainties are 2σ and purely statistical.

T	Precursor	[N₂]	$k_{CH3OCH2+O2}$	T	Precursor	[N₂]	$k_{CH3OCH2+O2}$
290	H₂O₂/H₂O	1.33	9.44 ± 0.51	298	Urea/H₂O₂	6.26	1.10 ± 0.26
291	H₂O₂/H₂O	2.05	9.24 ± 0.71	298	Urea/H₂O₂	4.53	1.09 ± 0.33
290	H₂O₂/H₂O	3.45	9.13 ± 0.62	298	Urea/H₂O₂	7.35	0.83 ± 0.36
292	H₂O₂/H₂O	4.44	10.04 ± 1.43	376	Urea/H₂O₂	0.95	0.66 ± 0.15
291	H₂O₂/H₂O	6.06	9.94 ± 1.62	376	Urea/H₂O₂	1.76	0.47 ± 0.24
367	H₂O₂/H₂O	1.29	6.12 ± 0.32	376	Urea/H₂O₂	3.66	0.39 ± 0.21
364	H₂O₂/H₂O	2.89	6.58 ± 0.35	460	Urea/H₂O₂	0.60	0.56 ± 0.23
364	H₂O₂/H₂O	8.32	6.08 ± 0.96	460	Urea/H₂O₂	1.36	0.42 ± 0.64
447	H₂O₂/H₂O	1.15	4.20 ± 0.20	460	Urea/H₂O₂	5.04	0.47 ± 0.95
439	H₂O₂/H₂O	4.13	5.25 ± 0.26	495	Urea/H₂O₂	1.09	0.35 ± 0.13
439	H₂O₂/H₂O	6.92	5.89 ± 0.59	495	Urea/H₂O₂	3.28	0.43 ± 0.06
486	H₂O₂/H₂O	1.13	3.55 ± 0.17	495	Urea/H₂O₂	6.07	0.51 ± 0.12
481	H₂O₂/H₂O	2.16	3.90 ± 0.41	495	Urea/H₂O₂	9.81	0.60 ± 0.20
482	H₂O₂/H₂O	3.86	4.56 ± 0.53	294	CH₃OCH₂Br	1.04	6.00 ± 0.37
482	H₂O₂/H₂O	6.53	6.28 ± 1.10	294	CH₃OCH₂Br	2.25	7.43 ± 0.98
298	Urea/H₂O₂	1.16	1.43 ± 0.24	294	CH₃OCH₂Br	4.51	7.55 ± 0.58
298	Urea/H₂O₂	2.27	1.31 ± 0.48	294	CH₃OCH₂Br	7.39	6.96 ± 1.94

Temperature units are Kelvin. Nitrogen density units are 10^{17} molecule cm⁻³. Rate coefficient units are 10^{-12} cm³ molecule⁻¹ s⁻¹.

4.7 Experimental OH Yields for the CH₃OCH₂ + O₂ Reaction

OH yields from well-skipping in the DME system were obtained over 4.1 – 32.6 Torr of N₂, and 291 – 483 K (thermal production of OH from stabilised RO₂ radicals begins above approximately 500 K). All OH yields measured are presented in Table 4-3. Treating these data with a Stern-Volmer analysis (Figure 4-24) demonstrates an increase in yield with increasing temperatures, and the suppression of yields at higher pressures. This is consistent with what would be expected of OH yields from reaction R 4-10, a process deactivated by the pressure-dependent stabilisation of the RO₂* radical (reaction R 4-9). At room temperature (black filled circles, Figure 4-24), yields were particularly

low at higher pressures, which is reflected in the greater uncertainties due to the less pronounced biexponential decays.

Table 4-3: Details of all OH yields measured for the DME system. Uncertainties are 2σ and purely statistical.

T / K	$[N_2]^a$	Yield / %	Precursor	T / K	$[N_2]^a$	Yield / %	Precursor
290	1.33	52 ± 1	H_2O_2/ H_2O	298	1.16	55 ± 1	Urea/H_2O_2
291	2.05	47 ± 2	H_2O_2/ H_2O	298	2.27	40 ± 1	Urea/H_2O_2
290	3.45	28 ± 1	H_2O_2/ H_2O	298	4.53	26 ± 1	Urea/H_2O_2
292	4.44	26 ± 2	H_2O_2/ H_2O	298	6.26	19 ± 2	Urea/H_2O_2
291	6.06	21 ± 2	H_2O_2/ H_2O	298	7.35	11 ± 1	Urea/H_2O_2
367	1.29	65 ± 1	H_2O_2/ H_2O	376	0.95	70 ± 1	Urea/H_2O_2
364	2.89	44 ± 1	H_2O_2/ H_2O	376	1.76	55 ± 2	Urea/H_2O_2
364	8.32	21 ± 1	H_2O_2/ H_2O	376	3.66	40 ± 4	Urea/H_2O_2
447	1.15	72 ± 1	H_2O_2/ H_2O	460	0.60	80 ± 2	Urea/H_2O_2
439	4.13	42 ± 1	H_2O_2/ H_2O	460	1.36	71 ± 2	Urea/H_2O_2
439	6.92	34 ± 2	H_2O_2/ H_2O	460	5.04	58 ± 14	Urea/H_2O_2
486	1.13	76 ± 2	H_2O_2/ H_2O	495	1.09	80 ± 1	Urea/H_2O_2
481	2.16	65 ± 3	H_2O_2/ H_2O	495	3.28	57 ± 1	Urea/H_2O_2
482	3.86	47 ± 3	H_2O_2/ H_2O	495	6.07	43 ± 2	Urea/H_2O_2
482	6.53	32 ± 3	H_2O_2/ H_2O	495	9.81	29 ± 3	Urea/H_2O_2

^{a}Units are 10^{17} molecule cm^{-3}.

Comparison with OH yields obtained by Eskola et al. [89] in nitrogen shows good agreement with the relative measurements conducted using CH_3OCH_2Br photolysis at room temperatures when considering quenching coefficient uncertainties (see Table 4-4). The quenching coefficient is determined from the slope of the Stern-Volmer plots, where the gradient k_M/k_C is determined from the Stern-Volmer relationship in equation E 4-9. A plot of reciprocal yield against [M] is used, and the intercept is either fixed at 1, or floated to be determined by the data. Here k_M represents the quenching rate for N_2, and k_C the rate for OH yields in the absence of bath gas. At ~442 K, the quenching coefficient uncertainty ranges measured in the current work and by Eskola et al. at 450 K are in

agreement. Room temperature yields from Maricq et al. [211] were included, and are not close to agreement with this work.

$$1/\alpha = k_M/k_C[M] + 1 \qquad\qquad \text{E 4-9}$$

Reciprocal yields were fit using weighted linear analyses, and intercepts are fixed at unity, imposing a 100% OH yield at $[N_2] = 0$ molecule cm^{-3}. Also presented are Stern-Volmer plots with OH yield intercepts floated (Figure 4-25), where the intercepts were still unity within uncertainties. A comparison of the yields from H_2O_2/H_2O and $H_2O_2/urea$ precursors was also presented in Figure 4-10 in section 4.4.

A pressure range as extensive as that explored by Eskola et al. [89] is not possible using the current method, as the very low yields measured by Eskola et al. (<10%), are difficult to extract from a biexponential decay. This does not affect the quality of the Stern-Volmer plot however, as the lowest pressures obtainable allow [M] to be explored over close to an order of magnitude, and the inset to Figure 4-24 shows the quenching coefficients extrapolate well to pressures beyond the limitations in this work. At higher temperatures (and therefore yields), this technique will successfully retrieve yields over a wider pressure range.

Comparison with other previous studies of OH yields in the DME system (Table 4-4) put our measurements close to agreement with data obtained by Rosado-Reyes et al. [213] at room temperature, but not at higher temperatures. The studies by Sehested et al. [210] and Maricq et al. [211] agree poorly with this work's quenching coefficients. The discrepancy with these three studies may be a result of difficult products to detect in their experimental methods, particularly formaldehyde, and the indirect nature of the previous studies.
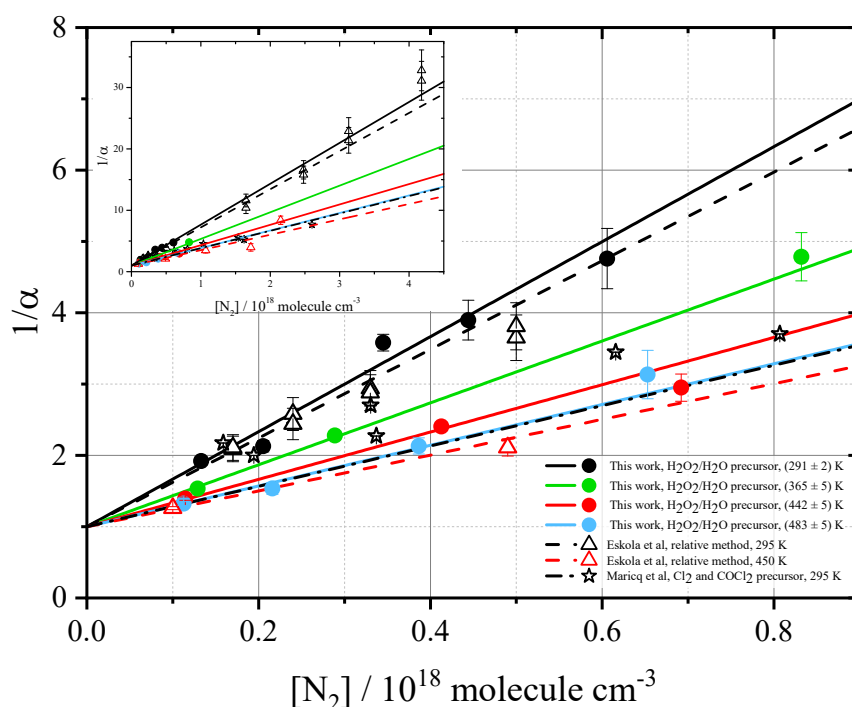
Figure 4-24: Stern-Volmer plot of OH yields in nitrogen, comparing this work (filled circles, solid lines) to Eskola et al. [89] (open triangles, dashed lines) and Maricq et al. [211] (open stars, dash-dotted line). Inset shows full pressure range of Eskola et al. data. The intercepts are fixed to unity. There were no uncertainties reported for the Maricq et al. data, where they referred to another study for their best estimate.

Table 4-4: Comparison of quenching coefficients for $CH_3OCH_2 + O_2$ obtained in the current work with previous measurements. M = N_2 for all measurements.

Reference	Precursor	Technique[a]	T / K	P / Torr	k_M/k_C[b]
Sehested et al. [210]	Cl + DME	FTIR	296	0.38 – 940	3.13 ± 0.51
Maricq et al. [211]	Cl + DME	TIR	295	4.9 – 80.3	4.3
			350	5.0 – 50.0	2.9
Rosado-Reyes et al. [213]	Cl + DME	TIR	295	10 – 200	7.15
			450	10 – 200	0.87
Eskola et al. [89]	CH_3OCH_2Br	LIF/RM	295	5.3 – 95.3	6.05 ± 0.54
		LIF/RM	450	unknown	2.51 ± 0.48
	Cl + DME	LIF/AM	295	5 – 25.01	4.71 ± 0.14
		LIF/AM	450	5 – 99.98	2.36 ± 0.12
This work	OH + DME	LIF	291	4.1 – 18.8	6.66 ± 1.06
		LIF	365	4.9 – 31.3	4.34 ± 0.47
		LIF	442	5.3 – 31.5	3.32 ± 0.66
		LIF	483	5.7 – 32.6	2.86 ± 0.35

[a]Initialisms: FTIR, Fourier transform infrared spectroscopy; TIR, transient infrared; RM, relative method; AM, absolute method. [b]Units are 10^{-18} cm^3 molecule^{-1}. Uncertainties are statistical at the 2σ level.

The current work does have some limitations, primarily higher pressures cannot be explored using this technique, as a result of the ~10% lower limit on the ability to detect yields (which decrease at higher pressures). Alongside pressure limitations, there is a constraint concerning temperature, where this method will not work above the temperature at which the fuel of interest begins to propagate by a thermal route (reaction R 4-4) via QOOH decomposition. For DME this is approximately 230 °C. To make measurements of well-skipping OH formation above this temperature would require much more complicated analysis, as multiple OH regeneration processes can take place concurrently. If only QOOH decomposition was occurring, then measurements of R + O_2 rate coefficients would still be accurate using the method presented in this work, however yields would be perturbed. If a second oxygen addition (O_2 + QOOH) was taking place, then both yields and rate coefficients would not be accurately measurable using the

current analysis method. DME is the simplest ether, but more complex fuels (such as DEE), would have more than one possible initial abstraction site, and therefore isomers of the R radical. The method presented does not differentiate between different R radical isomers, and as such would present yields and rate coefficients as averaged values.
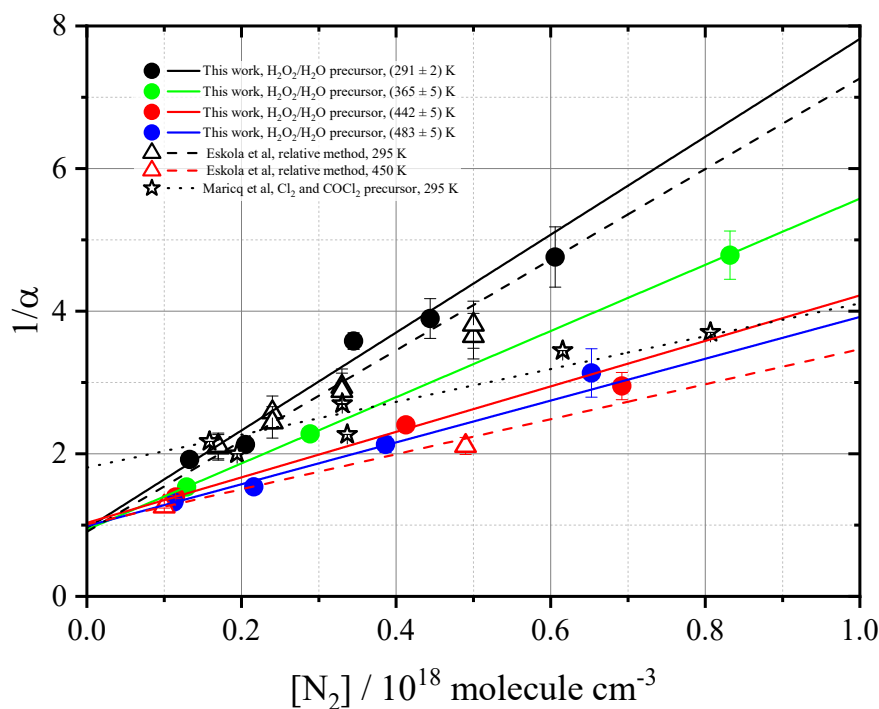
Figure 4-25: Stern-Volmer plot of OH yields in nitrogen. Comparing this work (filled symbols) to Eskola et al. [89] (open triangles) and Maricq et al. [211] (open stars). The intercepts are floated. There are no uncertainties reported for the Maricq et al. data, where they referred to another study for their best estimate.

Floated intercepts for the current work's OH yield measurements in Figure 4-25, gave the following OH yields at [M] = 0: (from low to high temperature) $(105 \pm 23)\%$, $(107 \pm 1)\%$, $(97 \pm 6)\%$, and $(101 \pm 5)\%$, where errors refer to the statistical uncertainty at 1σ level. This suggests pinning the intercepts of the Stern-Volmer plots to unity is suitable, and it is possible the yields at all temperatures do tend towards 100%, however, more measurements of OH yields would clearly define the intercepts more robustly.

4.8 Additional Experimental Parameters

For experimental data, global fitting was used to analyse traces grouped together at the same temperature and pressure, but obtained over a range of $[O_2]$. A wide variation in DME concentration was not normally used across a group of traces, and as such, obtaining k_{OH+DME} from a narrow range of [DME] results in a poorly defined bimolecular rate coefficient for OH + DME, however, Figure 4-26 demonstrates measurements in this work are still mostly in agreement with k_{OH+DME} measured by Carr et al. [186] previously in this laboratory, when uncertainties are considered. 15% is approximately the greatest deviation of this work from the Arrhenius parameterisation given by Carr et al. Regardless, the ability to ascertain k_{OH+DME} has no direct effect on the outcome of $k_{CH3OCH2+O2}$ and OH yield determinations.
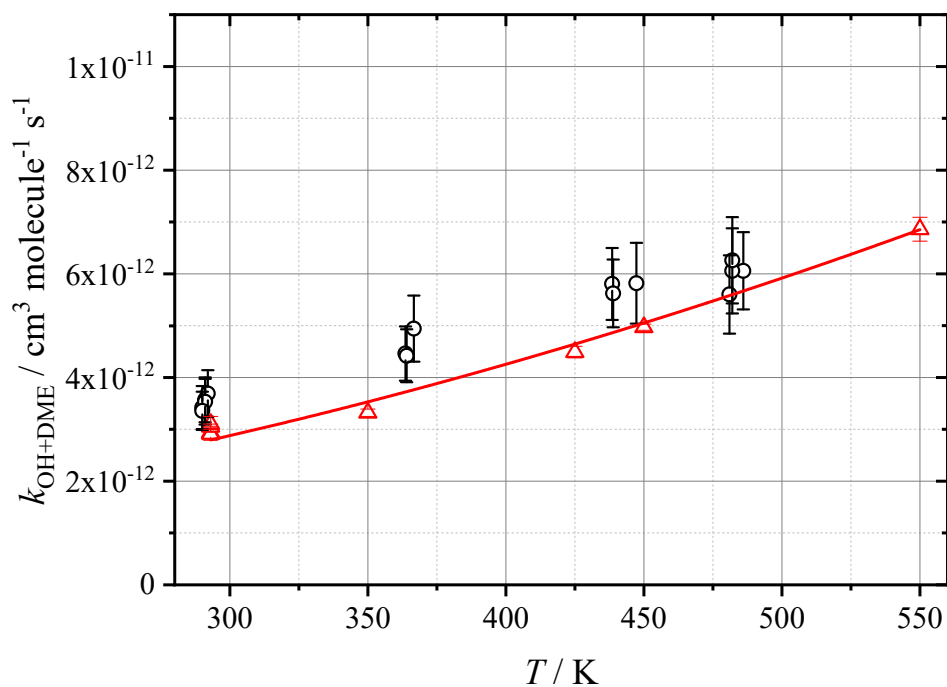
Figure 4-26: Comparison of k_{OH+DME} measured in this work from global analysis (black), with Carr et al. [186] (red) where errors are 95% confidence limits. Uncertainties in this work are 2σ + 10% of measured k_{OH+DME}. Arrhenius fit for Carr et al. data is the reported fit for their whole data set (195 – 800 K).

k_x from global analysis are also presented in Figure 4-27, and are mostly negligible (less than 200 s^{-1}, comparable to the loss of OH in the system). Further, when the error bars are considered, the values determined for k_x are even less significant, and there appears to be no real trend with pressure or temperature. This suggests that any real rates

determined by the k_x parameter are likely not decomposition of the CH_3OCH_2 radical, as this would be expected to increase with temperature.
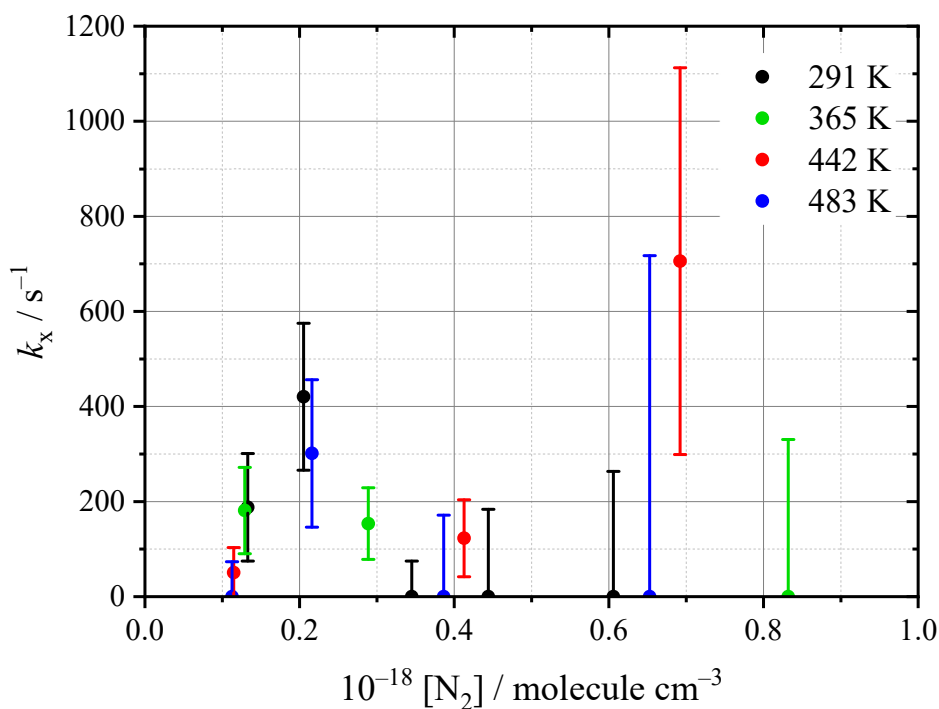
Figure 4-27: Rates obtained for k_x from global analysis of H_2O_2/H_2O experiments in the DME system.

Comparisons between $k_{CH3OCH2+O2}$ retrieval by global analysis and single trace bimolecular determination of $k_{CH3OCH2+O2}$ at room temperature are shown in Figure 4-28, and differ only slightly, likely as a result of global analysis being non-weighted. The uncertainties on the globally determined parameters are reduced, which is expected as a result of the constraints imposed upon the analysis using this method.
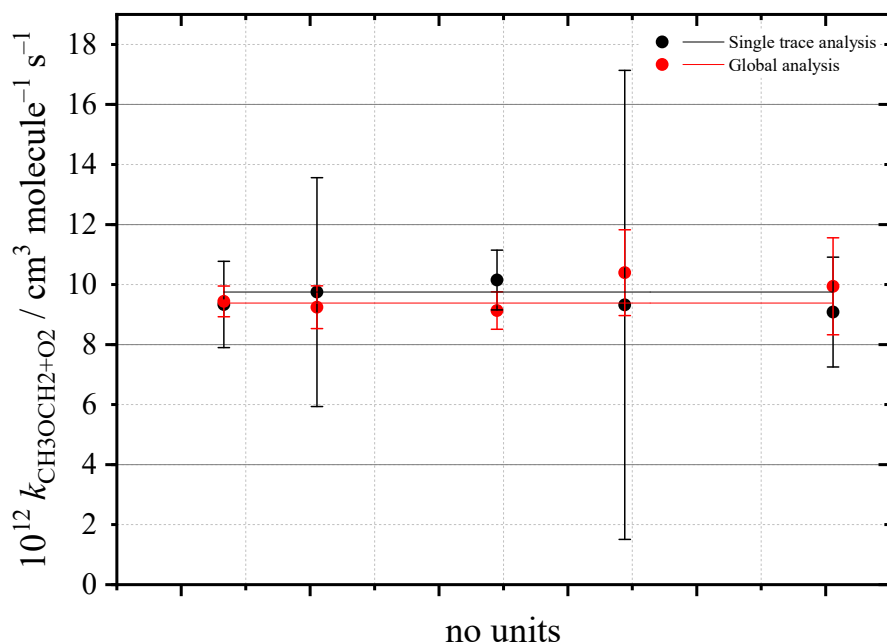
Figure 4-28: Global weighted/unweighted analysis comparison with single trace weighted/unweighted analysis for the DME system. Uncertainties on data are 2σ statistical, and the x-axis is arbitrary to allow visualisation of weighted average values. Average values are (9.75 ± 0.63) and (9.38 ± 0.42) × 10⁻¹², where uncertainties are the 95% confidence limits. Data are for 291 K H₂O₂/H₂O precursor experiments.

4.9 Methyl *tert*-Butyl Ether, Trimethyl Orthoformate, and Di-*n*-Butyl Ether Systems

No conclusive evidence for well-skipping was found for experiments investigating the DBE, MTBE, and TMOF systems. Similar experiments were conducted to those outlined in this chapter, and no consistent reproducible linear dependence of $(k'_b + k'_c)$ on oxygen was observed at low pressure. Often at the lowest concentrations of $[O_2]$ ($\sim 10^{14}$ molecule cm^{-3}) no biexponential decays were observed, and so the range of $[O_2]$ that was investigated may have been higher than the experiments for DME and DEE. The investigation into the effect [ether] has on the ability to retrieve well-skipping parameters (section 4.5) was conducted prior to the DBE experiments, but not those for MTBE and TMOF, and so it is possible that optimal conditions were not used, thus chemical activation in these systems should not be totally dismissed. All experiments however, were carried out after conclusive evidence for well-skipping in the DEE and DME systems had been observed, and so the same should have been possible for MTBE and TMOF were chemical activation occurring.

The absence of chemically activated OH from the DBE, MTBE and TMOF systems under conditions where chemically activated OH production is observed for

DEE/O_2 and DME/O_2 suggests that the transition state barrier to OH may be much closer in energy to the R + O_2 entrance channel (or indeed above this value). Modelling conducted in Chapter 6 section 6.8 using MESMER demonstrated the inhibition of OH yields by raising this transition state. Additionally, chemical activation in MTBE may be absent due to the seven-membered ring transition state between RO_2 and QOOH radicals being less entropically favourable compared to the six-membered ring formed in the DME system. Ogura et al. [220] calculated that the *A* factor for a seven-membered ring is only 12% of the six-membered ring equivalent. The larger size of DBE and MTBE may also increase the likelihood of collisional stabilisation into the potential energy surface wells, inhibiting chemical activation, however chemical activation and significant well-skipping was observed for the comparably-sized DEE molecule, which makes this less probable for MTBE. DBE is significantly larger than DEE. Additionally, the higher transition state barrier for QOOH ↔ OH in the MTBE system, as opposed to that for DME, could be harder to surmount as a result of the negative effects of entropy, and ring strain, required for formation of the 4,4-dimethyl-1,3-dioxolane species (see Figure 6-32 in Chapter 6). Finally, steric hindrance may play a role in the rearrangement of RO_2 to QOOH for DBE, where long side chains are present.

4.10 Conclusions

A method for determining R + O_2 rate coefficients at low temperature and pressure has been presented, with details of the analysis of biexponential OH decays arising from chemical activation. OH yields obtained using this technique are in agreement with those made by Eskola et al. [89] (room temperature quenching coefficients k_M/k_C = (6.66 ± 1.06) × 10^{-18} and (6.05 ± 0.54) × 10^{-18} cm^3 molecule^{-1} respectively), and k(CH$_3$OCH$_2$ + O_2) was measured to within 5%, or in agreement considering uncertainties, at all pressures considered. Eskola et al. observed no pressure dependence for measurements in helium at room temperature. This is consistent with measurements in the current work which were carried out in N_2 bath gas, and appeared to be at the high pressure limit. R + O_2 measurements at higher temperatures (442 – 483 K) reproduced the positive pressure dependence seen by Eskola et al.

Simple chemical kinetic modelling was conducted to simulate chemical activation data, and rationalise the difficulty in extracting parameters from biexponential OH decays that do not exhibit well-separated time constants. Lower concentrations of oxygen, and

high concentrations of DME were shown to achieve ideal conditions for biexponential analysis, and yield a more robust $R + O_2$ rate coefficient.

The limitations of this experimental method for determining $R + O_2$ rate parameters are threefold; the molecule must well-skip; parameters are particularly difficult to extract once OH yields are reduced to ~10%, typically at low temperatures and high pressures; and at higher temperatures, other mechanisms for the regeneration of OH are possible, where more complex analysis would be required to identify the rate parameters from chemical activation accurately. Given the ability to deliver the correct concentrations of reactants, and a fuel which exhibits well-skipping, this method enables measurements of $R + O_2$ rate coefficients for molecules which don't have a readily-available brominated precursor.

Chapter 5 Kinetic Study of $C_2H_5OC_2H_4 + O_2$ Rate Parameters

5.1 Abstract

This chapter presents the first rate coefficients and OH yields measured for the $C_2H_5OC_2H_4 + O_2$ reaction relevant to the low temperature oxidation of DEE. The rate coefficient $k_{C2H5OC2H4+O2}$ is reported at 298 – 464 K, in 5.2 – 28.4 Torr of nitrogen. At room temperature, $k_{C2H5OC2H4+O2} = (3.10 \pm 0.55) \times 10^{-11}$ cm^3 molecule^{-1} s^{-1}, where the uncertainty is statistical at the 2σ level. Measurements showed the rate coefficient to be independent of pressure, although theoretical predictions showed the presence of a positive dependence at very low pressures. The temperature dependence of the R + O$_2$ rate coefficient can be parameterised by $k_{C2H5OC2H4+O2}$(298–464 K) = $(4.1 \pm 2.2) \times 10^{-12} \times e^{(-5.0\pm1.9)/RT}$ cm^3 molecule^{-1} s^{-1}, where the uncertainties are statistical and calculated at the 2σ level.

Two methods were used to determine the OH yields experimentally, and were in excellent agreement with one another. Under comparable conditions, the experimental OH yields were lower than those observed for the CH$_3$OCH$_2$ + O$_2$ reaction in Chapter 4, which can be attributed to the increased likelihood of the larger $C_2H_5OC_2H_4O_2$ molecule undergoing collisional deactivation.

Ab initio calculations at the CCSD(T)/Jun-cc-pVTZ//M06-2X/Jun-cc-pVTZ level were carried out on the low temperature oxidation surface of DEE, and the experimentally observed rate parameters were compared to the theoretical calculations using master equation methods, where a significant lowering (by ~7 kcal mol^{-1}) of the transition state barrier to the formation of OH was required in order to achieve good agreement between the experimental data and the master equation model. Relative to the R + O$_2$ entrance channel, the *ab initio* energies calculated for the RO$_2$ and QOOH species were –34.8 and –25.6 kcal mol^{-1} respectively. Energies for the transition state barriers corresponding to RO$_2 \leftrightarrow$ QOOH, and QOOH $\rightarrow$ OH, were calculated to be –15.1 and –3.7 kcal mol^{-1} respectively. The transition state barrier for decomposition of the R radical was found to be 23.7 kcal mol^{-1}. The rate parameters for the DEE R + O$_2$ reaction are also compared to those measured for the DME system.

5.2 Introduction

Diethyl ether is a potential biofuel alternative to conventional fossil fuels, bearing a similar chemical structure to dimethyl ether and oxymethylene ether, both of which have already been the subject of academic [87, 89, 185, 186, 221, 222] and industrial research [26, 29], demonstrating potential to reduce emissions, increase octane numbers and improve fuel efficiency [26, 73]. Optimal use of biofuels in novel engines, such as the HCCI engine, will require the autoignition mechanisms of the fuels used to be well understood [223], however there is not yet a complete understanding of the chain-branching mechanism that is crucial to the autoignition process. The reaction between the ethoxy ethyl R radical ($C_2H_5OC_2H_4$) formed during the reaction between DEE and OH (reaction R 5-1), and molecular O_2 (reactions R 5-2, R 5-3, and R 5-4), is a reaction integral to our understanding of the behaviour of the DEE-derived R radical, which is in turn key to DEE's low temperature combustion behaviour.

The R + O_2 reaction and subsequent mechanism is analogous to that of DME discussed in Chapter 4, with the added complexity of the two initial abstraction sites present within its structure, and therefore increased reaction pathways for O_2 addition and internal rearrangements. The R radical formed in reaction R 5-1 can either be the α- or β-radical, to which the addition of oxygen results in the formation of an energetically excited RO_2^* peroxy radical, on either the α (reaction R 5-2) or β site (reaction R 5-3). As established in Chapter 3, abstraction from the α site is expected to dominate the mechanism. In this work, a non-site specific approach has been used to observe the R + O_2 reaction kinetic parameters, and as such, addition of oxygen to the α or β site cannot be distinguished between. For this reason, the overall addition of O_2 to the generic DEE R radical $C_2H_5OC_2H_4$ given in reaction R 5-4 will be used to refer to the total of the reaction involving both sites. All subsequent reaction species will also be written in generic terms that do not refer to specific sites.

$$C_2H_5OC_2H_5 + OH \rightarrow C_2H_5OC_2H_4 + H_2O \qquad \text{R 5-1}$$

$$CH_3CH_2OCHCH_3 + O_2 \leftrightarrow CH_3CH_2OCH(O_2)CH_3^* \qquad \text{R 5-2}$$

$$CH_3CH_2OCH_2CH_2 + O_2 \leftrightarrow CH_3CH_2OCH_2CH_2O_2^* \qquad \text{R 5-3}$$

$$C_2H_5OC_2H_4 + O_2 \rightarrow C_2H_5OC_2H_4O_2^* \qquad \text{R 5-4}$$

The energetically excited peroxy radical formed in reaction R 5-4 can undergo pressure-dependent stabilisation to the RO_2 species (reaction R 5-5), a radical which is relatively stable. Competitive reactions exist, whereby RO_2 can undergo re-dissociation back to reactants (particularly at high temperatures), or form an excited *QOOH radical. Subsequent rapid decomposition of this radical to OH and acetaldehyde (reaction R 5-6) is the well-skipping source of OH yields measured in this work.

$$C_2H_5OC_2H_4O_2^* \xrightarrow{M} C_2H_5OC_2H_4O_2 \qquad \text{R 5-5}$$

$$C_2H_5OC_2H_4O_2^* \leftrightarrow C_2H_4OC_2H_4OOH^* \rightarrow 2CH_3CHO + OH \qquad \text{R 5-6}$$

An internal hydrogen abstraction enables the formation of QOOH from RO_2, and four different pathways are available for this mechanism (Figure 5-1), where varying ring sizes are formed depending on the initial DEE abstraction site, and the site of hydrogen abstraction in the rearrangement. The most probable pathway here is that of the α–α rearrangement; the majority of R radicals that form RO_2 species will be α R radicals, six-membered rings are favoured, and SAR predictions by Aschmann and Atkinson [224] suggest isomerisations (by alkoxy radicals) are enhanced by a factor of 13 when the abstraction occurs adjacent to the ether O atom group. Destabilisation of the *QOOH species is not considered, due to the higher energy of the stabilised form's energy in comparison with the RO_2 well depth shifting the equilibrium towards the RO_2* species in the first step of reaction R 5-6.
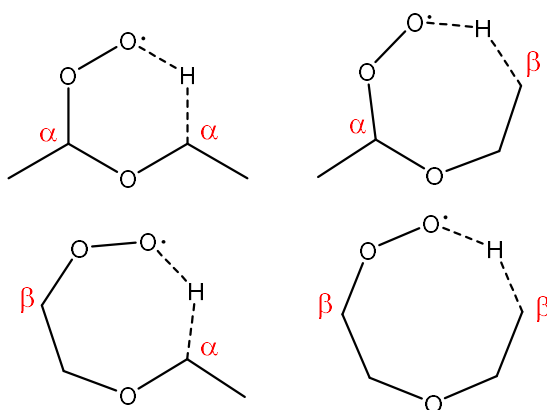
Figure 5-1: Possible ring formations in the rearrangement of RO₂ to QOOH for the DEE system.

The mechanism presented in Scheme 5-1 illustrates the reaction mechanisms for the dominant pathways of the measurements in this section.
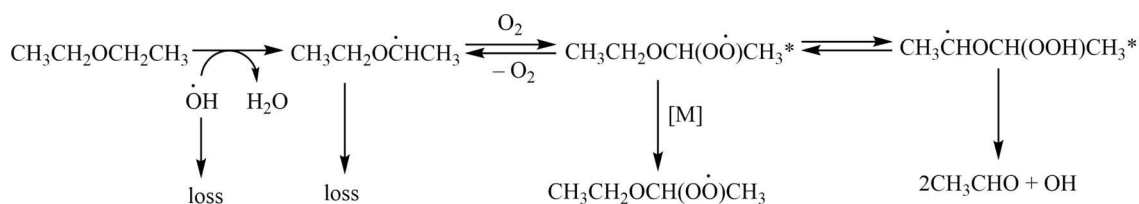
Scheme 5-1: Simplified reaction scheme for the DEE chemical activation mechanism, where the most dominant pathway (H abstraction occurring at the α site, and RO₂ to QOOH rearrangement occurring via a six-membered ring) is shown.

No previous experimental studies on the R + O_2 reaction rate coefficient for the diethyl ether system exist, and usage of the brominated molecule method employed for dimethyl ether studies would only allow the study of the minor R radical formed from β position hydrogen abstraction in the OH + DEE reaction. Using the new method proposed in Chapter 4, reaction R 5-4 can now be studied using diethyl ether and an OH precursor.

Despite no measurements of DEE's R + O_2 rate parameters, there have been some theoretical studies on the oxidation surface for diethyl ether following hydrogen abstraction of the parent fuel. Di Tommaso et al. [115], Sakai et al. [225], Sandhiya et al. [226], Wang and Wang [227], Hu et al. [228], have calculated some, or all, of the species this chapter focuses on, using varying methods and basis sets. More details are provided in the discussion in section 5.8.1.

5.3 Experimental

The experimental setup used in this chapter is largely the same as that used throughout the rest of this work, and virtually identical to that in Chapter 4. The usual conventional slow flow laser flash photolysis setup was combined with laser-induced fluorescence to monitor OH. The reactants were DEE (Sigma-Aldrich, ≥99%), OH precursor (hydrogen peroxide, H_2O_2, Sigma-Aldrich, 50% (w/w) in H_2O), buffer gas (N_2, BOC, oxygen-free), and O_2 (BOC, 99.5%). On average, experiments were carried out at lower pressures than the majority of the work in this thesis, between 5 and 28 Torr of nitrogen. Higher pressures were not explored, as the suppression of yields led to difficulty

in extracting rate parameters under these conditions. Temperatures reported above room temperature have an associated uncertainty of approximately ±10 K, due to the calibrations presented in Chapter 2.

Contact of hydrogen peroxide with the metal pipes and consequent decomposition results in some oxygen always being delivered to the system, which was estimated to be approximately $(0.4 – 5.1) \times 10^{14}$ molecule cm^{-3} (the method for estimating this oxygen concentration was discussed in Chapter 4), and varies depending on pressure, flow and precursor. Photolysis of the hydrogen peroxide at 248 nm was used to generate the hydroxyl radicals, as described previously, and was the source of OH for all experiments in this work. Reactions were studied under pseudo-first order conditions where [ether] >> [OH]. Extensive details of the analyses of kinetic traces were presented in Chapter 4, but some further details specific to the diethyl ether experiments can be found in section 5.4.

5.4 Alternative Data Analyses

Treatment of data for the diethyl ether chemical activation experiments was carried out using the same principles as those outlined in Chapter 4. Additionally, some experiments were conducted in a slightly different manner. The following description outlines an experimental scenario used for some DEE experiments to obtain OH yields from chemical activation, with no information on $R + O_2$ rate coefficients. An example of a biexponential decay and a bimolecular plot obtained by the same technique used for DME measurements are shown in Figure 5-2 and Figure 5-3 respectively.
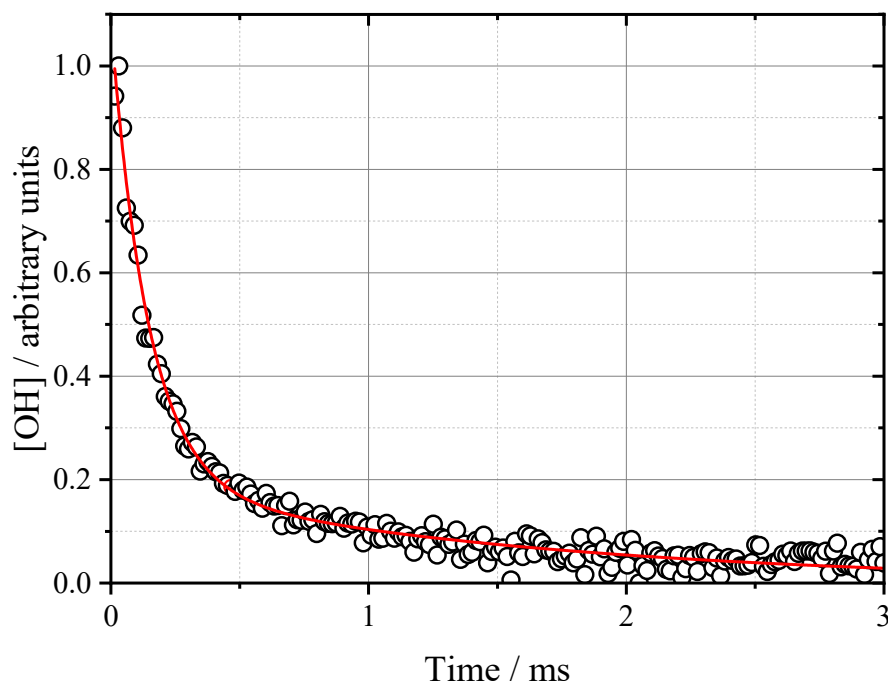
Figure 5-2: An example biexponential decay, where parameters $k_b' = (1070 \pm 150)$ s^{-1}, $k_c' = (690 \pm 100)$ s^{-1}, $k_d = 400$ s^{-1} fixed, and $k_a' = (5390 \pm 350)$ s^{-1}, at $[O_2] = 5.9 \times 10^{13}$ molecule cm^{-3}. All uncertainties are 2σ and statistical. Experimental conditions were 464 K, 7 Torr N_2, and $[DEE] \approx 4.8 \times 10^{14}$ molecule cm^{-3}.
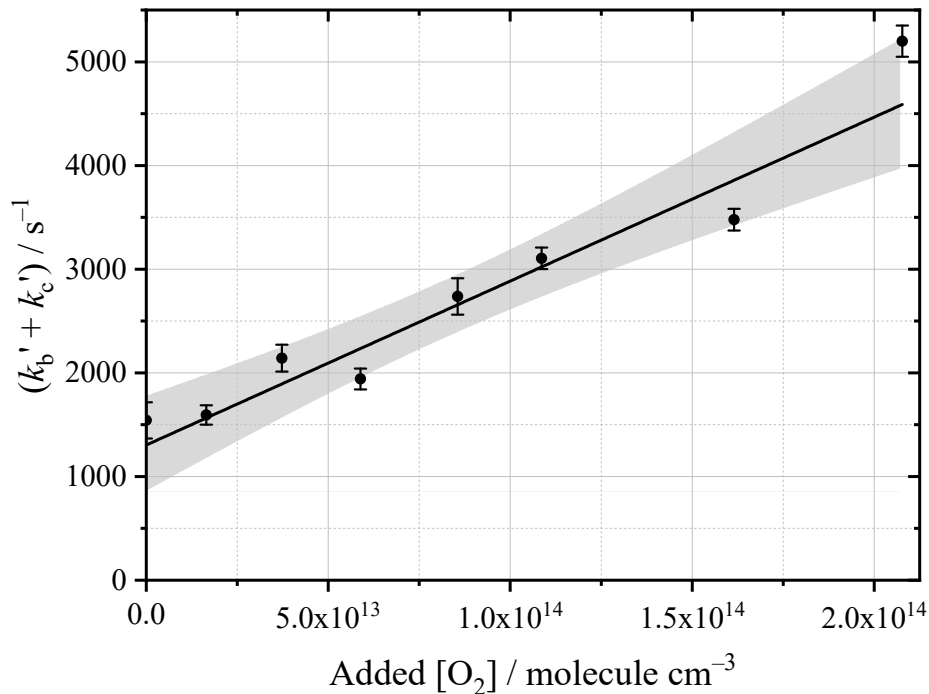
Figure 5-3: Bimolecular plot for the determination of the $C_2H_5OC_2H_4 + O_2$ rate coefficient, at 464 K, 7 Torr N_2, $[DEE] \approx 4.8 \times 10^{14}$ molecule cm^{-3}. $k_{C2H5OC2H4+O2} = (1.58 \pm 0.36) \times 10^{-11}$ cm^3 molecule^{-1} s^{-1}. Shaded area represents the bounds of the 95% confidence limits. All uncertainties are 2σ and statistical.

Where all the experiments concerning DME used small amounts of oxygen to produce biexponential decays, under a high enough oxygen concentration (approximately 10^{15} molecule cm^{-3}), the biexponential decay reverts back to a single exponential decay, where the very fast OH recycling from the chemical activation process results in a slower decay than that of a kinetic trace in the absence of O_2 (other than O_2x). The difference between the bimolecular rate coefficient measured in the absence and presence of oxygen gives the OH yield from chemical activation (Figure 5-4 and equation E 5-1). OH yields have been measured in this way previously at the University of Leeds [229, 230].

$$\text{OH yield} = \frac{k_{\text{bim}}(\text{no } O_2) - k_{\text{bim}}(O_2)}{k_{\text{bim}}(\text{no } O_2)} \times 100 \qquad \text{E 5-1}$$

To analyse the single exponential decays obtained by this no/high oxygen regime, the same global treatment of the biexponential equation described in Chapter 4 can be used. However, the traces contain no information about $k_{\text{C2H5OC2H4+O2}}$, only OH yields, and as such only $k_{\text{C2H5OC2H4+O2}}$ obtained from the low oxygen experiments, with a bimolecular analysis of R + O_2, are reported in this work. Instead, single trace analysis of the decays in the presence and absence of O_2 was used, with weighted linear least squares analysis of the bimolecular plots, as in the Figure 5-4 example. For the bimolecular plots in the absence of added O_2, the small amount of O_2 always present in the system often resulted in biexponential decays. The analysis of these decays meant the k_a' parameter was used for the no-O_2 decays, and the bimolecular plots have no [DEE] = 0 intercepts, as this is included as k_d in the biexponential decay equation. The bimolecular plot in the presence of O_2, where decays are single exponential, will include a [DEE] = 0 intercept.
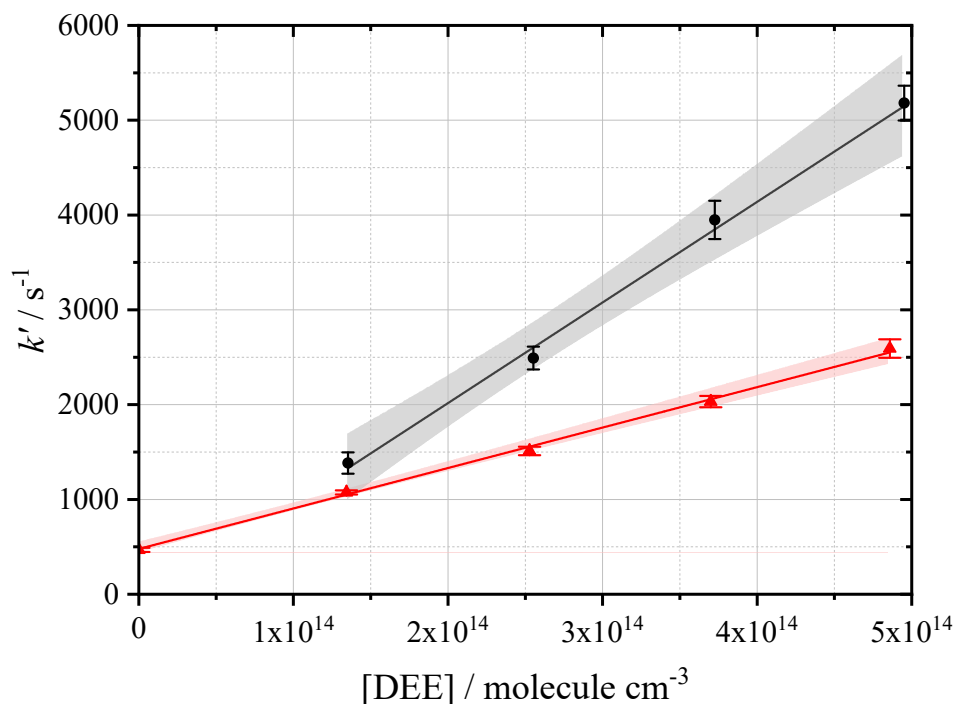
Figure 5-4: Bimolecular plot in the absence (black circles) and presence (red triangles, $[O_2] = 2 \times 10^{15}$ molecule cm^{-3}) of oxygen. Determination at 457 K, 7 Torr N$_2$, k_{OH+DEE}(no O$_2$) = (1.06 ± 0.09) × 10^{-11} cm^3 molecule^{-1} s^{-1}, k_{OH+DEE}(O$_2$) = (4.27 ± 0.22) × 10^{-12} cm^3 molecule^{-1} s^{-1}, OH yield = (60 ± 10)%. Error bars are purely statistical at the 2σ level, as are the uncertainties on returned parameters. Shaded areas represent the bounds of the 95% confidence limits. The intercepts are (–110 ± 270) s^{-1} (black), and (480 ± 40) s^{-1} (red).

5.5 Temperature Dependent Measurements of the C$_2$H$_5$OC$_2$H$_4$ + O$_2$ Reaction

Measurements of the R + O$_2$ rate coefficient ($k_{C2H5OC2H4+O2}$) in N$_2$ for DEE have been made in this work, and are the first observation of this bimolecular rate coefficient. The data are presented in Figure 5-5, where the values obtained for $k_{C2H5OC2H4+O2}$ are shown as a function of temperature. All rate coefficients measured are also presented in Table 5-2. The bimolecular rate coefficient for C$_2$H$_5$OC$_2$H$_4$ + O$_2$ in this work exhibits a negative temperature dependence, consistent with the behaviour anticipated for a barrierless addition reaction, and not dissimilar to that seen for the formation of RO$_2$ radicals in the analogous DME system (Chapter 4).
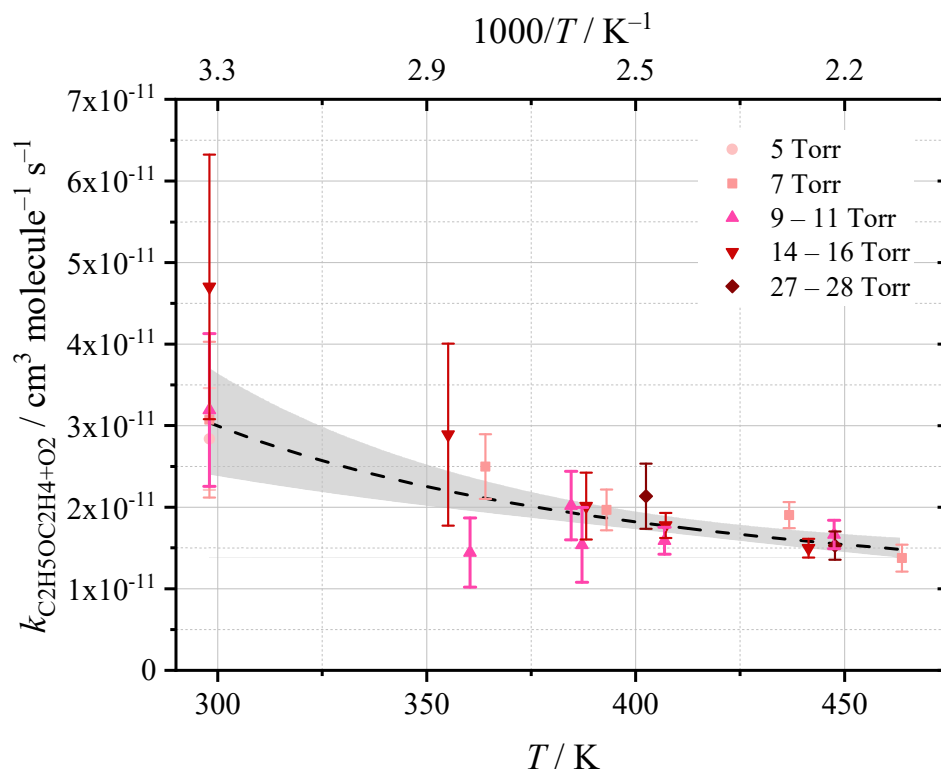
Figure 5-5: The C₂H₅OC₂H₄ + O₂ rate coefficient measured as a function of temperature. Errors are 2σ and statistical. Grey shaded area represents the 95% confidence bands. $A = (4.1 \pm 2.2) \times 10^{-12}$ **cm³ molecule⁻¹ s⁻¹.** $E_a = (-4.97 \pm 1.86)$ **kJ mol⁻¹. Uncertainties are statistical at the 2σ level. Approximate total pressure ranges are shown.**

The magnitudes of the $C_2H_5OC_2H_4 + O_2$ rate coefficients measured for diethyl ether are larger than often estimated for $R + O_2$ reactions, where typically rate coefficients between $(1 - 10) \times 10^{-12}$ cm³ molecule⁻¹ s⁻¹ would be anticipated. Experimentally, a wide range (over two orders of magnitude) of rate coefficients have been reported for the addition of O_2 to R radicals. Some examples are listed in Table 5-1. A relationship between molecular structure and rate coefficient is unknown, although previously a relationship between the ionisation potential of the R radical and k_{R+O_2} was proposed, discussed in Chapter 4. The ionisation energy of the DEE-derived R radical is expected to be lower than that for DME's analogous R radical, which would suggest the prediction of a faster $R + O_2$ coefficient for the DEE system in comparison to DME.

Table 5-1: Examples of R + O₂ rate coefficients measured previously.

Reaction and reference	R radical structure	k_{R+O2}
Ethyl + O₂ [231]		1.50×10^{-13}
Vinoxy + O₂ [232]		2.6×10^{-13}
Neopentyl + O₂ [233]		1.6×10^{-12}
Methyl + O₂ [231]	$\cdot\, CH_3$	2.2×10^{-12}
Isobutyl + O₂ [233]		2.9×10^{-12}
Propionyl + O₂ [200]		5.4×10^{-12}
Acetyl + O₂ [200, 205]		$(5–6) \times 10^{-12}$
Methylvinyl + O₂ [234]		7.2×10^{-12}
Cyclohexyl + O₂ [233]		1.4×10^{-11}
Cyclopentyl + O₂ [233]		1.7×10^{-11}
Ethynyl + O₂ [235]	$HC\equiv C\cdot$	3.3×10^{-11}

Rate coefficients are in units of cm³ molecule⁻¹ s⁻¹.

Perhaps unsurprisingly, the $C_2H_5OC_2H_4 + O_2$ rate coefficient measured is not orders of magnitude different to that reported for $CH_3OCH_2 + O_2$ in the previous chapter, but it is approximately three times larger; the average room temperature $k_{C2H5OC2H4+O2} = (3.10 \pm 0.55) \times 10^{-11}$ cm³ molecule⁻¹ s⁻¹. Furthermore, the Arrhenius parameterisation demonstrates that the data suggests a barrierless addition reaction, as expected, with an Arrhenius fit-derived barrier of (-5.0 ± 1.9) kJ mol⁻¹, statistically indistinguishable from the barrier determined for the $CH_3OCH_2 + O_2$ reaction in Chapter 4. The bimolecular rate

coefficient for reaction R 5-4 was also measured as a function of pressure using the method outlined above, presented in Figure 5-5, and is compared to master equation calculations later in this chapter. No significant pressure dependence is clear from these measurements, although the relatively narrow range of pressures accessible via this method should be noted. A model developed by Yasunaga et al. [236] for the validation of DEE shock tube experiments from 900 – 1900 K used a temperature independent rate coefficient of $k_{C2H5OC2H4+O2} = 0.64 \times 10^{-11}$ cm^3 molecule^{-1} s^{-1}. It is difficult to compare the study with this work, given the large difference in temperature, however the rate coefficient presented here should provide more robust information to base model estimations upon. The model developed by Yasunaga et al. is not sensitive to the R + O$_2$ rate coefficient when varied by a factor of two.

Further developments to the Yasunaga et al. [236] DEE model were made by both Tran et al. [237] and Serinyel et al. [238], for the validation of high pressure flame speeds, and jet stirred reactor experiments respectively. Tran et al. observed no large sensitivity to the main DEE oxidation reaction pathways, where the mechanism was instead dominated by H-abstraction and radical decomposition. This is unsurprising given the experiments were more relevant to the nature of high temperature combustion outlined in Chapter 1. Their estimated $k_{C2H5OC2H4+O2}$ values used were 0.8×10^{-11} cm^3 molecule^{-1} s^{-1} at 298 K, and 1.5×10^{-11} cm^3 molecule^{-1} s^{-1} at 460 K, which are in good agreement at the highest temperatures of this study, but do not reflect the negative temperature dependence reported here (until approximately 600 K, where their rate coefficient begins to decrease; an unusual temperature dependence that is not explained). The further modifications to the model by Serinyel et al. enabled a comparison to experiments conducted using a jet-stirred reactor between 450 – 1250 K, where strong low temperature chemistry was indicated at 10 atm. The R + O$_2$ rate coefficient proposed was adapted from work by Goldsmith et al. [239], and resulted in an overestimation by approximately 65% at ~460 K ($k_{C2H5OC2H4+O2} = 2.3 \times 10^{-11}$ cm^3 molecule^{-1} s^{-1}) compared with the value obtained in this work. The measurements presented here will be more important at the lower temperatures relevant to the study by Serinyel et al., and would help constrain the temperature dependence used for extrapolation to higher temperatures.

Table 5-2: Rate coefficients, $k_{C2H5OC2H4+O2}$, measured in this work. Uncertainties are 2σ and purely statistical.

T/K	$10^{-17}[N_2]^a$	$10^{11} k_{C2H5OC2H4+O2}{}^b$	T/K	$10^{-17}[N_2]^a$	$10^{11} k_{C2H5OC2H4+O2}{}^b$
298	1.65	2.84 ± 0.62	393	1.72	1.97 ± 0.25
298	2.23	3.07 ± 0.96	402	6.62	2.14 ± 0.40
298	3.31	3.19 ± 0.94	407	2.66	1.59 ± 0.17
298	4.86	4.70 ± 1.62	407	3.29	1.78 ± 0.15
355	4.30	2.89 ± 1.12	437	1.55	1.90 ± 0.16
360	2.56	1.45 ± 0.42	441	3.01	1.50 ± 0.11
364	1.89	2.50 ± 0.40	447	2.44	1.67 ± 0.18
385	2.26	2.02 ± 0.42	448	6.13	1.53 ± 0.17
387	2.33	1.54 ± 0.46	464	1.45	1.38 ± 0.17
388	3.75	2.01 ± 0.41			

^{a}units are molecule cm^{-3}. ^{b}units are cm^3 molecule^{-1} s^{-1}.

5.6 Experimental OH Yields for the $CH_3CH_2OCHCH_3 + O_2$ Reaction

OH yields from well-skipping in the DEE system were obtained over 5.2 – 28.4 Torr of N_2, and 298 – 496 K (thermal production of OH from stabilised RO_2 radicals begins above approximately 500 K). Treating these data with a Stern-Volmer analysis (Figure 5-6) demonstrates an increase in yield with increasing temperatures, and the suppression of yields at higher pressures. This is consistent with what would be expected of OH yields from reaction R 5-4, a process deactivated by the pressure-dependent stabilisation of the RO_2* radical (reaction R 5-5). At room temperature (black filled circles, Figure 5-6), yields were particularly low above 5 Torr (approximately 15% and below), which is reflected in the greater uncertainties due to the less pronounced biexponential decays when using the method reliant on these decays. There were no discernible differences between measurements made using the two methods for obtaining OH yields, other than the larger uncertainties on the high/no O_2 method as a result of the non-global approach to analysis. The previous study on the DME system by Eskola et al. [89] at the University of Leeds did not always achieve as good agreement when using various methods (see Table 4-4 quenching coefficients in Chapter 4). All yields, with details of uncertainties and the method used are presented in Table 5-3, and Figure 5-7 differentiates between the yields obtained using both techniques to illustrate this agreement. Quenching coefficients, k_M/k_C, determined from the slope of the Stern-Volmer plots are included in Table 5-4.
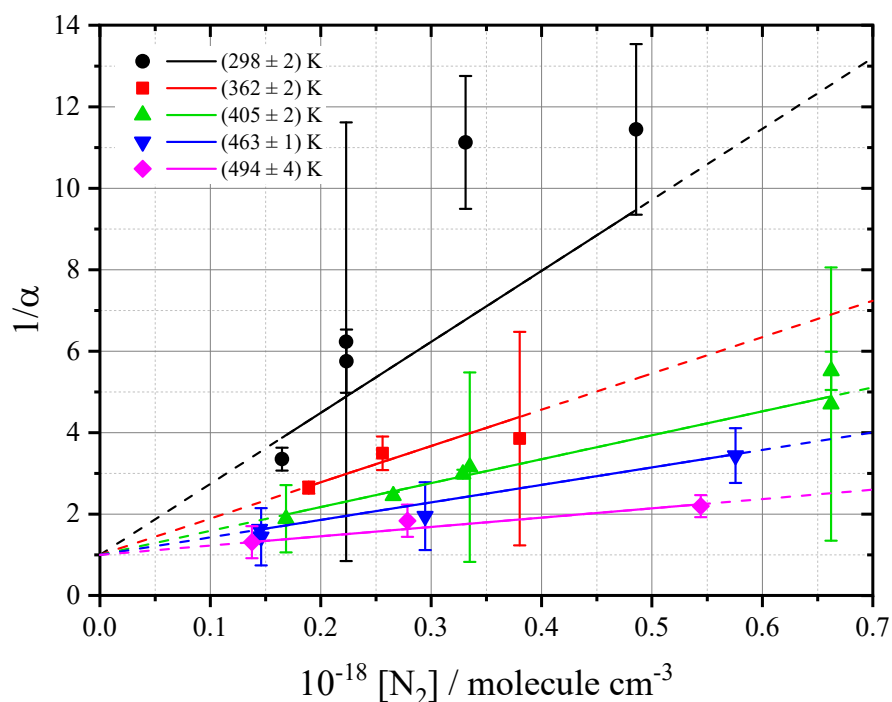
Figure 5-6: Stern-Volmer analysis of OH yields, over a temperature range 298 – 494 K. Fits pinned to intercept of 1 (i.e. 100% yield at 0 Torr pressure). A shared intercept of 0.95 is found when not pinned. Dashed lines are extrapolated past data points. Note a few temperatures are omitted (listed in Table 5-3, as they had no other pressure values to fit a line through). Error bars are statistical at the 2σ level.
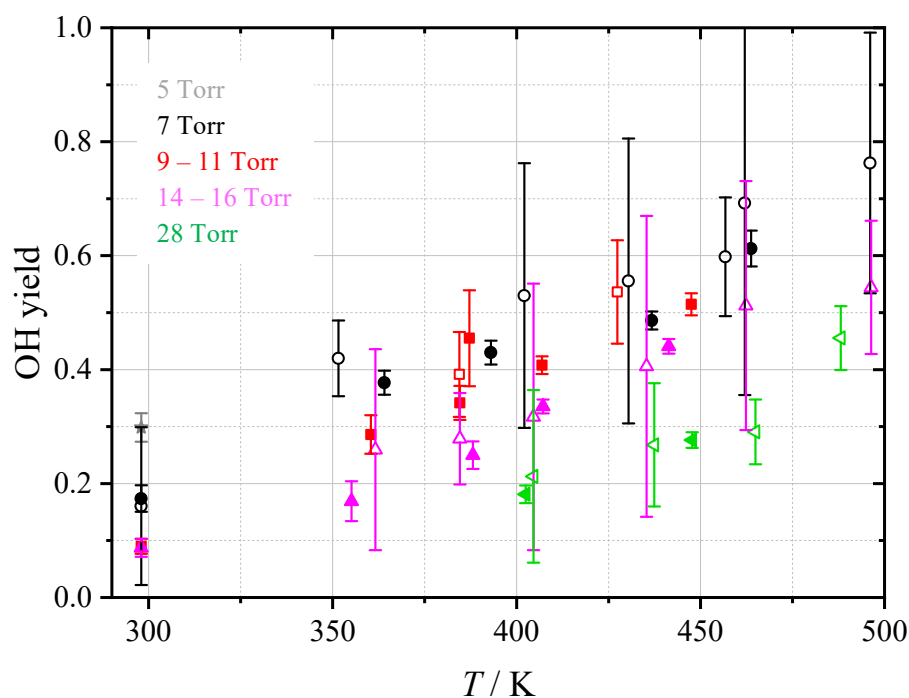
Figure 5-7: Comparison of yields obtained from two methods. Filled symbols indicate yields obtained by the addition of low O₂ concentrations to obtain a bimolecular for the R + O₂ rate coefficient, where the OH yield was extracted by global analysis. Open symbols indicate the yield was extracted from analysis of the bimolecular rate coefficient in the absence and presence of added O₂. Uncertainties are statistical at the 2σ level.

Reciprocal yields were fit using weighted linear analyses, and intercepts are fixed at unity, imposing a 100% OH yield at $[N_2] = 0$ molecule cm^{-3}, which still allowed a good fit to the data. The only possible exception to this observation is the 298 K set of data, where there exists only two well-defined measurements, and three OH yields with particularly large uncertainties.

Table 5-3: OH yields measured for the DEE system. Uncertainties are 2σ and purely statistical.

T / K	$[N_2]^a$	Yield^b	Method	T / K	$[N_2]^a$	Yield^b	Method
298	1.65	30 ± 3	Low O_2	298	2.23	16 ± 14	High/no O_2
298	2.23	17 ± 2	Low O_2	352	1.95	42 ± 7	High/no O_2
298	3.31	9 ± 1	Low O_2	362	3.80	26 ± 18	High/no O_2
298	4.86	9 ± 2	Low O_2	363	7.26	1 ± 18	High/no O_2
355	4.30	17 ± 4	Low O_2	384	2.24	39 ± 7	High/no O_2
360	2.56	29 ± 3	Low O_2	385	3.80	28 ± 8	High/no O_2
364	1.89	38 ± 2	Low O_2	402	1.69	53 ± 23	High/no O_2
385	2.26	34 ± 3	Low O_2	405	3.35	32 ± 23	High/no O_2
387	2.33	46 ± 8	Low O_2	405	6.62	21 ± 15	High/no O_2
388	3.75	25 ± 2	Low O_2	427	1.99	54 ± 9	High/no O_2
393	1.72	43 ± 2	Low O_2	430	1.55	56 ± 25	High/no O_2
402	6.62	18 ± 2	Low O_2	435	3.06	41 ± 26	High/no O_2
407	2.66	41 ± 2	Low O_2	437	6.20	27 ± 11	High/no O_2
407	3.29	34 ± 1	Low O_2	457	1.47	60 ± 10	High/no O_2
437	1.55	49 ± 2	Low O_2	462	1.46	69 ± 34	High/no O_2
441	3.01	44 ± 1	Low O_2	462	2.95	51 ± 22	High/no O_2
447	2.44	51 ± 2	Low O_2	465	5.76	29 ± 6	High/no O_2
448	6.13	28 ± 1	Low O_2	488	5.44	46 ± 6	High/no O_2
464	1.45	61 ± 3	Low O_2	496	1.38	76 ± 23	High/no O_2
				496	2.79	54 ± 12	High/no O_2

^{a}Units are 10^{17} molecule cm^{-3}. ^{b}Yields are in %.

A Stern-Volmer plot with OH yield intercepts allowed to float is shown in Figure 5-8, which differs from the analogous plot for the DME system, where the intercepts are

not close to unity. From 298 – 494 K, the corresponding intercepts at $[N_2] = 0$ are –2.0, 0.49, 0.40, 1.04, and 1.13. Translated into OH yields, this suggests yields of –50%, 205%, 249%, 96%, and 88%. For comparison, floated intercepts for the DME system suggested yields between 97% and 107%. Clearly, the yields at zero pressure are mostly not realistic, and this is largely due to a lack of sufficient data points to properly characterise the fits, without pinning to an intercept of 1. A greater range of differing temperatures was explored for the DEE system compared to the DME experiments, so as to provide more information to the master equation calculations in this chapter. As such, there are fewer 'groups' of data to construct extensive Stern-Volmer plots. This is not an issue for the master equation analysis (see Figure 5-16), but does not translate well to illustrative figures.
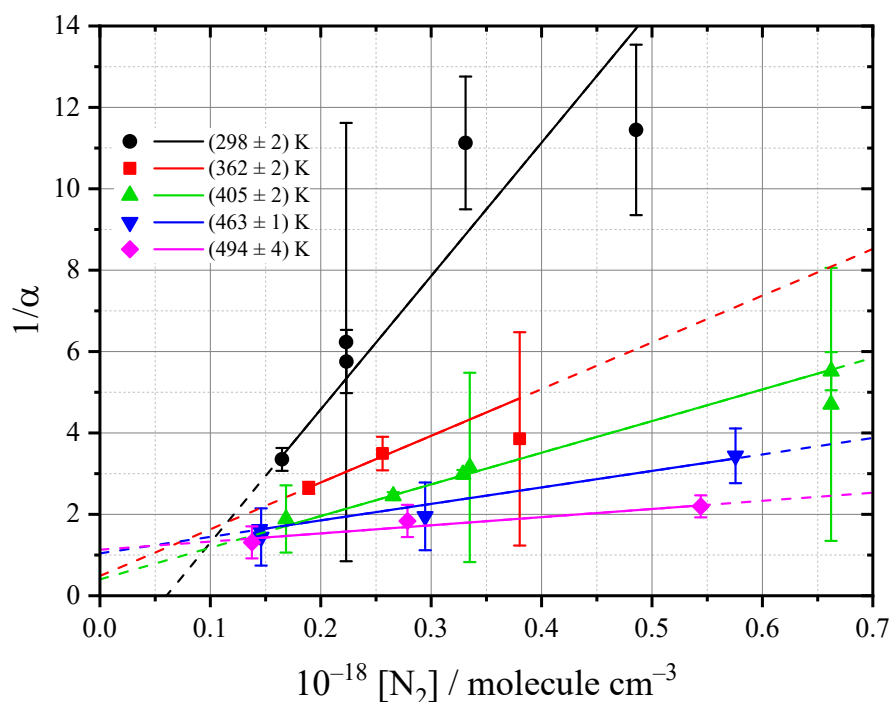
Figure 5-8: The same Stern-Volmer plot as in Figure 5-6, but with intercepts floated. Intercepts are –2.0, 0.49, 0.40, 1.04, and 1.13 with increasing temperature from 298 – 494 K. Error bars are statistical at the 2σ level.

Table 5-4: Quenching coefficients for $C_2H_5OC_2H_4 + O_2$ obtained in the current work for the fits in Figure 5-6. M = N_2 for all measurements.

T / K	P / Torr	k_M/k_C / 10^{-18} cm^3 molecule^{-1}
298 ± 2	$5.2 - 15.3$	17.44 ± 6.87
362 ± 2	$7.1 - 14.2$	8.91 ± 1.28
405 ± 2	$7.0 - 27.8$	5.87 ± 0.48
463 ± 1	$7.0 - 27.7$	4.30 ± 0.45
494 ± 4	$7.1 - 27.5$	2.29 ± 0.76

Uncertainties on quenching coefficients are statistical at the 2σ level.

5.7 Additional Experimental Parameters

Much like the DME experiments, a wide variation in DEE concentration was not normally used across a group of traces, and so k_{OH+DEE} from a narrow range of [DEE] should yield a poorly defined bimolecular rate coefficient for OH + DEE, however, Figure 5-9 demonstrates measurements in this work are approximately in agreement with k_{OH+DEE} measured in Chapter 3, when uncertainties on the direct OH + DEE measurements are considered. Above approximately 400 K it is possible that k_{OH+DEE} measured in this chapter (black circles) begin to measure a slower rate coefficient than the Arrhenius parameterisation previously obtained (red squares).

k_x as a function of pressure is displayed in Figure 5-10 obtained using the global analysis method. As in the DME system, these values showed no dependence on temperature, which is not included in this figure. The rates are not dissimilar to DME, where they are relatively slow (<750 s^{-1}) and virtually statistically insignificant. There is some evidence that the rate may increase at low pressure. This may possibly indicate the k_x parameter is accounting for some diffusion at very low pressures, where OH loss may deviate from the typical rates of ~200 s^{-1} and exhibit non-exponential decay behaviour.
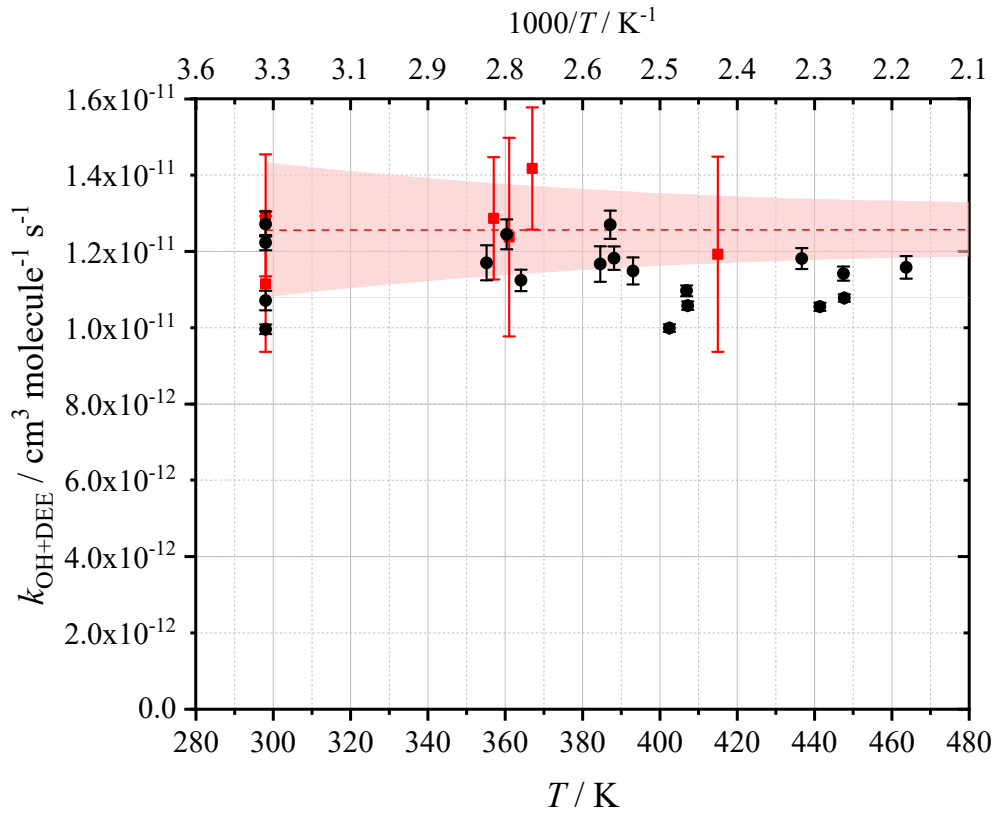
Figure 5-9: Comparison of k_{OH+DEE} measured in this work from global analysis (black), with direct measurements of k_{OH+DEE} in Chapter 3 (red). Uncertainties are 2σ and statistical, and the red shaded area represents the 95% confidence limits of the direct measurements.
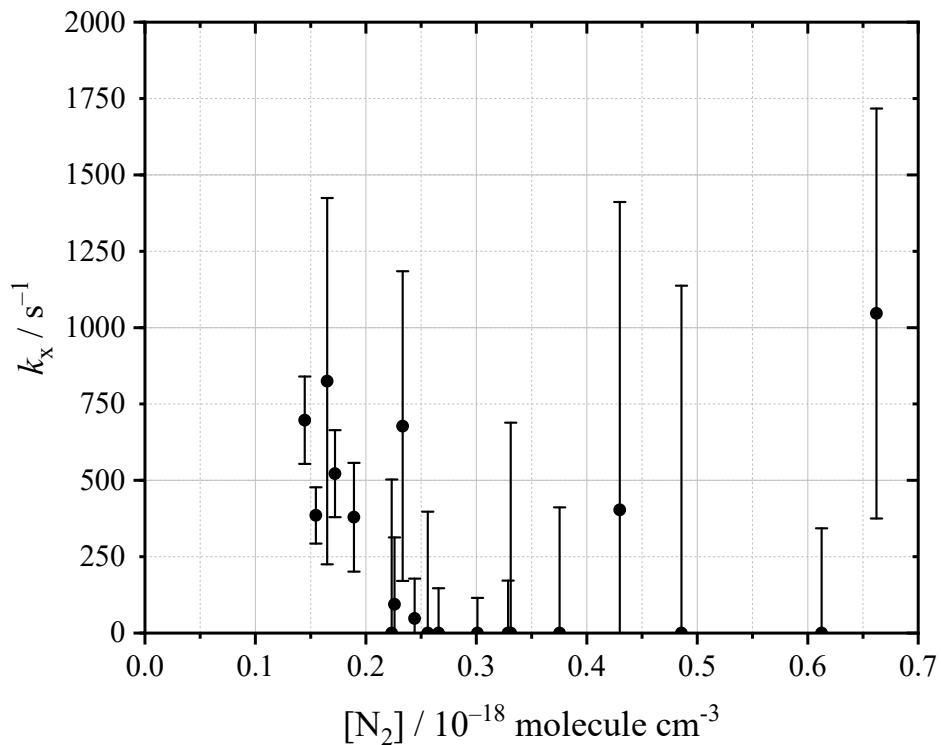
Figure 5-10: Rates of k_x obtained for the DEE system as a function of pressure. Uncertainties are statistical at the 2σ level.
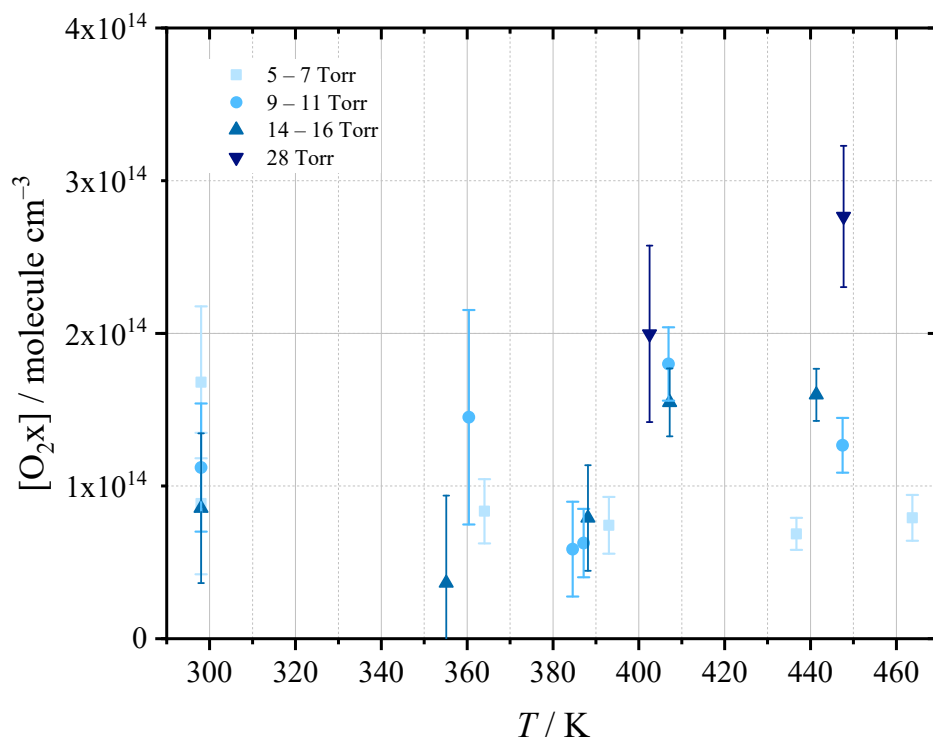
Figure 5-11: Values obtained for O₂x in the DEE experiments as a function of temperature using the H₂O₂/H₂O precursor and global analyses. Uncertainties are statistical at the 2σ level.

The oxygen concentration delivered to the system by decomposition of the H_2O_2 precursor is presented as a function of temperature in Figure 5-11, with pressures specified. The amount of oxygen in the system is comparable to those for the DME experiments (see Chapter 4) as expected; O₂x should depend on the precursor, not the ether. No dependence on temperature is clear, but there is some evidence here of increasing oxygen at higher pressures, but it is not an extreme increase (approximately a factor of 2 – 3 from 5 to 28 Torr).

5.8 Theoretical Comparison

The rate coefficient and OH yield data obtained for reaction R 5-4 were fitted using Energy Grained Master Equation (EGME) calculations in the MESMER (Master Equation Solver for Multi Energy-well Reactions) package, based on *ab initio* calculations for the stationary points of the low temperature DEE oxidation potential energy surface. A hindered rotor model was used.

5.8.1 *Ab Initio* Calculations

The potential energy surface calculated is shown in Figure 5-12, where the black line represents the calculated surface with no master equation fitting. Optimised geometries of the species were calculated using the density functional theory (DFT) functional M06-2X and the Jun-cc-pVTZ basis set, along with zero point energies (ZPEs), force constant matrices, rotational constants, and vibrational frequencies. The stationary point energies of the M06-2X/Jun-cc-pVTZ optimised geometries were calculated using high performance coupled cluster calculations with single, double, and triple excitations, using the CCSD(T) method and the Jun-cc-pVTZ basis set. The Jun-cc-pVXZ basis sets remove the diffuse functions from H and He atoms, and the highest angular momentum diffuse functions from other atoms. However, Gaussian 09 always introduces s and p diffuse functions.

During the calculation of the density of states, a harmonic oscillator approximation was generally used for vibrational frequencies, but a hindered rotor description for vibrational frequencies of bonds was also used in place of this for some species (see Figure 5-13). Internal rotation around bonds in the stationary points were described using the hindered rotor approach, where a relaxed scan of the dihedral angle, in 15° steps, was used to determine the potential. These were calculated using M06-2X/Jun-cc-pVTZ. The Gaussian 09 [240] suite of programs was used to calculate geometries, frequencies, rotational constants and relative stationary point energies for the DEE α R radical, RO_2, QOOH and R decomposition product species and transition states. Complete basis set extrapolations would ideally have been carried out, but were not, as they were computationally prohibitive. The CCSD(T) method, and the calendar basis sets [241] (Jun, Jul etc.) were chosen as a result of the computational limits, and their suitability for this system has been demonstrated previously by Sandhiya et al. [226]. Dr. Diogo J. Medeiros conducted the initial *ab initio* calculations at the M06-2X/Jun-cc-pVTZ level for all species other than those involved in decomposition of the R radical.
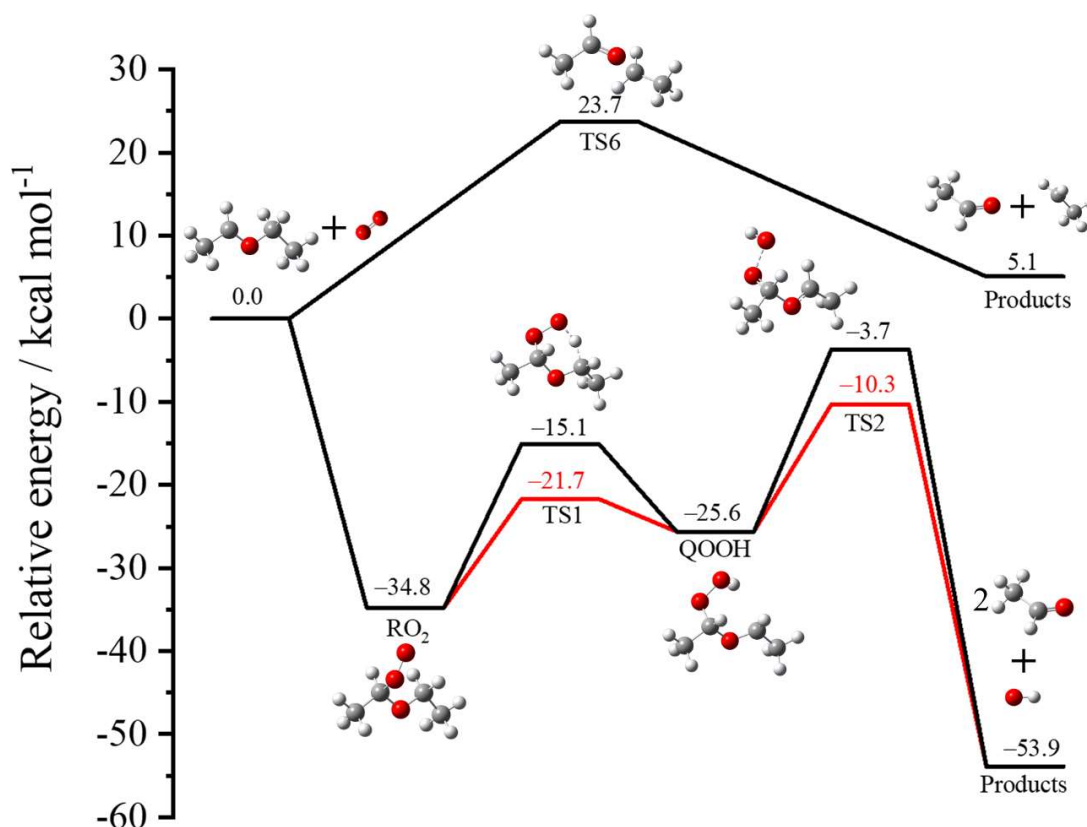
Figure 5-12: Calculated PES (black) for the DEE R + O₂ model with adjusted MESMER values (red).

Only the dominant α site abstraction pathway was considered in the calculations, where 95% of abstractions are expected to occur [161]. Calculations for the alternative pathway from the β abstraction site in future studies could help to determine branching ratios, and the contribution of both sites to OH yields and the kinetics of the R + O₂ reactions. Transition state pathways for the rearrangement of $CH_3CH_2OCH(O_2)CH_3$ to $CH_3CHOCH(OOH)CH_3$ (TS1), decomposition of $CH_3CHOCH(OOH)CH_3$ (TS2), and decomposition of $CH_3CH_2OCHCH_3$ (TS6) were all considered. It is possible there are more decomposition pathways for the QOOH radical, similar to the DME system [89], but only one was considered due to restrictions, where calculations were computationally expensive and time-consuming. At the temperatures where measurements of the $C_2H_5OC_2H_4 + O_2$ rate coefficient were made (approximately lower than 470 K), the pathway for decomposition of the R radical via TS6 is not expected to contribute significantly. The *ab initio* calculations are summarised in Table 5-5, and the details of rotational constants and vibrational frequencies are presented in Appendix C.
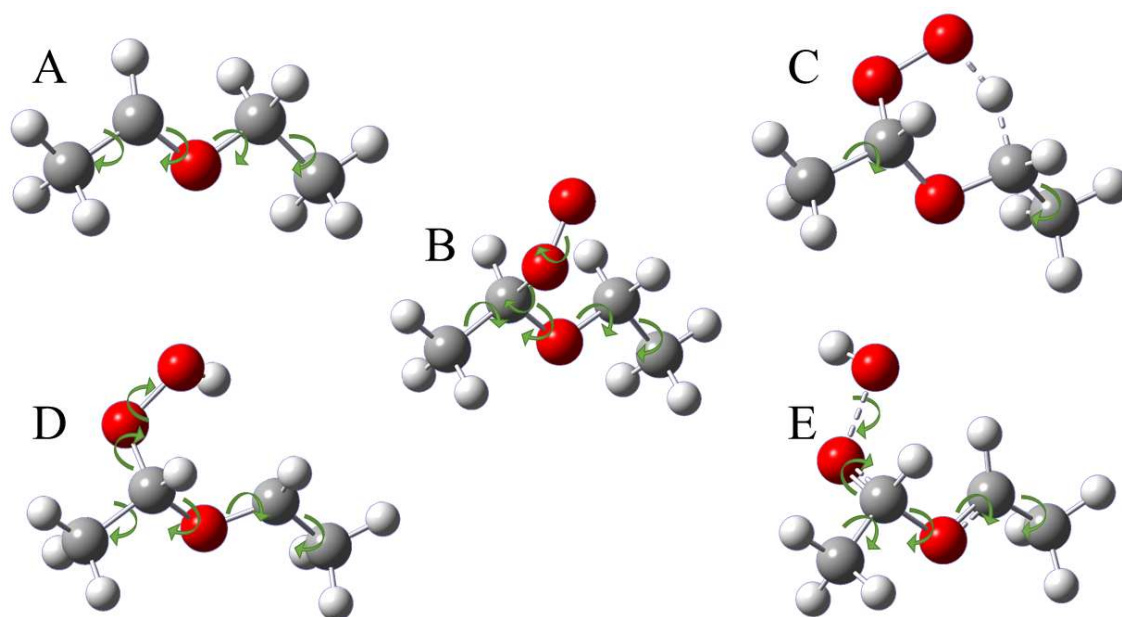
Figure 5-13: Internal hindered rotations calculated for species R (A), RO$_2$ (B), TS1 (C), QOOH (D), and TS2 (E).

Previous *ab initio* calculations carried out on relevant species are summarised in Table 5-5, where the earliest calculation by Di Tommaso et al. [115] is the only study to compute the single point energies of all the same species as this work, but the B3LYP/6-311++G(d,p) methodology is of a much lower level than presented here, and so the RO$_2$, QOOH, TS2, and TS6 species differ by several kcal mol^{-1}. Sakai et al. [225] however used the CBS-QB3 methodology to obtain a value for TS2 (–13.6 kcal mol^{-1}) more comparable to that of Di Tommaso than this work. This suggests the MESMER prediction of a lower barrier for the decomposition of QOOH to products (discussed in section 5.8.2) is not unrealistic, and a different transition state to the one found in this chapter may properly identify the route to efficient OH yields observed in the chemical activation experiments.

Reasonable agreement (within ~3 kcal mol^{-1}) is found between the calculations in this work and Sakai et al. [225], Sandhiya et al. [226], and Wang and Wang [227], for the well-depths of the RO$_2$ and QOOH species. More focused on the atmospheric oxidation of DEE, these studies did not give consideration to the decomposition of the R and QOOH radicals. A study by Hu et al. [228] was targeted towards compression ignition modelling, and only concerned itself with the decomposition of the R radical, where they refined MP2/6-311(d,p) calculations at G3 single point energies, based on single point energy calculations at MP2, MP4, and QCI levels, using different basis sets. Their calculated

barrier height for TS6 (24.0 kcal mol^{-1}) is in excellent agreement with the value reported in this thesis (23.7 kcal mol^{-1}).

Table 5-5: Comparison of calculated energies for the DEE surface.

Methodology	Ref	RO$_2$	TS1	QOOH	TS2	TS6
CCSD(T)/Jun-cc-pVTZ //M062-X/Jun-cc-pVTZ	This work	−34.8	−15.1	−25.6	−3.7	23.7
B3LYP/6-311+G(d,p)	Di Tommaso et al.	−31.8	−14.6	−17.0	−10.8	19.2
CBS-QB3	Sakai et al.	−37.5	−20.1	−28.7	−13.6	na
UCCSD(T)/Aug-cc-pVDZ//UM06-2X/6-311++G(d,p)	Sandhiya et al.	−37.4	−14.7	−26.9	na	na
UCBS-QB3//M06-2X/6-311++G(2df,2p)	Wang and Wang	−37.7	−19.7	−28.8	na	na
G3//MP2/6-311(d,p)	Hu et al.	na	na	na	na	24.0

All energies are in units of kcal mol^{-1} and are ZPE corrected. Relative to the energy of the α R radical (and O$_2$ for all but TS6). References are Di Tommaso et al. [115], Sakai et al. [225], Sandhiya et al. [226], Wang and Wang [227], and Hu et al. [228].

5.8.2 MESMER Analysis

Using the ZPEs, vibrational frequencies, force constant matrices and rotational constants obtained from the *ab initio* calculations on the diethyl ether oxidation surface described above (Figure 5-12), master equation solving was carried out using the MESMER software package, which solves the EGME. The MESMER model consists of a bimolecular source term (reaction R 5-4), energy wells for isomers, transition states to isomers, and product energy wells that act as infinite sinks for the system (Figure 5-14).
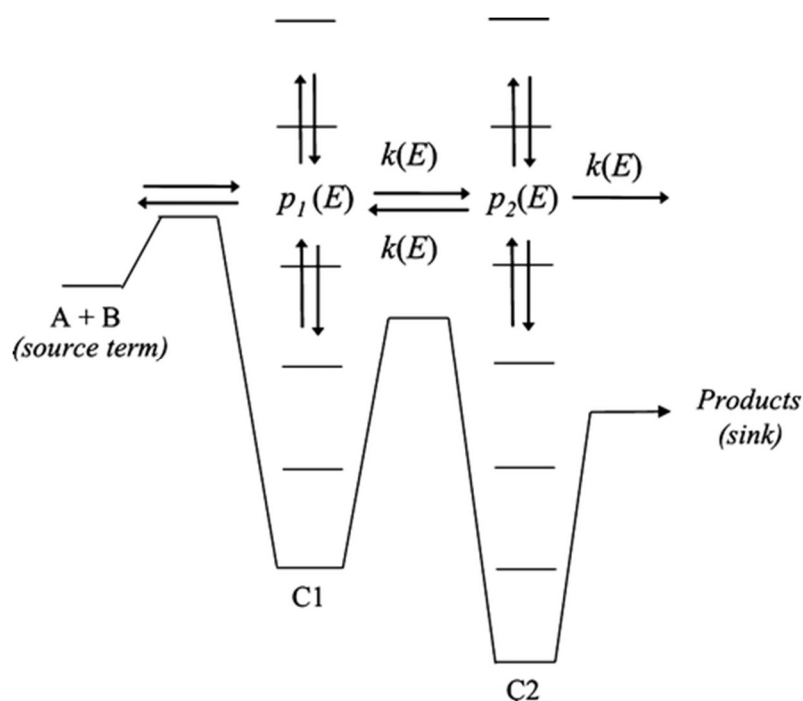
Figure 5-14: Representation of the Energy Grained Master Equation model for a generic association reaction, with two wells (C1 and C2), and an irreversible product channel. Taken from Glowacki et al. [242].

Energies of the species were partitioned into 100 cm^{-1} grains, and collisional energy transfer was modelled using the exponential down term, $\langle \Delta E \rangle_{\text{down}}$, the average energy transferred downwards during collision with the bath gas. Collision with the bath gas can also transfer energy upwards to the species. Each grain of the system is populated or depopulated through collisional energy transfer into another grain. Population by the bimolecular reaction between O_2 and $CH_3CH_2OCHCH_3$, and depopulation by dissociation and/or re-dissociation to products and reagents respectively, both also take place. The probability of energy transfer between two grains is determined by the exponential down model and decreases exponentially with separation of the two grains. The parameter for energy transfer is given below (equation E 5-2),

$$\langle \Delta E \rangle_{\text{down}} = \langle \Delta E \rangle_{\text{down,ref}} \left(\frac{T}{T_{\text{ref}}} \right)^n \qquad \text{E 5-2}$$

here, n was fixed to 0.25 for the N_2 bath gas [243], and T_{ref} refers to 293 K.

Densities of states were calculated assuming rigid rotors for external rotations, and treating vibrations as harmonic oscillators. Hindered rotor models were also used for some vibrational modes. In each energy grain, microcanonical rate coefficients for the

unimolecular reactions are calculated via microcanonical transition state/RRKM theory (equation E 5-3):

$$k(E) = \frac{W(E)}{h\rho(E)}$$

E 5-3

where $W(E)$ is the sum of rovibrational states at the optimised geometry, and $\rho(E)$ is the density of rovibrational states. For the barrierless association reaction R 5-4, the inverse Laplace transform (ILT) approach was used. Here, the microcanonical dissociation $k(E)$s are determined using experimental measurements of the reaction rate coefficient. Phenomenological rate coefficients were calculated by MESMER using the Bartis and Widom approach to select the chemically significant eigenvalues present in the master equation [244].

The EGME can be described by equation E 5-4:

$$\frac{\mathrm{d}p}{\mathrm{d}t} = \mathbf{M}p$$

E 5-4

where p is the population density vector, and $\mathbf{M}$ is the transition matrix, which describes the population evolution as a function of time, brought about by collisional energy transfer and reactions. Solving equation E 5-4 gives equation E 5-5:

$$p = \mathbf{U}e^{\Lambda t}\mathbf{U}^{-1}p(0)$$

E 5-5

here, $\mathbf{U}$ is a matrix of eigenvectors from the diagonalization of $\mathbf{M}$, Λ represents the vector of the corresponding eigenvalues, and $p(0)$ represents the starting conditions of each energy grain. For the RO_2 to QOOH hydrogen shift (TS1), the asymmetric Eckart tunnelling correction model [245] was used.

In total, 58 experimentally determined data points for rate coefficients and OH yields have been used to fit the MESMER model by optimising parameters on the DEE PES. The Marquardt algorithm was used to fit the rate data to the calculated surface, providing a practical assessment of the agreement between the *ab initio* calculations and

experiments, and to predict the high pressure limit for reaction R 5-4. 39 of the data points were OH yields, and 19 were measurements of the $R + O_2$ rate coefficient. Two models were fit to the data; the first relied on vibrational constants to calculate the density of states for species; the second incorporated the hindered rotor calculations outlined above, to describe internal rotations of dihedral bond angles (Figure 5-13). The fit to the model was obtained by reducing the value of the statistical measure of goodness of fit, χ^2, where this relates the experimental values of a parameter to the parameter calculated by MESMER in equation E 5-6:

$$\chi^2(A^\infty, \langle\Delta E\rangle_{\text{down}}, E_{\text{TS1}}, E_{\text{TS2}}) = \sum_{i=1}^{58} \frac{\left(k_{\text{i,ob}}(p_i, T_i) - k_{\text{i,mod}}(p_i, T_i)\right)^2}{\sigma_i^2} \qquad \text{E 5-6}$$

where A^∞ was the Arrhenius pre-exponential factor for reaction R 5-4, $\langle\Delta E\rangle_{\text{down}}$ was the exponential down energy transfer parameter, E_{TS1} and E_{TS2} were the single point energies for the respective transition states, $k_{\text{i,ob}}(p_i, T_i)$ was the experimentally observed value for a set of conditions, $k_{\text{i,mod}}(p_i, T_i)$ was the modelled value at the same conditions, and σ_i was the uncertainty in the experimentally determined value. The Levenberg-Marquardt algorithm was used to reduce χ^2.

In the above fitting routine, n^∞, the temperature exponent term for reaction R 5-4 was fixed at a value of -1.2, and attempts to float the parameter showed it was insensitive to variation by a factor of two. The single point energy for TS1 was linked to the single point energy for TS2, based on the difference between the two *ab initio* energy calculations. TS2's energy was adjusted, and will primarily have been characterised by the OH yields measured in this work, with TS1's energy floating relative to TS2. The activation energy of reaction R 5-4 was set to 0, consistent with a barrierless association reaction.

A similar fit was found for both the model with, and without, hindered rotor description of bonds, where a χ^2 value of 86 and 100 was found respectively. An ideal fit would provide a χ^2 value equivalent to the total number of data points, so in this case, χ^2 = 58 would indicate a perfect fit. The value for the minimised χ^2 reported by MESMER scales linearly with the uncertainties on experimentally determined data provided (i.e. doubling all experimental uncertainties will give an identical MESMER fit, with uncertainties on fitted parameters twice as large). As such, all uncertainties provided to

MESMER for yields and rate coefficients were statistical at the 2σ level, hence, the uncertainty on returned MESMER parameters are propagated 2σ uncertainties.

Correlation plots are shown in Figure 5-15 and Figure 5-16 for the reaction R 5-4, $C_2H_5OC_2H_4 + O_2$, rate coefficient and OH yields respectively, where the modelled data are plotted against the experimental determinations, with x error bars representing the 2σ uncertainties in the measured values. Weighted linear fits to the data in the correlation plots show very similar fits for both MESMER models, where near perfect 1:1 correlations are present, with the intercepts pinned at 0.
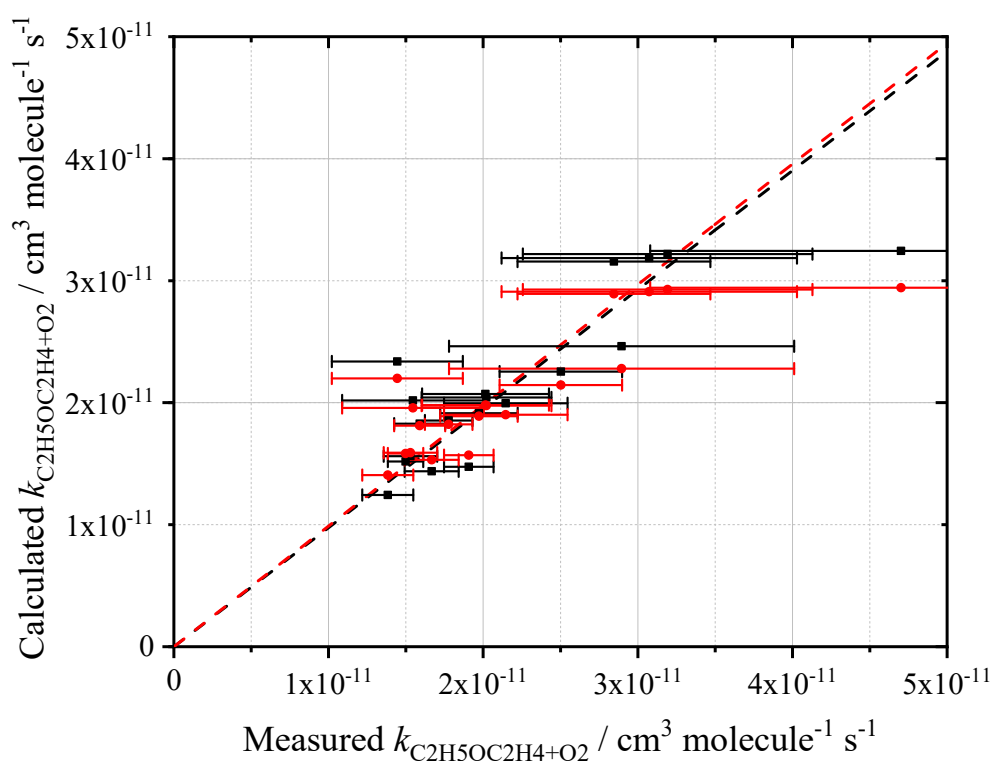
Figure 5-15: Correlation plot for the modelled reaction R 5-4 rate coefficients against experimentally observed rate coefficients. Black data are for the MESMER model using hindered rotors, and red for the vibration-only model. Fits to the data are pinned to the origin, and the slopes are 0.98 and 0.99 for the black and red lines respectively. Uncertainties are statistical at the 2σ level.
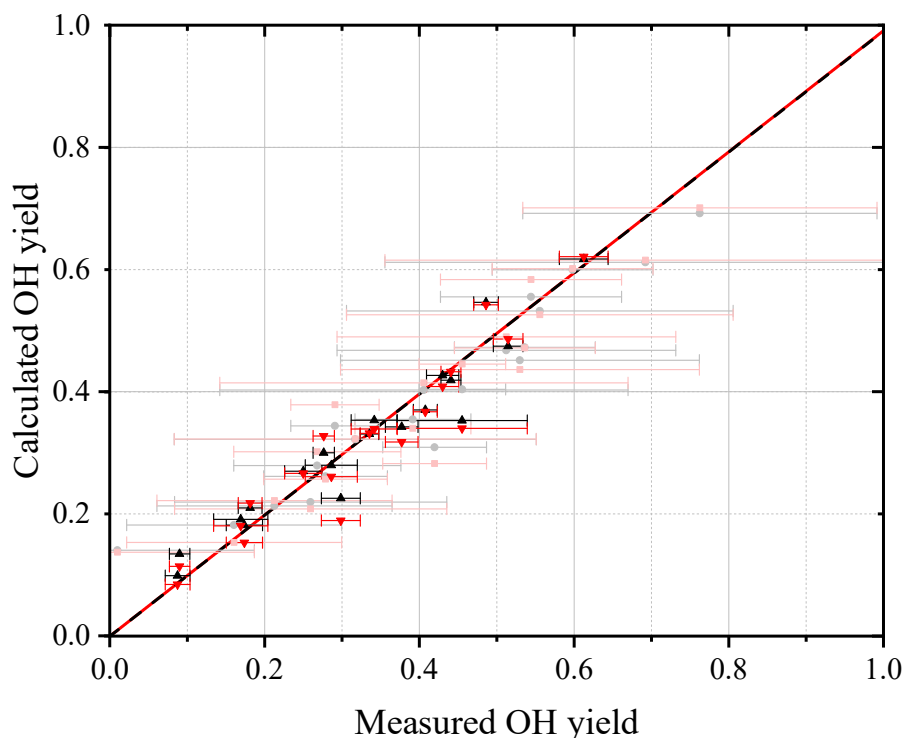
Figure 5-16: Correlation plot for the modelled OH yields against experimentally observed OH yields. Black data are for the MESMER model using hindered rotors, and red for the vibration-only model. Lighter coloured yields were obtained from the high O₂/no O₂ bimolecular determination, and inherently have larger error bars. Fits to the data are pinned to the origin, and both lines have a slope of 0.99. Uncertainties are statistical at the 2σ level.

Results for the floated parameters in the two models outlined above are listed in Table 5-6. There is a small difference of 1.2×10^{-12} cm^3 molecule^{-1} s^{-1} in the reaction R 5-4 pre-exponential factor for the two models when considering uncertainties. The largest discrepancy is between the single point energies found for TS2, the transition state for QOOH decomposition to OH. This should be a well-defined parameter as a result of the large number of OH yields generated using two methods provided to the model, where this barrier (which has the highest energy of the transition states post O$_2$ addition to the R radical), controls the amount of QOOH* able to decompose via well-skipping to OH radicals. The small relative uncertainty of 0.3 kcal mol^{-1} in both models reflects the sensitivity of the model and data to TS2. The difference of 3 kcal mol^{-1} between the vibration-only model and the hindered rotor model is a significant discrepancy, and may suggest the greater density of states available to the RO$_2$ and QOOH species energy wells in the hindered rotor model reduces the amount of chemical activation possible. In comparison to the energy wells, the calculations for TS1 provide hindered rotations for only two bonds (compared to six in RO$_2$), thus increasing the density of states in TS1 to

a lesser degree than the adjacent energy wells. This issue will not be present in the vibration-only model, and thus TS2 and TS1 are not required to be as low to account for the shift in equilibrium to the reactant sides of the transition states.

Table 5-6: Adjusted parameters found by the reduction of χ^2 when fitting the MESMER models to the experimentally observed rate coefficients and OH yields.

Parameter	MESMER model		*Ab initio*
	Hindered rotors	Vibration only	
E_{TS1}	(-21.7 ± 0.3)	(-18.1 ± 0.3)	-15.1
E_{TS2}	(-10.3 ± 0.3)	(-6.7 ± 0.3)	-3.7
A^{∞}	$(3.34 \pm 0.22) \times 10^{-11}$	$(2.87 \pm 0.13) \times 10^{-11}$	na
$\langle \Delta E \rangle_{down}$	(599 ± 184)	(590 ± 186)	na
χ^2	86	100	na

Units of E = kcal mol^{-1} and relative to R + O$_2$, A units = cm^3 molecule^{-1} s^{-1}, $\langle \Delta E \rangle_{down}$ units = cm^{-1}.

Given the calculated *ab initio* energy barrier for TS2 at the CCSD(T)/Jun-cc-pVTZ level was -3.69 kcal mol^{-1} relative to the R + O$_2$ entrance channel, a required change of ~3 – 7 kcal mol^{-1} with the MESMER fitting routine is a significant adjustment, and suggests the energies for TS2 are not being calculated accurately. There is the possibility that the experimental data are systematically wrong, however, the observations are qualitatively consistent with the reaction studied, and the agreement between the two OH yield generation methods is excellent. In the previous study by Eskola et al. [89] at the University of Leeds, their use of MESMER to fit experimental data for the CH$_3$OCH$_2$ + O$_2$ surface *ab intio* calculations also led to large adjustments in transition state barriers. For the analogous DME system, TS1 was lowered by ~5 kcal mol^{-1}, and TS2 was lowered by ~10 kcal mol^{-1}. This highlights the importance of using laboratory measurements to adjust *ab initio* calculations, and suggests that the transition states in particular are not currently described well by theoretical calculations. As a result of allowing the transition state energies to float, the Stern-Volmer plot in Figure 5-17 is recreated well by the MESMER modelled predictions for the OH yields. Interestingly, MESMER does not predict an intercept of 1, and therefore suggests 100% OH yields are not possible. MESMER intercepts in Figure 5-17 correspond to a range of (64 – 85)% yields of OH in increasing temperature. Physically this would suggest that some RO$_2$/QOOH molecules will never dissociate to generate OH.
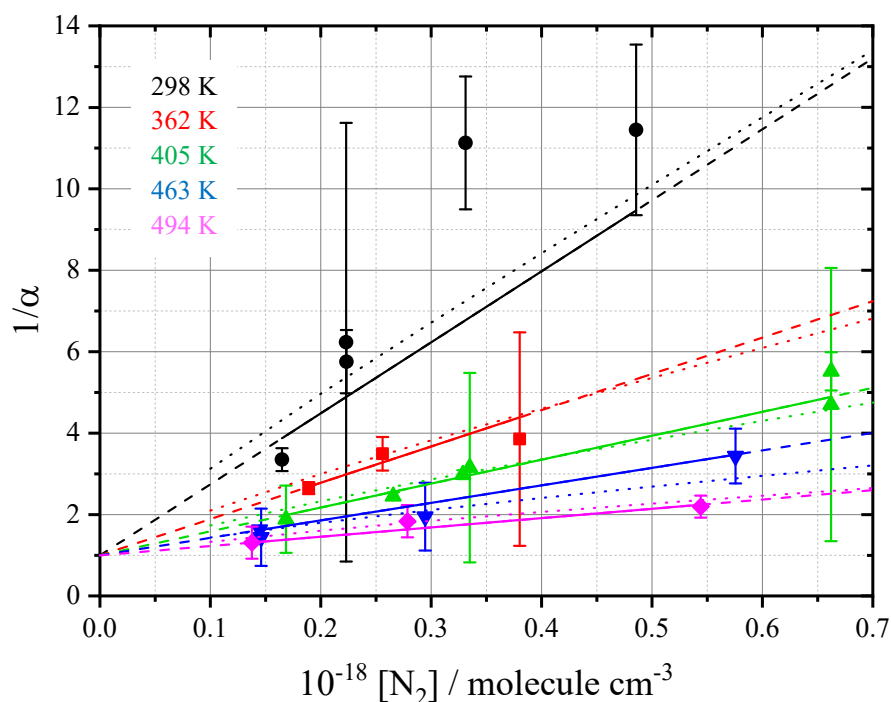
Figure 5-17: Stern-Volmer treatment of OH yields, with dotted lines representing the MESMER predictions. Instrumentally weighted fits were used, and intercepts for experimental data were set to unity. Intercepts on the MESMER fits = 1.56, 1.45, 1.35, 1.23, 1.18, from low to high temperature. Uncertainties are statistical at the 2σ level.

Finally, a value close to 600 cm^{-1} for $\langle \Delta E \rangle_{\text{down}}$ in both models (Table 5-6) is unusually high, considering a typical system in nitrogen bath gas would be expected to have a collisional transfer energy of 175 – 275 cm^{-1} [246]. The large uncertainties on both values however, may place this parameter as low as ~400 cm^{-1}, and a comparison of the same model (simulating, rather than fitting to data) ran with fixed $\langle \Delta E \rangle_{\text{down}}$ values of 300 cm^{-1} and 100 cm^{-1} in Figure 5-18, shows very little effect on the simulated reaction R 5-4 rate coefficient temperature dependence at the high pressure limit. On the contrary, yields are greatly affected by the change in average energy transferred during collisional deactivation, as would be expected (Figure 5-19).

With $\langle \Delta E \rangle_{\text{down}}$ fixed at 100 cm^{-1}, the model achieves a significantly less good fit, with a $\chi^2 \approx 170$, an A^{∞} over twice as large as that reported in Table 5-6, and the model still required an adjustment of TS2 down by over 4 kcal mol^{-1} from the *ab initio* value. Attempting to fit the data to the model with the initial TS2 *ab initio* value (–3.7 kcal mol^{-1}) fixed, yields a $\chi^2 > 6000$, and thus is not able to fit the data satisfactorily.
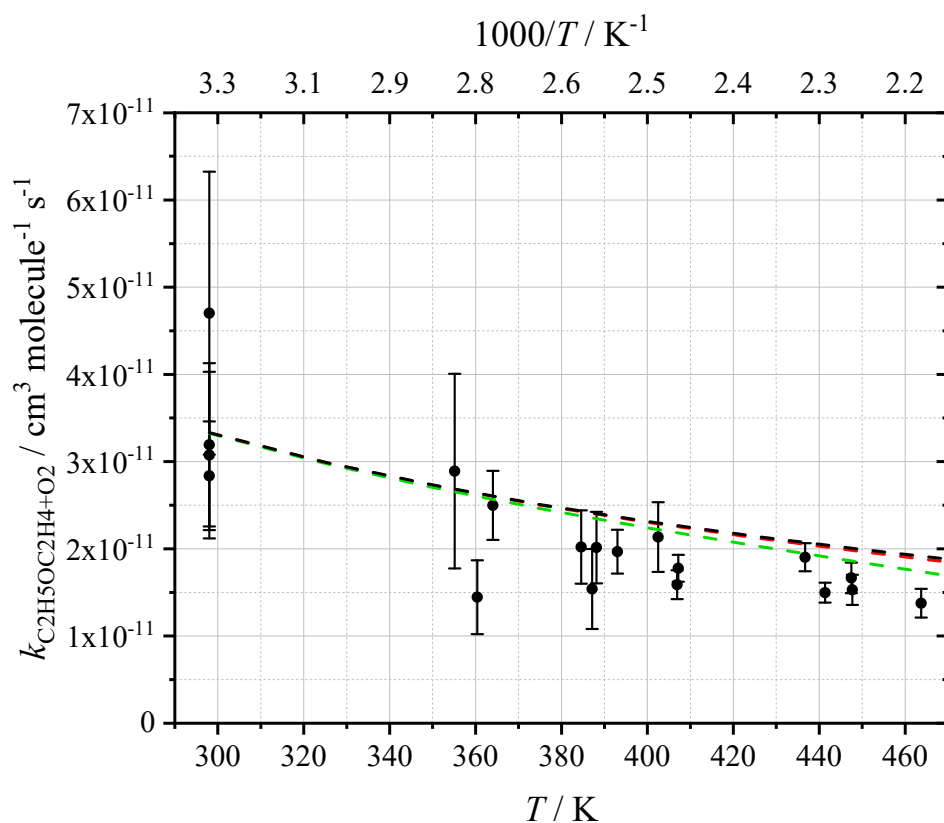
Figure 5-18: $k_{C2H5OC2H4+O2}$ **dependence on temperature with the high pressure limit calculated by MESMER (black). Red and green lines are MESMER fits where** $\langle \Delta E \rangle_{down}$ **was fixed at 300 cm^{-1} and 100 cm^{-1} respectively. Uncertainties are statistical at the 2σ level.**
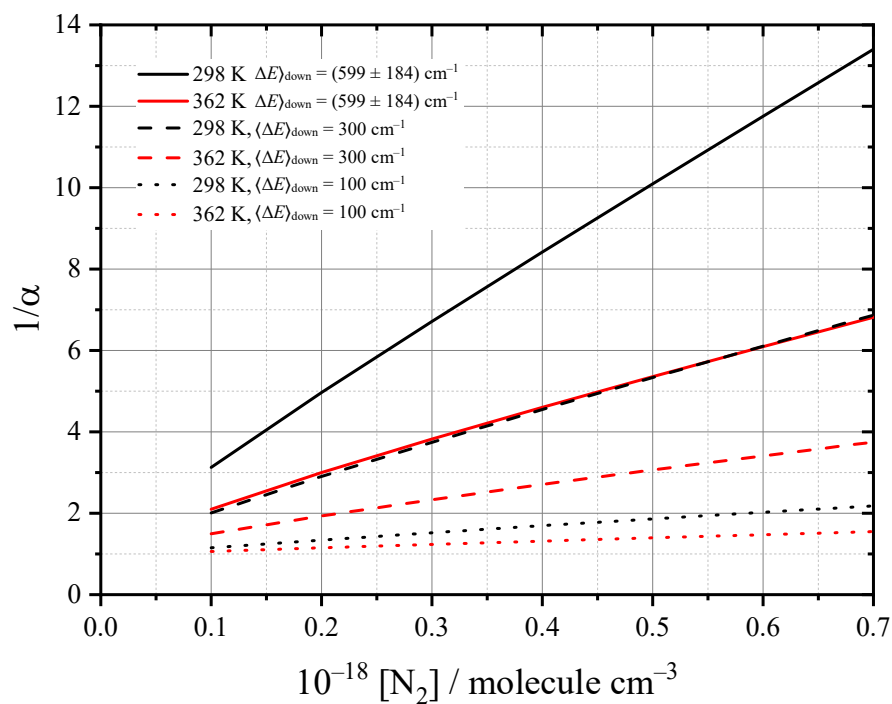
Figure 5-19: Stern-Volmer plot for MESMER predicted yields at varying $\langle \Delta E \rangle_{down}$ **values. Only two temperatures are displayed, for clarity.**

The prediction of the high pressure limit for reaction R 5-4 in the hindered rotor MESMER model does qualitatively predict the negative temperature dependence of the bimolecular rate coefficient, and predicts a slight pressure dependence across the range of total gas density explorable in this work in Figure 5-20. The measurements of the R + O_2 rate coefficient presented here as a function of pressure, do not have small enough uncertainties (particularly at low temperatures), enough pressures explored, or a large enough pressure *range* explored, to confidently identify any pressure dependence. However, the comparison to the MESMER model in Figure 5-18, where experimental measurements are approximately 20% slower than the MESMER predicted rate coefficients at higher temperatures, does suggest the experimental observations may not have always been at the high pressure limit for the reaction.
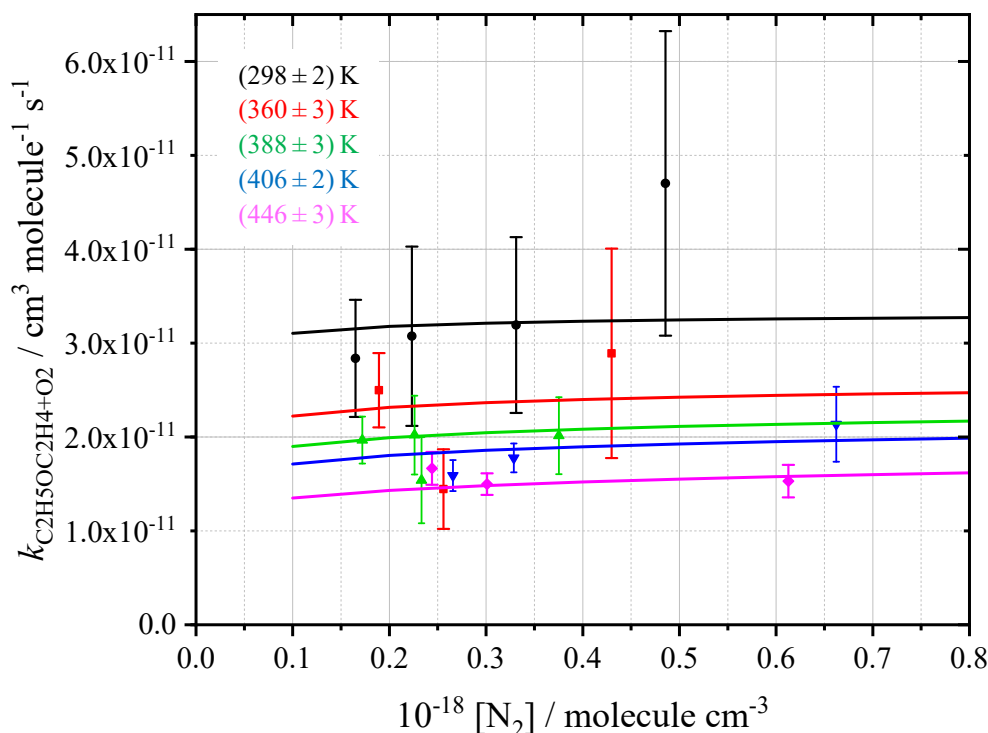
Figure 5-20: $k_{C2H5OC2H4+O2}$ as a function of total pressure, with lines for MESMER fits. Uncertainties are statistical at the 2σ level.

In general, good agreement was found between the MESMER model including hindered rotors, and the experimental measurements of the R + O_2 rate coefficients and OH yields, with significant adjustment of transition state barriers and the downward collisional energy transfer parameter, $\langle \Delta E \rangle_{down}$. A difference of approximately +3 kcal mol^{-1} in the energy for TS2 was the primary difference when comparing the vibrational

frequency-only model with the hindered rotor description model. At the current *ab initio* level used in this work, CCSD(T)/Jun-cc-pVTZ//M06-2X/Jun-cc-pVTZ, there will be a different MESMER model fitting result to that found if calculations with the complete basis set extrapolation were possible, as this would affect the fixed well-depths used for the RO_2 and QOOH species, and the relative difference enforced between TS1 and TS2. The energies for RO_2 and QOOH were not defined by the experimental data for the system when floated. Experiments measuring the interception of the QOOH radical by O_2 would go some way to defining the equilibrium, and therefore the difference in energy between the two radicals.

5.9 Comparative Discussion of $C_2H_5OC_2H_4 + O_2$ and $CH_3OCH_2 + O_2$

Both dimethyl and diethyl ether produced negative temperature dependences for the R + O_2 reaction rate coefficient (Figure 5-21), the major difference being the magnitude of the rate coefficients. From room temperature to approximately 450 K, the $C_2H_5OC_2H_4 + O_2$ rate coefficient remains approximately three times faster than that for $CH_3OCH_2 + O_2$ (3 to 1.5×10^{-11} cm^3 molecule^{-1} s^{-1}, and 1 to 0.5×10^{-11} cm^3 molecule^{-1} s^{-1}). The α site expected to be the major pathway for the DEE R radical is activated by proximity to the –O– group, and also the adjacent methyl group, so a faster rate is expected than the equivalent rate for the DME R radical, where only the adjacent –O– is able to contribute. The possibility of addition to the β site in the DEE system may also increase the rate coefficient.

Figure 5-22 presents the quenching coefficients obtained for the DEE and DME systems, where the higher quenching coefficients for DEE represent lower yields. This can be explained by the larger size of the $C_2H_5OC_2H_4$ molecule, where it is more likely to undergo collisional deactivation, be thermalised into a local energy minima, and not well-skip directly to the OH product. At the highest temperatures, this effect becomes less pronounced and the quenching coefficients of the two systems begin to converge.
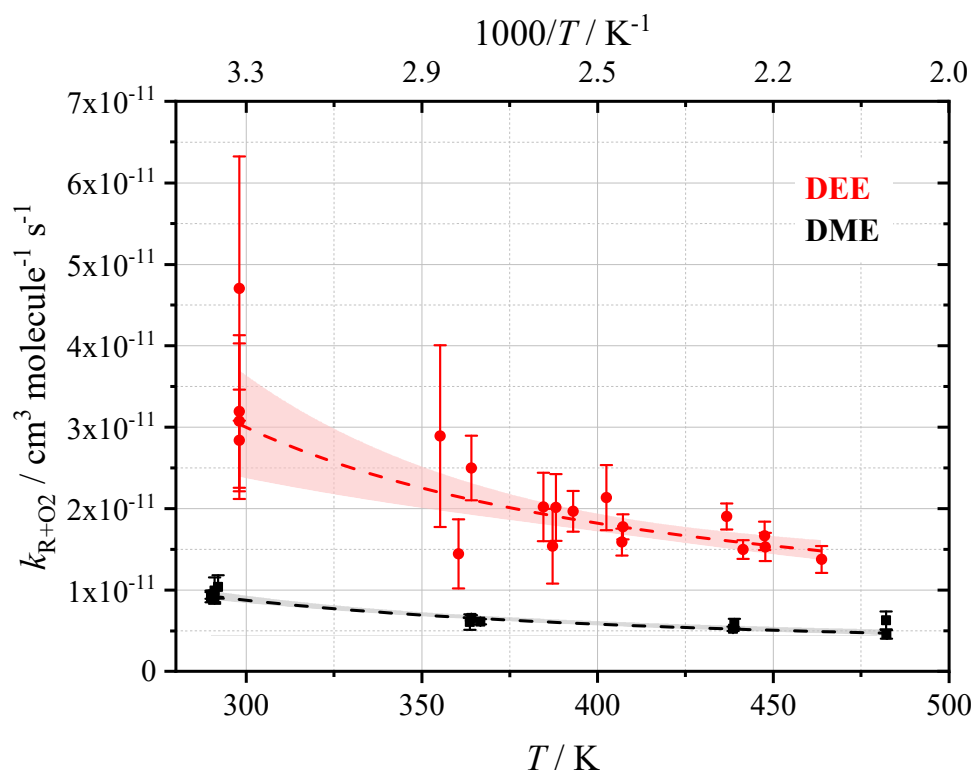
Figure 5-21: Comparison of measured R + O₂ rate coefficients for DEE (red) and DME (black), as a function of temperature. Uncertainties are statistical at the 2σ level.
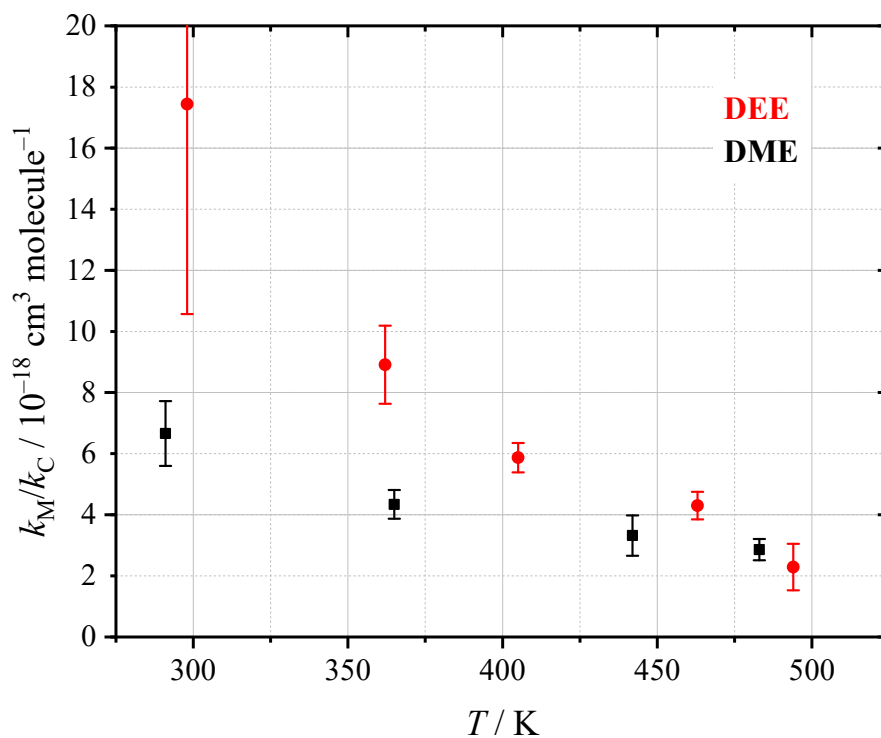
Figure 5-22: Comparison of the quenching coefficients obtained for the DEE and DME systems as a function of temperature.

5.10 Conclusions

Measurements of the rate parameters for the diethyl ether R + O_2 system have been presented for the first time across a range of temperatures, 298 – 464 K, and pressures, 5.2 – 28.4 Torr of N_2. Comparisons to the equivalent observations for the DME system were made, where rate parameters for the $C_2H_5OC_2H_4$ + O_2 reaction exhibit a bimolecular rate coefficient approximately three times larger than CH_3OCH_2 + O_2, and the quenching coefficient measured in N_2 for OH yields from DEE was greater than for DME. This difference was attributed to the greater probability of collisional quenching for the larger molecule.

Experimentally determined OH yields and R + O_2 rate parameters were compared to *ab initio* calculations of the DEE low temperature oxidation surface, where stationary point energies of R + O_2, RO_2, QOOH, product, and transition state species were determined at the CCSD(T)/Jun-cc-pVTZ//M06-2X/Jun-cc-pVTZ level. Master equation solving using the MESMER code showed that a reduction in the theoretical values of the $RO_2 \leftrightarrow$ QOOH and QOOH $\rightarrow$ OH transition state barriers of ~7 kcal mol^{-1} was required to achieve good agreement with the observed rate parameters, suggesting the *ab initio* calculations do not describe the transition states accurately.

Future work should focus on a greater range of $C_2H_5OC_2H_4$ + O_2 rate parameters, where the optimal experimental conditions determined in Chapter 4 could be used to provide a more comprehensive characterisation of the pressure dependence (at lower pressures) of the R + O_2 rate coefficient. Theoretical calculations could also extend to a more complete description of the low temperature combustion surface. If any initial hydrogen abstraction occurring at the β site of the DEE molecule proceeds to contribute to the R + O_2 reaction and OH yields, the MESMER package may be able to provide information on the branching ratios.

Chapter 6 Other Sources of OH Regeneration

6.1 Abstract

This chapter presents some initial results obtained concerning OH regeneration in the low temperature combustion regime of ethers beyond the $R + O_2$ chemical activation source discussed in previous chapters. These results are speculative, and not fully understood in a quantitative manner, however they are important observations, likely related to the decomposition of QOOH radicals, and potentially the interception of QOOH radicals by O_2, a key step in the autoignition of fuels.

Observations of rapid OH growth and decays for experiments using DME, DEE, and DBE, in the presence of O_2 and absence of OH precursor, have been measured above ~480 K, 500 K, and 700 K respectively. Abstraction reactions between the fuel and $O(^3P)$ atoms have been proposed as the most likely mechanism for the growths after a series of experimental tests were conducted. Biexponential decays of OH for the same fuels were also measured, although the extent to which O atom chemistry contributes to these recycling traces is not known. MTBE and TMOF did not exhibit the same chemistry, and biexponential decays observed above 478 K and 568 K for these ethers in the presence of O_2 have been analysed, providing OH yields invariant with O_2. A mechanism for the MTBE yields has been proposed, with an HO_2 formation channel causing the relatively low $(35 \pm 5)\%$ OH yields.

A complex fitting scheme was developed, incorporating the $O(^3P)$ + fuel reactions, and early attempts to analyse a large number of growth/decay traces using the scheme indicates there are other regeneration processes occurring on a longer time scale. The further regeneration mechanisms (involving QOOH) that these results imply are taking place, are complemented by some experiments conducted using an alternate experimental setup to that used to obtain the majority of data in this thesis, where no indication of O atom chemistry was seen. Under high O_2 concentrations, and an O atom-free reaction cell experiment, cool flame behaviour was observed using DEE, where photolysis-independent OH concentrations increased as a function of $[O_2]$. The perturbation of these flames by LIF was carried out, however the OH yields and recycling parameters obtained via biexponential analyses of the OH decays are not fully understood.

6.2 Background and Previous Work

Following the initial abstraction reaction involving a fuel and a small species (e.g. OH) (Chapter 3), and the addition of oxygen to the R radical formed (Chapter 4 and Chapter 5), several reactions leading to, and causing, chain-branching, are believed to be the key to the autoignition of fuels in low temperature combustion mechanisms. A schematic PES illustrating these reactions is presented in Figure 6-1, with the chain-branching pathway highlighted in green and red.
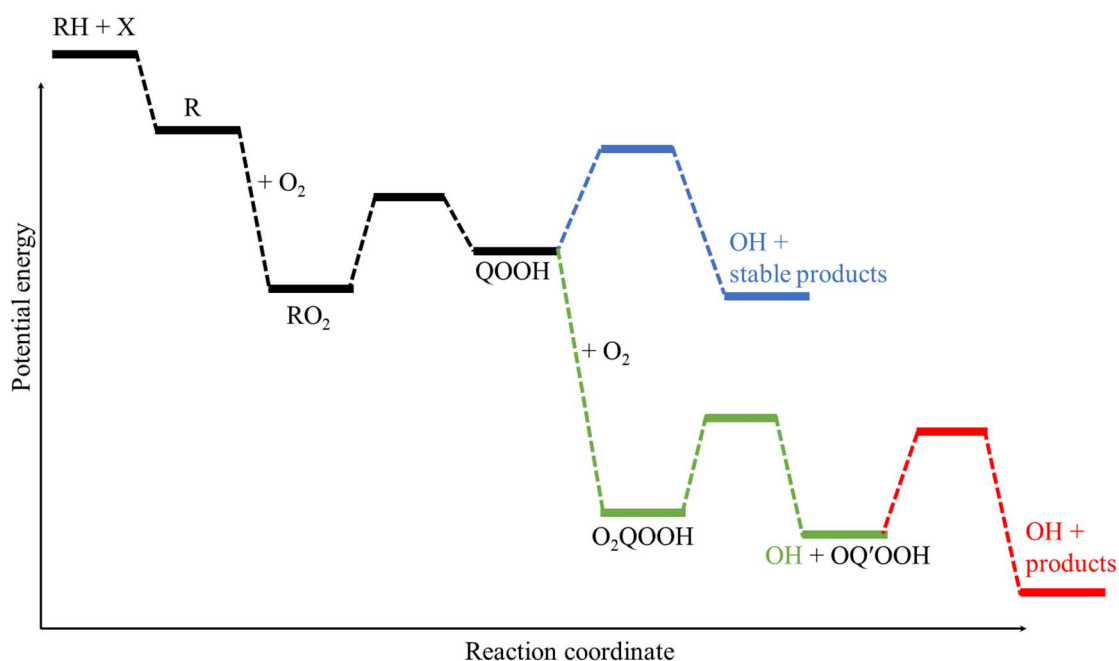
Figure 6-1: Generic low temperature combustion potential energy surface, showing propagation (blue and green) and chain-branching OH formation (green to red).

Rearrangement of the RO_2 species to QOOH, via an internal hydrogen abstraction, can occur initially, and the equilibrium usually lies heavily towards RO_2 (reaction R 6-1). QOOH can thermally decompose to yield one OH, thus propagating the system of radicals, in reaction R 6-2. Alternatively, given high enough oxygen concentrations, the QOOH species can be intercepted by O_2, to form the QOOH-peroxy radical in reaction R 6-3. The higher energy of the QOOH well-depth makes this O_2 interception particularly difficult experimentally, where sufficiently high O_2 concentrations would result in quenching of fluorescence signal in a typical LIF experiment. From here, chain propagation can take place via reaction R 6-4, where the peroxy species falls apart to generate the first OH radical, and a ketohydroperoxide species, OQ′OOH (following

isomerisation). The second OH radical (and thus the branching species) arises from further decomposition of the OQ′OOH species in reaction R 6-5.

$$RO_2 \leftrightarrow QOOH \qquad \text{R 6-1}$$
$$QOOH \rightarrow OH + products \qquad \text{R 6-2}$$
$$QOOH + O_2 \rightarrow O_2QOOH \qquad \text{R 6-3}$$
$$O_2QOOH \rightarrow OH + OQ′OOH \qquad \text{R 6-4}$$
$$OQ′OOH \rightarrow OH + products \qquad \text{R 6-5}$$
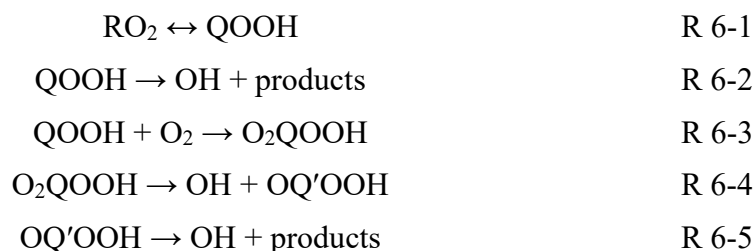
In the DME system, significant research has been carried out on the chain-branching mechanism [87, 88, 94-96, 247-249], but the details are still not fully understood. Research by Jenkin et al. [250] proposed that the observed formation of HCHO reported by Japar et al. [180] can arise by the decomposition of the QOOH radical, where an internal hydrogen abstraction occurs (reaction R 6-6). Decomposition of the QOOH radical leads to the formation of formaldehyde (reaction R 6-7). The final OH product, formed by decomposition of the QOOH radical, requires high temperatures in order to provide the reaction enough energy to breach the energy barriers [89].

$$CH_3OCH_2O_2 \rightarrow CH_2OCH_2O_2H \qquad \text{R 6-6}$$
$$CH_2OCH_2O_2H \rightarrow 2HCHO + OH \qquad \text{R 6-7}$$
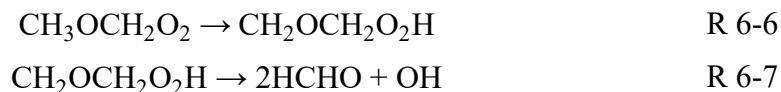
Decomposition of the O_2QOOH radical (formed in reaction R 6-8) produces the hydroperoxymethyl formate (HPMF) species and an OH radical (reaction R 6-9). The resultant production of two radicals (OH and OCH_2OCHO) (reaction R 6-10) from the decomposition of HPMF gives rise to autoignition of DME. The OCH_2OCHO radical also produces an HCO_2 radical and formaldehyde (CH_2O) by decomposition (reaction R 6-11) [95].

$$CH_2OCH_2O_2H + O_2 \rightarrow O_2H_2OCH_2O_2H \qquad \text{R 6-8}$$
$$O_2CH_2OCH_2O_2H \rightarrow HO_2CH_2OCHO + OH \qquad \text{R 6-9}$$
$$HO_2CH_2OCHO \rightarrow OCH_2OCHO + OH \qquad \text{R 6-10}$$
$$OCH_2OCHO \rightarrow CH_2O + HCO_2 \qquad \text{R 6-11}$$
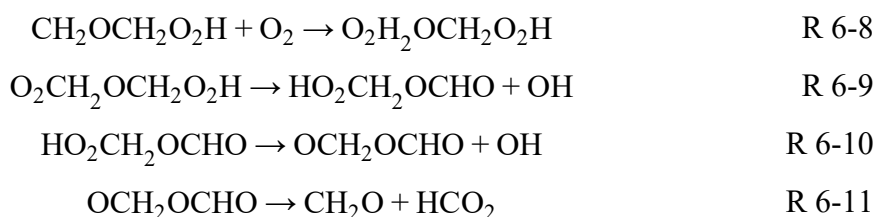
Curran et al. [94] originally proposed the temperature range 550 – 600 K for chain-branching via HPMF decomposition (reaction R 6-10), and >600 K as the temperature at which decomposition of the hydroperoxy methyl methoxy (reaction R 6-7) radical begins to dominate the mechanism, giving rise to only one hydroxyl radical. Zhao et al. [96] built on the work carried out by Curran, to build an extensive reaction scheme for modelling DME combustion, and found chain branching should occur below 700 K via reaction R 6-10 given enough O_2 is present.

Andersen and Carter hypothesised the potential chain-branching products, suggesting those formed in reaction R 6-10 [247, 248], but predicting an additional route to OH formation (reaction R 6-12) as the most probable.

$$HO_2CH_2OCHO \rightarrow HCOOH + CHO + OH \qquad\qquad R\ 6\text{-}12$$

Figure 6-2 shows the potential surface proposed by Andersen and Carter [249] as the "most efficient", containing two relatively low energy barriers, and the direct production of two OH radicals as part of the chain-branching route.
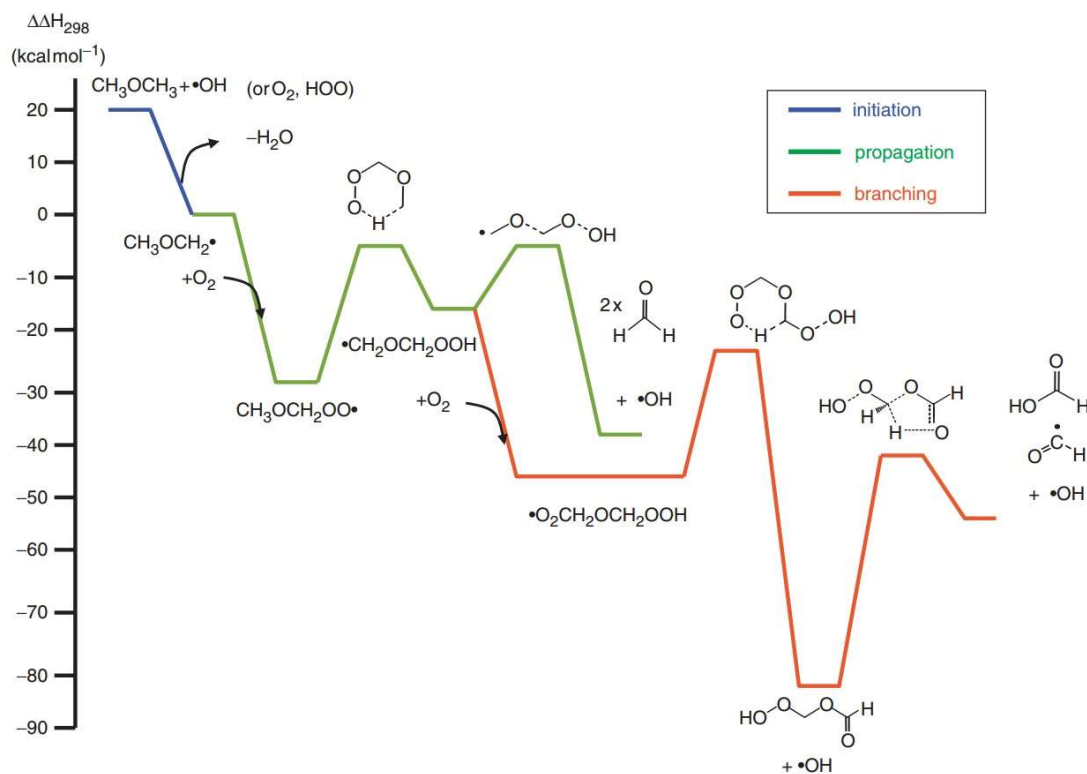
Figure 6-2: Potential energy surface suggested for dimethyl ether combustion, with possible chain branching route, figure from Andersen and Carter [249].

The final steps towards chain-branching are particularly difficult to monitor experimentally, but some progress has been made, where Moshammer and co-workers have now detected HPMF using mass spectrometry [87, 88]. Other studies have focused on the low temperature oxidation mechanism of DME, through *ab initio* calculations [220, 227, 251].

In theory, any ether molecule may follow this general mechanism, but the extent to which the molecule will regenerate OH via QOOH decomposition, or chain branch, will depend heavily on the heights of the barriers, relative well-depths of the RO_2/QOOH species, structures of transition states, and possibly the structures of the OH co-products. In the case of diethyl- and di-*n*-butyl- ether, their larger structures will lead to more possibilities for abstraction, rearrangement, and addition, and therefore increasingly complex mechanisms.

The most developed mechanism for the reaction of DEE with OH comes from several publications by Di Tommaso et al. [115, 252-254], where the mechanism is similar to that of DME, with the added complexity of two unique abstraction sites present. The α site is expected to dominate, as a result of the C–H bond weakened through proximity to the O atom. Hence, the α R radical is the major species formed during the initial abstraction reaction, and Di Tommaso and co-workers present a mechanism for the low temperature combustion mechanism of this radical. The rearrangement of RO_2 to QOOH in the case of DEE will proceed preferentially via a six-membered ring transition state between both α carbon sites adjacent to the oxygen. The QOOH can undergo decomposition to propagate the reaction with formation of an OH radical (see Figure 6-3), favouring the formation of two acetaldehyde molecules, but with an alternative route resulting in a four-membered ring species.
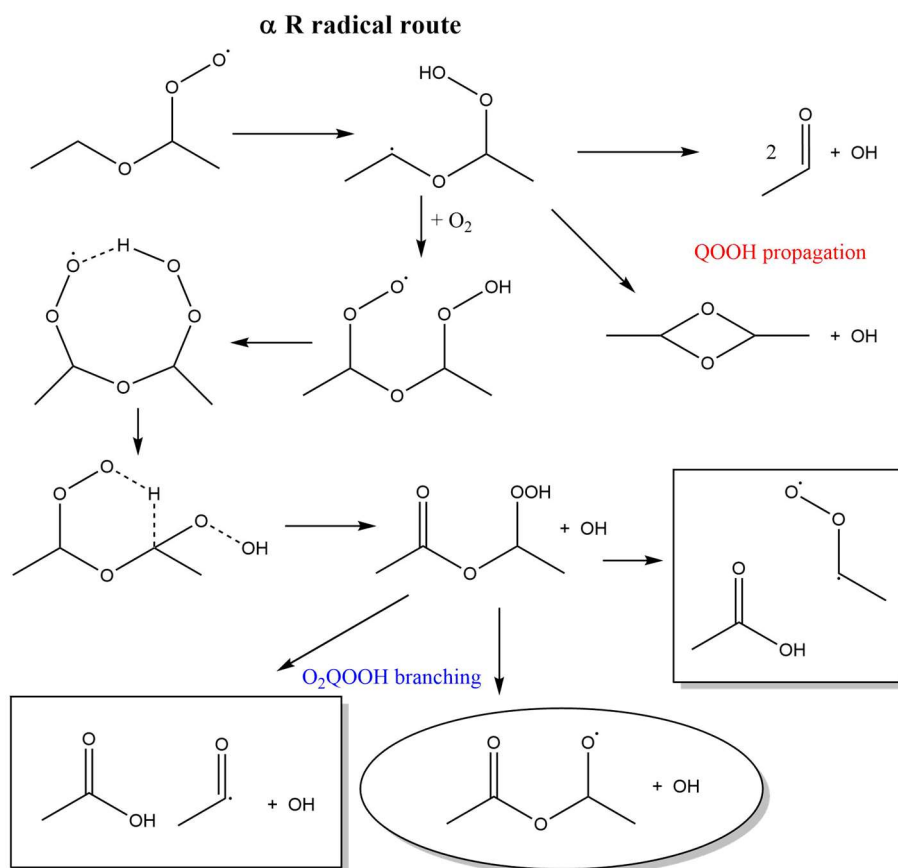
Figure 6-3: Possible OH regeneration routes in the DEE low temperature combustion mechanism proposed by Di Tommaso et al. [115] for the α R radical.

The O_2QOOH species proceeds via an eight-membered ring (although it is not clear why a ring this large should form, stabilisation by an O–H interaction is proposed as the reason), followed by a six-membered ring, to form the ketohydroperoxide species. This is analogous to HPMF in the DME system, and can decompose via six routes. Three routes are shown in Figure 6-3, where the products circled form in a barrierless reaction that would be kinetically favourable, and therefore more likely on the timescales of combustion. The other route to OH formation, and the most competitive reaction that does not generate an OH radical, are both displayed (30.3 kcal mol^{-1} and 26.7 kcal mol^{-1} barriers respectively).

Hu et al. proposed that the minor channel, arising from β abstraction of the DEE molecule, will proceed through a seven-membered ring transition state for the RO$_2$ → QOOH rearrangement, where the –OO• group abstracts the internal hydrogen on the α site of the opposing carbon chain. At 4 atm pressure and 600 K, they predict approximately 92% of the initial fuel abstraction will occur at the α site. Almost 7% are β abstractions, and the remainder are negligible contributions of fuel decomposition. Hu

et al. show the route to the QOOH-peroxy species, and imply this molecule decomposes to smaller species. A suggested route to chain-branching OH radical formation is shown in Figure 6-4, based on that of the α radical.

β R radical route

QOOH propagation

+ O₂

O₂QOOH branching

+ OH

+ OH

+ OH
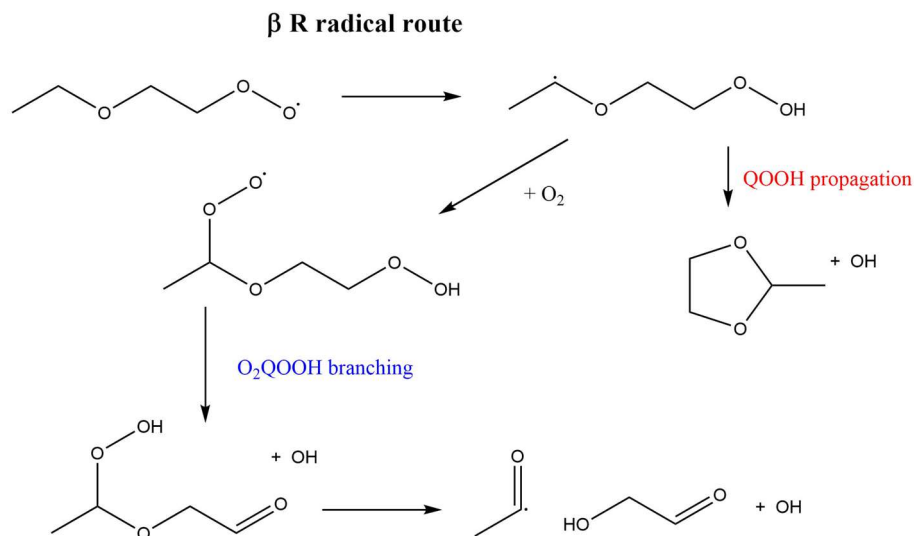
Figure 6-4: Possible OH regeneration routes for the DEE β R radical proposed by Hu et al. [228], with O₂QOOH decomposition products also suggested.

Ab initio studies have sought to increase knowledge of DEE's low temperature autoignition mechanism [220, 225-228, 252-255], but without laboratory measurements of the important reactions and species, verifying the validity of computation calculations is challenging.

To our knowledge, no *ab initio* studies exist on the low temperature chain-branching mechanism of DBE, however Thion et al. [172] have studied its oxidation in a jet-stirred reactor (JSR), and Cai et al. [170] used flames and a laminar flow reactor to develop a kinetic model and validate the model against ignition delay times. Cai et al. suggested the only chain-branching route possible was that beginning with the γ R radical (Figure 6-5), and that despite the α R radical dominating the process (followed by γ, β, then δ), no OH is formed via this route. Thion et al. proposed this route was the dominant process in chain-branching, and suggested other smaller species (such as the propyl radical formed during the ketohydroperoxide decomposition step), also contributed to the complex chemistry where multiple OH regeneration routes exist. The QOOH-peroxy radical formed from the α radical containing the –OO and –OOH groups on either side of the ether –O– was suggested by Cai et al. to be six times more likely than the alternative O₂QOOH species (with both oxygenated groups on the same carbon side chain). Cai et

al. also proposed that despite no chain-branching routes arising from the β and δ R radicals, both are able to propagate OH via decomposition of the QOOH radicals. Five-membered ring species make these pathways possible, whereas the analogous routes for the α and γ mechanisms would require unfavourable four-membered ring species formations. These proposed routes are summarised in Figure 6-5, where the mechanisms begin with the relevant RO_2 radicals. The number of potential routes here, and additional reactions such as decomposition of R radicals, and the smaller radical branching pathways, highlight the complexity of a large molecule like DBE in comparison to DME and DEE.
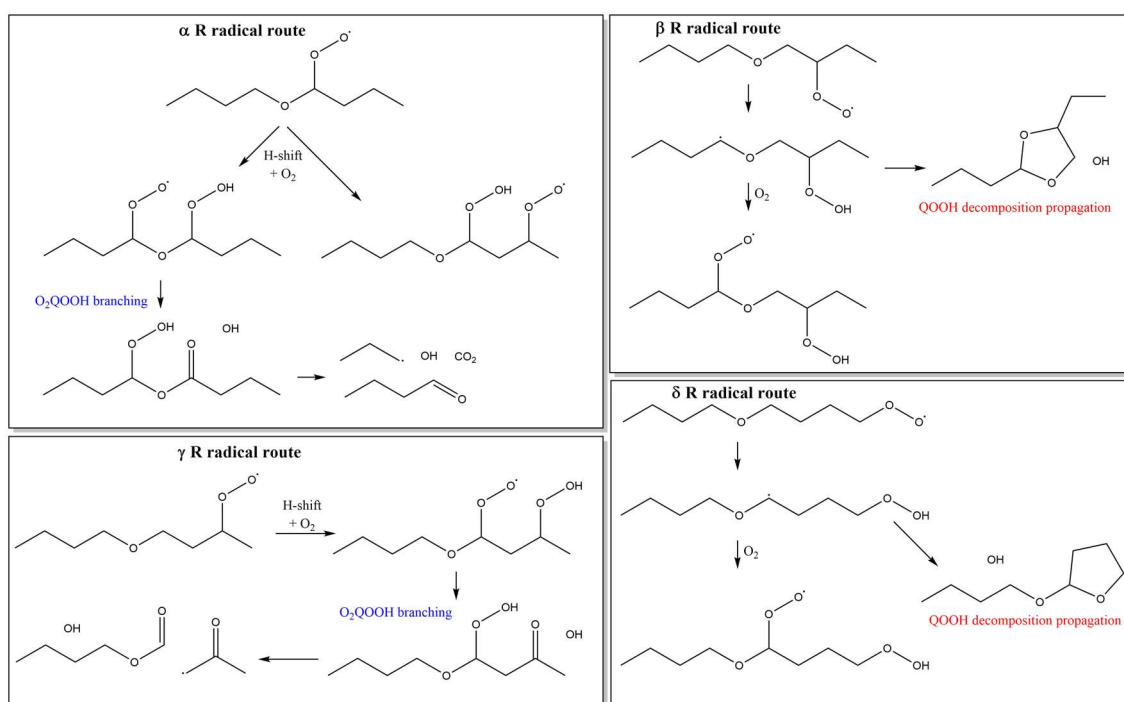
Figure 6-5: Suggested di-*n*-butyl ether OH regeneration mechanisms under low temperature combustion conditions.

Cool flames arise as a result of the branching mechanisms described, and manifest themselves physically by a sudden temperature rise of approximately 100 K [86, 256]. The increasing reaction rate is quenched before the reaction completes, when only 5 – 10% of the fuel has been consumed. A negative temperature dependence region is the cause of the arrested reaction rate, and is brought about by the reversal of the R + O_2 addition reaction (studied in Chapter 4 and Chapter 5) at higher temperatures (approaching 700 K). Under these conditions, the abstraction of a hydrogen from the R radical by O_2 becomes more important, and results in HO_2 formation – a much less

reactive radical than OH. Formation of R radicals via H abstraction by HO_2 will be slow in competition with the $HO_2 + HO_2$ reaction. Here, H_2O_2 and O_2 are formed, and the hydrogen peroxide will not decompose to form a significant number of OH radicals. Now, branching agents are destroyed more rapidly than they are formed (in the absence of RO_2 formation), hence the reaction is quenched until the $R + O_2$ addition reaction equilibrium is shifted to the products once more. Experimentally, C. Morley [257] demonstrated that photolytic perturbation of cool flames was possible, using a pre-heated gas flow reactor with heptane/air mixtures at ~800 K, in 1 atm N_2. Extra OH radicals were generated by photolysis of H_2O_2 (naturally present), to 'perturb' the cool flame, and the decay of the OH radicals was detected by laser-induced fluorescence, probing as a function of time. Decays exhibited triexponential behaviour that was attributed to the generalised model of autoignition (assigning rates for termination, propagation, and branching). These experiments demonstrated that it should be possible to extract rate coefficients for complex mechanisms under low temperature autoignition conditions.

6.3 Experimental

The majority of experiments in this chapter were carried out using the typical experimental setup described in Chapter 2. Di-*n*-butyl and diethyl ether were sometimes delivered using a bubbler method as described in Chapter 3 using Antoine parameters from Yaws and Yang [151]. The typical H_2O_2/H_2O precursor was used, if needed, and the laser wavelengths used were 248 nm (photolysis), and 308 nm (probe). For some experimental checks, an ozone box (Thermo Scientific 49C Ozone Analyzer) was used, to detect absorption at 254 nm. Reagents used in this chapter were OH precursor (hydrogen peroxide, H_2O_2, Sigma-Aldrich, 50% (w/w) in H_2O), buffer gas (N_2, BOC, oxygen-free), O_2 (BOC, 99.5%), H_2 (BOC, high purity), DME (Argo International Ltd, 99.8%), DEE (Sigma-Aldrich, ≥99%), DBE (Sigma-Aldrich, 99.3%), MTBE (Sigma-Aldrich, 99%), TMOF (Sigma-Aldrich, 99.8%), and CH_4 (BOC, >99.9%).

For the experiments in section 6.7, a different experimental setup was utilised (Figure 6-6). This has been described in detail previously [258, 259], but briefly, the primary difference between this and the setup used most, are the ability to achieve higher pressures as a result of the FAGE technique. FAGE, meaning fluorescence assay by gas expansion, involves the expansion of a high pressure reaction cell, through a small pinhole, into a low pressure detection region (approximately ≤1 Torr). In this way, high

pressure experiments (up to 2 atm) can be undertaken, with fluorescence monitoring taking place in the detection region free of significant quenching.

Here, a stainless steel tube (22 mm internal diameter), 0.5 metre long, allowed preheating of the gas that flowed along the tube. Calibrated MFCs were used to deliver the reactants, precursor, and buffer gas at a flow rate of approximately 10000 sccm, and the temperature was monitored by calibrated K-type thermocouples near the pinhole. Gases (N_2 and O_2) were delivered from cylinders, and liquids (H_2O_2 and DEE) from thermostatted bubblers, with N_2 backing flow. The photolysis pulsed was generated by an excimer laser operating on KrF (Lambda Physik, Compex 200, 10 Hz) to generate 248 nm light. At the end of this tube, the pinhole (approximately <0.15 mm diameter) caused expansion of the gas into the detection cell. Flow rates of approximately 1200 sccm in this cell gave pressures of 0.3 – 5 Torr. Excess gas from the reaction cell was passed out through exhaust channels.
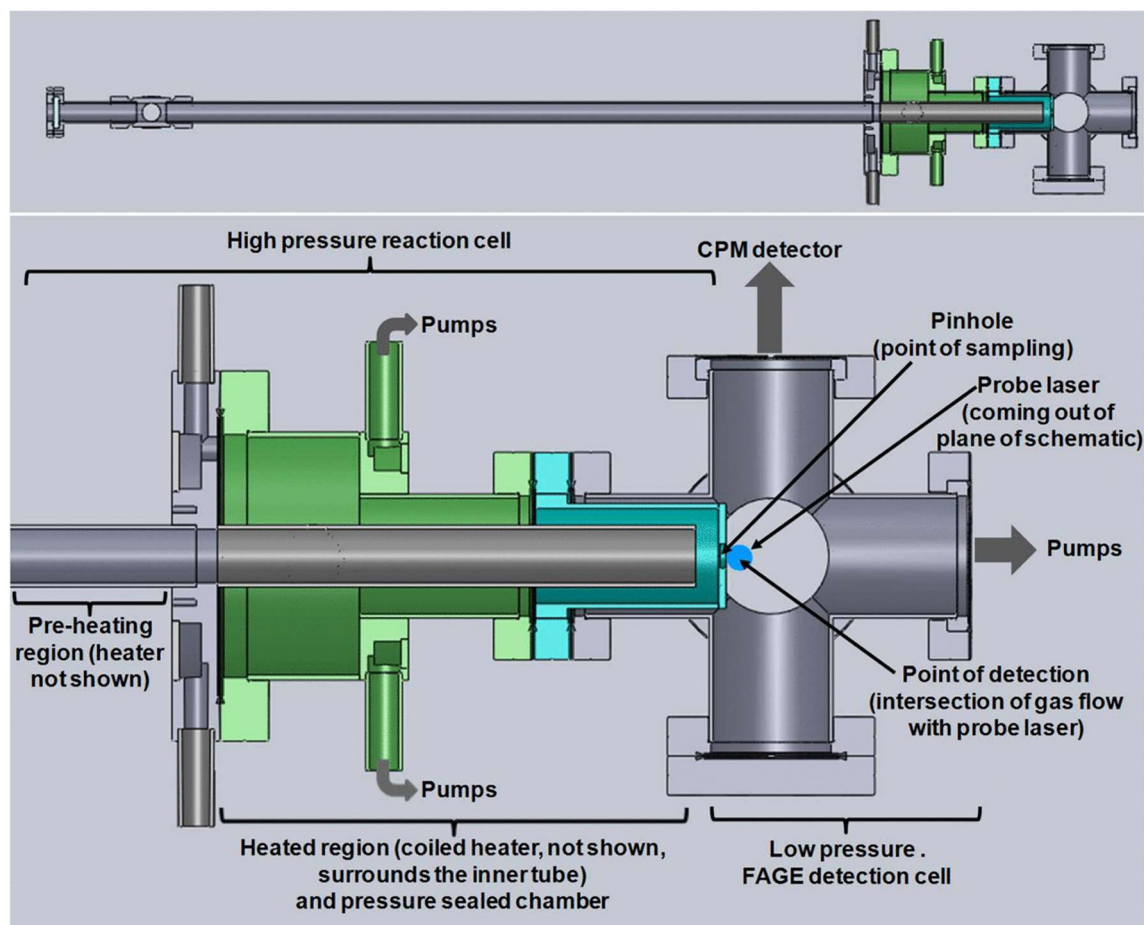
Figure 6-6: Schematic diagram of the FAGE instrument used in section 6.7, reproduced from Stone et al. [258], showing the full instrument in the upper panel.

OH radicals in the expanded jet region were detected by off-resonance LIF at 308 nm collected using a filter (305 ± 5 nm, Barr Associates) and a PMT (Perkin-Elmer C1943P), and the probe laser was 282 nm light generated by frequency doubling the output of a dye laser (Continuum, Rhodamine 6G dye), pumped by a Nd:YAG laser (Quantel, Q-smart 850). A delay generator (BNC DG535) was used to vary the delay between the photolysis and probe laser to generate a time-resolved OH decay, which were averaged 5 – 30 times, and analysed using the same single exponential and biexponential equations employed throughout this thesis.

Experiments using this alternate setup allowed higher pressures and greater O_2 concentrations to be explored in comparison to the typical setup used throughout this thesis. A further advantage was the lack of any interfering chemistry observed, which is discussed further in section 6.7.

Biexponential decays in this chapter were analysed using the basic biexponential analytical scheme described in Chapter 3 (Scheme 6-3). It should be noted that k_b, the recycling parameter, can be as a result of several processes, such as QOOH decomposition, O_2QOOH decomposition, and ketohydroperoxide decomposition. Any single exponential decays were analysed in the typical manner used throughout this thesis. Other analyses employed a more complex analytical scheme, and are described in detail in section 6.6.

$$RH + OH \xrightarrow{k_a'} R\cdot \xrightarrow{+\,O_2} RO_2 \xrightarrow{k_b} OH$$

$$\big\downarrow k_d \qquad\qquad\qquad \big\downarrow k_c$$

$$\text{loss} \qquad\qquad\qquad\qquad \text{loss}$$
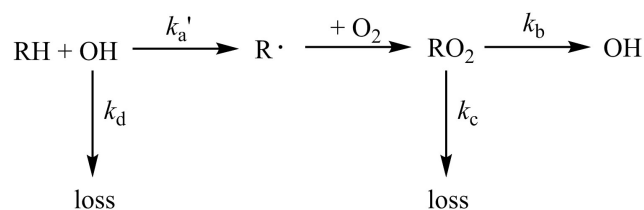
Scheme 6-1: Simplified reaction scheme for biexponential analysis equation parameters.

6.4 Observation of Chain-branching?

Biexponential kinetic decay traces were often obtained in the presence of oxygen (see Figure 6-7) when not in the chemical activation range of conditions (i.e. high pressure (≥50 Torr), temperature (≥~480 K), and oxygen (>~10^{15} molecule cm^{-3})). Evidence of OH recycling seen in this trace was observed for the DME, DEE, and DBE systems. For these ethers, biexponential behaviour was observed in the presence of O_2 at temperatures

as low as 510 K, 450 K, and 483K respectively, however the effect is heavily dependent on several conditions, including $[O_2]$, [ether], and possibly pressure and flow.
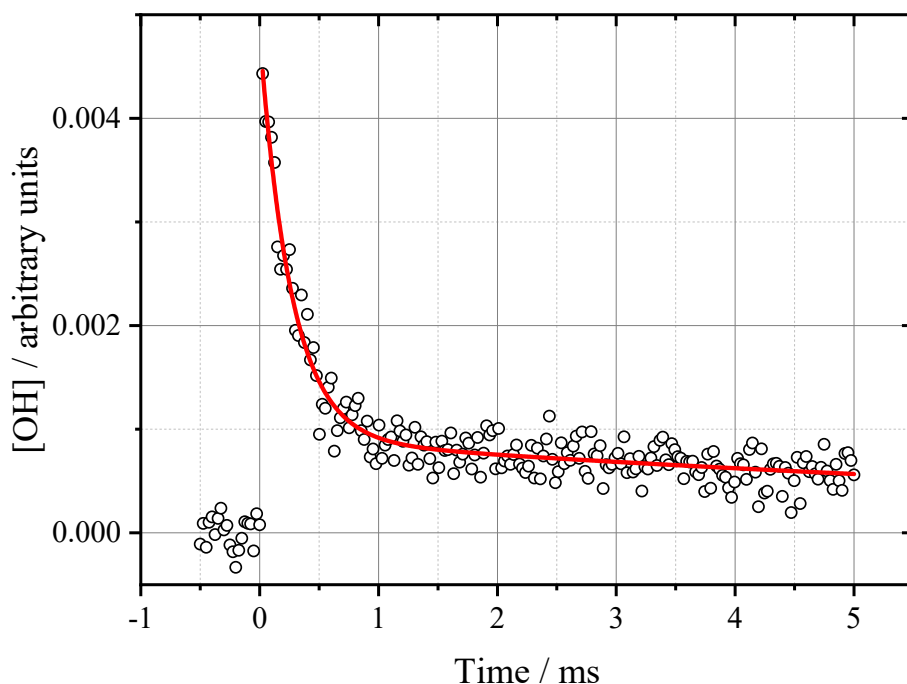
Figure 6-7: Biexponential decay of OH in reaction between DME and OH. Trace obtained at 552 K and 108 Torr N_2, where [DME] = 5.1 × 10^{14} molecule cm^{-3} and $[O_2]$ = 2.5 × 10^{17} molecule cm^{-3}. Red line is a biexponential fit: k_a' = (2730 ± 150) s^{-1}, k_b = (750 ± 110) s^{-1}, k_c = (30 ± 40) s^{-1}, k_d = 340 s^{-1}. Errors are statistical, calculated at the 2σ level.

A range of oxygen concentrations was explored to attempt to draw conclusions about its effects on the recycling seen, and increasing the amount of oxygen present was often shown to increase the amount of recycling measured from biexponential decays, for experiments with DME and DEE. The dependence of the recycling parameter, k_b, upon oxygen concentration often yielded a plot with a similar shape to those in Figure 6-8. The plot shows a form which has two clear plateaus at low and high oxygen concentration, and it is possible that these "limits" represent rates for reactions such as QOOH decomposition, or chain-branching reactions. However, not all dependences looked like this, and sometimes k_b increased more linearly with oxygen concentration. Currently there is no consistent and well-understood trend.
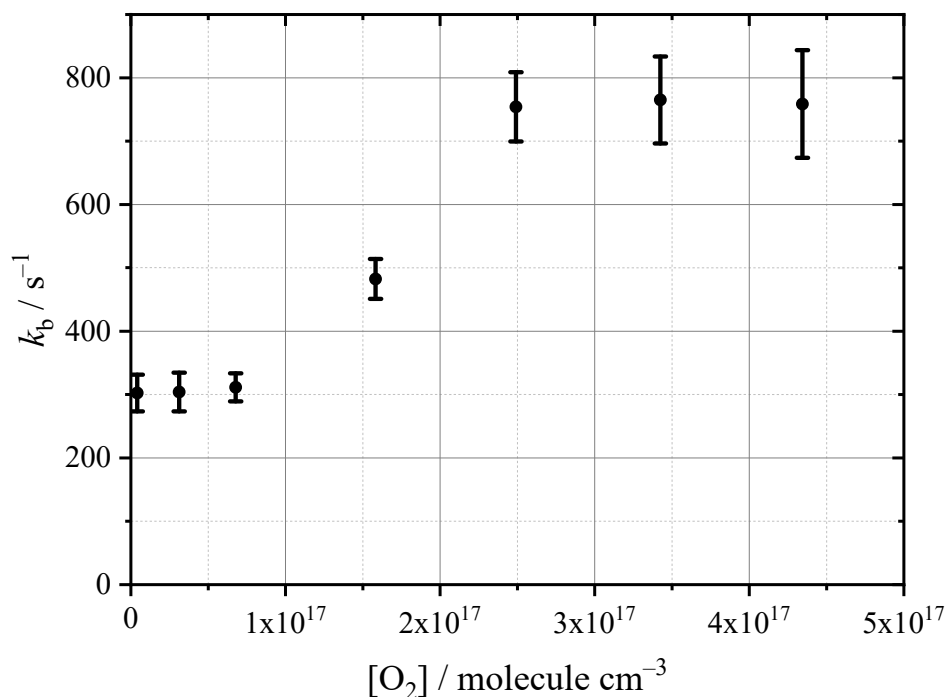
Figure 6-8. Example of k_b dependence on oxygen concentration for DME at ~600 K. Error bars are statistical, calculated at the 1σ level.

Over a narrower and more specific range of temperatures and oxygen concentrations to those above, OH decays were obtained which conformed neither to a biexponential or a single exponential fit. These shapes exhibited a portion of constant OH signal, or sometimes even an increase, after the initial fast decay usually observed. An OH decay of this nature suggested OH was temporarily being produced on a scale greater than propagation and removal. Figure 6-9 is an example of this type of OH kinetic trace, which was seen for all three ethers.

Beyond shoulders, more extreme manifestations of what was believed to be 'partial' chain-branching mechanisms were observed for the ethers, where large growths of OH signal were measured under *largely* reproducible experimental conditions. It generally followed that the strength (i.e. height) of growths from strongest to weakest was DBE > DEE > DME. An example of this behaviour, shown here for the DBE system, is presented in Figure 6-10, where a range of oxygen concentrations are presented. At the peak levels of OH growth, the signal height is approximately 100% larger than $[OH]_0$ generated by the photolysis laser.
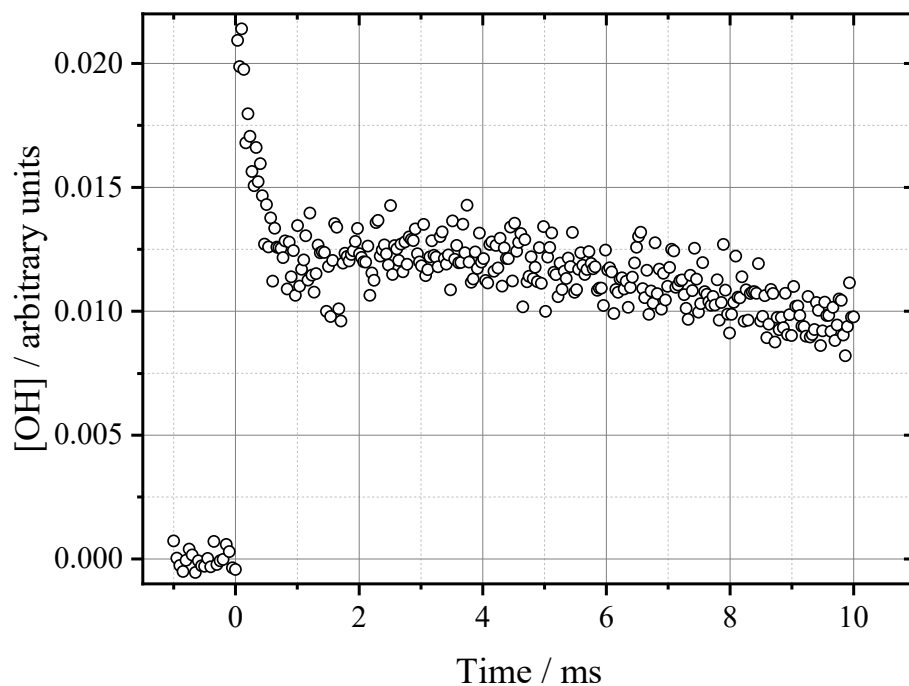
Figure 6-9. DME experiment exhibiting a temporary growth 'shoulder'. Experimental conditions were $T = 590$ K, in 61 Torr N_2, [DME] $= 4.7 \times 10^{14}$ molecule cm^{-3}, and [O_2] $= 8.2 \times 10^{16}$ molecule cm^{-3}.
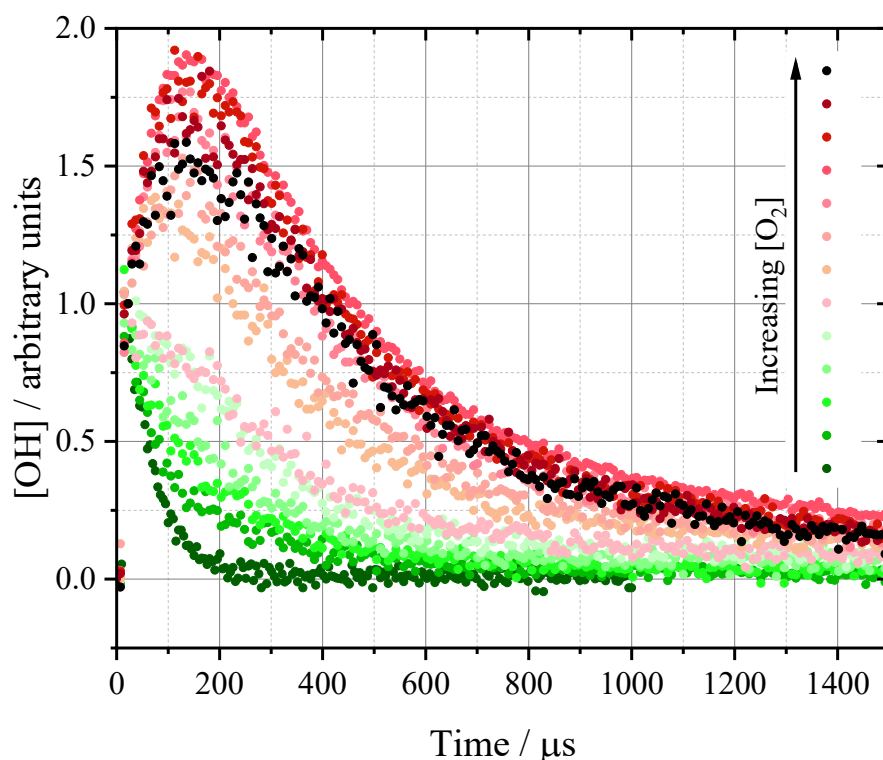
Figure 6-10: Example of large OH signal growth observed in the presence of oxygen for the DBE system. Lowest [O_2] $= 0$ molecule cm^{-3}; [O_2] range $= (0.3 - 23) \times 10^{16}$ molecule cm^{-3}. Experimental conditions were $T = 762$ K, in ~52 Torr N_2.

The boundaries of where shoulders and growths were observed are mapped out in Table 6-1, although it is important to note that the causes of the significant OH production (explained later in this chapter) were present but hidden at other temperatures, such as temperatures where biexponential decays were observed, and not solely where they were visible 'by eye' as shoulders or growths. Further, the boundaries mapped out in Table 6-1 give an indication of where the OH production source is occurring, but does not expressly rule out other conditions where experiments may not have been conducted (e.g. above 230 Torr for the diethyl ether system, and many other pressures for DBE where experiments were not conducted).

Table 6-1: Approximate conditions mapped out for the observation of OH 'branching' for DME, DEE, and DBE.

Ether	P range / Torr	T range / K
DME	Below 150	480 – 545
DEE	To at least 230	500 – 650
DBE	~50	Above 700 K

Initial assumptions, that chain-branching was occurring in the reaction cell, were questioned as a result of two main features of the growth traces – the short timescale of the OH growth signal, and the rapid consumption of the 'branching' OH radicals.

It is not clear why chain-branching would begin to turn off on such a short timescale, indeed, branching by definition suggests it should increase until the fuel is consumed, which would not occur this rapidly. Similarly, HO_2 formation channels should only become competitive at long timescales. One potential explanation could be the 'final' products formed in a low temperature oxidation surface (for example formaldehyde in the case of DME) consuming the OH radicals formed by chain-branching at a more competitive rate. However, if this were the case, it is likely that these species would form their own R and RO_2 radicals, and undergo chain-branching themselves. For this to occur, it would also suggest that the products of the system are being formed after approximately 150 µs in the example presented in Figure 6-10, which is not expected. This is directly related to the other issue referred to above – the short timescale of the OH growth signal. Not only does the maximum OH signal occur at ~150 µs, but the rise in OH occurs instantaneously at $t = 0$ in the high $[O_2]$ extreme growth traces. Simple numerical simulations using the Kintecus software package, based on

estimated rate coefficients for the reactions leading to chain branching, and approximate reactant concentrations and conditions used in experiments, indicated an induction period would be observable, and OH signal increases would not occur at $t = 0$.

Figure 6-11 presents experimental evidence that supported the uncertainty in the chain-branching observation. Signal in the absence of the hydrogen peroxide precursor confirmed the likelihood that there was alternate chemistry taking place in the reaction cell. The signal in this example, using DEE, was significant (approximately half that with the precursor present), and disappeared when oxygen was also omitted from the experiment.
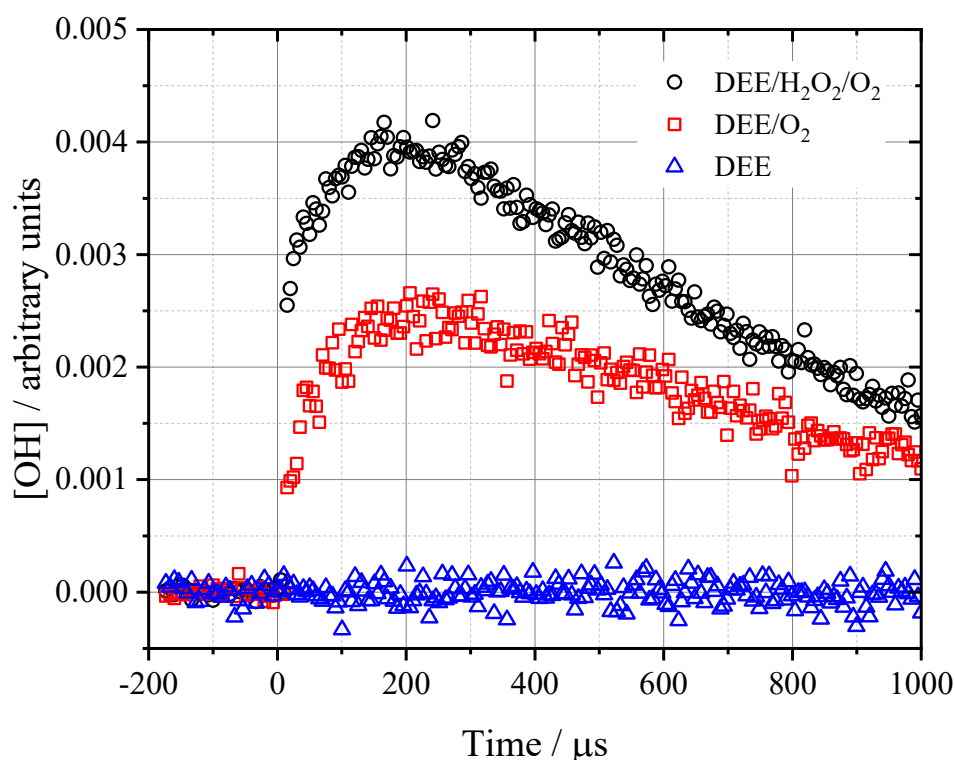
Figure 6-11: Example of signal in the absence of hydrogen peroxide, where the fuel was diethyl ether. Experimental conditions were $T = 558$ K, in 38 Torr N_2, $[O_2] = 1.5 \times 10^{17}$ molecule cm^{-3} when present, and $[DEE] = 2.3 \times 10^{15}$ molecule cm^{-3}.

Ultimately, further experiments such as these, in the absence of an OH precursor, will be the only reliable way to characterise the full extent, and boundary conditions reported in Table 6-1, of the extraneous chemistry causing OH shoulders and growths. Following the observation of precursor-free OH signal, investigations into the possible source of the hydroxyl radicals were carried out, and will be presented throughout the remainder of this chapter. The majority of experimental tests conducted involved DBE

and/or DEE, but there is no obvious reason they would not also apply to DME, although the extent of the effect is assumed to be lesser for DME.

6.5   Potential Source of OH

Probable causes of OH growth were considered, and two were ruled out through experimental tests. The first was decomposition of the fuel in the reaction cell, where high temperatures could be causing the fuels to decompose directly to R radicals, which proceed to form RO_2 radicals and ultimately chain-branch. This mechanism would require no precursor for hydrogen abstraction of the fuels, and a build-up of radicals could potentially occur in the cell. However, the significant OH signal at $t = 0$ in Figure 6-10 would suggest that photolysis is still resulting in the majority of the OH signal, even if some decomposition is occurring. If fuel decomposition was the cause of OH growth, it would likely occur more gradually, and OH fluorescence signal would accumulate over time.

Based on this observation of strong prompt OH formation in the absence of H_2O_2, the second potential source of OH considered was photolysis of the fuels, although it is not immediately clear how photolysing the straight chain ethers under consideration would lead to instant OH formation. Regardless, this theory was ruled out based on experiments where the repetition rate of the lasers was reduced from the typical 10 Hz rate, to 5 Hz, 2 Hz, and 1 Hz (Figure 6-12).
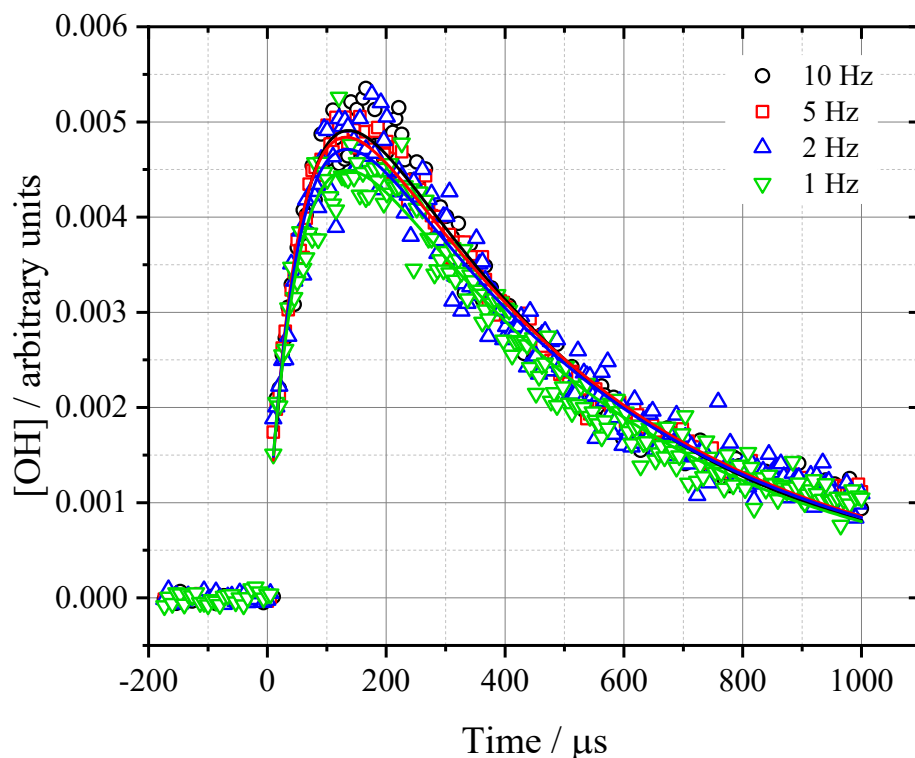
Figure 6-12: Repetition rate experiments on DBE under 'branching' conditions in the presence of O_2, at 750 K, and 50 Torr N_2. H_2O_2 was present in these experiments. From 10 to 1 Hz, growth rates were (16410 ± 1620) s^{-1}, (17370 ± 1320) s^{-1}, (16810 ± 2190) s^{-1}, (16470 ± 1930) s^{-1}, and decay rates were (2250 ± 80) s^{-1}, (2150 ± 60) s^{-1}, (2150 ± 100) s^{-1}, and (2150 ± 90) s^{-1}. Uncertainties are statistical at the 2σ level.

Figure 6-12 demonstrates the invariance of the rates of OH generation and removal in a 'branching' trace generated using DBE, when fit with a simple growth and decay exponential equation. Were the ethers being photolysed by the excimer laser, a build-up of radicals would be expected, and a change in repetition rate would affect the concentration of radicals and thus the kinetics of the OH traces. For this experiment, and Figure 6-13, where the excimer laser fluence was varied, all growth and decay rates agree well within uncertainty ranges.
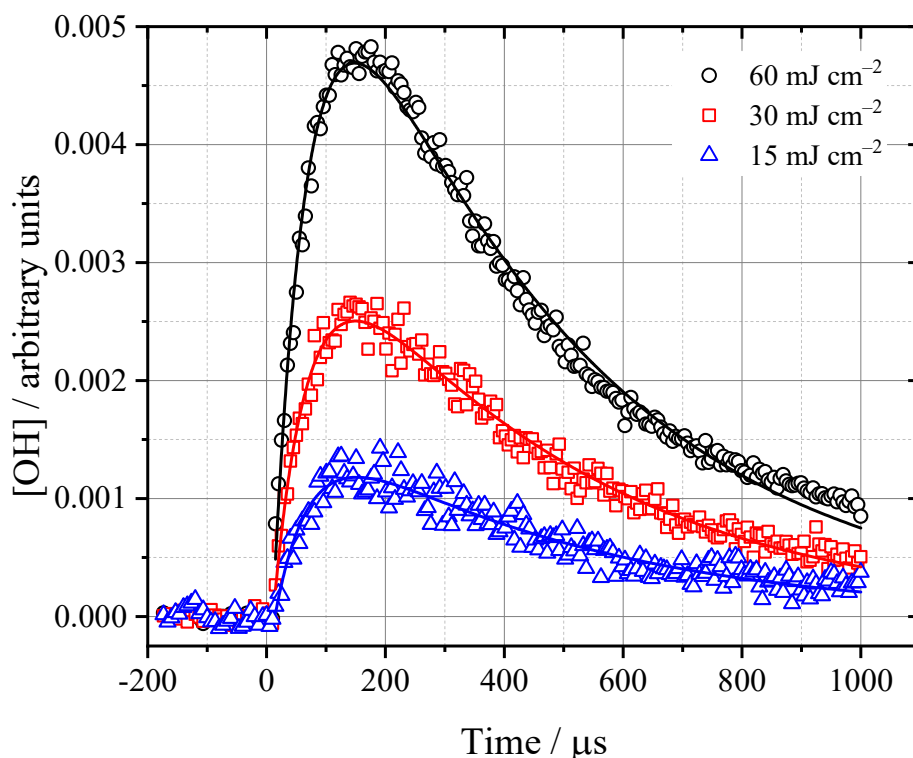
Figure 6-13 Laser power effect on H₂O₂-free DBE experiment, approximate fluencies given in legend. Experimental conditions were $T = 753$ K, in 53 Torr N₂, [DBE] $= 8.6 \times 10^{14}$ molecule cm⁻³, and [O₂] $= 1.5 \times 10^{17}$ molecule cm⁻³. Note the fits are not perfect in the tail. From high fluence to low, growths were (16540 ± 910) s⁻¹, (16630 ± 1390) s⁻¹, and (17090 ± 2860) s⁻¹. Decays were (2330 ± 60) s⁻¹, (2270 ± 80) s⁻¹, and (2210 ± 170) s⁻¹. Uncertainties were statistical at the 2σ level.

Further evidence for the lack of fuel photolysis is presented in Figure 6-14, where the effect of laser fluence on the OH decay under single exponential conditions was verified. Here, unlike the two previous experiments, no oxygen was present, resulting in no OH growth. The returned parameters of the pseudo-first order rate coefficient for the reaction between DBE and the hydroxyl radical are in agreement within uncertainties, suggesting none, or no significant fraction, of the fuel is photolysed. Photolysis of the fuel would result in a lower DBE concentration, and as such the high laser energy experiments would result in a slower pseudo-first order rate coefficient. This test was performed virtually at the high temperature limit of the reaction cell, 750 K; any absorption cross section is expected to increase with temperature, and therefore any photolysis would be more extreme. At room temperature, the absorption cross sections for DME [260] and DEE [261] have been reported as <4.0 and 9.4×10^{-19} cm² molecule⁻¹ respectively at 248 nm. Regardless, the single exponential k' parameter was not affected by the change in photolysis power.
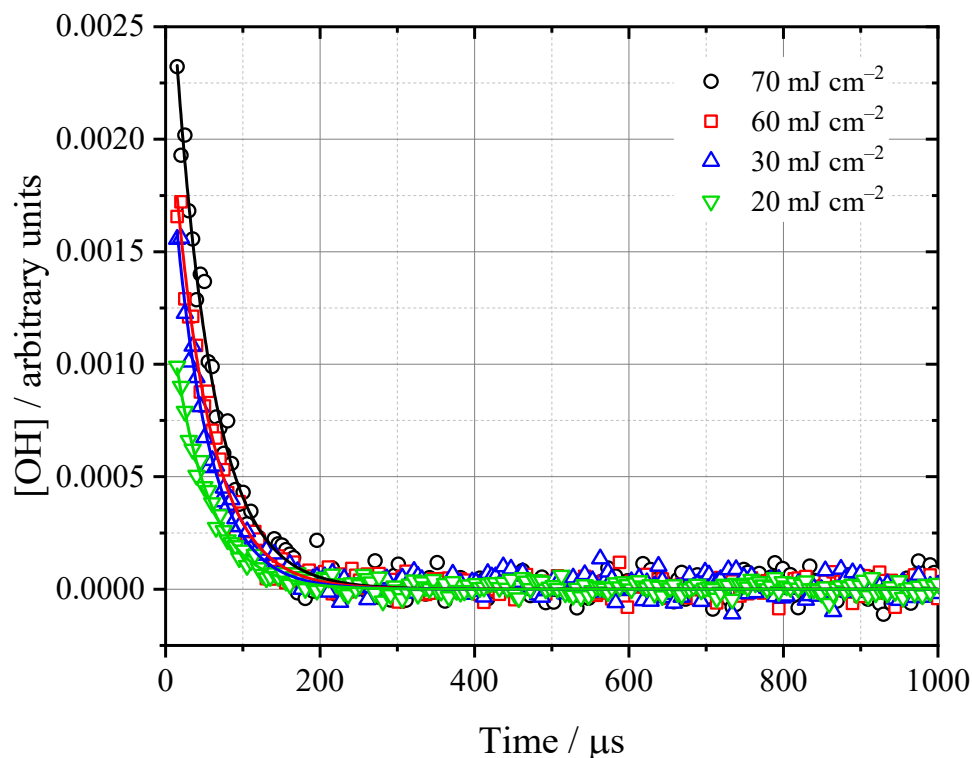
Figure 6-14: Single exponential decays of OH + DBE unaffected by laser power. Experimental conditions were T = 761 K, in 51 Torr N_2, and [DBE] = 8.6 × 10^{14} molecule cm^{-3}. No O_2 was present, to ensure single exponential decays. From high to low fluence, k' = (20470 ± 900) s^{-1}, (20950 ± 950) s^{-1}, (22350 ± 1120) s^{-1}, and (21820 ± 1020) s^{-1}. Uncertainties are statistical at the 2σ level.

Finally, the reaction between oxygen atoms and the fuel, RH, was considered as a possible source of OH generation in the reactor. The heavy dependence of signal growth on oxygen shown in Figure 6-10 suggests this mechanism could be possible, under the assumption that O_2 is directly or indirectly a precursor to the formation of O atoms. O + fuel reactions would undergo hydrogen abstraction to directly form OH radicals. It is unclear where O atoms would arise from in the reaction cell, and what follows are further tests to attempt to identify this source.

6.5.1   Potential Source of O Atoms

Ozone present in the reaction cell was originally thought to be a possible photolytic precursor for O atoms, but several tests ruled out this possibility. An ozone box was attached to the outlet of the reaction cell during some 'branching' diethyl ether experiments, and the concentrations detected were monitored by absorption at 254 nm. Tests showed some absorption at this wavelength (~50 ppb levels), however any species

that absorbs at 254 nm could cause this detection, and so the presence of any ozone was not specifically confirmed. RO_2 species may potentially absorb at this wavelength, but the radicals' lifetimes were expected to be too short for them to reach the ozone detector.

Further tests were carried out in the same reaction cell, where a cool flame was established using H_2, O_2 and N_2 (approximately 750 – 850 K, ~50 Torr, ~(0.5 – 1.5) × 10^{17} molecule cm^{-3} O_2, and ~(0.1 – 2.0) × 10^{16} molecule cm^{-3} H_2). Here, no excimer laser was required for significant OH fluorescence signal to be generated, and balancing of the hydrogen and oxygen delivered to the reaction cell to optimal conditions led to increases in the OH signal so significant that the PMT was overloaded. As the OH signal rose, the temperature of the reaction cell could be seen to rise similarly, by temperatures up to 100 K in the most extreme cases. In these cool flame experiments, there must be some radicals present in the cell to initiate the chain-branching mechanism.

Under the same conditions that a cool flame was observed, the ozone box was used to monitor the species exiting the reaction cell, in the absence of hydrogen. There was no detection of species absorbing at 254 nm under these conditions. This ruled out any mechanism for O_3 formation by some reaction between two O_2 molecules on the surface of the cell walls. It still did not rule out some formation mechanism for ozone by a surface reaction between the fuel and O_2. This was presumed to be the most probable mechanism based on the experiments thus far, and Figure 6-15 and Figure 6-16 go some way to corroborating this theory.

Figure 6-15 displays the dependence of OH growth, in a precursor-free experiment, on the concentration of diethyl ether. Prompt OH signal, and maximum of the signal growth, can both be seen to reduce as the concentration of ether is reduced. Similarly, in Figure 6-16 the reduction in [O_2] causes the OH signal generated in the absence of H_2O_2 to tend towards zero, where the signal is minimal at approximately 5 × 10^{16} molecule cm^{-3} O_2. Both dependences presented here suggest the mechanism generating OH in the reaction cell is heavily dependent on both fuel *and* oxygen. It should be noted that no effects below 10^{16} molecule cm^{-3} O_2 were observed, which is significantly above the O_2 concentrations used for the experiments in Chapter 4 and Chapter 5, and as such, they were not affected by the extraneous chemistry presented in this chapter. Additionally, the high temperatures required for the onset of H_2O_2-free signal were not explored in Chapter 4 and Chapter 5.
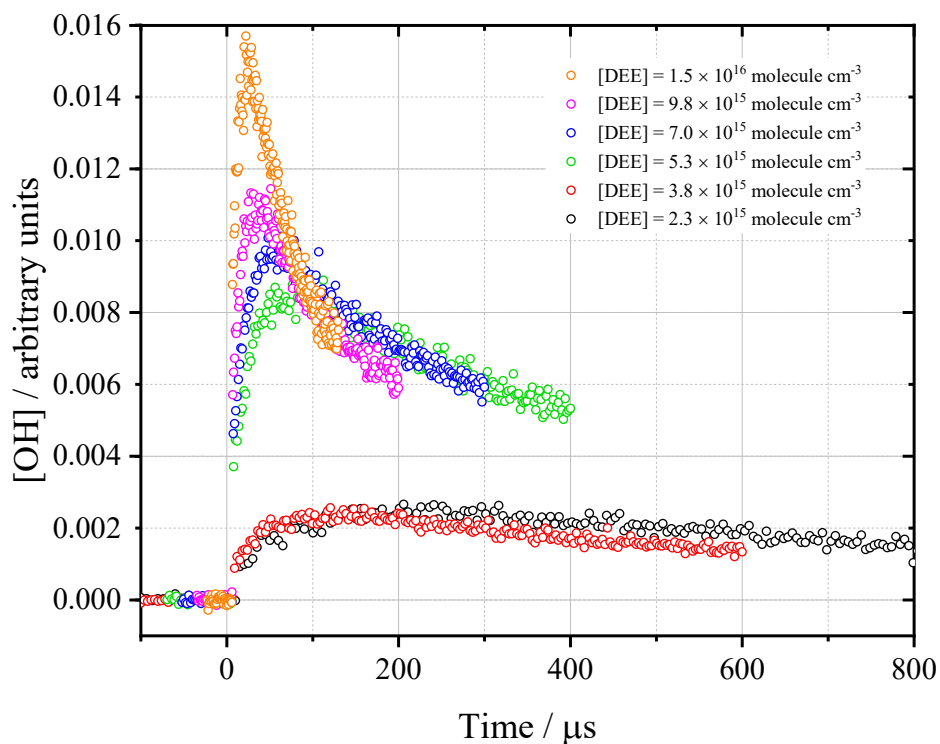
Figure 6-15: Example of growth dependence on fuel concentration for the DEE system, H₂O₂-free. Experimental conditions were T = 557 K in 40 Torr N₂, and [O₂] = 1.5 × 10¹⁷ molecule cm⁻³.
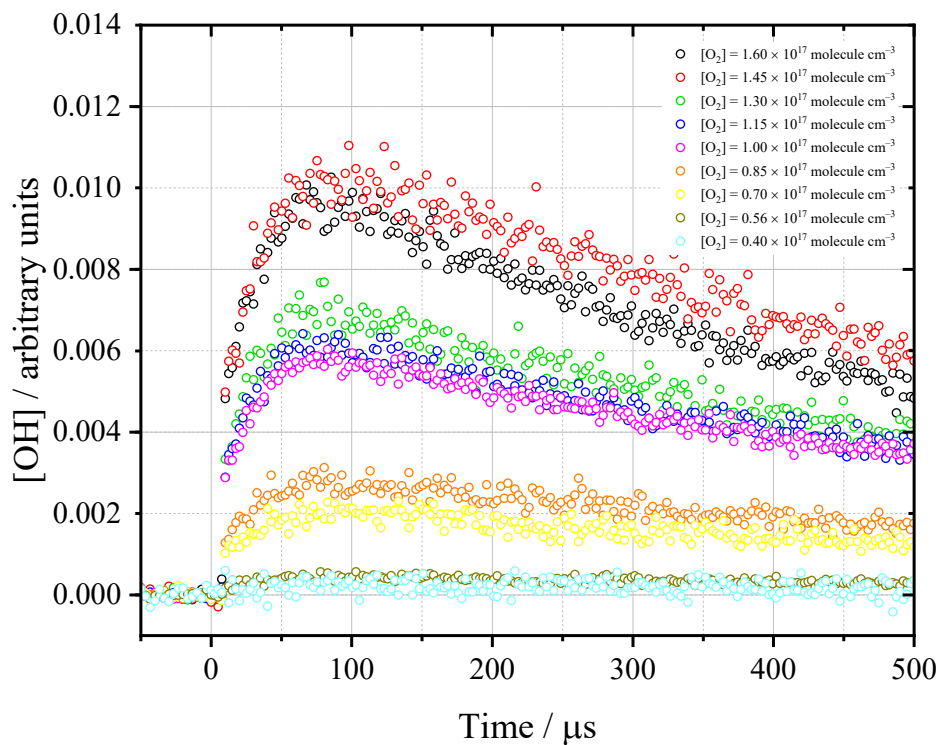
Figure 6-16: Example of growth dependence on O₂ concentration for the DEE system, H₂O₂-free. Experimental conditions were T = 556 K, in 39 Torr N₂, and [DEE] = 5.2 × 10¹⁵ molecule cm⁻³.

Further, the type of fuel appears to be of importance to this mechanism. Methane was examined for the same behaviour, but no signal in the presence of oxygen and absence of hydrogen peroxide was observed. Multiple isomers of butanol have been shown by a co-worker to display the same behaviour as the ether fuels here [262], in the same experimental setup, and also a different setup. Oxygenated fuels may therefore be integral to the chemistry that occurs between the fuel and oxygen to generate OH.

A test was carried out (Figure 6-17) to determine the presence of $O(^1D)$ atoms in the system. In an experiment with O_2, N_2, and DEE, were O_3 photolysis occurring, at low pressures of N_2 significant amounts of $O(^1D)$ should be generated. In the presence of DEE, a fast growth in OH (from the $O(^1D) + DEE \rightarrow OH + C_2H_5OC_2H_4$ reaction; k_{bim} on the order of 10^{-10} cm^3 molecule^{-1} s^{-1}) would be observed on short timescales. Rate coefficients for $O(^1D)$ + hydrocarbons reactions, such as n-butane, n-pentane, and n-heptane have been observed as fast as ~5×10^{-10} cm^3 molecule^{-1} s^{-1} previously [263, 264]. A simulation of an expected OH growth is included in Figure 6-17, with a growth rate based on the $O(^1D) + DEE$ rate coefficient above, and a decay rate based on the OH + DEE reaction measured in this work. The absence of this in Figure 6-17 suggests photolysis of O_3 may not be present.

Finally, tests were carried out where the excimer laser was turned off during an OH growth experiment, and all signal disappeared. This suggests the process was dependent on photolysis, and attempts to fit the data based on the O + fuel reaction occurring were made. The source of O atoms was still unclear, but $O(^3P)$ atoms were deemed to be the most likely cause of OH growths.
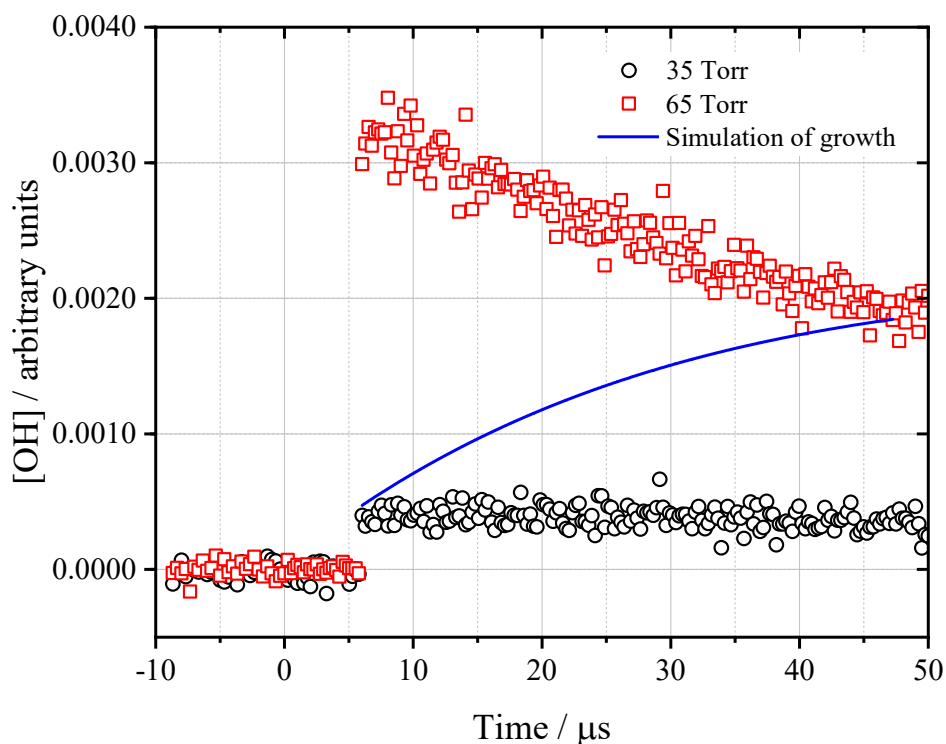
Figure 6-17: Test for O(^{1}D) using diethyl ether, [DEE] = 2.9, 5.4 × 10^{14} molecule cm^{-3}, [O$_2$] = 5.3, 9.9 × 10^{16} molecule cm^{-3}, H$_2$O$_2$-free, T = 475 K, experiments conducted in N$_2$. The blue line represents a simulated OH growth from the O(^{1}D) + DEE reaction, based on bimolecular rate coefficient of k_{bim} = 10^{-10} cm^3 molecule^{-1} s^{-1}.

6.6   Analysis of Data

Preliminary attempts to analyse the data generated from these experiments have been carried out. A reaction scheme (Scheme 6-2) was proposed for the generation of instant OH following the addition of O(^{3}P) to the fuel, RH, and the generation of OH by the expected propagation route via addition of O$_2$ to the R radical species. The details and derivation of this fit equation are provided in Appendix D.
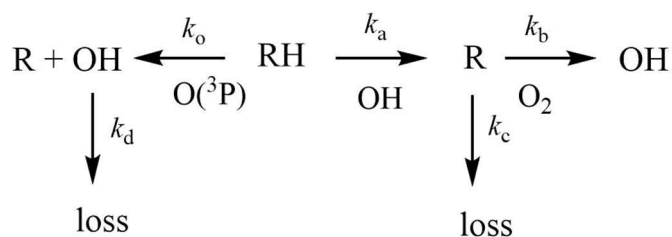
Scheme 6-2: Proposed reaction scheme for growth behaviour, used to derive multi-exponential fit to the data.

Global analysis using this scheme was carried out on multiple traces, including those with large OH growths, smaller shoulders, and simpler biexponential decays, for a given set of traces at specific a pressure and temperature. The best method for utilising this fit is still not fully understood, and is highly dependent on the system and chemistry taking place, but for the purposes of these preliminary fits, shared parameters were $k_{O+ether}$, $k_{OH+ether}$, and k_c. $k_{O+ether}$ and $k_{OH+ether}$ are the bimolecular rate coefficients for the relevant pseudo-first order rate coefficients, k_o and k_a respectively. For the fit to calculate these parameters, the ether concentration for each trace was defined. Ill-defined parameters were generally returned for k_c when treated as local to each trace, thus k_c was shared. This is a good example of a parameter which may be shared or local, based on whether it should have a dependence on O_2 for the ether combustion system of the relevant experiment.

Reasonably good fits to data with extreme OH growths in the DBE system are presented in Figure 6-18, where the signal varies as a function of oxygen. It is primarily the lowest oxygen concentration traces (biexponential decays, no growth), where the fit deviates the most.
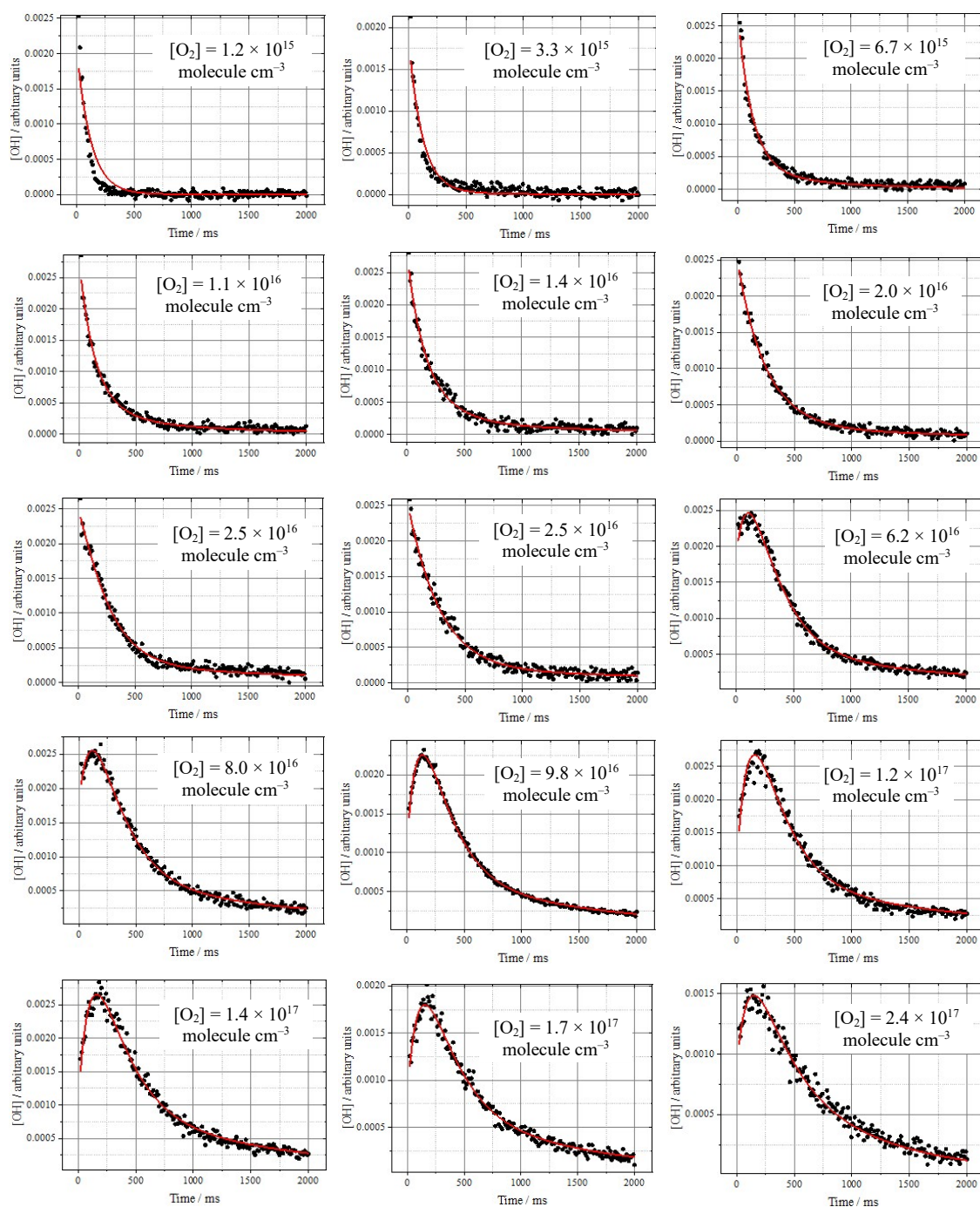
Figure 6-18: Global fit using the O(^{3}P) analytical equation for DBE experiments, where $T = 715$ K, in 50 Torr N$_2$. The loss parameter for OH, k_d, was fixed at 100 s^{-1}. [DBE] range = $(6.6 - 7.5) \times 10^{14}$ molecule cm^{-3}, [O$_2$] range = $(0.12 - 24) \times 10^{16}$ molecule cm^{-3}, H$_2$O$_2$ was the OH precursor.

Shared parameters returned from the global analysis of the traces in Figure 6-18 are $k_{OH+DBE} = (1.2 \pm 0.1) \times 10^{-11}$ cm^3 molecule^{-1} s^{-1}, $k_{O+ether} = (5.8 \pm 0.1) \times 10^{-12}$ cm^3 molecule^{-1} s^{-1}, and $k_c = (110 \pm 115)$ s^{-1}. Uncertainties are statistical at the 2σ level. The value obtained for k_{OH+DBE} is ~30% lower than the uncorrected bubbler value measured in Chapter 3, but given the complexity of the data, this shows reasonable agreement. An

example where $k_{OH+ether}$ is fixed at a known value is explored for the DEE system later in Figure 6-20. The bimolecular rate coefficient measured for the O + DBE reaction returned here can be compared with a previous study by Buchta et al. [265] who used discharge flow to study the reaction of O atoms with DBE and DEE, between 298 and 873 K. Arrhenius parameters reported by Buchta et al. give $k_{O+DBE} = 4.6 \times 10^{-12}$ cm^3 molecule^{-1} s^{-1} at 715 K, which is 22% lower than the value in this work. However, the upper uncertainty limit of their rate coefficient could yield $k_{O+DBE} = 8.1 \times 10^{-12}$ cm^3 molecule^{-1} s^{-1}, and so given the nature of the complex data in this chapter, there is reasonably good agreement for the measurement of O + DBE. This supports the possibility that hydrogen atom abstraction by O atoms is occurring under these conditions. Similarly, Liu et al. [266] undertook a flash photolysis study of the same reactions between 240 – 400 K, where extrapolated Arrhenius parameters to 715 K would report $k_{O+DBE} = 4.0 \times 10^{-12}$ cm^3 molecule^{-1} s^{-1}, and for the upper limit $k_{O+DBE} = 5.3 \times 10^{-12}$ cm^3 molecule^{-1} s^{-1}. The upper limits calculated here are based on statistical uncertainties provided by the authors for these previous measurements.

The dependences of the k_b recycling parameter and O(^{3}P):OH ratio are presented as a function of [O$_2$] in Figure 6-19. A significant amount of O atoms in comparison to OH is suggested here, where the ratio peaks at approximately 10:1. A possible explanation for a decrease in the O(^{3}P):OH ratio at the highest O$_2$ concentrations is the consumption of O(^{3}P) atoms by reaction with O$_2$. However, it is difficult to compare absolute amounts of O(^{3}P), as it is related to the amount of OH assigned by the fitting equation. This amount of OH will be quenched at high O$_2$ concentrations, and the quenching coefficient needed to determine absolute OH concentrations is not known for these experiments. Values determined for k_b at the lowest O$_2$ concentrations are unreliable, however there is a clear increase in recycling at mid to high concentrations. This is consistent with a process such as the QOOH + O$_2$ reaction where a dependence on O$_2$ would be expected, although the slow first order rate coefficients obtained would suggest there is not a great amount of propagation or chain-branching occurring.
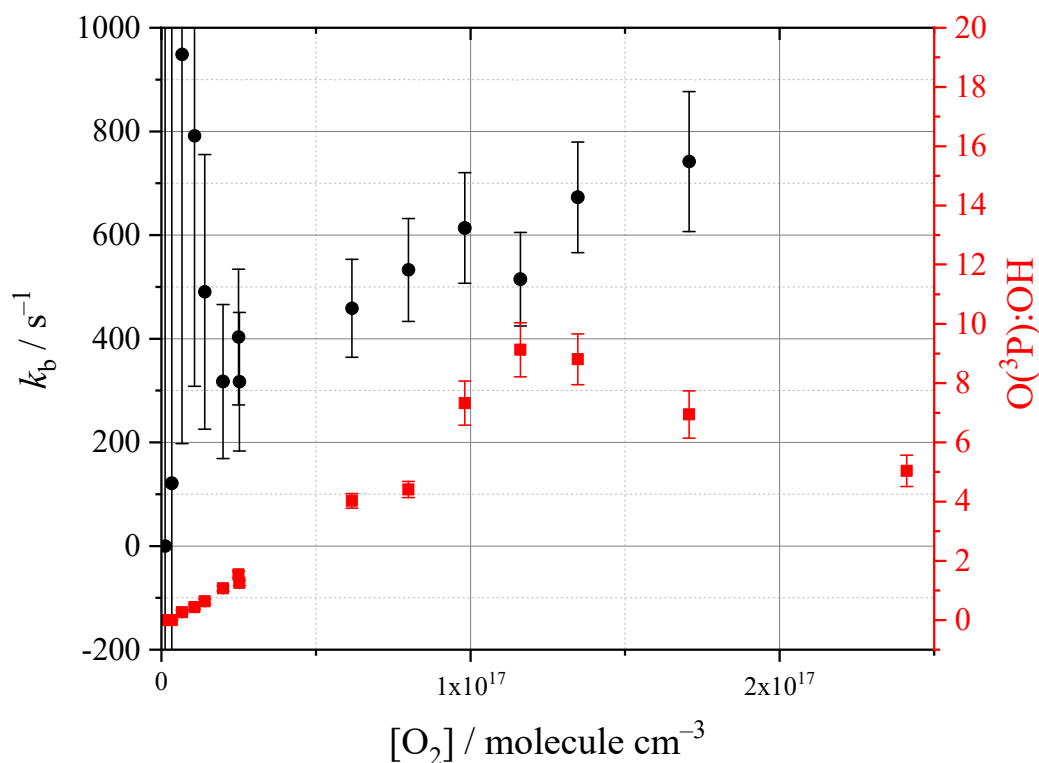
Figure 6-19: k_b and O(^{3}P):OH as a function of oxygen concentration for the DBE dataset in Figure 6-18. Error bars refer to statistical 2σ uncertainties. Experimental conditions were the same as those in Figure 6-18.

A dataset for the DEE system, exhibiting traces with shoulders, rather than large growths, is presented in Figure 6-20. This set was fit with the same equation used above, but k_{OH+DEE} and k_{O+DEE} were fixed to 2.1×10^{-12} cm^3 molecule^{-1} s^{-1} and 1.3×10^{-11} cm^3 molecule^{-1} s^{-1} respectively, in order to aid in constraining the fits to the traces, with the extraction of accurate k_b values to characterise OH reycling the ultimate goal. The latter value is based on this work's measurement for the bimolecular rate coefficient between OH and DEE (Chapter 3), and the abstraction by O(^{3}P) rate coefficient was based on the measurement by Buchta et al. [265] at 600 K, the only known study of O + DEE at these temperatures. The shared parameter k_c was returned as (830 ± 180) s^{-1}.

For the majority of kinetic decays, the biexponential traces, and those showing shoulders at early times, are captured remarkably well by the fit. Decay number 8 is noticeably poor, but this is likely due to its short timescale, resulting in no tail to provide information on OH at long timescales – it is a shorter timescale version of the prior trace.
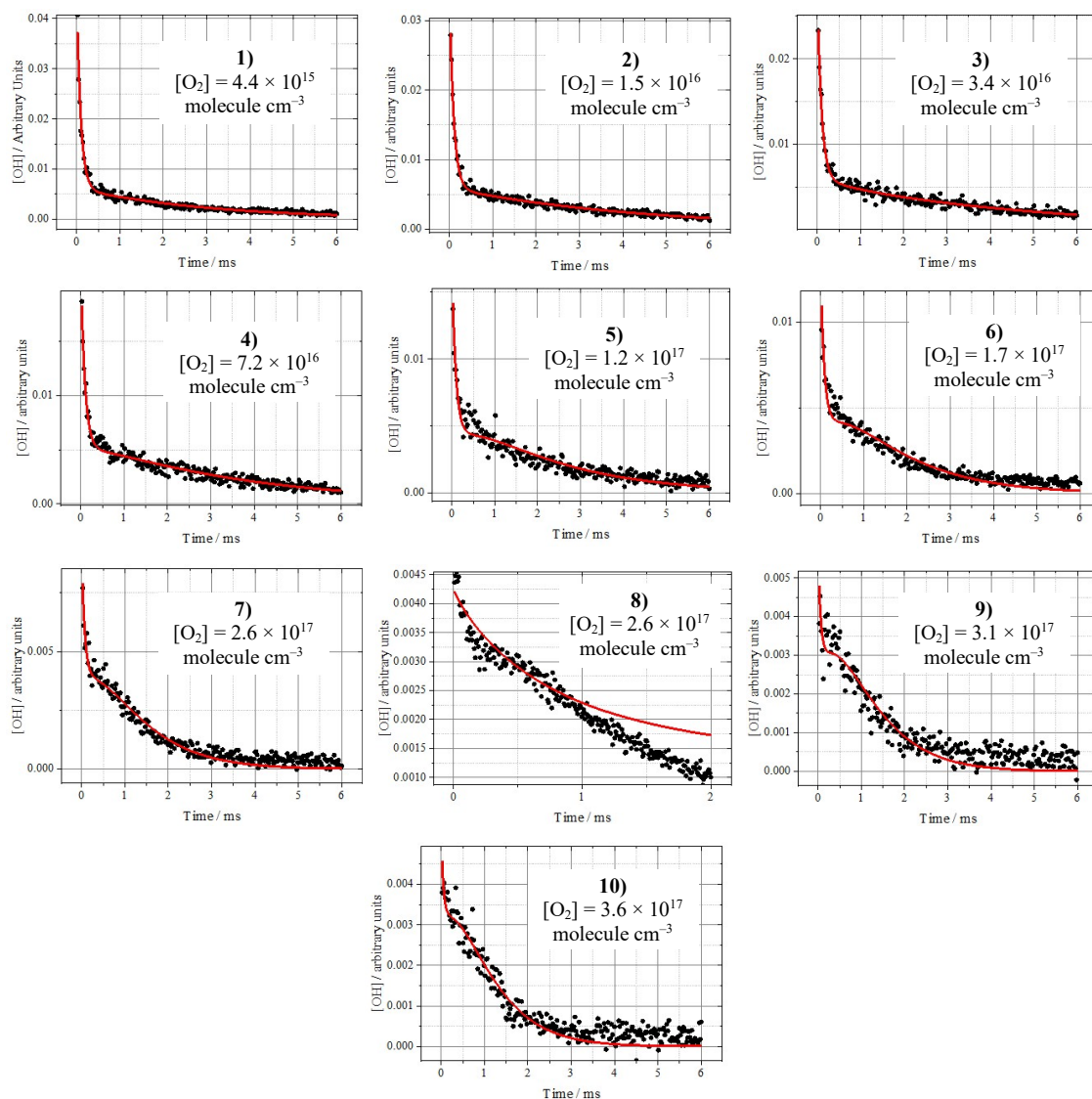
Figure 6-20: Global fits to DEE experiments, in ~59 Torr N$_2$, T = 600 K. [O$_2$] range = (0.4 − 36) × 10^{16} molecule cm^{-3}, [DEE] range = (7.0 − 7.2) × 10^{14} molecule cm^{-3}. k_d was fixed at 100 s^{-1}, H$_2$O$_2$ was the OH precursor.

In general the long timescale tails are not captured well by the analysis at high [O$_2$], for example in traces 9 and 10. Significant OH signal remains above the fit, suggesting there may be significant recycling of OH in the system that is not described in Scheme 6-2. Reactions such as O$_2$QOOH → OH are potential sources of OH propagation which would not be fit well by the scheme. Figure 6-21 presents the dependence on oxygen of the k_b recycling parameter, and the ratio of O(^{3}P) to OH. Here, the magnitude of the reycling parameters are greater than those for DBE in Figure 6-19 at comparable [O$_2$], and the concentration of O(^{3}P) atoms doesn't reliably reach as high relative concentrations. These two differences may indicate that in kinetic decays such as these, where there are no OH growths, the analytical scheme has difficulty assigning and

aportioning the true source of OH – hydrogen abstraction by O atoms, or true OH recycling.
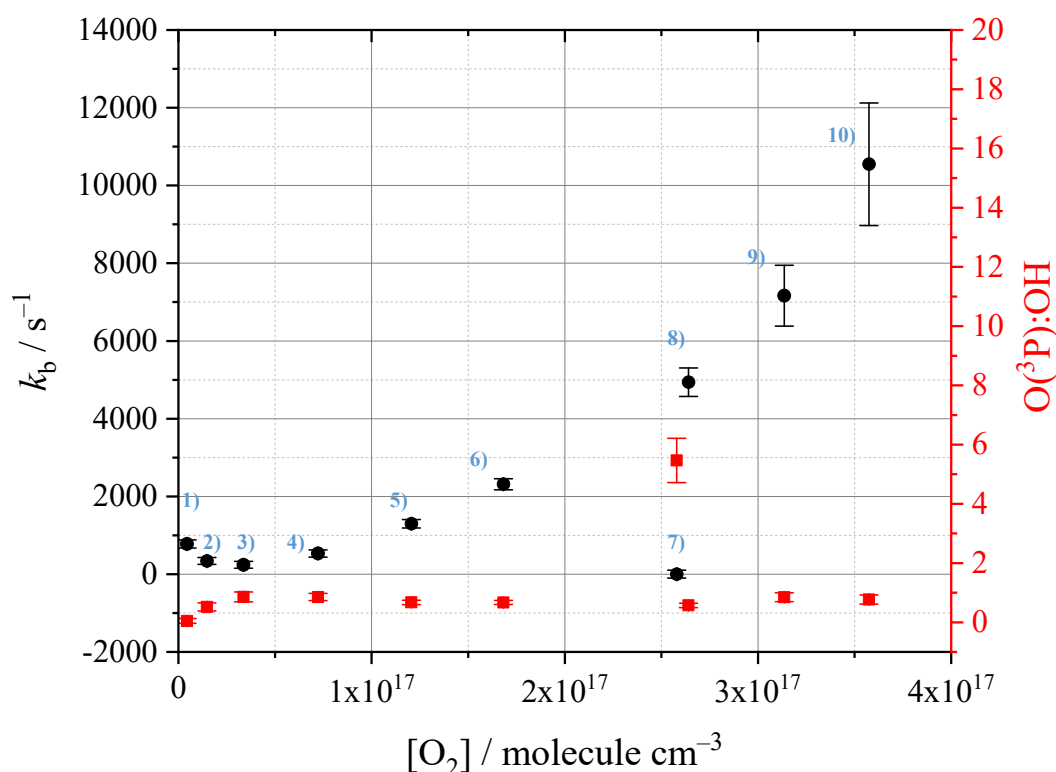
Figure 6-21: k_b and O(^{3}P):OH as a function of oxygen concentration for the DEE dataset in Figure 6-20. Error bars refer to statistical 2σ uncertainties. Experimental conditions were the same as those in Figure 6-20, and the blue numbers indicate the corresponding graph.

Evidently, despite reasonably good reproduction of the complex kinetic traces by the reaction scheme, the fits are not perfect, and it is difficult to place too much confidence in the parameters extracted. It appears there is another process of OH regeneration occuring at longer timescales, but the accuracy of O(^{3}P) + fuel rate coefficients extracted from extreme growth traces appears promising. Knowledge of the initial O(^{3}P):OH ratio would aid the analytical equation in assigning where OH recycling is originating from, but this requires good knowledge of the initial source of O atoms.

Similarly, good knowledge of the low temperature oxidation system for the relevant fuel would allow the constraint of parameters', such as k_b, dependences on [O$_2$], by enforcing a specific shape (e.g. the S-shapes in Figure 6-8).

Based on the evidence provided by the experiments carried out, it is believed that the 'extra' OH, and O(^{3}P) in the reaction cell in the absence of H_2O_2 may be a result of

some decomposition of the fuel, where R radicals result in a build-up of some precursor to O(^{3}P) and OH. Radicals such as RO$_2$, QOOH, or possibly other species such as ROOH molecules, could potentially photolyse to both O atoms and OH. Differing amounts of species, depending on the fuel or [O$_2$], would likely result in different ratios of O:OH being generated by the photolysis laser (red data in Figure 6-19 and Figure 6-21).

Experiments that show evidence for the presence of a slight cool flame support the theory of RH decomposition, and an example is presented in Figure 6-22. Here, a slight but clear dependence on oxygen concentration is observed for the pre-photolysis laser fluorescence detection. This suggests some O$_2$-dependent formation of OH, such as QOOH decomposition.
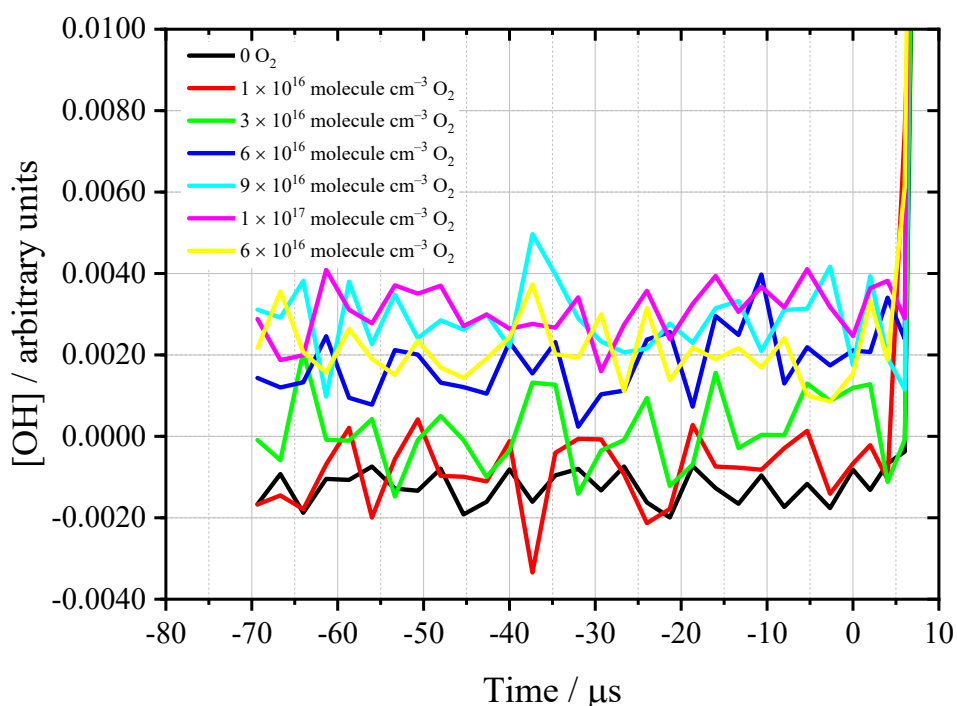
Figure 6-22: Baseline OH fluorescence dependence on [O₂], at 500 K, using DEE and H₂O₂. The yellow line displays a repeat experiment of the 6 × 10¹⁶ molecule cm⁻³ O₂ experiment, to confirm the gradual increase in OH signal was not merely a slow rise in signal quality over time.

An example of a pre-photolysis OH signal with no O$_2$-dependence in Figure 6-23 at significantly higher temperatures, suggests DBE may not decompose and form a cool flame in the same way. It is possible that the ROOH species is formed, or even RO$_2$ radicals, but the decomposition of QOOH to OH for di-*n*-butyl ether may not take place. Less, or no, contribution of low temperature oxidation to the OH growth traces for the

DBE system may explain the apparent ability for the fits to the data in Figure 6-18 to capture the tails better, and the smaller magnitude of the k_b parameters when comparing DBE in Figure 6-19 to DEE in Figure 6-21. Here, any baseline signal dependence on [O_2] was relatively small, but the next section will demonstrate proof of similar behaviour in more extreme examples.
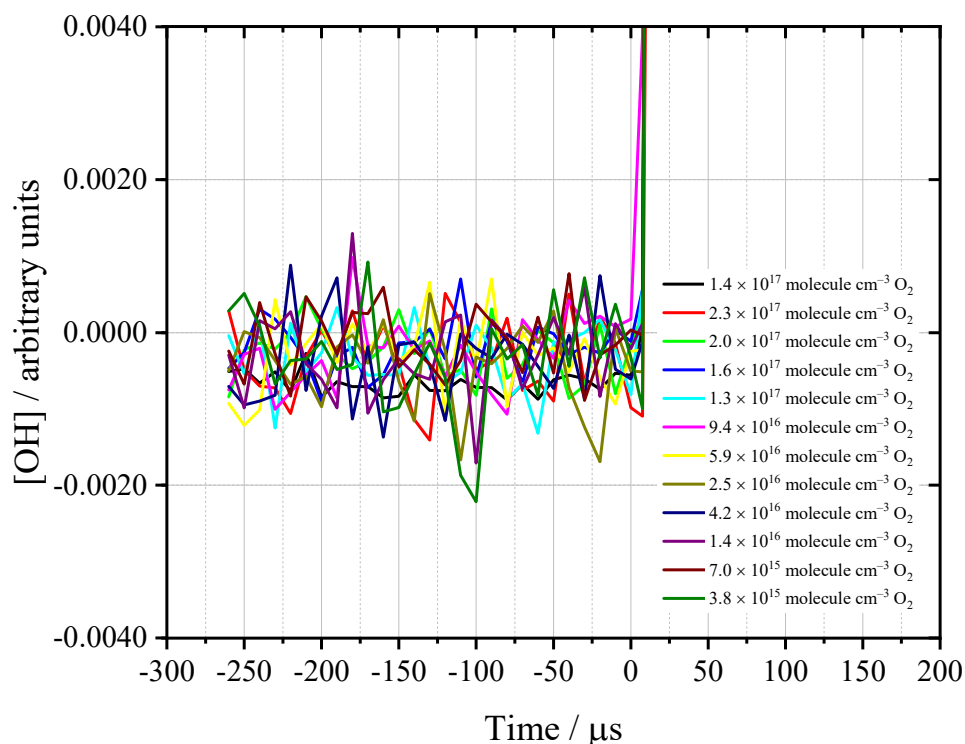
Figure 6-23: Baseline OH fluorescence independence on [O_2], at 760 K, using DBE and H_2O_2.

6.7   O Atom-free Experiments

In order to measure accurate k_b values with no interference from O + ether reactions, preliminary attempts at 'clean' OH regeneration experiments were carried out using the alternative high pressure experimental setup described in this chapter. No evidence for ozone (or 254 nm light absorbing species) was observed using this experimental setup. One possible reason for this is the nature of the two different instruments used. Here, the flow is laminar, and so the sampling region in the centre of the detection cell likely only contains species from the centre of the high pressure flow tube. If the formation $O(^3P)$ occurs on the walls, as is believed, then this gas will not be probed by the laser. The experiment used for the bulk of the measurements in this chapter will have a more turbulent flow, entering the reaction cell and mixing more thoroughly.

Despite the apparent absence of O atoms in the system, and indeed no large OH growths were observed from ~490 K – 600 K for diethyl ether, a very strong dependence on [O_2] was observed for the OH baseline signal when no OH precursor was used. Figure 6-24 presents a set of experiments over a large range of oxygen concentrations, which the high pressure system permits. This is clear evidence of cool flame behaviour in the diethyl ether system.
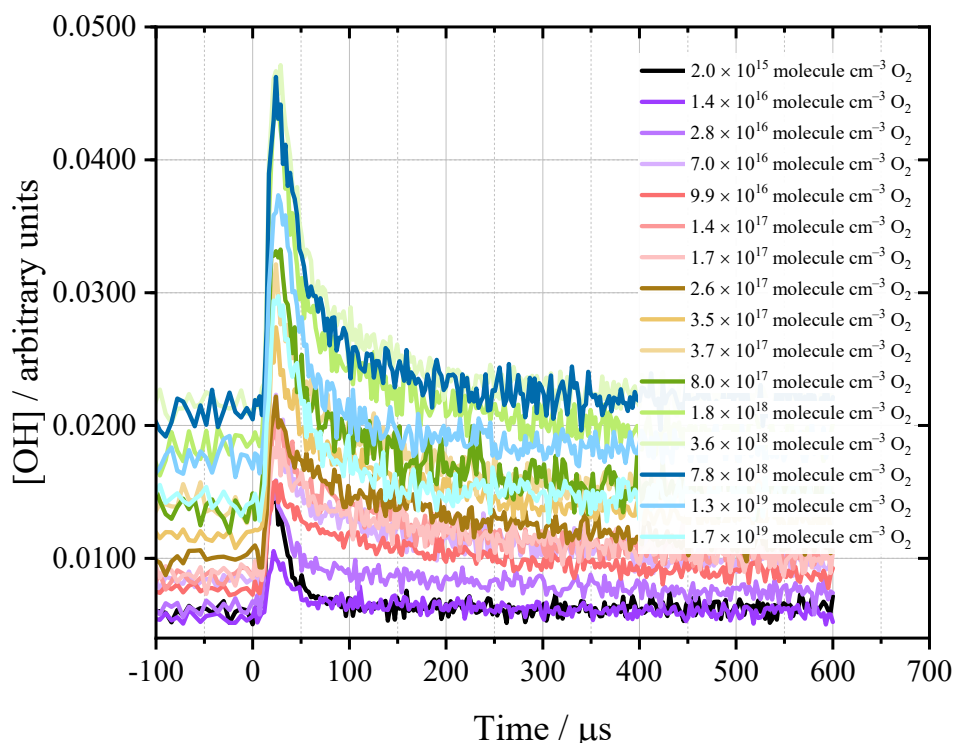
Figure 6-24: Diethyl ether cool flame experiments, at 600 K and ~1650 Torr N_2 (and O_2). [DEE] ≈ 9.5 × 10^{15} molecule cm^{-3}. No OH precursor was used.

As the oxygen concentration in Figure 6-24 is increased, generally the OH signal increases, however at the highest concentrations, a reduction in signal is noticeable. This was as a result of quenching by the oxygen present, and can be accounted for. Experiments where only N_2, H_2O_2, and varying amounts of oxygen are present, allow the extraction of a quenching coefficient by plotting the reciprocal of the OH signal height against total [O_2] (Figure 6-25). This OH signal height (S_0) is determined relative to the pre-photolysis baseline OH signal at $t = 0$.

The correction from the quenching coefficient, when applied to the mean OH baseline signal as a function of [O_2], shows the true effect of oxygen on the cool flame

signal, and confirms there is no decrease in signal at high [O$_2$], merely a plateau. The quenching-corrected and un-corrected data are presented in Figure 6-26.
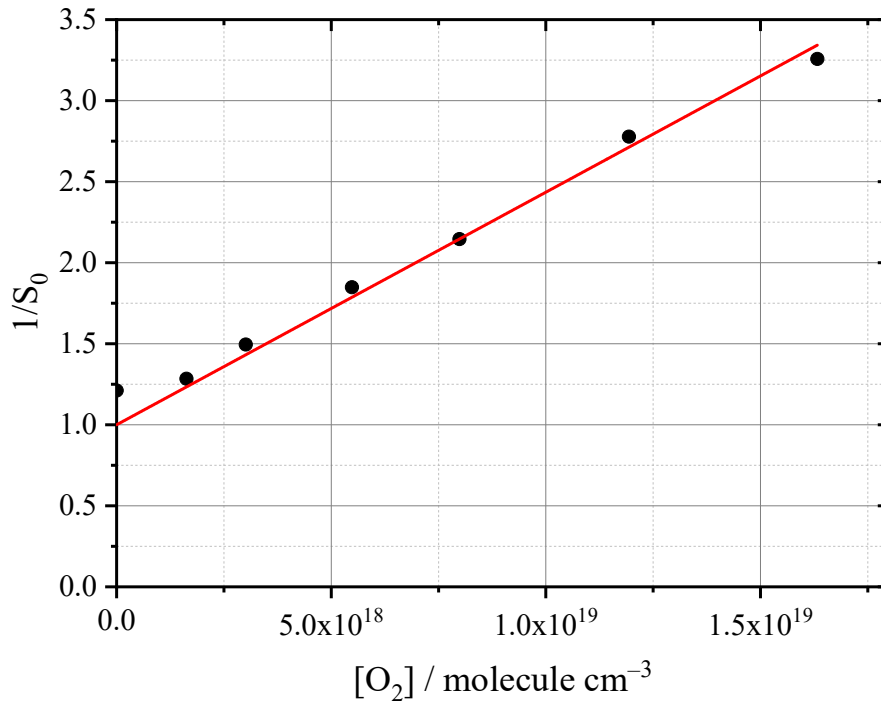
Figure 6-25: Quenching coefficient plot. Intercept fixed to unity, and the determined quenching coefficient = (1.43 ± 0.05) × 10^{-19} cm^{-3} molecule. S$_0$ is the initial OH fluorescence signal height at t = 0. Experimental conditions were 600 K, in ~1650 Torr N$_2$ (and O$_2$).
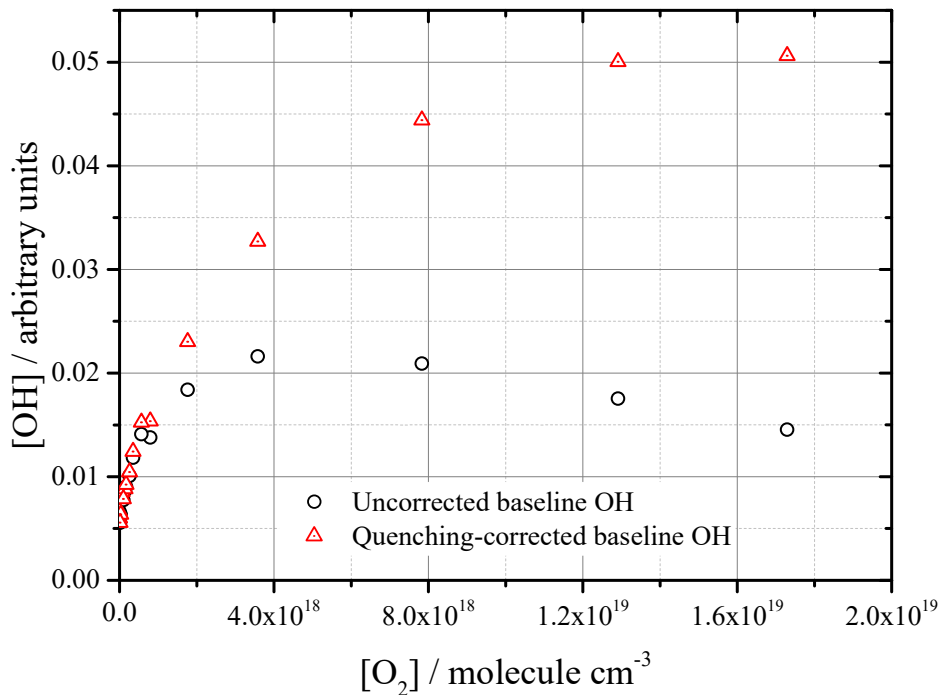
Figure 6-26: Mean pre-photolysis baseline OH signal as a function of oxygen concentration, before (black circles) and after (red triangles) correction for signal quenching. Experimental conditions were the same as those for Figure 6-24.

Decays shown in Figure 6-24 appear biexponential in nature, and appeared to fit the biexponential equation scheme well. It is however, not clear exactly which reaction is being monitored by extracting these parameters. The recycling parameter from the typical biexponential fit used throughout this thesis, k_b, and the yield parameter, are presented as a function of $[O_2]$, in Figure 6-27. From the changing magnitude of these values, there appears to be a transition at approximately 2×10^{17} molecule cm^{-3} oxygen, where yield and k_b both begin to decrease. However, it is not currently possible to say what the source of OH regeneration is before this point, and after. It may be a transition from QOOH decomposition, to O_2QOOH decomposition, although it is unclear why increasing $[O_2]$ from $(0 - 2) \times 10^{17}$ molecule cm^{-3} would cause an increase in k_b, given that the decomposition of QOOH should be independent of $[O_2]$. It could potentially be the R + O_2 reaction giving rise to a dependence on $[O_2]$, but it is expected to be a much faster reaction than this, and only dependent on oxygen at very low $[O_2]$ (approximately 10^{15} molecule cm^{-3}).

Nevertheless, the preliminary experiments conducted in this section indicate that 'clean' experiments, devoid of any O atoms, should be possible, and with greater study into the mechanisms occurring under these conditions, extraction of true k_b values and rate coefficients should be possible. This may provide valuable information on the reaction between QOOH and O_2, which is integral to the chain-branching mechanism for the low temperature autoignition of fuels.
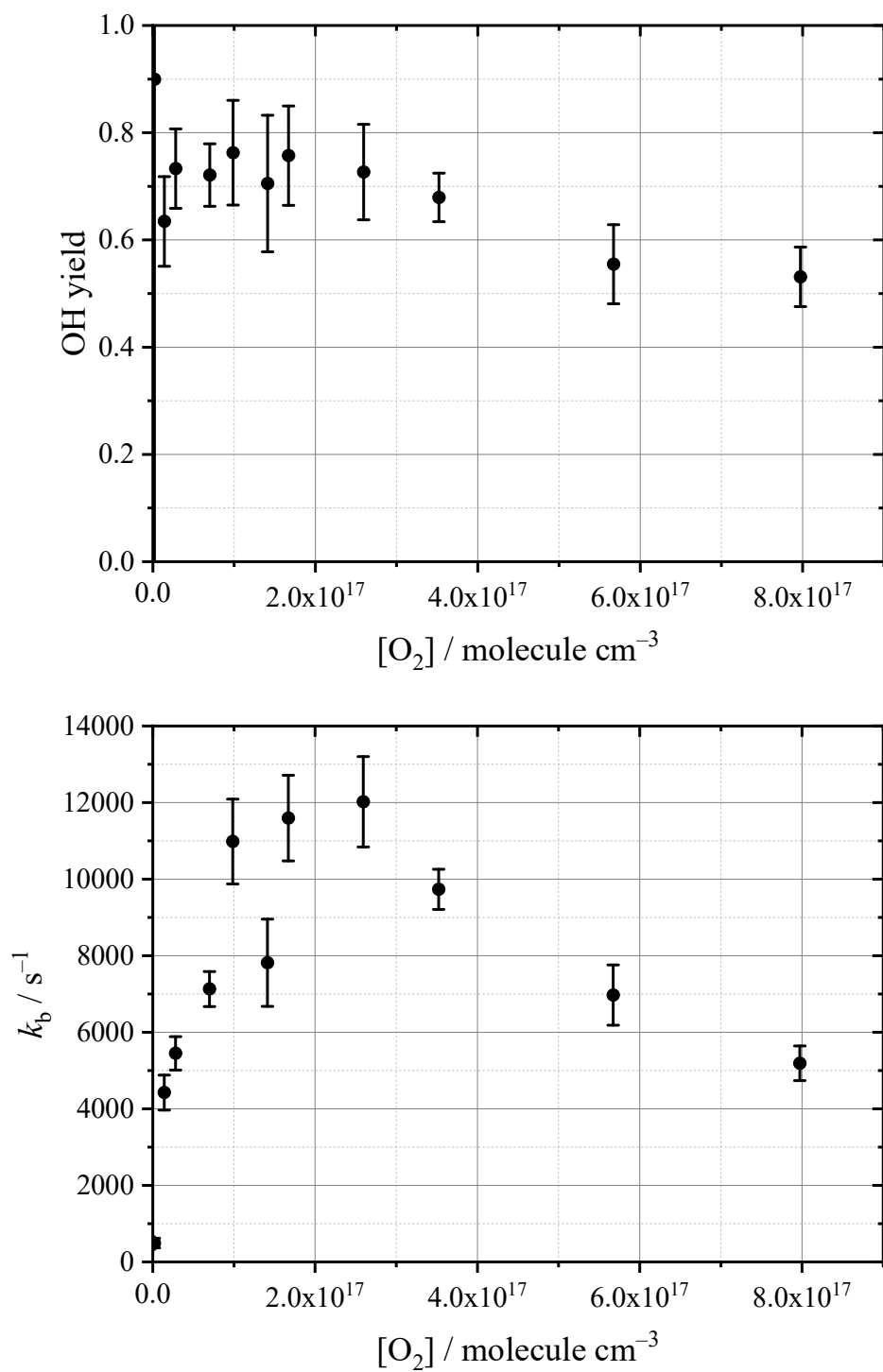
Figure 6-27: OH yield (above), and OH recycling rate (below), as a function of oxygen. Experimental conditions were the same as those for Figure 6-24; $T = 600$ K, in ~1650 Torr N$_2$ (and O$_2$).

6.8 OH Regeneration in the Methyl *tert*-Butyl Ether and Trimethyl Orthoformate Systems

Investigations into the low temperature oxidation systems of MTBE and TMOF did not exhibit any of the significant OH growth behaviours described in this chapter for DME, DEE and DBE. However, OH regeneration for MTBE and TMOF was observed in the non-well-skipping regime, where the total pressures and temperatures were too high to be consistent with chemical activation. Indeed, no evidence of well-skipping was found for these ethers (see Chapter 4). OH regeneration manifested itself in the form of biexponential decays, examples of which are presented in Appendix A (Figure A 10). From these kinetic traces, the recycling parameter, k_b, was extracted (based on Scheme 6-3), OH yields were calculated, and their dependence on O_2 was explored. Here, k_b represents the regeneration of OH by some method, most probably decomposition of the QOOH radical.

$$RH + OH \xrightarrow{k_a'} R\cdot \xrightarrow{+O_2} RO_2 \xrightarrow{k_b} OH$$

$$\downarrow k_d \qquad\qquad\qquad\qquad \downarrow k_c$$

$$loss \qquad\qquad\qquad\qquad\qquad loss$$
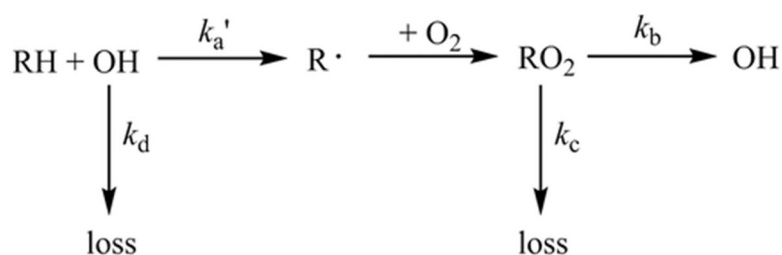
Scheme 6-3: Scheme used for analysis of biexponential traces in the MTBE and TMOF systems.

OH recycling began at 568 K and 478 K for MTBE and TMOF respectively, and the relevant range of parameters explored for *significant* OH yields was 618 – 700 K and 478 – 767 K respectively. With OH recycling in the presence of oxygen for the MTBE system only occurring at higher temperatures, the formation mechanism was attributed to a route over a potential energy barrier high enough to inhibit OH formation in a system at lower thermal energy. Figure 6-28 shows a general schematic potential energy pathway expected for ether oxidation, where the internal rearrangement of the RO_2 radical to the QOOH radical, and subsequent decomposition to OH and products is the most likely mechanism for OH recycling.
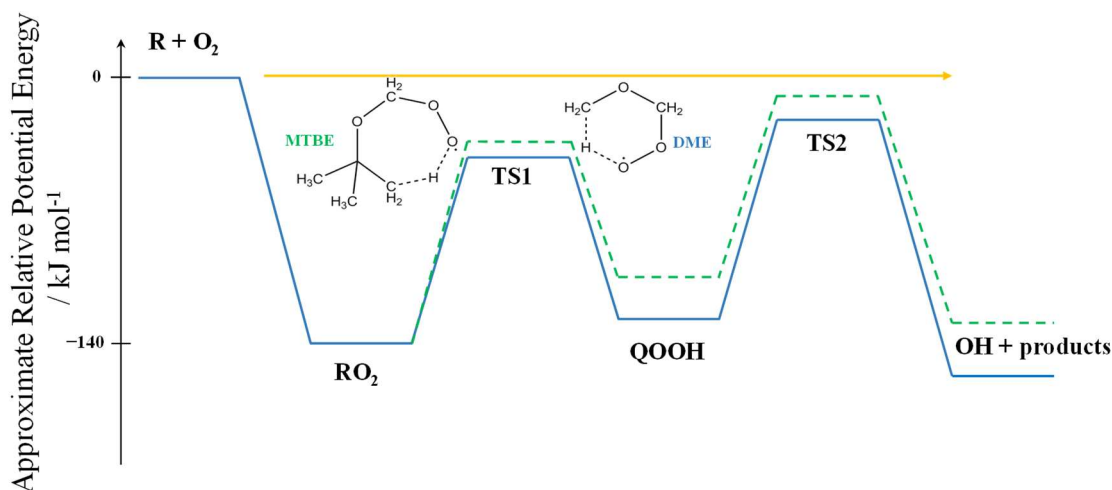
Figure 6-28: Generic potential energy surface for R radical low temperature combustion propagation for DME (blue solid line) and MTBE (green dashed line), including possible chemical activation route (gold line). Ring structures for the main MTBE abstraction route and DME are shown for the $RO_2 \rightarrow QOOH$ transition state, and approximate relative potential energies are shown for the $R + O_2$ and RO_2 species, based on those for DME.

Figure 6-28 also includes the formally direct route to OH production by chemically activated decomposition of the RO_2 adduct (discussed in Chapter 4). The energies of the RO_2, QOOH, OH + products and the associated transition states are based on the values for DME [89]. For MTBE, the actual PES will be more complex as there are two different R radicals corresponding to initial abstraction from the CH_3 or t-C_4H_9 groups. The k_b parameter (Scheme 6-3) for the biexponential fitting equation represents OH formed via this surface, and the k_c parameter represents the R radical not returning OH, which could be due to radical-radical reactions of the more stable RO_2 radical, formation of HO_2, or at higher temperatures, decomposition of the R radical. In comparison to the DME/O_2 system, the MTBE/O_2 system shows two significant differences. First, the yield of OH was significantly lower for MTBE/O_2 than DME/O_2 and second, there was no evidence for interception of the QOOH when high concentrations of oxygen were used. The details of these observations are briefly outlined and then linked to differences in the potential energy surfaces for DME/O_2 and MTBE/O_2.
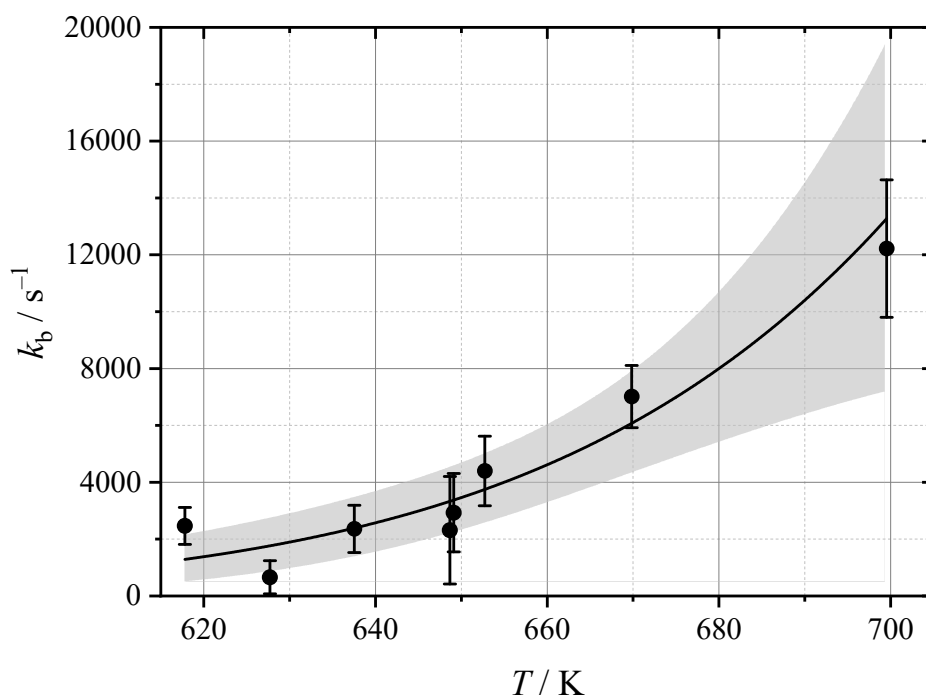
Figure 6-29: Figure 9. MTBE recycling rate coefficient, k_b, against temperature. Error bars are purely statistical at the 2σ level. Grey shaded area represents the bounds of the 95% confidence limits. The data can be described by k_b(618–701 K) = (6.05 ± 3.8) × 10^{11} × e$^{-(103±37)/RT}$ s^{-1}, where the uncertainties are statistical at the 2σ level. H$_2$O$_2$ was the OH precursor.

Figure 6-29 shows the positive temperature dependence of the recycling rate coefficient, k_b. Over the temperature range where the experiments could be conducted, the OH recycling rate coefficient exhibits an Arrhenius-like temperature dependence that is consistent with a process proceeding over a barrier. The data can be parameterised as k_b(618–701 K) = 6.05 × 10^{11} × exp$\left[\frac{-103}{RT}\right]$ s^{-1}, where the maximum value of the 95% confidence limit uncertainty across the temperature studied was 64%. This parameterisation yields an activation energy of (103 ± 66) kJ mol^{-1}, which is comparable to the barrier height for TS2 expected based on DME [89]. Values for k_b presented in Figure 6-29 were obtained as a weighted average of all O$_2$ concentration experiments ([O$_2$] ≈ 10^{15} – 10^{18} molecule cm^{-3}) for a given temperature, as no significant and reproducible dependence upon oxygen was seen (see Figure 6-30).
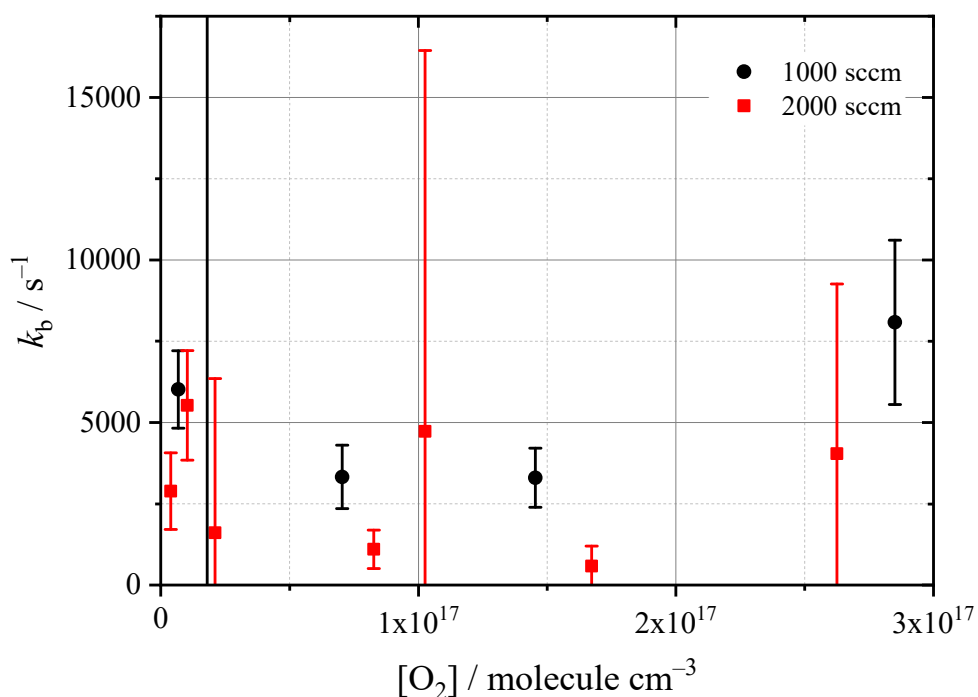
Figure 6-30: Example of MTBE OH recycling rate independence on oxygen concentration. Measurements made at 650 K, 60 Torr N₂, 1000 sccm flow (black circles) and 2000 sccm flow (red triangles). [MTBE] = 2 × 10¹⁶ molecule cm⁻³ (black circles), and [MTBE] = 1.2 × 10¹⁶ molecule cm⁻³ (red triangles). Error bars are purely statistical at the 2σ level.

The relationship between k_b and k_c for a given set of experimental conditions allows calculation of the percentage yield of OH using equation E 6-1:

$$\text{OH yield} = \frac{k_b}{k_b + k_c} \times 100 \qquad \text{E 6-1}$$

Here, the OH formation parameter, k_b, is expressed as a percentage of the total removal of the R radical ($k_b + k_c$). An average yield of $(36 \pm 5)\%$ (standard deviation was used to calculate the uncertainty in average yield for both molecules) was measured for MTBE across all temperatures, over the same range of [O₂] that was present in the k_b data presented above. Yields below approximately 620 K are not considered for MTBE, due to the low magnitude (<1000 s⁻¹) of the temperature-dependent k_b parameters measured (Figure 6-29). At this order of magnitude, k_b is more likely to be perturbed by other slow chemistry, such as radical-radical reactions. The yields are presented in Table 6-2.
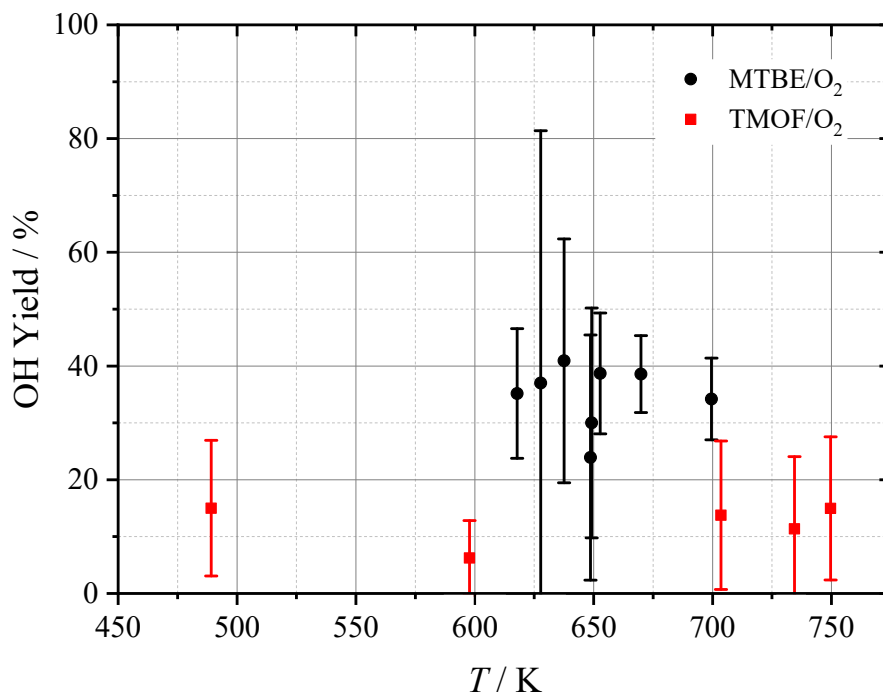
Figure 6-31: OH yields against temperature for MTBE/O₂ (black circles) and TMOF/O₂ (red squares). Error bars are purely statistical at the 2σ level.

At high concentrations of oxygen ($[O_2] > 10^{16}$ molecule cm^{-3}) in DME and DEE systems, the evidence presented in the previous sections of this chapter suggests there may be the interception of QOOH (to form O₂QOOH) before decomposition to OH and co-products taking place. However, at comparable concentrations of oxygen, there is no evidence for any change in mechanism in the MTBE/O₂ system; comparable concentrations of O₂ do not appear to intercept the MTBE-derived QOOH radicals.

Table 6-2: Obtained OH yields for MTBE and TMOF systems. Uncertainties are statistical at the 2σ level.

T / K	P / Torr	MTBE OH yield / %	T / K	P / Torr	TMOF OH yield / %
618	134	35 ± 11	478	111	15 ± 12
628	58	37 ± 44	598	64	6 ± 7
638	134	41 ± 21	705	70	14 ± 13
649	57 – 79	24 ± 22	767	119	11 ± 13
649	60 – 70	30 ± 20	748	135	15 ± 13
653	134	39 ± 11			
670	134	39 ± 7			
700	134	34 ± 7			

The above observations on the behaviours for the DME/O$_2$ and MTBE/O$_2$ systems can be related to differences in the PES for these two systems. The OH yields observed from MTBE/O$_2$ were relatively low (Figure 6-31) compared to similar ether biofuels, where yields closer to 100% would be expected for a molecule such as DME [89], and Figure 6-27 shows an example of yields of above 60% for DEE. Low yields suggest OH propagation is a minor channel of the low temperature oxidation system, and that another, non-OH producing reaction, dominates after the initial hydrogen abstraction from the ether. Decomposition of QOOH to HO$_2$, H$_2$CO and *iso*-butene [267-269] is the reaction reported as the major channel for the MTBE QOOH decomposition (Figure 6-32). The analogous decomposition for the QOOH radical for DME (Figure 6-32) would be to the less favourable HO$_2$ + ethylene oxide channel (HO$_2$ + H$_2$CO + ^{3}CH$_2$ is highly endothermic) and therefore this route does not dominate the DME system, resulting in higher OH yields.
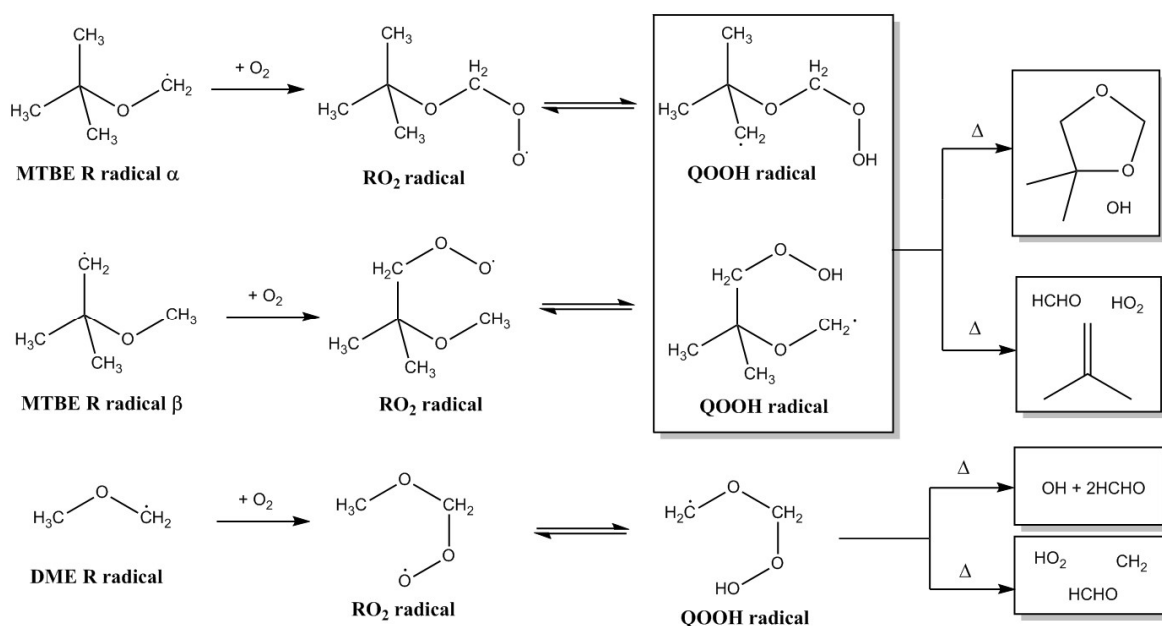
Figure 6-32: Comparison of R radical route to OH propagation, or HO$_2$ formation, for MTBE and DME.

The observation of a small, but still significant, OH yield contradicts some mechanistic studies on MTBE oxidation; for example, Brocard et al. [267] have no route to OH formation from the QOOH radicals formed following abstraction at the α C–H of MTBE and only *iso*-butene, methanol and formaldehyde are reported as products from a JSR study at 726 K by Glaude et al. [269] However, Ciajolo et al. [268] in another JSR

study, do report the production of yields of 4,4-dimethyl-1,3-dioxolane with identification by GC/MS. Direct comparison of yields with this work is not possible as it is not possible to account for the consumption of the dioxolane in the longer residence times of the JSR. However, the observations of this work and the earlier study of Ciajolo et al. suggest the need for further development of MTBE models to account for OH production from QOOH species.

Based on the dominant initial abstraction in OH + MTBE being from the α hydrogen, the R radical in DME and MTBE both contain the C–O–CH$_2$ radical group and hence the well depth of the RO$_2$ for both DME and MTBE should be very similar (Figure 6-28). In MTBE, the RO$_2$ → QOOH internal abstraction requires breaking a stronger primary C–H bond (not activated through close proximity to the ether oxygen as in DME), but for both MTBE and DME, a similar OO–H bond is formed. Therefore the transition state for the internal abstraction (TS1, Figure 6-28) and the QOOH radical will both be higher in energy. This would explain the lack of QOOH interception by O$_2$ observed for MTBE.

The higher the energy of the QOOH radical with respect to the RO$_2$ species, the harder it becomes to intercept QOOH with O$_2$. By using the MESMER code [242], a model based around the analogous potential energy surface for DEE (comparable to DME, but closer in molecular complexity to MTBE) can be adjusted to demonstrate similar results to those seen in this work. Calculations were based on conditions of 500 K and 25 Torr N$_2$. OH yields arising from chemical activation for DEE can be inhibited by raising the barrier out to the OH product (TS2, Figure 6-28) by approximately 12 kJ mol^{-1}. Similarly, the likelihood of chain-branching via the formation of O$_2$QOOH can be lowered by reducing the well-depth of the QOOH species. Raising the height of QOOH relative to RO$_2$ by ~20 kJ mol^{-1} can increase the RO$_2$:QOOH concentration ratio by approximately a factor of ten, where ten times more O$_2$ would be required to form O$_2$QOOH. While this MESMER modelling is only semi-quantitative, it shows the changes in the PES required to bring agreement with our experiment observations, see Figure 6-28. The only parameters adjusted here were the energies of TS2, QOOH, and TS1.

Trimethyl orthoformate had a significantly lower average OH yield of $(10 \pm 3)\%$ (Figure 6-31), and there is no clear route to HO$_2$ formation from TMOF's mechanism. As such, the mechanism behind the low TMOF yields is not understood. Additionally, there was no oxygen dependence seen with the rate of OH recycling for TMOF, and the k_b

parameter returned was temperature-independent and of a very low order of magnitude ($<400 \text{ s}^{-1}$), which may be perturbed by secondary chemistry in the system, such as radical-radical reactions. It was also noted that at ~690 K, OH fluorescence was present in the absence of H_2O_2, suggesting that TMOF was acting as a precursor to hydroperoxides at high temperature (Figure 6-33). It is not clear what mechanism gives rise to this signal, but the lack of growth suggests it is a different mechanism to that already discussed for DME, DEE, and DBE.
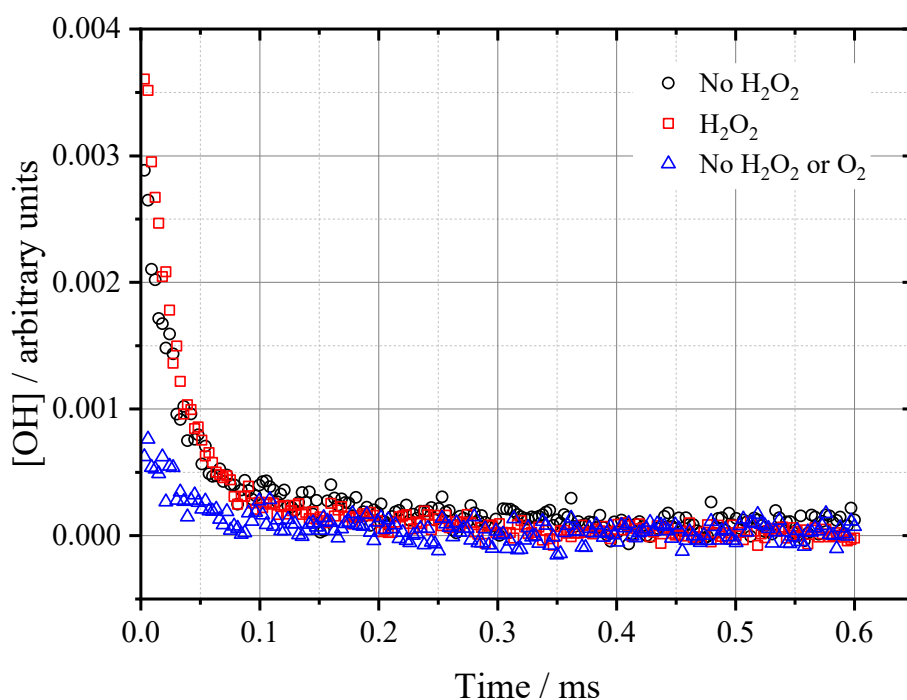
Figure 6-33: Example of OH fluorescence signal in the absence of H₂O₂ precursor and oxygen for TMOF experiments. H₂O₂ and O₂ present (red squares), no H₂O₂ (black circles), and no H₂O₂ or O₂ (blue triangles). Decays were measured at 62 Torr N₂, 693 K, [TMOF] = 4.9 × 10¹⁵ molecule cm⁻³. [O₂] = 1.5 × 10¹⁶ molecule cm⁻³ when present.

6.9   Conclusions

The observation of large OH signal growths in the presence of O_2 for DME, DEE, and DBE has been attributed to the formation of $O(^3P)$ atoms in the reaction cell, where abstraction of hydrogen atoms from the parent fuel species results in near-instant OH formation. Analysis of these traces indicate further processes, such as decomposition of QOOH, and interception of QOOH by O_2 to initiate branching, may be occurring at longer timescales. The elucidation of these recycling parameters is hindered by the O + fuel

chemistry that dominates kinetic traces, and as such, the nature of the O formation mechanism, and methods to mitigate this, should form the basis of important research required in the future.

Interfering processes from the O atoms observed here, have been seen for other fuels (butanol), and in different, but similar reaction cells used at the University of Leeds by Dr S. Sime [262]. Potentially, the chemistry observed in this chapter may interfere with other studies, particularly as the focus of autoignition chemistry research shifts more from early reactions (i.e. H atom abstraction), to the kinetics of later reactions, such as O_2 + QOOH. Under conditions involving high oxygen concentrations, intermediate temperatures, and the source determined here as chemistry occurring on the walls of the reactor, this behaviour will greatly inhibit future work. To this end, this chapter also demonstrated that O atom-free experiments are possible using an experimental setup where the flow should result in LIF sampling from gases that have not come into contact with the reactor walls. Combined with the FAGE technique, these experiments allowed the study of DEE in the presence of very high oxygen concentrations (~10^{19} molecule cm^{-3}) and demonstrated the presence of a cool flame. It is possible that coupling a PTR-MS detection instrument to the system under the conditions yielding biexponential decays and cool flames, would help identify compounds that are only expected to be present as a result of the chain-branching mechanism, such as ketohydroperoxides.

The first observation of biexponential decays have been reported for MTBE and TMOF above 568 K and 478 K respectively, in the presence of O_2. Evidence of OH recycling in both systems allowed OH yields to be measured. A low average OH yield of $(10 \pm 3)\%$ was measured for the TMOF system, but yields were higher for MTBE $(36 \pm 5)\%$. OH yields far below 100% for MTBE were attributed to an alternative QOOH decomposition route, where the dominating channel was formation of HO_2. In contrast, the mechanism giving rise to such low yields for trimethyl orthoformate was not understood, and requires further investigation. The observation of OH signal in the presence of only TMOF with N_2, suggests the biexponential decays observed are subject to a large degree of uncertainty. The low yields, and decreased reactivity of MTBE, is perhaps of no surprise, given its primary use a fuel additive for gasoline, where its high octane number (~110 [40]) will aid in knock reduction. Typically, for a diesel-like fuel such as DME or DEE, a high cetane rating is required, indicating its propensity to undergo autoignition. Essentially, this is the opposite of MTBE's properties.

For both the MTBE and TMOF systems, future experimental studies will look at low temperature kinetics and direct measurements of the yields of HO_2 using a modified version of our high pressure OH detection system to allow for the detection of HO_2 via the FAGE technique. Furthermore, this system would allow the addition of up to $\sim 10^{19}$ molecules cm^{-3} of oxygen to increase the likelihood of QOOH interception, in the same manner as the experiments using DEE in section 6.7.

Chapter 7 Summary and Future Work

Making use of potentially carbon-neutral biofuels in novel combustion engines will require a detailed understanding of the reactions that occur under low temperature conditions in order to optimise their application. This thesis has investigated the ether family of biofuels, and presented experimental observations concerning three stages of their low temperature combustion mechanisms. The first, presented in Chapter 3, is the initiation by the OH radical (reaction R 7-1) to produce the R radical. Chapter 4 and Chapter 5 provide measurements of the second stage, concerning the reaction between the R radical and O_2 (reaction R 7-2), producing the RO_2 radical or proceeding via the formally direct channel to OH. Finally, Chapter 6 considered the propagation and chain-branching reactions involving the QOOH radical (formed through rearrangement of the RO_2 species) in reaction R 7-3.

$$RH + OH \rightarrow R + H_2O \qquad \text{R 7-1}$$

$$R + O_2 \rightarrow \text{products} \qquad \text{R 7-2}$$

$$2OH \overset{O_2}{\leftarrow} QOOH \rightarrow OH \qquad \text{R 7-3}$$
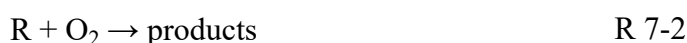
Laser flash photolysis – laser-induced fluorescence was used to study the reaction between OH and various ethers (reaction R 7-1) from room temperature to approximately 740 K. The first temperature dependent study of OH + TMOF was carried out, extending the previous room temperature measurement reported by Platz et al. [152] up to 744 K. The temperature dependence was parameterised by $k_{OH+TMOF}(298–744\ K) = (8.0 \pm 12.2) \times 10^{-13}\ [(T/298)^{(2.6\pm1.2)} + (T/298)^{(-8.1\pm4.6)}] \times e^{(2.7\pm3.9)/RT}\ cm^3\ molecule^{-1}\ s^{-1}$.

Similar investigations into the reaction kinetics of OH + DEE and OH + DBE extended the current knowledge of their respective rate coefficients. In the case of OH + DEE, this was done by bridging the gap between measurements made by Tully and Droege [165] at 442 K, and the value reported by Tranter and Walker [132] at 753 K. The rate coefficients measured in this work displayed good agreement with the work of Tully and Droege, although no temperature dependence was observed. In particular, the temperature-independent value we recommend, of $k_{OH+DEE}(298–727\ K) = (1.28 \pm 0.21) \times 10^{-11}\ cm^3\ molecule^{-1}\ s^{-1}$ is in disagreement with the high temperature value reported by Tranter and Walker ($k_{OH+DEE} = (2.04 \pm 0.38) \times 10^{-11}\ cm^3\ molecule^{-1}\ s^{-1}$).

For the reaction between OH and DBE, the rate coefficients reported by Mellouki et al. [113] up to 372 K were extended to 732 K in this thesis, although the rate coefficients measured here were approximately 25% faster than those in the literature. This was attributed to uncertainties in DBE/N_2 bulb compositions as a result of its low vapour pressure. Despite this, the parameterisation of the temperature dependence, k_{OH+DBE}(298–732 K) = (3.05 ± 7.13) × 10^{-12} $(T/298)^{(1.31\pm1.62)}$ × $e^{(6.35\pm5.83)/RT}$ cm^3 molecule^{-1} s^{-1}, was qualitatively reliable, where the negative temperature dependence below ~350 K seen in the literature was observed in this work. Consequently, the plateau to a temperature-independent rate coefficient above this temperature was deemed reliable, and had not previously been observed. Nevertheless, future work should focus on further testing of the DBE/N_2 bulb compositions, to verify the source of the discrepancy between this work and the literature. The reaction of OH with the established fuel additive, MTBE, and alternative fuel, DME, were also investigated from 298 – 727 K and 298 – 673 K respectively, with comparison to previous measurements. Overall, agreement with the majority of previous studies at room temperature was found, and rate coefficients of $k_{OH+MTBE}$ = (2.81 ± 0.32) × 10^{-12} cm^3 molecule^{-1} s^{-1}, and k_{OH+DME} = (2.66 ± 0.09) × 10^{-12} cm^3 molecule^{-1} s^{-1} were reported at room temperature.

Comparisons between the five ethers were drawn, where differences in the magnitude of their reaction rate coefficients were typically attributed to the activating effect of neighbouring functional groups on the abstraction sites, and the number of sites available. SAR predictions of the rate coefficients by Kwok and Atkinson [190] were generally in good agreement, although the temperature dependence of OH + DBE was predicted poorly, and the nature of TMOF as a polyether meant it was not described accurately by the SAR. Negative temperature dependences close to room temperature, and below, were seen for OH + TMOF and for OH + DBE very clearly. This behaviour has been observed before, and is attributed to complex formation between the OH radical and the fuel molecule. The appearance of this at a higher temperature for OH + DBE in comparison to literature observations of the same behaviour for DME and DEE is likely as a result of its increased size, where complex formation becomes more probable. Measurements below room temperature would be of mechanistic interest for all ethers, particularly TMOF and MTBE where this phenomenon has not yet been measured previously. Deuteration of the ether molecules would also be useful, allowing site-specific measurements of the abstraction rate coefficients. A study of a similar nature has

previously been conducted, concerning ethanol, at the University of Leeds by Carr et al. [270].

What can be thought of as the second step in low temperature oxidation, reaction R 7-2, was studied in Chapter 4 and Chapter 5, with the former focused on the presentation of the technique used. This method relied on the presence of biexponential decays at low pressures and oxygen concentrations, brought about by the recycling of OH through the formally direct channel to OH. The DME system was used to study the reaction between the $CH_3OCH_2 + O_2$ reaction, and good agreement for the bimolecular rate coefficient and OH yields was found when compared with work by Eskola et al. [89]. Numerical integration analysis of experimental conditions demonstrated the sensitivity of the technique to reactant concentrations, but ultimately, provided a fuel has the ability to undergo chemical activation for the $R + O_2$ reaction, this method will be applicable to many molecules, allowing the determination of the rate coefficient at low pressures and relatively low temperatures. Previous studies indicate this technique should be applicable to reactions such as OH + ketones [200], aldehydes [133, 200-205], dialdehydes [206, 207], and esters [208]. Previously, a precursor molecule for the desired R radical would have been necessary.

The ability to measure $R + O_2$ rate coefficients for many diesel-like biofuels will be important for characterising the temperature dependence and magnitude of the rate coefficients, and for constraining their extrapolation up to higher temperatures important for combustion modelling and the negative temperature regime. Should this chemical activation process interfere with other laboratory measurements, then the ability to quantify the reaction will also be an advantage. The potential for this technique to be applied to other molecules was demonstrated in Chapter 5, where the DEE/O_2 system was explored.

Measurements of the $C_2H_5OC_2H_4 + O_2$ rate coefficient were reported for 298 – 464 K, in 5.2 – 28.4 Torr of N_2. OH yields were also measured, where a larger quenching coefficient than that of the $CH_3OCH_2 + O_2$ reaction indicated increased collisional deactivation due to the increased molecule size. These rate parameters were compared to *ab initio* calculations of the DEE oxidation PES carried out at the CCSD(T)/Jun-cc-pVTZ//M06-2X/Jun-cc-pVTZ level using RRKM/master equation methods in MESMER [242]. The computational calculations performed using Gaussian 09 [240] were in reasonable agreement with previous calculations by Di Tommaso et al. [115], Sakai et al. [225], Sandhiya et al. [226], Wang and Wang [227], and Hu et al. [228],

although the transition state barrier energies from QOOH to OH reported by Di Tommaso et al. and Sakai et al. were approximately $7 - 10$ kcal mol^{-1} lower than the value determined in this work (-3.7 kcal mol^{-1} relative to the R + O_2 entrance channel). An adjustment in this barrier down by approximately 7 kcal mol^{-1} was required to achieve good agreement between the theoretical model and experimental yields and rate coefficients. The PES developed only considers the R radical formed from initial H abstraction from DEE at the α site, and $RO_2 \leftrightarrow$ QOOH rearrangement from the opposing α site. As such, future work exploring calculations of the other pathways possible may help to identify branching ratios of OH yields. Application of the rate coefficients for R + O_2 in the DEE system to combustion models would also be of interest, where the effect on ignition delay times is of relevance to a fuel's use in HCCI and other novel engines.

The potential for other ethers (such as isomers of dipropyl ether) to well-skip will also be of interest. No evidence for chemical activation using di-*n*-butyl ether was observed, potentially due to its large size, however further investigation should be carried out to verify this.

Experiments divulged in Chapter 6 described a series of tests to investigate large OH growths initially proposed to be chain-branching in the DME, DEE, and DBE systems under conditions of high [O_2] and moderate to high temperature. Ultimately, it was determined that the $O(^3P)$ + fuel reaction was very likely responsible for producing OH on short timescales, and that the O atoms arose from fuel/O_2 surface chemistry producing a photolytic precursor for O. A definitive test for the presence of O atoms could be carried out using a technique such as LIF [271]. Future work should focus on identifying the source of O atoms, and attempting to mitigate their formation under these conditions. Preliminary attempts to analyse the data were made by deriving an analytical equation to account for the extraneous reaction, and the typical OH regeneration routes expected in low temperature combustion mechanisms. Generally, good fits were achieved, although there was difficulty in sufficiently capturing the OH decay at longer timescales. Measurements of $O(^3P)$ + ether reactions would be useful in attempting to constrain the fits. It is likely that O + fuel reactions interfered with more simple biexponential decays (i.e. not exhibiting growth), and attempts to ascertain how to properly analyse these data are ongoing.

Using a different experimental setup, that still relied on the LFP–LIF technique, experiments were conducted on the DEE/O_2 system in the absence of any evidence for $O(^3P)$ atoms. Biexponential decays were still obtained, and cool flames were observed,

providing strong evidence of chemistry occurring through the mechanisms in reaction R 7-3. There is much more work to be done here, where we are potentially observing OH yields and recycling rate parameters that exhibit O_2-dependent transitions from an OH propagation process via QOOH thermal decomposition, to the addition of O_2 to the QOOH radical (leading to chain-branching). Building on the work conducted by C. Morley [257], this experimental setup would allow the detection of HO_2, as well as OH, and greater control over the pressure of the system. A proton transfer reaction-mass spectrometry instrument can also be attached to the detection cell, to monitor additional species formed under low temperature combustion conditions. The same experimental setup could be used in future work to measure yields of HO_2, which was proposed as the major product of the MTBE/O_2 system, explaining the relatively low OH yields observed $(35 \pm 5)\%$ for the first time using biexponential decays. This finding was consistent with MTBE's use as an anti-knock agent.

This thesis has made measurements of kinetic parameters concerning the three stages of the low temperature combustion mechanism described here. The third stage, surrounding chain-branching, is really at the heart of the main knowledge gap surrounding autoignition in the literature, but it is difficult to accurately identify and measure these branching processes experimentally, without good characterisation of the earlier processes. Chapter 6 demonstrated this issue, and further modelling and experimental work of the earlier steps can help to constrain models. Once this is achieved, data potentially exhibiting the branching processes may begin to make more sense, and the elucidation of rates associated with branching should be possible. Thus, the rate parameters presented here concerning OH + ether and R + O_2 reactions, comprise a small but important contribution to the gradual accumulation of knowledge concerning low temperature biofuel combustion.

References

1. Hartmann, D.L., Klein Tank, A.M., Rusticucci, M., Alexander, L.V., Brönnimann, S., Charabi, Y.A.R., Dentener, F.J., Dlugokencky, E.J., Easterling, D.R., Kaplan, A., Soden, B.J., Thorne, P.W., Wild, M. and Zhai, P.M. *Observations: Atmosphere and Surface.* Cambridge, United Kingdom and New York, NY, USA, 2013.

2. British Antarctic Survey. *Ice Cores and Climate Change.* [Online]. 2015. [Accessed 18/10/2019]. Available from: bas.ac.uk

3. Collins, M., Knutti, R., Arblaster, J., Dufresne, J.-L., Fichefet, T., Friedlingstein, P., Gao, X., Gutowski, W.J., Johns, T., Krinner, G., Shongwe, M., Tebaldi, C., Weaver, A.J. and Wehner, M. *Long-term Climate Change: Projections, Commitments and Irreversibility.* Cambridge, United Kingdom and New York, NY, USA, 2013.

4. Myhre, G., Shindell, D., F.-M., B., Collins, W., Fuglestvedt, J., Huang, J., Koch, D., Lamarque, J.-F., Lee, D., Mendoza, B., Nakajima, T., Robock, A., Stephens, G., Takemura, T. and Zhang, H. *Anthropogenic and Natural Radiative Forcing.* Cambridge, United Kingdom and New York, NY, USA, 2013.

5. Jacob, D.J. *Introduction to Atmospheric Chemistry.* Princeton, New Jersey, USA: Princeton University Press, 1999.

6. Tyndall, J. Note on the Transmission of Radiant Heat through Gaseous Bodies. *Proceedings of the Royal Society of London.* 1859, **10**, pp.37-39.

7. Enting, I.G. The Interannual Variation in the Seasonal Cycle of Carbon Dioxide Concentration at Mauna Loa. *Journal of Geophysical Research: Atmospheres.* 1987, **92**(D5), pp.5497-5504.

8. MacFarling Meure, C., Etheridge, D., Trudinger, C., Steele, P., Langenfelds, R., van Ommen, T., Smith, A. and Elkins, J. Law Dome CO_2, CH_4 and N_2O Ice Core Records Extended to 2000 Years BP. *Geophysical Research Letters.* 2006, **33**(14), pp.n/a-n/a.

9. Kinley, R. Climate Change After Paris: From Turning Point to Transformation. *Climate Policy.* 2017, **17**(1), pp.9-15.

10. IPCC. *Climate Change 2014: Synthesis Report. Contribution of Working Groups I, II and III to the Fifth Assessment Report of the Intergovernmental Panel on Climate Change.* Geneva, Switzerland, 2014.

11. Mann, M.E. and Jones, P.D. Global Surface Temperatures Over The Past Two Millennia. *Geophysical Research Letters.* 2003, **30**(15).

12. Consoli, C. *Bioenergy and Carbon Capture and Storage.* Global CCS Institute, 2019.

13. Department for Business Energy & Industrial Strategy. *2018 UK Greenhouse Gas Emissions, Provisional Figures.* 2018.

14. Damyanov, A., Hofmann, P., Geringer, B., Schwaiger, N., Pichler, T. and Siebenhofer, M. Biogenous ethers: production and operation in a diesel engine. *Automotive and Engine Technology.* 2018, **3**(1), pp.69-82.

15. Le Feuvre, P. *Transport Biofuels: Tracking Clean Energy Progress.* [Online]. 2019. [Accessed 18/10/2019]. Available from: https://www.iea.org/tcep/transport/biofuels/

16. REN21. *Renewables 2019 Global Status Report.* Paris, France, 2019.

17. Department for Transport. *Renewable Fuel Statistics 2019 First Provisional Report.* 2019.

18. Renewable Energy World Editors. United Airlines Begins Regular Biofuel Use for Flights. *Renewable Energy World.* [Online]. 2016. [Accessed 18/10/2019]. Available from: http://www.renewableenergyworld.com/articles/2016/03/united-airlines-begins-regular-biofuel-use-for-flights.html

19. Field, C.B., Campbell, J.E. and Lobell, D.B. Biomass energy: the scale of the potential resource. *Trends in Ecology & Evolution.* 2008, **23**(2), pp.65-72.

20. Bergthorson, J.M. and Thomson, M.J. A Review of the Combustion and Emissions Properties of Advanced Transportation Biofuels and their Impact on Existing and Future Engines. *Renewable and Sustainable Energy Reviews.* 2015, **42**(0), pp.1393-1417.

21. Department for Business Energy & Industrial Strategy. *UK becomes first major economy to pass net zero emissions law.* [Online]. 2019. [Accessed 21/10/2019]. Available from: https://www.gov.uk/

22. Office of Energy Efficiency & Renewable Energy. *Hydrogen Storage.* [Online]. 2019. [Accessed 18/10/2019]. Available from: https://www.energy.gov/eere/fuelcells/hydrogen-storage

23. Bower, G. *Tesla Model 3 2170 Energy Density Compared to Bolt, Model S P100D.* [Online]. 2019. [Accessed 18/10/2019]. Available from: https://insideevs.com/news/

24. Qi, D.H., Chen, H., Geng, L.M. and Bian, Y.Z. Effect of diethyl ether and ethanol additives on the combustion and emission characteristics of biodiesel-diesel blended fuel engine. *Renewable Energy.* 2011, **36**(4), pp.1252-1258.

25. Ribeiro, N.M., Pinto, A.C., Quintella, C.M., da Rocha, G.O., Teixeira, L.S.G., Guarieiro, L.L.N., Rangel, M.D., Veloso, M.C.C., Rezende, M.J.C., da Cruz, R.S., de Oliveira, A.M., Torres, E.A. and de Andrade, J.B. The role of additives for diesel and diesel blended (Ethanol or biodiesel) fuels: A review. *Energy & Fuels.* 2007, **21**(4), pp.2433-2445.

26. Ford. *Ford Leads Project To Develop Near Zero Particulate Emission Diesel Cars That Could Run On Converted CO_2.* [Online]. 2015. [Accessed 18/10/2019]. Available from: https://media.ford.com/

27. Volvo. *Volvo Bio-DME Unique field test in commercial operations, 2010-2012.* [Leaflet]. 2010.

28. McMullen, C. *Key Takeaways from Volvo Group's New Sustainability Report.* [Online]. 2016. [Accessed 18/10/2019]. Available from: http://www.waste360.com/waste-reduction/key-takeaways-volvo-group-s-new-sustainability-report

29. Volvo. *The Volvo Group Annual and Sustainability Report.* Goteborg, Sweden, 2015.

30. Battin-Leclerc, F. Detailed chemical kinetic models for the low-temperature combustion of hydrocarbons with application to gasoline and diesel fuel surrogates. *Progress in Energy and Combustion Science.* 2008, **34**(4), pp.440-498.

31. The European Fuel Oxygenates Association. What Are Bio-Ethers? [Online]. 2018. [Accessed 23/10/2019]. Available from: https://www.petrochemistry.eu/

32. US Department of Energy. *Fuel Properties Comparison.* [Online]. 2019. [Accessed 18/10/2019]. Available from: https://afdc.energy.gov/fuels/properties

33. John, B. and Hansen, S. Fuels and Fuel Processing Options for Fuel Cells. In: *2nd International Fuel Cell Conference*, *Lucerne, CH*. 2004.

34. Semelsberger, T.A., Borup, R.L. and Greene, H.L. Dimethyl ether (DME) as an alternative fuel. *Journal of Power Sources.* 2006, **156**(2), pp.497-511.

35. The Engineering ToolBox. *Combustion.* [Online]. 2019. [Accessed 18/10/2019]. Available from: https://www.engineeringtoolbox.com/

36. Wang, M.Q. and Huang, H.S. *A full fuel-cycle analysis of energy and emissions impacts of transportation fuels produced from natural gas.* Argonne National Lab., IL (US), 2000.

37. Chetty, R. and Scott, K. Dimethoxymethane and trimethoxymethane as alternative fuels for fuel cells. *Journal of Power Sources.* 2007, **173**(1), pp.166-171.

38. Arcoumanis, C., Bae, C., Crookes, R. and Kinoshita, E. The potential of di-methyl ether (DME) as an alternative fuel for compression-ignition engines: A review. *Fuel.* 2008, **87**(7), pp.1014-1030.

39. Heuser, B., Jakob, M., Kremer, F., Pischinger, S., Kerschgens, B. and Pitsch, H. Tailor-Made Fuels from Biomass: Influence of Molecular Structures on the Exhaust Gas Emissions of Compression Ignition Engines. In: *22nd SAE Brasil International Congress and Display*, *Sao Paulo*. SAE International, 2013.

40. IEA Advanced Motor Fuels. *Fuel Ethers for Gasoline.* [Online]. 2019. [Accessed 21/10/2019]. Available from: https://www.iea-amf.org/

41. Institute for Occupational Safety and Health of the German Social Accident Insurance. *Dibutyl Ether.* [Online]. 2019. [Accessed 18/10/2019]. Available from: http://gestis-en.itrust.de/

42. IEA Advanced Motor Fuels. *Diesel and Gasoline.* [Online]. 2019. [Accessed 18/10/2019]. Available from: https://www.iea-amf.org/

43. International DME Association. *About DME.* [Online]. 2016. [Accessed 18/10/2019]. Available from: https://www.aboutdme.org/

44. GuangZhou Institute of Energy Conversion. *GIEC Builds 1000 ton/year Demonstration System and Achieves Great Progress on Key Technology of DME Synthesis from Biomass Gasification.* [Online]. 2011. [Accessed 18/10/2019]. Available from: http://english.giec.cas.cn/

45. Zhang, W. Automotive fuels from biomass via gasification. *Fuel Processing Technology.* 2010, **91**(8), pp.866-876.

46. Lv, Y., Wang, T., Wu, C., Ma, L. and Zhou, Y. Scale Study of Direct Synthesis of Dimethyl Ether from Biomass Synthesis Gas. *Biotechnology Advances.* 2009, **27**(5), pp.551-554.

47. International DME Association. *BASF and Linde Announce Commercialization Plans for CO_2-to-DME Production Process.* [Online]. 2019. [Accessed 18/10/2019]. Available from: https://www.aboutdme.org/

48. Oberon Fuels. *Oberon Fuels Secures $2.9 Million Grant from State of California for First-Ever Production of Renewable Dimethyl Ether (rDME) in United States.* [Online]. 2019. [Accessed 18/10/2019]. Available from: http://oberonfuels.com

49. Zhang, L. and Huang, Z. Life cycle study of coal-based dimethyl ether as vehicle fuel for urban bus in China. *Energy.* 2007, **32**(10), pp.1896-1904.

50. Kaiser, E.W., Wallington, T.J., Hurley, M.D., Platz, J., Curran, H.J., Pitz, W.J. and Westbrook, C.K. Experimental and Modeling Study of Premixed Atmospheric-Pressure Dimethyl Ether−Air Flames. *The Journal of Physical Chemistry A.* 2000, **104**(35), pp.8194-8206.

51. Park, S.H. and Lee, C.S. Combustion performance and emission reduction characteristics of automotive DME engine system. *Progress in Energy and Combustion Science.* 2013, **39**(1), pp.147-168.

52. Gao, J. and Nakamura, Y. Low-Temperature Ignition of Dimethyl Ether: Transition From Cool Flame to Hot Flame Promoted by Decomposition of HPMF (HO_2CH_2OCHO). *Combustion and Flame.* 2016, **165**, pp.68-82.

53. Naito, M., Radcliffe, C., Wada, Y., Hoshino, T., Liu, X., Arai, M. and Tamura, M. A Comparative Study On The Autoxidation Of Dimethyl Ether (DME) Comparison With Diethyl Ether (DEE) and Diisopropyl Ether (DIPE). *Journal of Loss Prevention in the Process Industries.* 2005, **18**(4–6), pp.469-473.

54. Rakopoulos, D.C., Rakopoulos, C.D., Giakoumis, E.G. and Dimaratos, A.M. Characteristics of performance and emissions in high-speed direct injection diesel engine fueled with diethyl ether/diesel fuel blends. *Energy.* 2012, **43**(1), pp.214-224.

55. Bailey, B., Eberhardt, J., Goguen, S. and Erwin, J. Diethyl Ether (DEE) as a Renewable Diesel Fuel. *SAE transactions.* 1997, **106**, pp.1578-1584.

56. Mack, J.H., Buchholz, B.A., Flowers, D.L. and Dibble, R.W. *The Effect of the Di-Tertiary Butyl Peroxide (DTBP) additive on HCCI Combustion of Fuel Blends of Ethanol and Diethyl Ether.* 2005. Available from: http://www.escholarship.org/uc/item/2j80r0t5

57. Mack, J.H., Flowers, D.L., Buchholz, B.A. and Dibble, R.W. Investigation Of HCCI Combustion Of Diethyl Ether And Ethanol Mixtures Using Carbon 14 Tracing And Numerical Simulations. *Proceedings of the Combustion Institute.* 2005, **30**(2), pp.2693-2700.

58. Miller Jothi, N.K., Nagarajan, G. and Renganarayanan, S. Experimental Studies On Homogeneous Charge CI Engine Fueled With LPG Using DEE as an Ignition Enhancer. *Renewable Energy.* 2007, **32**(9), pp.1581-1593.

59. Cheng, A.S. and Dibble, R.W. Emissions Performance of Oxygenate-in-Diesel Blends and Fischer-Tropsch Diesel in a Compression Ignition Engine. In.: SAE International, 1999.

60. Tree, D.R. and Cooley, W.B. A Comparison and Model of NOx Formation for Diesel Fuel and Diethyl Ether. In.: SAE International, 2001.

61. Anand, R. and Mahalakshmi, N.V. Simultaneous reduction of NOx and smoke from a direct-injection diesel engine with exhaust gas recirculation and diethyl ether. *Proceedings of the Institution of Mechanical Engineers, Part D: Journal of Automobile Engineering.* 2007, **221**(1), pp.109-116.

62. Mohanan, P., Kapilan, N. and Reddy, R.P. Effect of Diethyl Ether on the Performance and Emission of a 4 - S Di Diesel Engine. In.: SAE International, 2003.

63. Subramanian, K.A. and Ramesh, A. Operation of a Compression Ignition Engine on Diesel-Diethyl Ether Blends. *Proceedings of the ASME 2002 Internal Combustion Engine Division Fall Technical Conference.* 2002, (46628), pp.353-360.

64. Kim, J.K., Choi, J.H., Park, D.R. and Song, I.K. Etherification of n-Butanol to Di-n-Butyl Ether Over Keggin-, Wells-Dawson-, and Preyssler-Type Heteropolyacid Catalysts. *Journal of Nanoscience and Nanotechnology.* 2013, **13**(12), pp.8121-8126.

65. Beeckmann, J., Aye, M., Gehmlich, R. and Peters, N. *Experimental investigation of the spray characteristics of di-n-butyl ether (DNBE) as an oxygenated compound in diesel fuel.* SAE Technical Paper, 2010.

66. Gao, Z., Zhu, L., Zou, X., Liu, C., Tian, B. and Huang, Z. Soot reduction effects of dibutyl ether (DBE) addition to a biodiesel surrogate in laminar coflow diffusion flames. *Proceedings of the Combustion Institute.* 2019, **37**(1), pp.1265-1272.

67. Zubel, M., Pischinger, S. and Heuser, B. Assessment of the Full Thermodynamic Potential of C8-Oxygenates for Clean Diesel Combustion. *SAE International Journal of Fuels and Lubricants.* 2017, **10**(3), pp.913-923.

68. Guan, L., Tang, C., Yang, K., Mo, J. and Huang, Z. Experimental and Kinetic Study on Ignition Delay Times of Di-n-butyl Ether at High Temperatures. *Energy & Fuels.* 2014, **28**(8), pp.5489-5496.

69. Miyamoto, N., Ogawa, H. and Nabi, M.N. Approaches to extremely low emissions and efficient diesel combustion with oxygenated fuels. *International Journal of Engine Research.* 2000, **1**(1), pp.71-85.

70. Ziyang, Z., Hidajat, K. and Ray, A.K. Determination of adsorption and kinetic parameters for methyl tert-butyl ether synthesis from tert-butyl alcohol and methanol. *Journal of Catalysis.* 2001, **200**(2), pp.209-221.

71. Subramaniam, C. and Bhatia, S. Liquid phase synthesis of methyl tert-butyl ether catalyzed by ion exchange resin. *The Canadian Journal of Chemical Engineering.* 1987, **65**(4), pp.613-620.

72. Adams, J.M., Clement, D.E. and Graham, S.H. Synthesis of Methyl-t-Butyl Ether from Methanol and Isobutene Using a Clay Catalyst. *Clays and Clay Minerals.* 1982, **30**(2), pp.129-134.

73. Boot, M.D., Tian, M., Hensen, E.J.M. and Mani Sarathy, S. Impact of Fuel Molecular Structure on Auto-Ignition Behavior – Design Rules for Future High Performance Gasolines. *Progress in Energy and Combustion Science.* 2017, **60**, pp.1-25.

74. Kisenyi, J., Savage, C. and Simmonds, A.C. *The impact of oxygenates on exhaust emissions of six European cars.* SAE Technical Paper, 1994.

75. Chou, D.C. and Long, J. *Comparison of the Exhaust Emissions from California Phase 1 (without oxygenates) and Phase 2 (with oxygenates) Fuel: A Case Study of 11 Passenger Vehicles.* SAE Technical Paper, 1996.

76. DePetris, C., Giglio, V., Police, G. and Prati, M.V. *The influence of gasoline formulation on combustion and emissions in spark-ignition engines.* SAE Technical Paper, 1993.

77. Lange, W., Müller, A., McArragher, J. and Schäfer, V. *The effect of gasoline composition on exhaust emissions from modern BMW vehicles.* SAE Technical Paper, 1994.

78. Reuter, R., Benson, J., Burns, V., Gorse, R., Hochhauser, A., Koehl, W., Painter, L., Rippon, B. and Rutherford, J. Effects of oxygenated fuels and RVP on automotive emissions: Auto. *SAE transactions.* 1992, **101**(4), pp.463-484.

79. Zervas, E., Montagne, X., Lahaye, J.J.E.s. and technology. Emission of alcohols and carbonyl compounds from a spark ignition engine. Influence of fuel and

air/fuel equivalence ratio. *Environmental Science and Technology.* 2002, **36**(11), pp.2414-2421.

80. Song, C.-L., Zhang, W.-M., Pei, Y.-Q., Fan, G.-L. and Xu, G.-P. Comparative effects of MTBE and ethanol additions into gasoline on exhaust emissions. *Atmospheric Environment.* 2006, **40**(11), pp.1957-1970.

81. Erickson, J.G. Alkyl Orthoformates. *The Journal of Organic Chemistry.* 1955, **20**(11), pp.1573-1576.

82. John, J.H.R., Rebello, P.R., Kavonic, C.M. and Stiff, A.J. *Fuels.* 1989.

83. Prakash, G.K.S., Smart, M.C., Olah, G.A., Narayanan, S.R., Chun, W., Surampudi, S. and Halpert, G. Performance of Dimethoxymethane and Trimethoxymethane in Liquid-Feed Direct Oxidation Fuel Cells. *Journal of Power Sources.* 2007, **173**(1), pp.102-109.

84. Wang, J.T., Lin, W.F., Weber, M., Wasmus, S. and Savinell, R.F. Trimethoxymethane as an Alternative Fuel for a Direct Oxidation PBI Polymer Electrolyte Fuel Cell. *Electrochimica Acta.* 1998, **43**(24), pp.3821-3828.

85. Narayanan, S.R., Vamos, E., Surampudi, S., Frank, H., Halpert, G., Surya Prakash, G.K., Smart, M.C., Knieler, R., Olah, G.A., Kosek, J. and Cropley, C. Direct Electro-oxidation of Dimethoxymethane, Trimethoxymethane, and Trioxane and Their Application in Fuel Cells. *Journal of The Electrochemical Society.* 1997, **144**(12), pp.4195-4201.

86. Pilling, M.J. and Seakins, P.W. *Reaction Kinetics.* Oxford University Press, 1996.

87. Moshammer, K., Jasper, A.W., Popolan-Vaida, D.M., Lucassen, A., Diévart, P., Selim, H., Eskola, A.J., Taatjes, C.A., Leone, S.R., Sarathy, S.M., Ju, Y., Dagaut, P., Kohse-Höinghaus, K. and Hansen, N. Detection and Identification of the Keto-Hydroperoxide ($HOOCH_2OCHO$) and Other Intermediates during Low-Temperature Oxidation of Dimethyl Ether. *The Journal of Physical Chemistry A.* 2015, **119**(28), pp.7361-7374.

88. Moshammer, K., Jasper, A.W., Popolan-Vaida, D.M., Wang, Z., Bhavani Shankar, V.S., Ruwe, L., Taatjes, C.A., Dagaut, P. and Hansen, N. Quantification of the Keto-Hydroperoxide ($HOOCH_2OCHO$) and Other Elusive Intermediates during Low-Temperature Oxidation of Dimethyl Ether. *The Journal of Physical Chemistry A.* 2016, **120**(40), pp.7890-7901.

89. Eskola, A.J., Carr, S.A., Shannon, R.J., Wang, B., Blitz, M.A., Pilling, M.J., Seakins, P.W. and Robertson, S.H. Analysis of the Kinetics and Yields of OH Radical Production from the $CH_3OCH_2 + O_2$ Reaction in the Temperature Range

195–650 K: An Experimental and Computational study. *The Journal of Physical Chemistry A.* 2014, **118**(34), pp.6773-6788.

90.   Zádor, J., Taatjes, C.A. and Fernandes, R.X. Kinetics of elementary reactions in low-temperature autoignition chemistry. *Progress in Energy and Combustion Science.* 2011, **37**(4), pp.371-421.

91.   Potter, D.G. *Characterisation of a FAGE Instrument and the Importance of DME Combustion Chain-Branching and Chemical Activation Modelling in HCCI Engines*. Unpublished, 2015.

92.   Fernandes, R.X., Zádor, J., Jusinski, L.E., Miller, J.A. and Taatjes, C.A. Formally direct pathways and low-temperature chain branching in hydrocarbon autoignition: the cyclohexyl + O_2 reaction at high pressure. *Physical Chemistry Chemical Physics.* 2009, **11**(9), pp.1320-1327.

93.   Taatjes, C.A. Uncovering the Fundamental Chemistry of Alkyl + O_2 Reactions via Measurements of Product Formation. *The Journal of Physical Chemistry A.* 2006, **110**(13), pp.4299-4312.

94.   Curran, H.J., Fischer, S.L. and Dryer, F.L. The reaction kinetics of dimethyl ether. II: Low-temperature oxidation in flow reactors. *International Journal of Chemical Kinetics.* 2000, **32**(12), pp.741-759.

95.   Curran, H.J., Pitz, W.J., Westbrook, C.K., Dagaut, P., Boettner, J.C. and Cathonnet, M. A wide range modeling study of dimethyl ether oxidation. *International Journal of Chemical Kinetics.* 1998, **30**(3), pp.229-241.

96.   Zhao, Z., Chaos, M., Kazakov, A. and Dryer, F.L. Thermal decomposition reaction and a comprehensive kinetic model of dimethyl ether. *International Journal of Chemical Kinetics.* 2008, **40**(1), pp.1-18.

97.   Tomlin, A.S., Agbro, E., Nevrlý, V., Dlabka, J. and Vašinek, M. Evaluation of Combustion Mechanisms Using Global Uncertainty and Sensitivity Analyses: A Case Study for Low-Temperature Dimethyl Ether Oxidation. *International Journal of Chemical Kinetics.* 2014, **46**(11), pp.662-682.

98.   Jääskeläinen, H. *Low Temperature Combustion.* [Online]. 2010. [Accessed 18/10/2019]. Available from: https://www.dieselnet.com/tech/engine_ltc.php

99.   Shudo, T. Influence of gas composition on the combustion and efficiency of a homogeneous charge compression ignition engine system fuelled with methanol reformed gases. *International Journal of Engine Research.* 2008, **9**(5), pp.399-408.

100. Shudo, T. and Yamada, H. Hydrogen as an Ignition-Controlling Agent for HCCI Combustion Engine by Suppressing the Low-Temperature Oxidation. *International Journal of Hydrogen Energy.* 2007, **32**(14), pp.3066-3072.

101. Manley, D.K., McIlroy, A. and Taatjes, C.A. Research Needs for Future Internal Combustion Engines. *Physics Today.* 2008, pp.47-52.

102. Blocquet, M., Schoemaecker, C., Amedro, D., Herbinet, O., Battin-Leclerc, F. and Fittschen, C. Quantification of OH and HO_2 radicals during the low-temperature oxidation of hydrocarbons by Fluorescence Assay by Gas Expansion technique. *Proceedings of the National Academy of Sciences of the United States of America.* 2013, **110**(50), pp.20014-20017.

103. Wilson, W.E., Jr. A Critical Review of the Gas-Phase Reaction Kinetics of the Hydroxyl Radical. *Journal of Physical and Chemical Reference Data.* 1972, **1**(2), pp.535-574.

104. Cox, R.A. and Cole, J.A. Chemical Aspects of the Autoignition of Hydrocarbon-Air Mixtures. *Combustion and Flame.* 1985, **60**(2), pp.109-123.

105. Fish, A. Chain Propagation in the Oxidation of Alkyl Radicals. In: *Oxidation of Organic Compounds.* American Chemical Society, 1968, pp.69-85.

106. Knox, J.H. *Photochemistry and Reaction Kinetics.* Cambridge: Cambridge University Press, 1967.

107. Pollard, R.T. Hydrocarbons. *Comprehensive Chemical Kinetics: Gas-Phase Combustion.* 1977, **17**.

108. Walker, R.W. and Morley, C. Basic Chemistry of Combustion. *Comprehensive Chemical Kinetics: Low-Temperature Combustion and Autoignition.* 1997, **35**.

109. Burke, U., Somers, K.P., O'Toole, P., Zinner, C.M., Marquet, N., Bourque, G., Petersen, E.L., Metcalfe, W.K., Serinyel, Z. and Curran, H.J. An ignition delay and kinetic modeling study of methane, dimethyl ether, and their mixtures at high pressures. *Combustion and Flame.* 2015, **162**(2), pp.315-330.

110. Mittal, G., Chaos, M., Sung, C.-J. and Dryer, F.L. Dimethyl Ether Autoignition In A Rapid Compression Machine: Experiments And Chemical Kinetic Modeling. *Fuel Processing Technology.* 2008, **89**(12), pp.1244-1254.

111. Yahyaoui, M., Djebaili-Chaumeix, N., Dagaut, P., Paillard, C.E. and Gall, S. Experimental and modelling study of gasoline surrogate mixtures oxidation in jet stirred reactor and shock tube. *Proceedings of the Combustion Institute.* 2007, **31**, pp.385-391.

112. Dagaut, P., Boettner, J.-C. and Cathonnet, M. Chemical kinetic study of dimethylether oxidation in a jet stirred reactor from 1 to 10 ATM: Experiments and kinetic modeling. *Symposium (International) on Combustion.* 1996, **26**(1), pp.627-632.

113. Mellouki, A., Teton, S. and Le Bras, G. Kinetics Of OH Radical Reactions With A Series Of Ethers. *International Journal of Chemical Kinetics.* 1995, **27**(8), pp.791-805.

114. Wang, Z., Zhang, X., Xing, L., Zhang, L., Herrmann, F., Moshammer, K., Qi, F. and Kohse-Höinghaus, K. Experimental and kinetic modeling study of the low- and intermediate-temperature oxidation of dimethyl ether. *Combustion and Flame.* 2015, **162**(4), pp.1113-1125.

115. Di Tommaso, S., Rotureau, P., Crescenzi, O. and Adamo, C. Oxidation mechanism of diethyl ether: a complex process for a simple molecule. *Physical Chemistry Chemical Physics.* 2011, **13**(32), pp.14636-14645.

116. Du, B. and Zhang, W. Theoretical study of the reaction mechanism and kinetics of the OH + trimethyl orthoformate ($(CH_3O)_3CH$) + O_2 reaction. *Computational and Theoretical Chemistry.* 2019, **1159**, pp.38-45.

117. Andrews, D.L. *Lasers in Chemistry.* Heidelberg: Springer-Verlag, 1986.

118. Atkinson, R., Baulch, D.L., Cox, R.A., Crowley, J.N., Hampson, R.F., Hynes, R.G., Jenkin, M.E., Rossi, M.J. and Troe, J. Evaluated kinetic and photochemical data for atmospheric chemistry: Volume I - gas phase reactions of O_X, HO_X, NO_X and SO_X species. *Atmospheric Chemistry and Physics.* 2004, **4**(6), pp.1461-1738.

119. Nicovich, J.M. and Wine, P.H. Temperature-dependent absorption cross sections for hydrogen peroxide vapor. *Journal of Geophysical Research: Atmospheres.* 1988, **93**(D3), pp.2417-2421.

120. Pędziwiatr, P., Mikołajczyk, F., Zawadzki, D., Mikołajczyk, K. and Bedka, A. Decomposition of Hydrogen Peroxide - Kinetics and Review of Chosen Catalysts. *Acta Innovations.* 2018, **26**, pp.45-52.

121. Mackenzie, R.C., Ritchie, M. and Kendall, J.P. The Thermal Decomposition of Hydrogen Peroxide Vapour. *Proceedings of the Royal Society of London. Series A. Mathematical and Physical Sciences.* 1944, **185**(1001), pp.207-224.

122. Willms, T., Kryk, H., Oertel, J., Hempel, C., Knitt, F. and Hampel, U. On the thermal decomposition of tert.-butyl hydroperoxide, its sensitivity to metals and its kinetics, studied by thermoanalytic methods. *Thermochimica Acta.* 2019, **672**, pp.25-42.

123. Atkins, P. and De Paula, J. *Elements of Physical Chemistry.* Fifth ed. Oxford University Press, USA, 2013.

124. Dunlop, J.R. and Tully, F.P. A kinetic study of hydroxyl radical reactions with methane and perdeuterated methane. *The Journal of Physical Chemistry.* 1993, **97**(43), pp.11148-11150.

125. Laidler, K.J. *Chemical Kinetics.* Second ed. London, UK: McGraw-Hill, 1965.

126. Cook, R.D., Davidson, D.F. and Hanson, R.K. High-Temperature Shock Tube Measurements of Dimethyl Ether Decomposition and the Reaction of Dimethyl Ether with OH. *The Journal of Physical Chemistry A.* 2009, **113**(37), pp.9974-9980.

127. Yasunaga, K., Simmie, J.M., Curran, H.J., Koike, T., Takahashi, O., Kuraguchi, Y. and Hidaka, Y. Detailed Chemical Kinetic Mechanisms of Ethyl Methyl, Methyl tert-Butyl and Ethyl tert-Butyl Ethers: The Importance of Uni-Molecular Elimination Reactions. *Combustion and Flame.* 2011, **158**(6), pp.1032-1036.

128. Davidson, D.F. and Hanson, R.K. Recent advances in shock tube/laser diagnostic methods for improved chemical kinetics measurements. *Shock Waves.* 2009, **19**(4), pp.271-283.

129. Bennett, P.J. and Kerr, J.A. Kinetics of the reactions of hydroxyl radicals with aliphatic ethers studied under simulated atmospheric conditions. *Journal of Atmospheric Chemistry.* 1989, **8**(1), pp.87-94.

130. Harry, C., Arey, J. and Atkinson, R. Rate constants for the reactions of OH radicals and Cl atoms with Di-n-Propyl ether and Di-n-Butyl ether and their deuterated analogs. *International Journal of Chemical Kinetics.* 1999, **31**(6), pp.425-431.

131. Smith, D.F., Kleindienst, T.E., Hudgens, E.E., McIver, C.D. and Bufalini, J.J. The Photooxidation of Methyl Tertiary Butyl Ether. *International Journal of Chemical Kinetics.* 1991, **23**(10), pp.907-924.

132. Tranter, R.S. and Walker, R.W. Rate Constants for the Reactions of H Atoms and OH Radicals with Ethers at 753 K. *Physical Chemistry Chemical Physics.* 2001, **3**(21), pp.4722-4732.

133. Kovács, G., Zádor, J., Farkas, E., Nádasdi, R., Szilágyi, I., Dóbé, S., Bérces, T., Márta, F. and Lendvay, G. Kinetics and mechanism of the reactions of CH_3CO and $CH_3C(O)CH_2$ radicals with O_2. Low-pressure discharge flow experiments and quantum chemical computations. *Physical Chemistry Chemical Physics.* 2007, **9**(31), pp.4142-4154.

134. Perry, R.A., Atkinson, R. and Pitts, J.N. Rate constants for the reaction of OH radicals with dimethyl ether and vinyl methyl ether over the temperature range 299–427 °K. *The Journal of Chemical Physics.* 1977, **67**(2), pp.611-614.

135. Wallington, T.J., Dagaut, P., Liu, R. and Kurylo, M.J. Gas-Phase Reactions of Hydroxyl Radicals with the Fuel Additives Methyl tert-Butyl Ether and tert-Butyl Alcohol over the Temperature Range 240-440 K. *Environmental Science and Technology.* 1988, **22**(7), pp.842-844.

136. Wallington, T.J., Liu, R., Dagaut, P. and Kurylo, M.J. The gas phase reactions of hydroxyl radicals with a series of aliphatic ethers over the temperature range 240–440 K. *International Journal of Chemical Kinetics.* 1988, **20**(1), pp.41-49.

137. Nelson, L., Rattigan, O., Neavyn, R., Sidebottom, H., Treacy, J. and Nielsen, O.J. Absolute And Relative Rate Constants For The Reactions Of Hydroxyl Radicals And Chlorine Atoms With A Series Of Aliphatic Alcohols And Ethers At 298 K. *International Journal of Chemical Kinetics.* 1990, **22**(11), pp.1111-1126.

138. Hansel, A., Jordan, A., Holzinger, R., Prazeller, P., Vogel, W. and Lindinger, W. Proton-Transfer Reaction Mass-Spectrometry - Online Trace Gas-Analysis at the ppb Level. *International Journal of Mass Spectrometry.* 1995, **149**, pp.609-619.

139. Lindinger, W. and Hansel, A. Analysis of Trace Gases at ppb Levels by Proton Transfer Reaction Mass Spectrometry (PTR-MS). *Plasma Sources Science & Technology.* 1997, **6**(2), pp.111-117.

140. Lindinger, W., Hansel, A. and Jordan, A. Proton-Transfer-Reaction Mass Spectrometry (PTR-MS): On-Line Monitoring of Volatile Organic Compounds at pptv Levels. *Chemical Society Reviews.* 1998, **27**(5), pp.347-354.

141. IONICON. *PTR-MS.* [Online]. 2017. [Accessed 23/10/2019]. Available from: http://www.ionicon.com/information/technology/ptr-ms

142. KORE. *Proton Transfer Reactor Time-of-Flight Mass Spectrometry (PTR-TOF-MS).* [Online]. 2013. [Accessed 23/10/2019]. Available from: http://www.kore.co.uk/ptrtof.htm

143. Baeza-Romero, M.T., Blitz, M.A., Goddard, A. and Seakins, P.W. Time-of-flight mass spectrometry for time-resolved measurements: Some developments and applications. *International Journal of Chemical Kinetics.* 2012, **44**(8), pp.532-545.

144. Howes, N.U.M., Mir, Z.S., Blitz, M.A., Hardman, S., Lewis, T.R., Stone, D. and Seakins, P.W. Kinetic studies of C_1 and C_2 Criegee intermediates with SO_2 using laser flash photolysis coupled with photoionization mass spectrometry and time

resolved UV absorption spectroscopy. *Physical Chemistry Chemical Physics.* 2018, **20**(34), pp.22218-22227.

145. Medeiros, D.J., Blitz, M.A., James, L., Speak, T.H. and Seakins, P.W. Kinetics of the Reaction of OH with Isoprene over a Wide Range of Temperature and Pressure Including Direct Observation of Equilibrium with the OH Adducts. *The Journal of Physical Chemistry A.* 2018, **122**(37), pp.7239-7255.

146. Potter, C.D. *A study of the mechanism of thermal decomposition of tetraborane(10) by mass spectrometry*. PhD thesis, University of Leeds, 1984.

147. Walker, R.W. and Morley, C. Chapter 1 Basic Chemistry of Combustion. In: Pilling, M.J. ed. *Comprehensive Chemical Kinetics*. Amsterdam: Elsevier, 1997, pp.1-124.

148. Daubert, T.E. and Danner, R.P. *Physical and Thermodynamic Properties of Pure Chemicals Data Compilation*. Washington, D.C.: Taylor and Francis. 1989.

149. NTP. *National Toxicology Program Chemical Repository Database*. Research Triangle Park, North Carolina: Institute of Environmental Health Sciences, National Institutes of Health. 1992.

150. Antoine, C. Vapor Pressure: a new relationship between pressure and temperature. *Comptes Rendus des Séances de l'Académie des Sciences.* 1888, **107**.

151. Yaws, C.L. and Yang, H.C. To Estimate Vapor Pressure Easily. Antoine Coefficients Relate Vapour Pressure to Temperature for Almost 700 Major Organic Compounds. *Hydrocarbon Processing.* 1989, **68**(10), pp.65-68.

152. Platz, J., Sehested, J., Nielsen, O.J. and Wallington, T.J. Atmospheric Chemistry of Trimethoxymethane, $(CH_3O)_3CH$; Laboratory Studies. *The Journal of Physical Chemistry A.* 1999, **103**(15), pp.2632-2640.

153. Porter, E., Wenger, J., Treacy, J., Sidebottom, H., Mellouki, A., Téton, S. and LeBras, G. Kinetic Studies on the Reactions of Hydroxyl Radicals with Diethers and Hydroxyethers. *Journal of Atmospheric Chemistry.* 1997, **101**(32), pp.5770-5775.

154. Wallington, T.J., Hurley, M.D., Ball, J.C., Straccia, A.M., Platz, J., Christensen, L.K., Sehested, J. and Nielsen, O.J. Atmospheric Chemistry of Dimethoxymethane ($CH_3OCH_2OCH_3$): Kinetics and Mechanism of its Reaction with OH Radicals and Fate of the Alkoxy Radicals $CH_3OCHO(\bullet)OCH_3$ and $CH_3OCH_2OCH_2O(\bullet)$. *The Journal of Physical Chemistry A.* 1997, **101**(29), pp.5302-5308.

155. Potter, D.G., Wiseman, S., Blitz, M.A. and Seakins, P.W. Laser Photolysis Kinetic Study of OH Radical Reactions with Methyl tert-Butyl Ether and Trimethyl Orthoformate under Conditions Relevant to Low Temperature Combustion: Measurements of Rate Coefficients and OH Recycling. *The Journal of Physical Chemistry A.* 2018, **122**(50), pp.9701-9711.

156. Potter, D.G., Blitz, M.A. and Seakins, P.W. A generic method for determining $R + O_2$ rate parameters via OH regeneration. *Chemical Physics Letters.* 2019, **730**, pp.213-219.

157. Shannon, R.J., Caravan, R.L., Blitz, M.A. and Heard, D.E. A Combined Experimental and Theoretical Study of Reactions Between the Hydroxyl Radical and Oxygenated Hydrocarbons Relevant to Astrochemical Environments. *Physical Chemistry Chemical Physics.* 2014, **16**(8), pp.3466-3478.

158. Shannon, R.J., Taylor, S., Goddard, A., Blitz, M.A. and Heard, D.E. Observation of a large negative temperature dependence for rate coefficients of reactions of OH with oxygenated volatile organic compounds studied at 86–112 K. *Physical Chemistry Chemical Physics.* 2010, **12**(41), pp.13511-13514.

159. Waddington, D.J. The Gaseous Oxidation of Diethyl Ether. *Proceedings of the Royal Society of London. Series A. Mathematical and Physical Sciences.* 1959, **252**(1269), pp.260-272.

160. Orlando, J.J. The atmospheric oxidation of diethyl ether: chemistry of the C_2H_5-O-CH(O)CH_3 radical between 218 and 335 K. *Physical Chemistry Chemical Physics.* 2007, **9**(31), pp.4189-4199.

161. Eberhard, J., Müller, C., Stocker, D.W. and Kerr, J.A. The photo-oxidation of diethyl ether in smog chamber experiments simulating tropospheric conditions: Product studies and proposed mechanism. *International Journal of Chemical Kinetics.* 1993, **25**(8), pp.639-649.

162. Lloyd, A.C., Darnall, K.R., Winer, A.M. and Pitts, J.N. Relative Rate Constants for the Reactions of OH Radicals with Isopropyl Alcohol, Diethyl and Di-n-propyl Ether at 305 ± 2 K. *Chemical Physics Letters.* 1976, **42**(2), pp.205-209.

163. Bennett, P.J. and Kerr, J.A. Kinetics of the reactions of hydroxyl radicals with aliphatic ethers studied under simulated atmospheric conditions: Temperature dependences of the rate coefficients. *Journal of Atmospheric Chemistry.* 1990, **10**(1), pp.27-38.

164. Semadeni, M., Stocker, D.W. and Kerr, J.A. Further studies of the temperature dependence of the rate coefficients for the reactions of OH with a series of ethers

under simulated atmospheric conditions. *Journal of Atmospheric Chemistry.* 1993, **16**(1), pp.79-93.

165. Tully, F.P. and Droege, A.T. Kinetics of the reactions of the hydroxyl radical with dimethyl ether and diethyl ether. *International Journal of Chemical Kinetics.* 1987, **19**(3), pp.251-259.

166. Notario, A., Mellouki, A. and Le Bras, G. Rate constants for the gas-phase reactions of Cl atoms with a series of ethers. *International Journal of Chemical Kinetics.* 2000, **32**(2), pp.105-110.

167. Atkinson, R., Baulch, D.L., Cox, R.A., Crowley, J.N., Hampson, R.F., Hynes, R.G., Jenkin, M.E., Rossi, M.J. and Troe, J. IUPAC Task Group on Atmospheric Chemical Kinetic Data Evaluation *Atmospheric Chemistry and Physics.* 2004, **2**(4), pp.1461-1738.

168. Atkinson, R. Kinetics of the gas-phase reactions of OH radicals with alkanes and cycloalkanes. *Atmospheric Chemistry and Physics.* 2003, **3**.

169. Orkin, V.L., Villenave, E., Huie, R.E. and Kurylo, M.J. Atmospheric Lifetimes and Global Warming Potentials of Hydrofluoroethers: Reactivity toward OH, UV Spectra, and IR Absorption Cross Sections. *The Journal of Physical Chemistry A.* 1999, **103**(48), pp.9770-9779.

170. Cai, L.M., Sudholt, A., Lee, D.J., Egolfopoulos, F.N., Pitsch, H., Westbrook, C.K. and Sarathy, S.M. Chemical kinetic study of a novel lignocellulosic biofuel: Di-n-butyl ether oxidation in a laminar flow reactor and flames. *Combustion and Flame.* 2014, **161**(3), pp.798-809.

171. Wullenkord, J., Tran, L.S., Bottchers, J., Graf, I. and Kohse-Hoinghaus, K. A laminar flame study on di-n-butyl ether as a potential biofuel candidate. *Combustion and Flame.* 2018, **190**, pp.36-49.

172. Thion, S., Togbé, C., Serinyel, Z., Dayma, G. and Dagaut, P. A chemical kinetic study of the oxidation of dibutyl-ether in a jet-stirred reactor. *Combustion and Flame.* 2017, **185**, pp.4-15.

173. Kramp, F. and Paulson, S.E. On the Uncertainties in the Rate Coefficients for OH Reactions with Hydrocarbons, and the Rate Coefficients of the 1,3,5-Trimethylbenzene and m-Xylene Reactions with OH Radicals in the Gas Phase. *The Journal of Physical Chemistry A.* 1998, **102**(16), pp.2685-2690.

174. Wallington, T.J., Andino, J.M., Skewes, L.M., Siegl, W.O. and Japar, S.M. Kinetics of the Reaction of OH Radicals with a Series of Ethers under Simulated

Atmospheric Conditions at 295 K. *International Journal of Chemical Kinetics.* 1989, **21**(11), pp.993-1001.

175. Arif, M., Dellinger, B. and Taylor, P.H. Rate Coefficients of Hydroxyl Radical Reaction with Dimethyl Ether and Methyl tert-Butyl Ether over an Extended Temperature Range. *The Journal of Physical Chemistry A.* 1997, **101**(13), pp.2436-2441.

176. Bonard, A., Daële, V., Delfau, J.-L. and Vovelle, C. Kinetics of OH Radical Reactions with Methane in the Temperature Range 295−660 K and with Dimethyl Ether and Methyl-tert-butyl Ether in the Temperature Range 295−618 K. *The Journal of Physical Chemistry A.* 2002, **106**(17), pp.4384-4389.

177. Cox, R.A. and Goldstone, A. Atmospheric Reactivity of Oxygenated Motor Fuel Additives. In: *Physico-Chemical Behaviour of Atmospheric Pollutants: Proceedings of the Second European Symposium*, 1982.

178. Picquet, B., Heroux, S., Chebbi, A., Doussin, J.F., Durand-Jolibois, R., Monod, A., Loirat, H. and Carlier, P. Kinetics of the Reactions of OH Radicals with Some Oxygenated Volatile Organic Compounds under Simulated Atmospheric Conditions. *International Journal of Chemical Kinetics.* 1998, **30**(11), pp.839-847.

179. Teton, S., Mellouki, A., Bras, G.L. and Sidebottom, H. Rate Constants for Reactions of OH Radicals with a Series of Asymmetrical Ethers and tert-Butyl Alcohol. *International Journal of Chemical Kinetics.* 1996, **28**(4), pp.291-297.

180. Japar, S.M., Wallington, T.J., Richert, J.F.O. and Ball, J.C. The Atmospheric Chemistry of Oxygenated Fuel Additives: t-Butyl Alcohol, Dimethyl Ether, and Methyl t-Butyl Ether. *International Journal of Chemical Kinetics.* 1990, **22**(12), pp.1257-1269.

181. Tuazon, E.C., Carter, W.P.L., Aschmann, S.M. and Atkinson, R. Products of the Gas-Phase Reaction of Methyl tert-Butyl Ether with the OH Radical in the Presence of NO_x. *International Journal of Chemical Kinetics.* 1991, **23**(11), pp.1003-1015.

182. Iuga, C., Osnaya-Soto, L., Ortiz, E. and Vivier-Bunge, A. Atmospheric Oxidation of Methyl and Ethyl tert-Butyl Ethers Initiated by Hydroxyl Radicals. A Quantum Chemistry Study. *Fuel.* 2015, **159**, pp.269-279.

183. Zavala-Oseguera, C., Alvarez-Idaboy, J.R., Merino, G. and Galano, A. OH Radical Gas Phase Reactions with Aliphatic Ethers: A Variational Transition State

Theory Study. *The Journal of Physical Chemistry A.* 2009, **113**(50), pp.13913-13920.

184. Atadinc, F., Selcuki, C., Sari, L. and Aviyente, V. Theoretical Study of Hydrogen Abstraction from Dimethyl Ether and Methyl tert-Butyl Ether by Hydroxyl Radical. *Physical Chemistry Chemical Physics.* 2002, **4**(10), pp.1797-1806.

185. Bänsch, C., Kiecherer, J., Szöri, M. and Olzmann, M. Reaction of Dimethyl Ether with Hydroxyl Radicals: Kinetic Isotope Effect and Prereactive Complex Formation. *The Journal of Physical Chemistry A.* 2013, **117**(35), pp.8343-8351.

186. Carr, S.A., Still, T.J., Blitz, M.A., Eskola, A.J., Pilling, M.J., Seakins, P.W., Shannon, R.J., Wang, B. and Robertson, S.H. Experimental and theoretical study of the kinetics and mechanism of the reaction of OH radicals with dimethyl ether. *The Journal of Physical Chemistry A.* 2013, **117**(44), pp.11142-11154.

187. DeMore, W.B. and Bayes, K.D. Rate Constants for the Reactions of Hydroxyl Radical with Several Alkanes, Cycloalkanes, and Dimethyl Ether. *The Journal of Physical Chemistry A.* 1999, **103**(15), pp.2649-2654.

188. Koizumi, H., Hironaka, K., Shinsaka, K., Arai, S., Nakazawa, H., Kimura, A., Hatano, Y., Ito, Y., Zhang, Y., Yagishita, A., Ito, K. and Tanaka, K. VUV-optical oscillator strength distributions of C_2H_6O and C_3H_8O isomers. *The Journal of Chemical Physics.* 1986, **85**(8), pp.4276-4279.

189. Mellouki, A., Le Bras, G. and Sidebottom, H. Kinetics and Mechanisms of the Oxidation of Oxygenated Organic Compounds in the Gas Phase. *Chemical Reviews.* 2003, **103**(12), pp.5077-5096.

190. Kwok, E.S.C. and Atkinson, R. Estimation of hydroxyl radical reaction rate constants for gas-phase organic compounds using a structure-reactivity relationship: An update. *Atmospheric Environment.* 1995, **29**(14), pp.1685-1695.

191. Robertson, S.H., Seakins, P.W. and Pilling, M.J. Low-Temperature Combustion and Auto-Ignition. In: Pilling, M.J. ed. *Comprehensive Chemical Kinetics.* Amsterdam: Elsevier, 1997.

192. Westbrook, C.K. Chemical Kinetics of Hydrocarbon Ignition in Practical Combustion Systems. *Proceedings of the Combustion Institute.* 2000, **28**(2), pp.1563-1577.

193. He, T.J., Wang, Z., You, X.Q., Liu, H.Y., Wang, Y.D., Li, X.Y. and He, X. A Chemical Kinetic Mechanism for the Low- and Intermediate-Temperature Combustion of Polyoxymethylene Dimethyl Ether 3 (PODE3). *Fuel.* 2018, **212**, pp.223-235.

194. Welz, O., Zador, J., Savee, J.D., Ng, M.Y., Meloni, G., Fernandes, R.X., Sheps, L., Simmons, B.A., Lee, T.S., Osborn, D.L. and Taatjes, C.A. Low-Temperature Combustion Chemistry of Biofuels: Pathways in the Initial Low-Temperature (550 K-750 K) Oxidation Chemistry of Isopentanol. *Physical Chemistry Chemical Physics.* 2012, **14**(9), pp.3112-3127.

195. Pilling, M.J. and Smith, M.J. A Laser Flash Photolysis Study of the Reaction $CH + O_2 \rightarrow CH_3O_2$ at 298 K. *The Journal of Physical Chemistry.* 1985, **89**(22), pp.4713-4720.

196. Slagle, I.R., Bencsura, Á., Xing, S.-B. and Gutman, D. Kinetics and Thermochemistry of the Oxidation of Unsaturated Radicals: $C_4H_5+O_2$. *Symposium (International) on Combustion.* 1992, **24**(1), pp.653-660.

197. Slagle, I.R., Park, J.-Y. and Gutman, D. Experimental Investigation of the Kinetics and Mechanism of the Reaction of n-Propyl Radicals with Molecular Oxygen from 297 to 635 K. *Symposium (International) on Combustion.* 1985, **20**(1), pp.733-741.

198. Wagner, A.F., Slagle, I.R., Sarzynski, D. and Gutman, D. Experimental and Theoretical Studies of the Ethyl + Oxygen Reaction Kinetics. *The Journal of Physical Chemistry.* 1990, **94**(5), pp.1853-1868.

199. Slagle, I.R., Bernhardt, J.R. and Gutman, D. Kinetics of the Reactions of SiH_3 with O_2 and N_2O. *Chemical Physics Letters.* 1988, **149**(2), pp.180-184.

200. Romero, M.T.B., Blitz, M.A., Heard, D.E., Pilling, M.J., Price, B. and Seakins, P.W. OH Formation from the $C_2H_5CO+O_2$ Reaction: An Experimental Marker for the Propionyl Radical. *Chemical Physics Letters.* 2005, **408**(4), pp.232-236.

201. Blitz, M.A., Heard, D.E. and Pilling, M.J. OH Formation from CH_3CO+O_2: A Convenient Experimental Marker for the Acetyl Radical. *Chemical Physics Letters.* 2002, **365**(5), pp.374-379.

202. Howes, N.U.M., Lockhart, J.P.A., Blitz, M.A., Carr, S.A., Baeza-Romero, M.T., Heard, D.E., Shannon, R.J., Seakins, P.W. and Varga, T. Observation of a New Channel, the Production of CH_3, in the Abstraction Reaction of OH Radicals with Acetaldehyde. *Physical Chemistry Chemical Physics.* 2016, **18**(38), pp.26423-26433.

203. Michael, J.V., Keil, D.G. and Klemm, R.B. Rate Constants for the Reaction of Hydroxyl Radicals with Acetaldehyde from 244–528 K. *The Journal of Chemical Physics.* 1985, **83**(4), pp.1630-1636.

204. Carr, S.A., Baeza-Romero, M.T., Blitz, M.A., Pilling, M.J., Heard, D.E. and Seakins, P.W. OH Yields from the CH_3CO+O_2 Reaction Using an Internal Standard. *Chemical Physics Letters.* 2007, **445**(4-6), pp.108-112.

205. Carr, S.A., Glowacki, D.R., Liang, C.-H., Baeza-Romero, M.T., Blitz, M.A., Pilling, M.J. and Seakins, P.W. Experimental and Modeling Studies of the Pressure and Temperature Dependences of the Kinetics and the OH Yields in the Acetyl + O_2 Reaction. *The Journal of Physical Chemistry A.* 2011, **115**(6), pp.1069-1085.

206. Romero, M.T.B., Glowacki, D.R., Blitz, M.A., Heard, D.E., Pilling, M.J., Rickard, A.R. and Seakins, P.W. A Combined Experimental and Theoretical Study of the Reaction Between Methylglyoxal and OH/OD radical: OH Regeneration. *Physical Chemistry Chemical Physics.* 2007, **9**(31), pp.4114-4128.

207. Lockhart, J., Blitz, M., Heard, D., Seakins, P. and Shannon, R. Kinetic Study of the OH + Glyoxal Reaction: Experimental Evidence and Quantification of Direct OH Recycling. *The Journal of Physical Chemistry A.* 2013, **117**(43), pp.11027-11037.

208. Hansen, J.C., Li, Y., Rosado-Reyes, C.M., Francisco, J.S., Szente, J.J. and Maricq, M.M. Theoretical and Experimental Investigation of the UV Cross Section and Kinetics of the Methyl Formate Peroxy Radical. *The Journal of Physical Chemistry A.* 2003, **107**(27), pp.5306-5316.

209. Eskola, A.J., Carr, S.A., Blitz, M.A., Pilling, M.J. and Seakins, P.W. Kinetics and Yields of OH Radical from the $CH_3OCH_2+O_2$ Reaction Using a New Photolytic Source. *Chemical Physics Letters.* 2010, **487**(1), pp.45-50.

210. Sehested, J., Møgelberg, T., Wallington, T.J., Kaiser, E.W. and Nielsen, O.J. Dimethyl Ether Oxidation: Kinetics and Mechanism of the $CH_3OCH_2 + O_2$ Reaction at 296 K and 0.38−940 Torr Total Pressure. *The Journal of Physical Chemistry.* 1996, **100**(43), pp.17218-17225.

211. Maricq, M.M., Szente, J.J. and Hybl, J.D. Kinetic Studies of the Oxidation of Dimethyl Ether and Its Chain Reaction with Cl_2. *The Journal of Physical Chemistry A.* 1997, **101**(28), pp.5155-5167.

212. Masaki, A., Tsunashima, S. and Washida, N. Rate Constants for Reactions of Substituted Methyl Radicals (CH_2OCH_3, CH_2NH_2, CH_2I, and CH_2CN) with O_2. *The Journal of Physical Chemistry.* 1995, **99**(35), pp.13126-13131.

213. Rosado-Reyes, C.M., Francisco, J.S., Szente, J.J., Maricq, M.M. and Frøsig Østergaard, L. Dimethyl Ether Oxidation at Elevated Temperatures (295−600 K). *The Journal of Physical Chemistry A.* 2005, **109**(48), pp.10940-10953.

214. Hong, Z., Farooq, A., Barbour, E.A., Davidson, D.F. and Hanson, R.K. Hydrogen Peroxide Decomposition Rate: A Shock Tube Study Using Tunable Laser Absorption of H_2O near 2.5 μm. *The Journal of Physical Chemistry A.* 2009, **113**(46), pp.12919-12925.

215. Ludwig, W., Brandt, B., Friedrichs, G. and Temps, F. Kinetics of the reaction $C_2H_5 + HO_2$ by time-resolved mass spectrometry. *The Journal of Physical Chemistry A.* 2006, **110**(9), pp.3330-3337.

216. *Kintecus.* www.kintecus.com, 2017.

217. Archibald, A.T., Petit, A.S., Percival, C.J., Harvey, J.N. and Shallcross, D.E. On the importance of the reaction between OH and RO_2 radicals. *Atmospheric Science Letters.* 2009, **10**(2), pp.102-108.

218. Griller, D. and Lossing, F.P. Thermochemistry of α-Aminoalkyl Radicals. *Journal of the American Chemical Society.* 1981, **103**(6), pp.1586-1587.

219. Lossing, F.P. Heats of Formation of Some Isomeric $[C_nH_{2n+1}O]+$ ions. Substitutional Effects on Ion Stability. *Journal of the American Chemical Society.* 1977, **99**(23), pp.7526-7530.

220. Ogura, T., Miyoshi, A. and Koshi, M. Rate Coefficients of H-Atom Abstraction from Ethers and Isomerization of Alkoxyalkylperoxy Radicals. *Physical Chemistry Chemical Physics.* 2007, **9**(37), pp.5133-5142.

221. Hu, E.J., Ku, J.F., Yin, G.Y., Li, C.C., Lu, X. and Huang, Z.H. Laminar Flame Characteristics and Kinetic Modeling Study of Ethyl Tertiary Butyl Ether Compared with Methyl Tertiary Butyl Ether, Ethanol, iso-Octane, and Gasoline. *Energy & Fuels.* 2018, **32**(3), pp.3935-3949.

222. Zhang, X., Oyedun, A., Kumar, A., Oestreich, D., Arnold, U. and Sauer, J. An Optimized Process Design for Oxymethylene Ether Production from Woody-Biomass-Derived Syngas. *Biomass and Bioenergy.* 2016, **90**, pp.7-14.

223. Tsolakis, A., Megaritis, A. and Yap, D. Application of Exhaust Gas Fuel Reforming in Diesel and Homogeneous Charge Compression Ignition (HCCI) Engines Fuelled with Biofuels. *Energy.* 2008, **33**(3), pp.462-470.

224. Aschmann, S.M. and Atkinson, R. Products of the gas-phase reactions of the OH radical with n-butyl methyl ether and 2-isopropoxyethanol: Reactions of ROC($\dot{O}$) < radicals. 1999, **31**(7), pp.501-513.

225. Sakai, Y., Ando, H., Chakravarty, H.K., Pitsch, H. and Fernandes, R. A computational study on the kinetics of unimolecular reactions of ethoxyethylperoxy radicals employing CTST and VTST. In: *Proceedings of the Combustion Institute, San Francisco*. 2015, pp.161-169.

226. Sandhiya, L., Ponnusamy, S. and Senthilkumar, K. Atmospheric oxidation mechanism of OH-initiated reactions of diethyl ether – the fate of the 1-ethoxy ethoxy radical. *RSC Advances.* 2016, **6**(84), pp.81354-81363.

227. Wang, S. and Wang, L. The atmospheric oxidation of dimethyl, diethyl, and diisopropyl ethers. The role of the intramolecular hydrogen shift in peroxy radicals. *Physical Chemistry Chemical Physics.* 2016, **18**(11), pp.7707-7714.

228. Hu, E., Chen, Y., Zhang, Z., Chen, J.-Y. and Huang, Z. Ab initio calculation and kinetic modeling study of diethyl ether ignition with application toward a skeletal mechanism for CI engine modeling. *Fuel.* 2017, **209**, pp.509-520.

229. Lockhart, J. *The Role of Chemical Activation in the Formation and Loss of Atmospheric Carbonyl Species*. PhD thesis, University of Leeds, 2014.

230. Lockhart, J., Blitz, M.A., Heard, D.E., Seakins, P.W. and Shannon, R.J. Mechanism of the Reaction of OH with Alkynes in the Presence of Oxygen. *The Journal of Physical Chemistry A.* 2013, **117**(26), pp.5407-5418.

231. Atkinson, R., Baulch, D.L., Cox, R.A., Crowley, J.N., Hampson, R.F., Hynes, R.G., Jenkin, M.E., Rossi, M.J. and Troe, J. IUPAC Task Group on Atmospheric Chemical Kinetic Data Evaluation *Atmospheric Chemistry and Physics.* 2006, **6**, p.3625.

232. Delbos, E., Fittschen, C., Hippler, H., Krasteva, N., Olzmann, M. and Viskolcz, B. Rate Coefficients and Equilibrium Constant for the $CH_2CHO + O_2$ Reaction System. *The Journal of Physical Chemistry A.* 2006, **110**(9), pp.3238-3245.

233. Wu, D. and Bayes, K.D. Rate constants for the reactions of isobutyl, neopentyl, cyclopentyl, and cyclohexyl radicals with molecular oxygen. *International Journal of Chemical Kinetics.* 1986, **18**(5), pp.547-554.

234. Slagle, I.R., Bernhardt, J.R. and Gutman, D. Kinetics of the reactions of unsaturated free radicals (methylvinyl and i-C_4H_3) with molecular oxygen. *Symposium (International) on Combustion.* 1989, **22**(1), pp.953-962.

235. Laufer, A.H. and Fahr, A. Reactions and Kinetics of Unsaturated C_2 Hydrocarbon Radicals. *Chemical Reviews.* 2004, **104**(6), pp.2813-2832.

236. Yasunaga, K., Gillespie, F., Simmie, J.M., Curran, H.J., Kuraguchi, Y., Hoshikawa, H., Yamane, M. and Hidaka, Y. A Multiple Shock Tube and

Chemical Kinetic Modeling Study of Diethyl Ether Pyrolysis and Oxidation. *The Journal of Physical Chemistry A.* 2010, **114**(34), pp.9098-9109.

237. Tran, L.-S., Pieper, J., Carstensen, H.-H., Zhao, H., Graf, I., Ju, Y., Qi, F. and Kohse-Höinghaus, K. Experimental and kinetic modeling study of diethyl ether flames. *Proceedings of the Combustion Institute.* 2017, **36**(1), pp.1165-1173.

238. Serinyel, Z., Lailliau, M., Thion, S., Dayma, G. and Dagaut, P. An experimental chemical kinetic study of the oxidation of diethyl ether in a jet-stirred reactor and comprehensive modeling. *Combustion and Flame.* 2018, **193**, pp.453-462.

239. Goldsmith, C.F., Green, W.H. and Klippenstein, S.J. Role of $O_2 + QOOH$ in Low-Temperature Ignition of Propane. 1. Temperature and Pressure Dependent Rate Coefficients. *The Journal of Physical Chemistry A.* 2012, **116**(13), pp.3325-3346.

240. *Gaussian 09.* Wallingford, CT, 2016.

241. Papajak, E., Zheng, J., Xu, X., Leverentz, H.R. and Truhlar, D.G. Perspectives on Basis Sets Beautiful: Seasonal Plantings of Diffuse Basis Functions. *Journal of Chemical Theory and Computation.* 2011, **7**(10), pp.3027-3034.

242. Glowacki, D.R., Liang, C.H., Morley, C., Pilling, M.J. and Robertson, S.H. MESMER: An Open-Source Master Equation Solver for Multi-Energy Well Reactions. *The Journal of Physical Chemistry A.* 2012, **116**(38), pp.9545-9560.

243. Blitz, M.A., Green, N.J.B., Shannon, R.J., Pilling, M.J., Seakins, P.W., Western, C.M. and Robertson, S.H. Reanalysis of Rate Data for the Reaction $CH_3 + CH_3 \rightarrow C_2H_6$ Using Revised Cross Sections and a Linearized Second-Order Master Equation. *The Journal of Physical Chemistry A.* 2015, **119**(28), pp.7668-7682.

244. Bartis, J.T. and Widom, B.J. Stochastic models of the interconversion of three or more chemical species. *The Journal of Chemical Physics.* 1974, **60**(9), pp.3474-3482.

245. Garrett, B.C. and Truhlar, D.G. Semiclassical tunneling calculations. *The Journal of Physical Chemistry.* 1979, **83**(22), pp.2921-2926.

246. Robertson, S.H., Glowacki, D.R., Liang, C.-H., Morley, C., Shannon, R., Blitz, M., Seakins, P.W. and Pilling, M.J. MESMER (Master Equation Solver for Multi-Energy Well Reactions), 2008-2013, an object oriented C++ program implementing master equation methods for gas phase reactions with arbitrary multiple wells. http://sourceforge.net/projects/mesmer.

247. Andersen, A. and Carter, E.A. A hybrid density functional theory study of the low-temperature dimethyl ether combustion pathways. I: Chain-propagation. *Israel Journal of Chemistry.* 2002, **42**(2-3), pp.245-260.

248. Andersen, A. and Carter, E.A. Hybrid Density Functional Theory Predictions of Low-Temperature Dimethyl Ether Combustion Pathways. II. Chain-Branching Energetics and Possible Role of the Criegee Intermediate. *The Journal of Physical Chemistry A.* 2003, **107**(44), pp.9463-9478.

249. Andersen, A. and Carter, E.A. First-principles-derived kinetics of the reactions involved in low-temperature dimethyl ether oxidation. *Molecular Physics.* 2008, **106**(2-4), pp.367-396.

250. Jenkin, M.E., Hayman, G.D., Wallington, T.J., Hurley, M.D., Ball, J.C., Nielsen, O.J. and Ellermann, T. Kinetic and Mechanistic Study of the Self-Reaction of Methoxymethylperoxy Radicals at Room Temperature. *The Journal of Physical Chemistry.* 1993, **97**(45), pp.11712-11723.

251. Xing, L.-l., Zhang, X.-y., Wang, Z.-d., Li, S. and Zhang, L.-d. New Insight into Competition between Decomposition Pathways of Hydroperoxymethyl Formate in Low Temperature DME Oxidation. *Chinese Journal of Chemical Physics.* 2015, **28**(5), pp.563-572.

252. Di Tommaso, S., Rotureau, P. and Adamo, C. Oxidation Mechanism of Aliphatic Ethers: Theoretical Insights on the Main Reaction Channels. *The Journal of Physical Chemistry A.* 2012, **116**(36), pp.9010-9019.

253. Di Tommaso, S., Rotureau, P., Benaissa, W., Gruez, P. and Adamo, C. Theoretical and Experimental Study on the Inhibition of Diethyl Ether Oxidation. *Energy & Fuels.* 2014, **28**(4), pp.2821-2829.

254. Di Tommaso, S., Rotureau, P., Sirjean, B., Fournet, R., Benaissa, W., Gruez, P. and Adamo, C. A mechanistic and experimental study on the diethyl ether oxidation. *Process Safety Progress.* 2014, **33**(1), pp.64-69.

255. Sakai, Y., Herzler, J., Werler, M., Schulz, C. and Fikri, M. A quantum chemical and kinetics modeling study on the autoignition mechanism of diethyl ether. *Proceedings of the Combustion Institute.* 2017, **36**(1), pp.195-202.

256. Pilling, M.J. and Smith, I.W. *Modern Gas Kinetics.* Blackwell Scientific Publications, 1987.

257. Morley, C. Photolytic perturbation method to investigate the kinetics of hydrocarbon oxidation near 800 K. *Symposium (International) on Combustion.* 1989, **22**(1), pp.911-918.

258. Stone, D., Blitz, M., Ingham, T., Onel, L., Medeiros, D.J. and Seakins, P.W. An instrument to measure fast gas phase radical kinetics at high temperatures and pressures. *Review of Scientific Instruments.* 2016, **87**(5), p.054102.

259. Speak, T.H., Blitz, M.A., Stone, D. and Seakins, P.W. A New Instrument of Time Resolved Measurement of HO$_2$ Radicals (in press), doi.org/10.5194/amt-2019-164. *Atmospheric Measurement Techniques.* 2019.

260. Feng, R., Cooper, G. and Brion, C.E. UV, VUV and soft X-ray photoabsorption of dimethyl ether by dipole (e,e) spectroscopies. *Chemical Physics.* 2000, **260**(3), pp.391-400.

261. Feng, R. and Brion, C.E. Quantitative photoabsorption of diethyl ether in the valence and carbon 1s inner shell regions (5–360 eV). *Chemical Physics.* 2002, **284**(3), pp.615-623.

262. Sime, S.L. *Kinetic studies of bio-butanol oxidation under low temperature combustion conditions*. PhD thesis, 2019.

263. Dillon, T.J., Horowitz, A. and Crowley, J.N. The atmospheric chemistry of sulphuryl fluoride, SO$_2$F$_2$. *Atmospheric Chemistry and Physics.* 2008, **8**(6), pp.1547-1557.

264. Dunlea, E.J. and Ravishankara, A.R. Kinetic studies of the reactions of O(^{1}D) with several atmospheric molecules. *Physical Chemistry Chemical Physics.* 2004, **6**(9), pp.2152-2161.

265. Buchta, C., Frerichs, H., Stucken, D., Tappe, M. and Wagner, H.G. Investigation of the Reactions of Diethylether, n-Dipropylether and n-Dibutylether with O(^{3}P) in the Gas Phase. *Zeitschrift für Physikalische Chemie.* 1991, **174**(2), p.129.

266. Liu, R., Dagaut, P., Huie, R.E. and Kurylo, M.J. A Flash Photolysis Resonance Fluorescence Investigation of the Reactions of Oxygen O(^{3}P) Atoms with Aliphatic Ethers and Diethers in the Gas Phase. *International Journal of Chemical Kinetics.* 1990, **22**(7), pp.711-717.

267. Brocard, J.C., Baronnet, F. and O'Neal, H.E. Chemical Kinetics of the Oxidation of Methyl tert-Butyl Ether (MTBE). *Combustion and Flame.* 1983, **52**, pp.25-35.

268. Ciajolo, A. Low-Temperature Oxidation of MTBE in a High-Pressure Jet-Stirred Flow Reactor. *Combustion Science and Technology.* 1997, **123**(1-6), pp.49-61.

269. Glaude, P.A., Battin-Leclerc, F., Judenherc, B., Warth, V., Fournet, R., Côme, G.M., Scacchi, G., Dagaut, P. and Cathonnet, M. Experimental and modeling study of the gas-phase oxidation of methyl and ethyl tertiary butyl ethers. *Combustion and Flame.* 2000, **121**(1), pp.345-355.

270. Carr, S.A., Blitz, M.A. and Seakins, P.W. Site-Specific Rate Coefficients for Reaction of OH with Ethanol from 298 to 900 K. *The Journal of Physical Chemistry A.* 2011, **115**(15), pp.3335-3345.

271. Dyer, M.J., Pfefferle, L.D. and Crosley, D.R. Laser-induced fluorescence measurement of oxygen atoms above a catalytic combustor surface. *Applied Optics*. 1990, **29**(1), pp.111-118.

Appendices

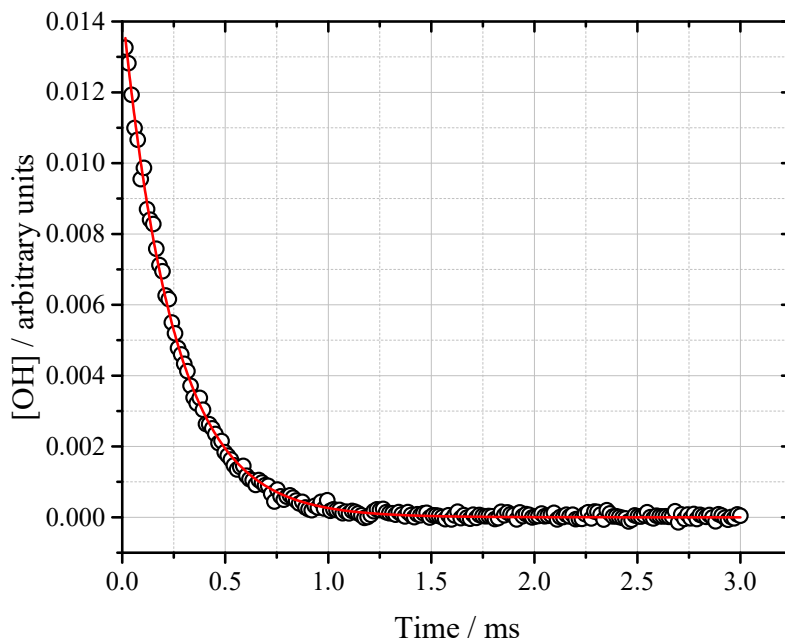**Appendix A: Example decays and bimolecular plots for OH + ether reactions**

Figure A 1: An example single exponential decay, measured at room temperature, 68 Torr N$_2$, [TMOF] = 7.3 × 10^{14} molecule cm^{-3}. Exponential fit yielded k' = (4000 ± 40) s^{-1}, where the uncertainty on is statistical at the 2σ level.
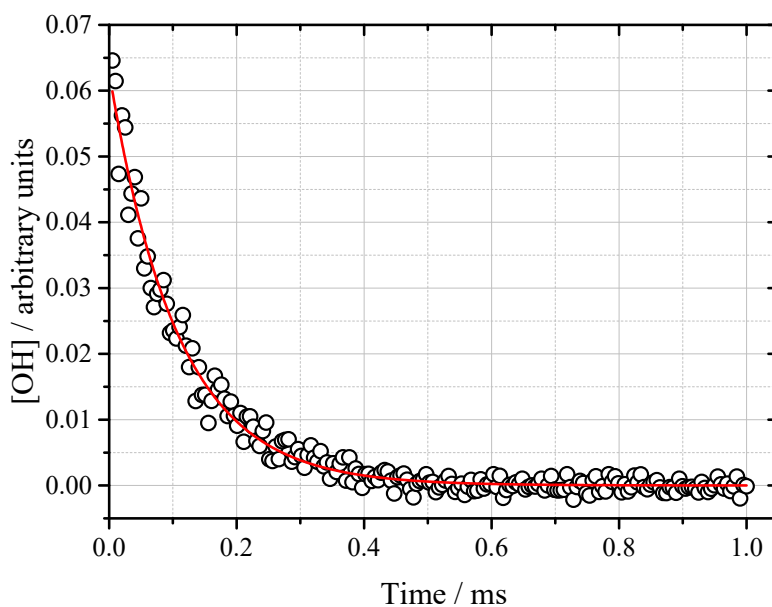
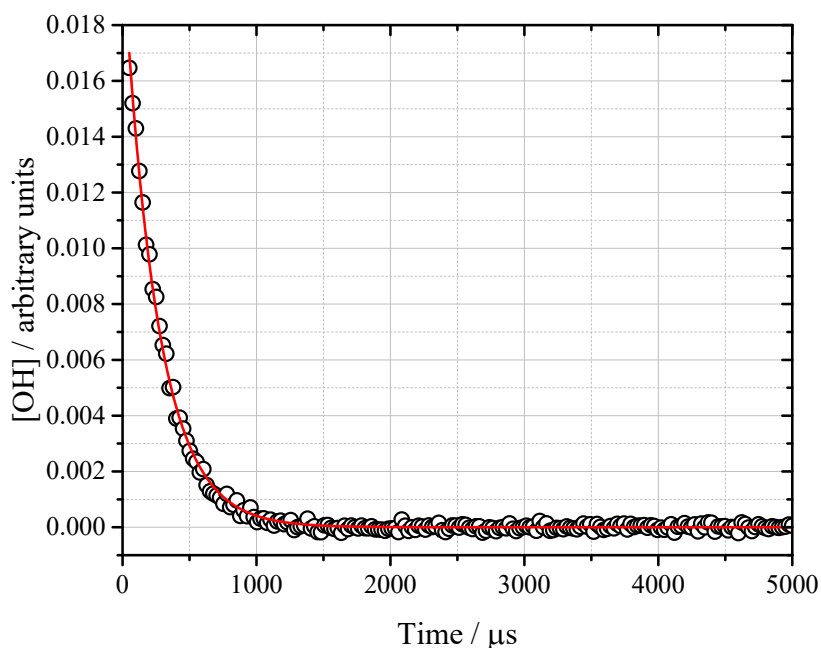**Figure A 2: Example single exponential decay for OH + DEE, [DEE] = 7.7 × 10^{14} molecule cm^{-3}. The exponential fit yielded k' = (9320 ± 340) s^{-1}. Uncertainty on returned parameter is 2σ and purely statistical. Experimental conditions were 298 K and 47 Torr N$_2$.**
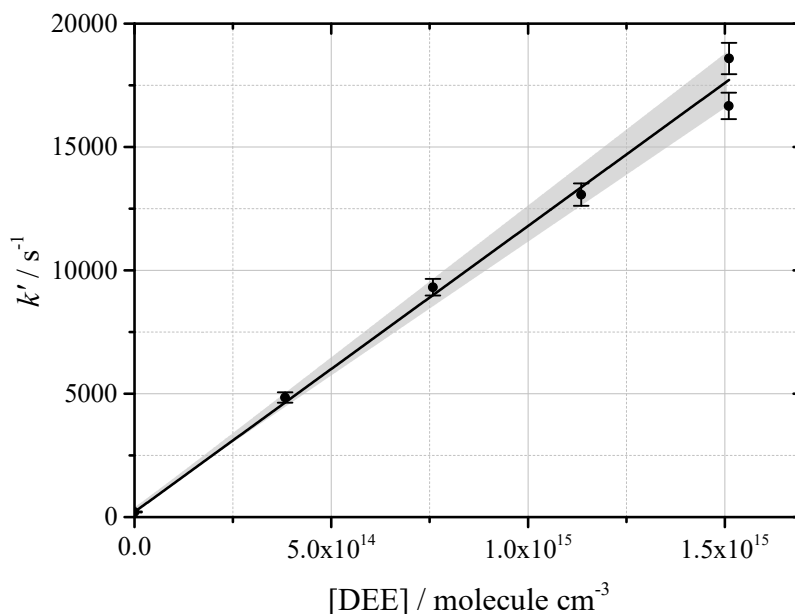
Figure A 3: Example bimolecular plot for OH + DEE at 298 K and 47 Torr N₂, k_{OH+DEE} = (1.14 ± 0.11) × 10⁻¹¹ cm³ molecule⁻¹ s⁻¹. Grey shaded area represents the bounds of the 95% confidence limits. Uncertainties on the rate coefficient are statistical at the 2σ level.
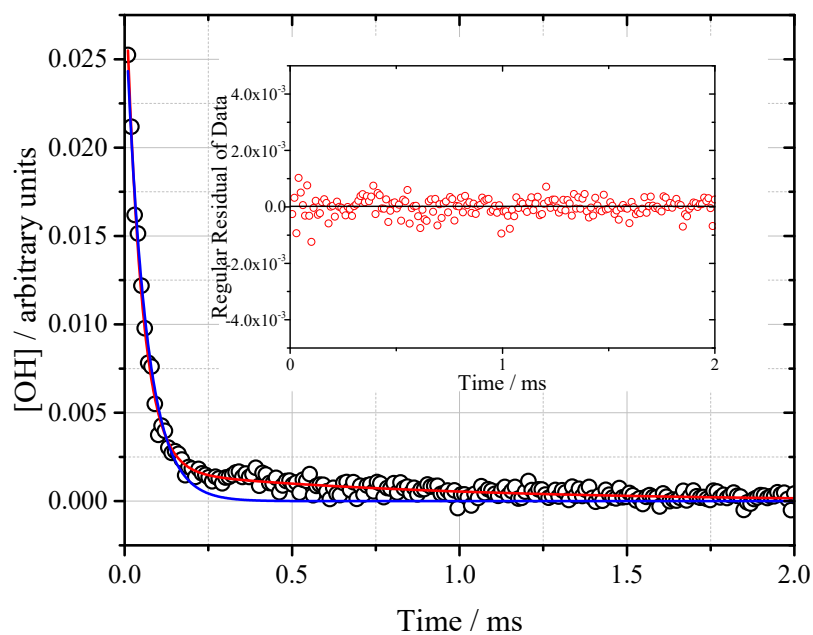
Figure A 4: Biexponential decay obtained with DEE using the *t*-BuOOH precursor. Experimental conditions were [DEE] = 1.6 × 10¹⁵ molecule cm⁻³, 415 K, and 30 Torr N₂. Parameters returned were k_a' = (19200 ± 780) s⁻¹, k_b = (1170 ± 160) s⁻¹, k_c = (1200 ± 210) s⁻¹, and k_d was fixed at 1150 s⁻¹. Single exponential fit returned k' = (16780 ± 1060) s⁻¹. Uncertainties are statistical at the 2σ level.

Figure A 5: Example single exponential decay for OH + DBE, [DBE] = 9.3 × 10¹³ molecule cm⁻³. The exponential fit yielded $k' = (3910 \pm 50)$ s⁻¹. Uncertainty on returned parameter is 2σ and purely statistical. Experimental conditions were 298 K and 29 Torr N₂.
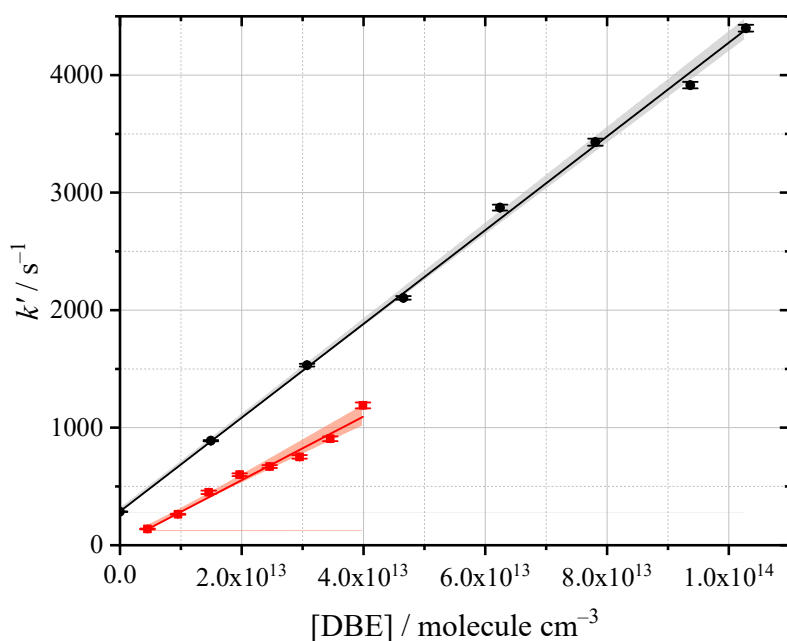

Figure A 6: Bimolecular plots for the OH + DBE reaction. Experimental conditions were 298 K and 29 Torr N₂ (black), and 572 K and 28 Torr N₂ (red). The rate coefficients were $k_{OH+DBE} = (3.99 \pm 0.09) \times 10^{-11}$ cm³ molecule⁻¹ s⁻¹ and $(2.70 \pm 0.27) \times 10^{-11}$ cm³ molecule⁻¹ s⁻¹ respectively. Note the high temperature measurement was biexponential, so no intercept is included in the plot. Uncertainties are statistical at the 2σ level. The intercepts are (290 ± 10) s⁻¹ (black), and (10 ± 30) s⁻¹ (red).
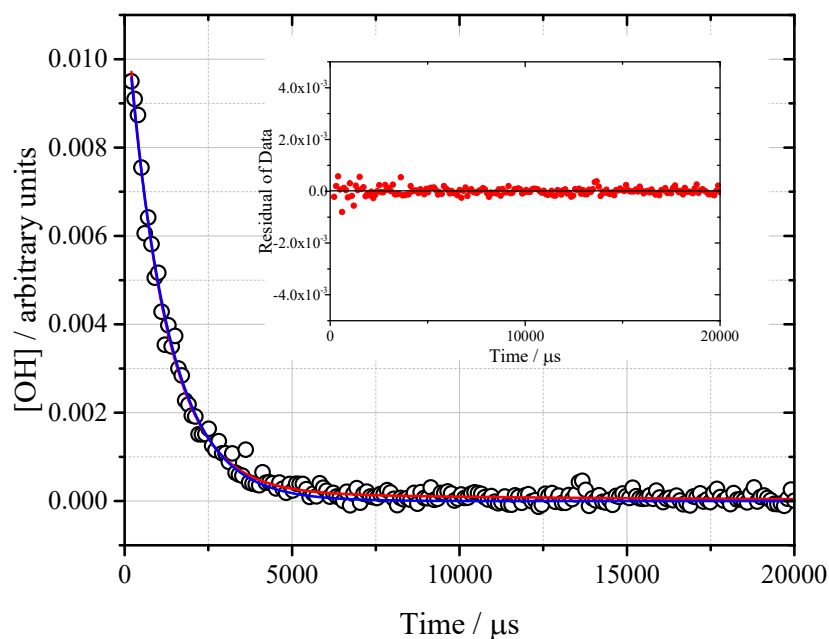
Figure A 7: Example biexponential decay for OH + DBE, at 572 K and 28 Torr N$_2$. Returned parameters were $k_a' = (750 \pm 30)$ s^{-1}, $k_b = (20 \pm 10)$ s^{-1}, $k_c = (80 \pm 70)$ s^{-1}, k_d was fixed at 120 s^{-1}. Single exponential $k' = (830 \pm 30)$. [DBE] = 3.0 × 10^{13} molecule cm^{-3}. Inset shows regular residuals of data.
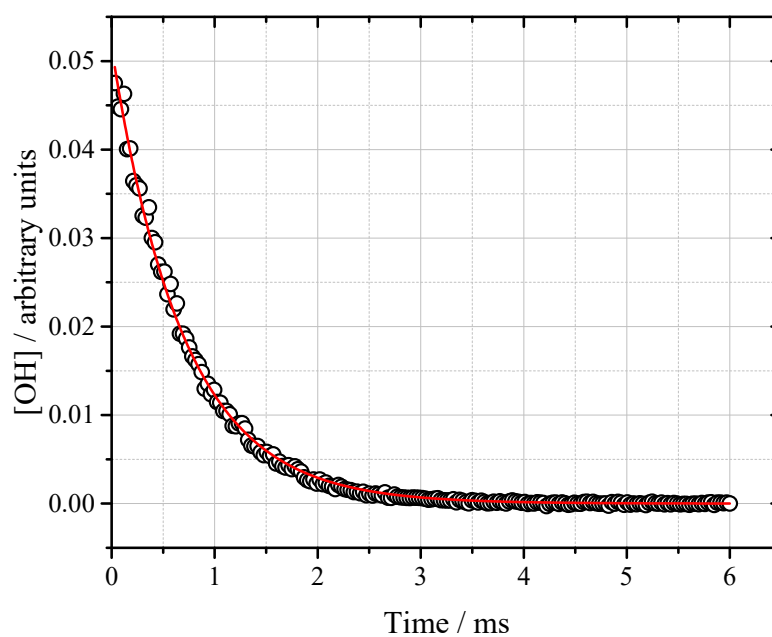

Figure A 8: An example single exponential decay for the OH + MTBE reaction, where [MTBE] = 4.7 × 10^{14} molecule cm^{-3}. An exponential fit yielded $k' = (1470 \pm 20)$ s^{-1}. Experimental conditions were 298 K and 29 Torr N$_2$.
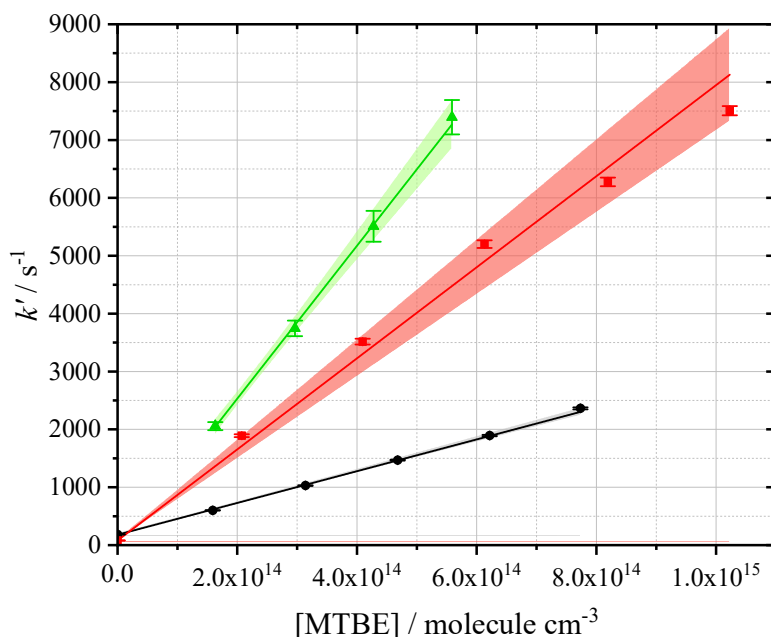
Figure A 9: Example bimolecular plots for OH + MTBE. Error bars are statistical at the 1σ level. Experimental conditions were 298K and 29 Torr N_2 (black); 495 K and 63 Torr N_2 (red); and 727 K and 46 Torr N_2 (green). $k_{OH+MTBE}$ = (2.81 ± 0.18) × 10^{-12} cm^3 molecule^{-1} s^{-1}, (7.27 ± 0.95) × 10^{-12} cm^3 molecule^{-1} s^{-1}, and (1.32 ± 0.12) × 10^{-11} cm^3 molecule^{-1} s^{-1} respectively. Shaded areas represent the 95% confidence limits. Note there is no intercept on the highest temperature, which was biexponential. Uncertainties on returned parameters are statistical at the 2σ level. Intercepts are (180 ± 10) s^{-1} (black), (80 ± 20) s^{-1} (red), and (−110 ± 130) s^{-1} (green).
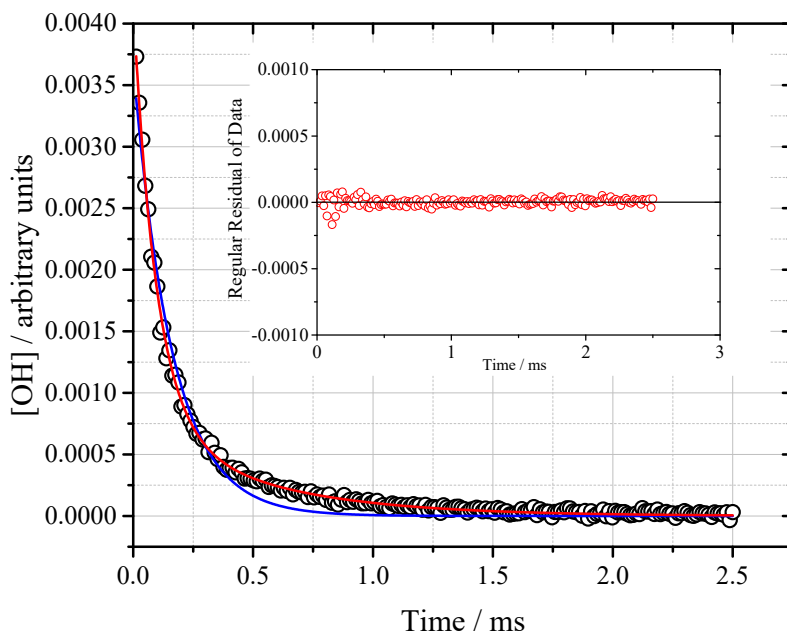

Figure A 10: Example OH + MTBE biexponential decay with a good fit to the biexponential equation (red line), and a poor fit to the single exponential equation (blue line), measured at 680 K, 45 Torr N_2. The inset shows the residuals for the biexponential fit. Parameters from the biexponential fit: k_a' = (8710 ± 250) s^{-1}, k_b = (1270 ± 140) s^{-1}, k_c = (2330 ± 200) s^{-1}, and k_d was fixed at 200 s^{-1}. [MTBE] = 6.09 ± 10^{14} cm^3 molecule^{-1} s^{-1}. Uncertainties are statistical at the 2σ level. The OH precursor used was H_2O_2.

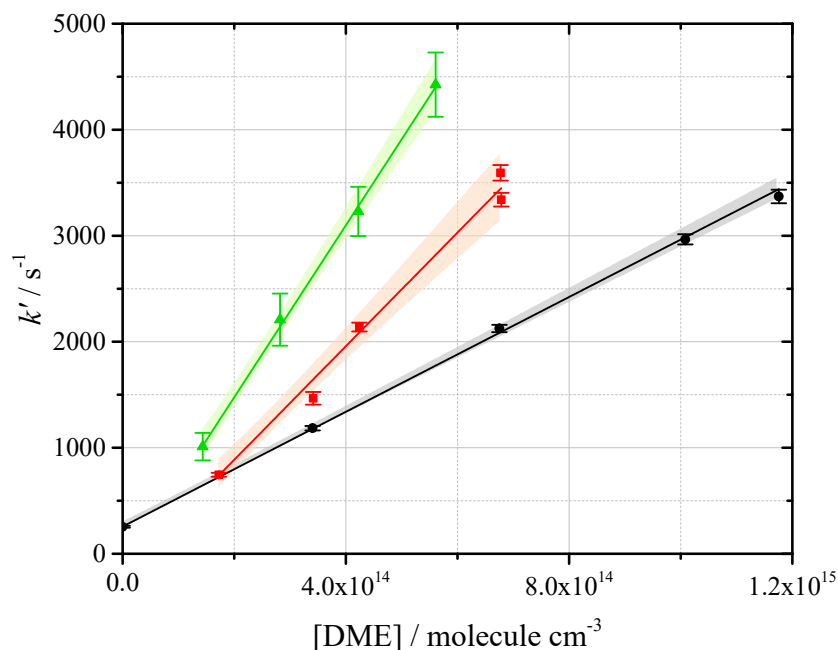**Figure A 11: Example OH + DME bimolecular plots at 298 K and 59 Torr N₂ (black),** k_{OH+DME} **= (2.71 ± 0.09) × 10⁻¹² cm³ molecule⁻¹ s⁻¹. At 543 K and 57 Torr N₂ (red),** k_{OH+DME} **= (5.36 ± 0.72) × 10⁻¹² cm³ molecule⁻¹ s⁻¹. At 634 K and 57 Torr N₂ (green),** k_{OH+DME} **= (8.11 ± 0.72) × 10⁻¹² cm³ molecule⁻¹ s⁻¹. The highest two temperatures are biexponential, hence no DME-free data are included. Returned parameter uncertainties are statistical at the 2σ level. Shaded areas represent the bounds of the 95% confidence limits. Intercepts are (260 ± 20) s⁻¹ (black), (–260 ± 330) s⁻¹ (red), and (–130 ± 150) s⁻¹ (green).**
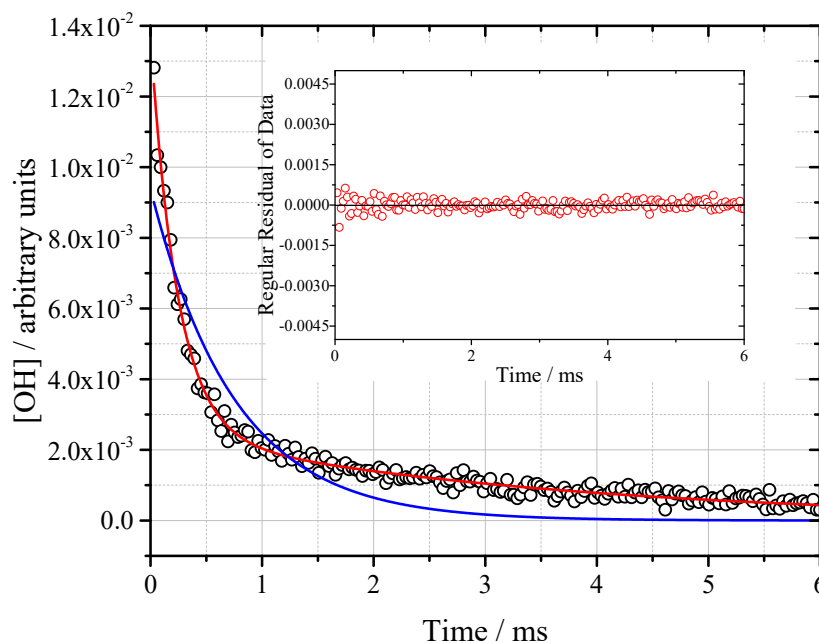
Figure A 12: Example OH + DME biexponential decay at 590 K and 57 Torr N₂, [DME] = 4.94 × 10¹⁴ cm³ molecule⁻¹ s⁻¹. Parameters returned are $k_a{}'$ **= (3320 ± 160) s⁻¹,** k_b **= (670 ± 60) s⁻¹,** k_c **= (320 ± 30) s⁻¹,** k_d **fixed at 140 s⁻¹. Single exponential fit yielded** k' **= (1340 ± 130) s⁻¹. Uncertainties on parameters are statistical at the 2σ level.**

Appendix B: OriginPro fitting equation for the interpretation of R + O₂ chemical activation data

```
// Fit Parameter(s):
double OH, double kd, double ka, double kro2, double yield, double b, double kx,
double ether, double O2, double O2x,
// Independent Variable(s):
double x,
// Dependent Variable(s):
double& y)
{
        // Beginning of editable part
        double S,M1,M2,L1,L2,kapseud,kbpseud,kcpseud;

        kapseud=ka*ether;
        kbpseud=(yield*kro2)*(O2+O2x);
        kcpseud=((kro2-(yield*kro2))*(O2+O2x))+kx;

        S=-(kd+kapseud);
        M1=kd+kapseud+kbpseud+kcpseud;
        M2=(kd+kapseud)*(kbpseud+kcpseud)-kapseud*kbpseud;
        L1=(-M1+sqrt(M1^2-4*M2))/2;
        L2=(-M1-sqrt(M1^2-4*M2))/2;

        y=OH*(((S-L2)/(L1-L2))*(exp(L1*x/1e3)-exp(L2*x/1e3))+exp(L2*x/1e3))+b
        // End of editable part
}
```

Appendix C: *Ab initio* calculation details for the DEE system

Species	Energy / kcal mol^{-1}	Rotational constants / cm^{-1}	Vibrational frequencies / cm^{-1}
R	0.0	0.688 0.076 0.071	91.03 114.50 180.40 196.90 259.67 432.36 454.96 575.68 816.63 879.24 973.29 1025.56 1109.95 1129.10 1186.80 1191.54 1280.77 1313.35 1379.91 1403.53 1422.87 1464.13 1469.56 1491.96 1499.46 1505.66 1530.26 3009.34 3031.15 3066.68 3069.79 3078.13 3129.30 3142.63 3146.79 3148.91
O$_2$	0.0	1.489	1762.06
RO$_2$	−34.8	0.129 0.061 0.044	77.11 101.94 118.93 188.03 193.47 243.11 310.29 382.79 433.19 563.41 570.95 824.74 833.72 881.79 979.04 1079.78 1111.26 1146.90 1183.23 1194.46 1231.37 1293.17 1314.36 1366.88 1384.22 1408.08 1423.65 1459.79 1484.11 1486.63 1493.56 1506.09 1531.16 3042.18 3062.61 3072.87 3089.57 3090.29 3139.66 3144.64 3157.93 3161.26
TS1	−15.1	0.135 0.068 0.049	127.35 178.60 209.43 215.17 291.86 321.89 420.27 471.26 502.73 571.83 632.92 859.33 881.31 899.16 976.24 1078.52 1110.04 1141.30 1155.15 1172.80 1196.78 1227.88 1288.32 1358.06 1380.62 1397.99 1421.43 1449.57 1484.36 1489.67 1492.16 1495.41 1655.50 3053.24 3068.29 3076.66 3080.67 3124.67 3155.29 3161.52 3164.93
QOOH	−25.6	0.125 0.063 0.044	83.23 109.24 159.46 190.76 202.42 214.20 297.27 376.65 408.25 436.90 560.88 610.65 648.14 877.61 905.07 992.01 1030.07 1054.72 1130.90 1136.76 1176.19 1202.95 1261.29 1372.97 1373.59 1402.60 1424.04 1434.09 1456.71 1471.12 1487.46 1492.65 1497.07 3005.90 3074.03 3086.67 3087.36 3140.85 3157.04 3165.09 3169.39 3754.22
TS2	−3.7	0.110 0.064 0.043	11.36 104.20 120.84 171.69 198.11 215.81 220.01 284.69 347.50 435.80 530.98 585.01 702.48 765.03 882.74 961.99 1003.60 1017.21 1044.48 1137.89 1173.59 1197.76 1318.12 1367.68 1393.90 1403.40 1414.29 1463.60 1473.11 1489.41 1490.35 1559.80 3000.59 3017.84 3069.75 3104.54 3149.84 3157.53 3166.32 3195.79 3864.15
OH	−53.9	18.804	3750.73
TS6	23.7	0.440 0.074 0.071	50.45 89.39 97.90 165.46 189.98 314.34 499.43 679.20 697.82 836.27 879.65 913.85 1022.95 1044.34 1099.77 1124.27 1225.20 1335.35 1389.05 1402.84 1459.33 1472.44 1484.45 1486.23 1494.15 1517.28 3010.94 3035.25 3049.14 3095.84 3102.41 3137.84 3145.94 3149.23 3244.63

Appendix D: Derivation of O(^{3}P) mechanism analytical equation
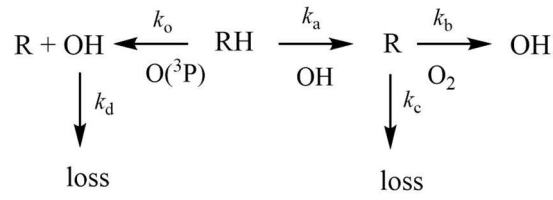
Scheme A 1: Proposed reaction scheme for growth behaviour, used for fit derivation.

$$\frac{d[OH]}{dt} = k_o[O] + k_b[R] - (k_a+k_d)[OH]$$

$$\frac{d[R]}{dt} = k_o[O] + k_a[OH] - (k_b+k_c)[R]$$

$A = -(k_a+k_d)$	$B = -(k_b+k_c)$	$C = k_o$ $D = k_b$ $E = k_a$	

$$\frac{d[OH]}{dt} = C[O] + D[R] + A[OH] \qquad \text{eqn. 1}$$

$$\frac{d[R]}{dt} = C[O] + E[OH] + B[R]$$

Multiply by opposite term in front of [R], to cancel out R term. (i.e. B and D)

$$B\frac{d[OH]}{dt} = BC[O] + BD[R] + BA[R]$$

$$D\frac{d[R]}{dt} = DC[O] + DE[OH] + DB[R]$$

$$B\frac{d[OH]}{dt} - D\frac{d[R]}{dt} = BC[O] + BA[OH] - DC[O] - DE[OH]$$

$$B\frac{d[OH]}{dt} = (BC - DC)[O] + (BA - DE)[OH] + D\frac{d[R]}{dt} \qquad \text{eqn. 2}$$

Second derivative of first OH rate eqn. 1:

$$\frac{d^2[OH]}{dt} = \frac{Cd[O]}{dt} + \frac{Dd[R]}{dt} + \frac{Ad[OH]}{dt} \qquad \text{eqn. 3}$$

Rearrange eqn. 2 for $D\frac{d[R]}{dt}$ and substitute into eqn. 3:

$$\frac{d^2[OH]}{dt} = \frac{Cd[O]}{dt} + \frac{Bd[OH]}{dt} + \frac{Ad[OH]}{dt} - (BC - DC)[O] - (BA - DE)[OH]$$

$$\frac{d^2[OH]}{dt} = \frac{Cd[O]}{dt} + \frac{(B+A)d[OH]}{dt} - (BC - DC)[O] - (BA - DE)[OH]$$

$$\frac{d^2[OH]}{dt} - \frac{(B+A)d[OH]}{dt} + (BA - DE)[OH] = \frac{Cd[O]}{dt} - (BC - DC)[O]$$

$F = -(B+A)$	$G = (BA - DE)$	$J = -(BC - DC)$

$$\frac{d^2[OH]}{dt} + F\frac{d[OH]}{dt} + G[OH] = \frac{Cd[O]}{dt} + J[O]$$

$[O] = [O]_0\, e^{-ko\times t}$, where k_o is the total of O + fuel and O + O_2

$$\frac{d[O]}{dt} = [O]_0 \times -k_o \times e^{-ko\times t}$$

$$\frac{d^2[OH]}{dt} + F\frac{d[OH]}{dt} + G[OH] = C[O]_0 \times -k_o e^{-ko \times t} + J[O]_0 e^{-ko \times t}$$

$$N = C[O]_0 \times -k_o \qquad O = J[O]_0$$

$$\frac{d^2[OH]}{dt} + F\frac{d[OH]}{dt} + G[OH] = Ne^{-ko \times t} + O_0 e^{-ko \times t}$$

$$H = N+O$$

$$= (N+O)e^{-ko \times t} = He^{-ko \times t}$$

$$y''(x) + fy'(x) + jy = He^{-ko \times t} \text{ solved:}$$

$$y(x) = [OH]_t = c_1 e^{t \times r1} + c_2 e^{t \times r2} + Pe^{-ko \times t} \qquad \text{eqn. 4}$$

$$r_1 = \frac{-F - \sqrt{F^2 - 4J}}{2} \qquad r_2 = \frac{-F + \sqrt{F^2 - 4J}}{2} \qquad P = \frac{H}{(-F \times k_o) + J + k_0^2}$$

Need to know what c_1, c_2 etc. equal.

Find expression for c_2 at $t = 0$:

At $t = 0$, $e^{0 \times r1}$ etc. $= 1$, so:

$$[OH]_0 = c_1 + c_2 + P$$

$$C_2 = [OH]_0 - c_1 - P \qquad \text{sub this into eqn. 4:}$$

$$[OH]_t = c_1 e^{t \times r1} + ([OH]_0 - c_1 - P)e^{t \times r2} + Pe^{-ko \times t} \qquad \text{eqn. 5}$$

Differentiate eqn.5:

$$\frac{d[OH]}{dt} = r_1 c_1 e^{t \times r1} + r_2([OH]_0 - c_1 - P)e^{t \times r2} + (-k_o P)e^{-ko \times t}$$

At $t = 0$ $\qquad \frac{d[OH]}{dt} = r_1 c_1 + r_2([OH]_0 - c_1 - P) + (-k_o P)$

When at $t = 0$, $[R]_0 = 0$, so eqn. 1 becomes $\frac{d[OH]}{dt} = C[O]_0 + A[OH]_0$

So, $\frac{d[OH]}{dt} = C[O]_0 + A[OH]_0 = r_1 c_1 + r_2([OH]_0 - c_1 - P) + (-k_o P)$

$$W = -k_o P$$

Rearrange this for c_1:

$$c_1 = \frac{C[O]_0 + A[OH]_0 - W + r_2 P - r_2[OH]_0}{(r_1 - r_2)}$$

Now have fit expression (eqn. 4), with c_2 in terms of c_1, and c_1 in terms of rates.